

# Alignment of energy levels in amorphous oxides and at semiconductor-water interfaces

Thèse N° 9142

Présentée le 28 février 2019

à la Faculté des sciences de base

Chaire de simulation à l'échelle atomique

Programme doctoral en science et génie des matériaux

pour l'obtention du grade de Docteur ès Sciences

par

**Zhendong GUO**

Acceptée sur proposition du jury

Prof. V. Michaud, présidente du jury

Prof. A. Pasquarello, directeur de thèse

Prof. J. Cheng, rapporteur

Dr P. Broqvist, rapporteur

Prof. N. Marzari, rapporteur

2019



There is only one heroism in the world:  
to see the world as it is, and to love it.  
— Romain Rolland

To everyone...





# Acknowledgements

Pursuing the Ph.D. degree at EPFL has been an amazing experience for me. This could not be achieved without all the people who support me throughout these years. Firstly, I would like to express my sincere gratitude to my advisor Prof. Alfredo Pasquarello for providing me this great opportunity to participate in doing research under his supervision, for letting me work on this interesting and comprehensive project in a comfortable environment at this beautiful place, for his continuous support of my Ph.D. study. All of my achievements would not have been possible without his trust and patience.

I would like to also gratefully thank Dr. Francesco Ambrosio, the postdoctoral assistant who supervised me during my whole Ph.D. study. His guidance helped me in all the time of research. I have learned a lot from him, from his knowledge contributing to the technical work of this thesis, and from his patience in revising all my publications.

During my stay at EPFL I met many friends with whom I enjoyed the sun and the snow, the joy and the sadness. Thanks to Miceli, Chen, Bouzid, Reshetnyak, Wiktor, Colleoni, Gono, Bischoff, Tal, Wu, Zhang, Ma, Lee, Gosalbez Martinez, Katukuri, Pasquier, Pizzochero, Eduardo. Many thanks also to Noemi, Tanya and Évéquoz for their help and their support. I also want to thank Zhang and Tang for the pleasure time they shared with me. All of you deserve a special thank but because of the little time I have, just accept my "Thank you!".

I would like to thank my family: my parents and my brother for supporting me spiritually. Their love provides me the infinite motivation and courage to finally achieve the goal.

Last but not the least, I thank Meihua for having followed me, stayed with me, chosen me, and loved me every day.

*Lausanne, January 2019*

Zhendong Guo



# Abstract

Amorphous oxides are currently key materials in many technological applications, e.g. as gate dielectrics in metal-oxide-semiconductor (MOS) devices, and as coating layers to protect water-splitting photoanodes from corrosion. It is experimentally demonstrated that a sizeable amount of impurities (e.g. carbon, nitrogen and hydrogen) are inevitably incorporated into these amorphous films either intentionally or unintentionally, due to doping or to the growth process. Defects, including both extrinsic and intrinsic, may induce some defect levels and impact the performance of these oxides in special applications. To understand their underlying role, we conduct a detailed investigation of defects in two representative amorphous oxides: amorphous  $\text{Al}_2\text{O}_3$  (am- $\text{Al}_2\text{O}_3$ ) and  $\text{TiO}_2$  (am- $\text{TiO}_2$ ), by combining *ab initio* molecular dynamics (MD) simulations and hybrid functional calculations. Our results indicate that oxygen vacancies and interstitials occur neither in am- $\text{Al}_2\text{O}_3$  nor in am- $\text{TiO}_2$  due to structural rearrangements which assimilate the defect structure, and that the injection of extra holes can lead to the formation of O-O peroxy linkages. In am- $\text{Al}_2\text{O}_3$ , hydrogen is found to be amphoteric. Based on localized Wannier functions, we identify the nominal charge state and the composition of the defect core units related to C and N impurities in am- $\text{Al}_2\text{O}_3$ , which are found to depend on the total charge set in the simulation cell. Through the adopted electron counting rule, we assess that carbon and nitrogen impurities are only found in neutral and in singly positive charge states, respectively, indicating that none of them gives charge transition levels in am- $\text{Al}_2\text{O}_3$ . In addition, those defect core units are shown to incorporate a varying number of oxygen atoms, by which their formation energy is dependent on the oxygen chemical potential. After excluding the role of oxygen vacancies in hole diffusion processes in am- $\text{TiO}_2$ , we focus on the formation of O-O pairs to accommodate extra holes and propose an exchange mechanism for hole transport in am- $\text{TiO}_2$  that relies on the simultaneous breaking and forming of O-O peroxy linkages that share one O atom. Through the use of nudged-elastic-band calculations, a hopping path as long as 1.2 nm with barriers of 0.3-0.5 eV is demonstrated, suggesting that hole diffusion through O-O peroxy linkages is viable in am- $\text{TiO}_2$ .

Water-splitting based on artificial photocatalysis at semiconductor-water interfaces represents a promising technology for the clean production of fuel. The main hindrance to the success of such a technology is the lack of highly efficient catalysts. When searching for the ideal material, the alignment of the redox levels at semiconductor-water interfaces is considered as an important criterion to assess the photocatalytic capacity of candidate semiconductor. In this work, we determine the band alignment between various semiconductors and liquid water

## Abstract

---

by combining MD simulations of atomistic interface models, electronic-structure calculations at the hybrid-functional and *GW* levels, and a computational standard hydrogen electrode (SHE). Our study comprises GaAs, GaP, GaN, CdS, ZnO, SnO<sub>2</sub>, rutile and anatase TiO<sub>2</sub>. For each semiconductor, we generate atomistic interface models with liquid water at the pH corresponding to the point of zero charge (pH<sub>ZPC</sub>). The MD simulations are started from initial configurations, in which the water molecules are either molecularly (*m*) or dissociatively (*d*) adsorbed on the semiconductor surface. The calculated band offsets are found to be strongly influenced by the adsorption mode at the semiconductor-water interface, leading to differences larger than 1 eV between *m* and *d* models of the same semiconductor. We then assess the accuracy of various *ab initio* electronic-structure schemes in determining the band alignment. Tuned hybrid-functionals, which reproduce the experimental band gap of the semiconductor, give the most accurate prediction of the relative positions of the band edges versus the SHE, showing a mean absolute error of 0.17 eV with respect to experimental data. In this work, we also try to identify the optimal photocatalyst for water-splitting by considering the surface coverage and the energy alignment. We determine surface concentrations of water molecules, protons, and hydroxyl ions adsorbed at the semiconductor-water interfaces mentioned above as a function of pH. This is achieved through the calculation of the acidity constants at the surface sites, which are derived from *ab initio* MD simulations and a grand-canonical formulation of adsorbates. Our method is validated by the excellent agreement of the resulting pH<sub>ZPC</sub> with experimental data. It is finally shown how the potential of a semiconductor material as photocatalyst for water splitting can be inferred by combining the nature of the surface coverage and the alignment of the band edges to the relevant redox levels.

**Keywords:** Amorphous, defect, hybrid functional, hole diffusion, semiconductor-water interfaces, band alignment, acidity constant

## Résumé

Les oxydes amorphes sont actuellement des matériaux essentiels dans de nombreuses applications technologiques, par exemple, comme diélectriques dans les dispositifs à semi-conducteurs en oxyde de métal (MOS), et en tant que couche de revêtement pour protéger les photoanodes qui séparent l'eau de la corrosion. Il a été démontré expérimentalement qu'une quantité non négligeable d'impuretés (carbone, azote et hydrogène, par exemple) est inévitablement incorporée à ces films amorphes, que ce soit intentionnellement ou non, en raison du dopage ou du processus de croissance. Les défauts, qu'ils soient d'origine extrinsèque ou intrinsèque, peuvent induire certains niveaux de défaut et avoir une incidence sur les performances de ces oxydes dans des applications spéciales. Afin de comprendre leur rôle, nous menons une étude détaillée des défauts dans deux oxydes amorphes représentatifs,  $\text{Al}_2\text{O}_3$  amorphe (am- $\text{Al}_2\text{O}_3$ ) et  $\text{TiO}_2$  (am- $\text{TiO}_2$ ), en combinant des simulations *ab initio* de dynamique moléculaire et des calculs avec des fonctionnels hybrides. Nos résultats indiquent que les lacunes en oxygène et les interstitielles d'oxygène ne se produisent ni dans l'am- $\text{Al}_2\text{O}_3$  ni dans l'am- $\text{TiO}_2$ , en raison de réarrangements structurels qui assimilent la structure du défaut, et que l'injection de trous supplémentaires peut conduire à la formation de liaisons peroxy. Dans am- $\text{Al}_2\text{O}_3$ , l'hydrogène se révèle amphotère. Sur la base de fonctions de Wannier localisées, nous identifions l'état de charge nominal et la composition de l'unité centrale du défaut liée aux impuretés C et N dans am- $\text{Al}_2\text{O}_3$ , dépendant de la charge totale définie dans la cellule de simulation. Grâce à la règle de comptage des électrons adoptée, nous déduisons que les impuretés de carbone et d'azote ne se trouvent respectivement que dans un état de charge neutre et dans un état de charge positif, ce qui indique qu'aucune d'entre elles ne donne des niveaux de transition de charge dans am- $\text{Al}_2\text{O}_3$ . De plus, il est démontré que ces unités centrales défectueuses incorporent un nombre variable d'atomes d'oxygène, grâce à quoi leur énergie de formation dépend du potentiel chimique de l'oxygène. Après avoir exclu le rôle des lacunes en oxygène dans la diffusion de trous dans am- $\text{TiO}_2$ , nous prenons en considération la formation de paires O-O induites par des trous supplémentaires, et proposons un mécanisme d'échange pour le transport de trous dans am- $\text{TiO}_2$ , reposant sur la rupture et la formation simultanées de liaisons peroxy O-O qui ont un atome d'oxygène en commun. Par nos calculs, nous avons démontré l'existence d'une trajectoire de longueur d'une 1,2 nm contenant des barrières de 0,3 à 0,5 eV, ce qui suggère que la diffusion de trous via des liaisons peroxy O-O est viable dans am- $\text{TiO}_2$ .

Le fractionnement de l'eau basé sur la photocatalyse artificielle à l'interface semiconducteur-eau représente une technologie prometteuse pour la production de carburant propre. Le

principal obstacle au succès de cette technologie est le manque de catalyseurs hautement efficaces. Dans la recherche du matériau idéal, l'alignement des niveaux d'oxydoréduction aux interfaces semiconducteur-eau est un critère important pour évaluer la capacité photocatalytique de semi-conducteurs candidats. Dans ce travail, nous déterminons l'alignement des bandes entre divers semi-conducteurs et l'eau liquide en combinant des simulations de dynamique moléculaire de modèles atomistiques d'interface, des calculs de structure électronique au niveau de fonctionnel hybride et de *GW*, et un électrode computationnel standard d'hydrogène (SHE). Notre étude comprend GaAs, GaP, GaN, CdS, ZnO, SnO<sub>2</sub>, rutile et anatase TiO<sub>2</sub>. Pour chaque semiconducteur, nous générons des modèles d'interface atomistique avec de l'eau liquide au pH correspondant au point de charge zéro (pH<sub>ZPC</sub>). Les simulations de dynamique moléculaire sont démarrées de configurations initiales, dans lesquelles les molécules d'eau sont adsorbées de manière moléculaire (*m*) ou dissociative (*d*) sur la surface du semiconducteur. Les décalages de bande calculés sont fortement influencés par le mode d'adsorption à l'interface semiconducteur-eau, ce qui entraîne des différences supérieures à 1 eV entre les modèles *m* et *d* du même semiconducteur. Nous évaluons ensuite la précision de divers schémas de structure électronique *ab initio* pour déterminer l'alignement des bandes. Il est à noter que les fonctionnels hybrides ajustés pour reproduire la bande interdite expérimentale du semi-conducteur donnent les prévisions les plus précises des positions des bandes énergétiques du semiconducteur par rapport au SHE, montrant une erreur absolue moyenne de 0.17 eV par rapport aux données expérimentales. Dans ce travail, nous essayons également d'identifier le photocatalyseur optimal pour la séparation de l'eau en considérant la couverture de surface et l'alignement d'énergie. Nous déterminons les concentrations en surface de molécules d'eau, de protons et d'ions hydroxyles adsorbés aux interfaces semiconducteur-eau mentionnées précédemment en fonction du pH. Ceci est réalisé par le calcul des constantes d'acidité sur les sites de la surface, à partir de simulations de dynamique moléculaire *ab initio* et d'une formulation grand-canonique d'adsorbats. Notre méthode est validée par l'excellent accord du pH<sub>ZPC</sub> résultant avec les données expérimentales. Nous montrons enfin comment on peut déduire le potentiel d'un matériau semiconducteur en tant que photocatalyseur pour la dissociation de l'eau en combinant la nature de la couverture de surface et l'alignement des bandes électroniques par rapport aux niveaux rédox correspondants.

**Mots-clés :** Amorphe, défaut, fonctionnel hybride, diffusion de trou, interfaces semiconducteur-eau, alignement de bande, constante d'acidité

# Contents

<b>Acknowledgements</b>	<b>i</b>
<b>Abstract (English/Français)</b>	<b>iii</b>
<b>1 Introduction</b>	<b>1</b>
1.1 Defect study in amorphous oxides . . . . .	2
1.2 Motivation for investigating defects in am- $\text{Al}_2\text{O}_3$ . . . . .	3
1.3 Motivation for investigating hole transport in am- $\text{TiO}_2$ . . . . .	4
1.4 Water-splitting photocatalysts . . . . .	4
1.5 Current research status of band alignment at semiconductor-water interfaces . . . . .	6
1.6 Outline of the thesis . . . . .	7
<b>2 Methodology</b>	<b>11</b>
2.1 Hybrid density functional theory . . . . .	11
2.1.1 PBE0 functional . . . . .	12
2.1.2 HSE functional . . . . .	12
2.2 Defect study . . . . .	13
2.2.1 Defect formation energy . . . . .	13
2.2.2 Finite-size corrections . . . . .	14
2.3 Thermodynamic integration . . . . .	15
2.4 Computational standard hydrogen electrode . . . . .	16
2.4.1 Free energy of formation of solutes . . . . .	16
2.4.2 Standard hydrogen electrode (SHE) . . . . .	17
2.5 Computational details . . . . .	19
2.5.1 Molecular dynamics simulations of semiconductor-water interfaces . . . . .	19
<b>3 Defects in amorphous <math>\text{Al}_2\text{O}_3</math></b>	<b>21</b>
3.1 Model generation . . . . .	21
3.2 Intrinsic defects in amorphous $\text{Al}_2\text{O}_3$ . . . . .	22
3.2.1 Oxygen vacancy . . . . .	22
3.2.2 Interstitial oxygen . . . . .	24
3.3 Extrinsic impurities in amorphous $\text{Al}_2\text{O}_3$ . . . . .	27
3.3.1 Hydrogen . . . . .	27
3.3.2 Carbon . . . . .	29

## Contents

---

3.3.3 Nitrogen . . . . .	35
3.4 Alignment to semiconductor band edges . . . . .	37
3.5 Conclusion . . . . .	38
<b>4 Transport of holes in amorphous TiO<sub>2</sub></b>	<b>41</b>
4.1 Model of amorphous TiO <sub>2</sub> . . . . .	41
4.2 Intrinsic defects in amorphous TiO <sub>2</sub> . . . . .	44
4.2.1 Oxygen vacancy . . . . .	44
4.2.2 Double hole polaron . . . . .	45
4.3 Hopping of holes in amorphous TiO <sub>2</sub> . . . . .	48
4.4 Conclusion . . . . .	49
<b>5 Alignment of energy levels at semiconductor-water interfaces</b>	<b>51</b>
5.1 Methods . . . . .	52
5.1.1 Electronic-structure calculations . . . . .	52
5.1.2 Band alignment at semiconductor-water interfaces . . . . .	57
5.2 Absolute energy levels of liquid water . . . . .	59
5.3 Electronic properties of semiconductors . . . . .	62
5.4 Interface models . . . . .	66
5.4.1 Generation protocol . . . . .	66
5.4.2 Structural properties of semiconductor-water interfaces . . . . .	68
5.5 Band alignment . . . . .	70
5.5.1 Assignment of semiconductor-water interfaces . . . . .	71
5.5.2 Experimental reference values . . . . .	73
5.5.3 Benchmark of electronic-structure methods . . . . .	75
5.5.4 Comparison with previous work . . . . .	78
5.6 Conclusion . . . . .	80
<b>6 Evaluation of photocatalysts for water splitting through combined analysis of surface coverage and energy-level alignment</b>	<b>83</b>
6.1 General motivation . . . . .	84
6.2 Theoretical formulation . . . . .	85
6.3 Method . . . . .	92
6.3.1 Calculation of deprotonation energy . . . . .	92
6.3.2 Electrostatic finite-size corrections . . . . .	93
6.3.3 Energy of zero-point motion . . . . .	94
6.4 Comparison of pH <sub>PZC</sub> and pK <sub>a</sub> achieved with semilocal and hybrid functionals	95
6.5 Acid-Base properties . . . . .	98
6.5.1 Acidity of semiconductor surfaces . . . . .	98
6.5.2 Surface concentration of adsorbates vs. pH . . . . .	100
6.6 Band alignment vs. pH . . . . .	102
6.7 Discussion and conclusion . . . . .	107



<b>7 Conclusion</b>	<b>109</b>
<b>A An appendix</b>	<b>113</b>
<b>Bibliography</b>	<b>141</b>
<b>Curriculum Vitae</b>	<b>143</b>



# 1 Introduction

The alignment of defect levels with respect to the band edges of host materials and that of electronic energy levels at a hetero-interface between two materials critically control the performance of related electronic devices in such diverse areas as semiconductor electronics, batteries, and electrochemical cells. The energy level alignment rests on the band edge energy offset, and theoretical approaches at various levels have been developed to determine this property. However, the corresponding energy level alignments in amorphous materials and at solid-electrolyte interfaces still present fundamental challenges, due to the extreme complexity of the structures. As a significant example, the alignment of defect levels in amorphous oxides, determines the potential performance of these oxides in various applications when sizeable concentrations of defects occur, which is of significance for the design of related devices. The relative alignment of the semiconductor band edges and the redox levels in liquid water corresponding to another representative example, clearly indicates the photocatalytic ability of the semiconductor to promote the hydrogen reduction and water oxidation reactions and is considered as a basic element in the design of highly efficient artificial photosynthesis systems. Motivated by these issues, we develop in this thesis first-principles approaches to achieve the alignment of energy levels in amorphous oxides and at semiconductor-water interfaces. We investigate the influence of possible defects in amorphous  $\text{Al}_2\text{O}_3$  and  $\text{TiO}_2$  on their electronic properties and evaluate photocatalysts for water splitting through a combined analysis of the surface coverage and energy-level alignment.

In the chapter of Introduction, we first report the current research status and challenge of defect studies in amorphous oxides (Section 1.1). We then present the motivations for conducting investigations of defects in am- $\text{Al}_2\text{O}_3$  (Section 1.2) and of hole transport in am- $\text{TiO}_2$  (Section 1.3). Next, the main processes in photocatalytic water splitting and the band alignment requirement for the oxygen and hydrogen evolution levels of ideal photocatalysts are reported in Section 1.4. In Section 1.5, we discuss the current research status of band alignment at semiconductor-water interfaces, and point out that most of the computational studies have been performed either neglecting the interactions at the semiconductor-water interface or adopting various approximations to cope with them, which may lead to large

errors and can affect the accuracy of oversimplified screening protocols. Finally, we present the outline of this thesis in Section 1.6.

### 1.1 Defect study in amorphous oxides

Amorphous oxides are an important class of materials and have found numerous technological applications, e.g., as electron collection electrodes in organic solar cells [1], channel layers in transparent thin-film transistors [2, 3], high capacity negative electrodes in lithium batteries [4, 5], and resistance switching layers in non-volatile memory devices [6]. It is experimentally demonstrated that these oxides inevitably contain plenty of defects, either intentionally or unintentionally as a result of the deposition process [7, 8, 9, 10, 11]. Therefore, there is considerable interest in understanding how defects, either intrinsic or extrinsic, affect the electronic properties, and consequently the performance of the material in the various applications. The general understanding of defects in crystalline materials has progressed noticeably through a profitable interaction between experiment and theory, the latter having evolved over the years and grown into relatively standard protocols for evaluating defect energies and concentrations [12, 13]. However, the study of defects in amorphous oxides has lagged behind. Two types of approaches are typically followed. One approach consists in putting aside the disordered nature of the oxide and taking various crystalline phases as suitable models for the amorphous oxide. In an alternative approach, one adopts a truly disordered model structure of the amorphous oxide, for instance, as generated by a quench from the melt through molecular dynamics (MD). In the latter case, the actual defect investigation then follows the standard protocol developed for studying defects in crystalline materials. However, neither scheme fully captures the ability of the amorphous oxide to incorporate defects through structural rearrangements.

The study of defects in a model structure of the amorphous oxide requires the consideration of various aspects, which are not common to the study of defects in a crystalline solid. First, a variety of sites needs to be taken under consideration to properly account for the different chemical environments occurring in the amorphous system. This aspect is generally dealt with in a statistical manner by considering a set of defect configurations that encompass the diversity in the amorphous oxide. A second difficulty arises when extracting the proper energetics. It is then necessary to disentangle the energy associated to the defect from the relaxation energy of the amorphous structure, which is only partially captured in a model of finite size and is subject to change upon defect generation or charge transition. To minimize this effect, it has been proposed to introduce a cycling procedure to optimally capture the relaxation energy of the amorphous structure [14, 15]. Third, the potential energy surface of amorphous materials can be rather complex with plenty of local energy minima, so that the relaxation of a defect created in an amorphous model generally leads to a local minimum, which may differ significantly both in structure and in energy from the equilibrium configuration. The use of MD and thermal annealing cycles facilitates the exploration of the potential energy surface and generally leads to more stable defect configurations [14, 15]. Fourth, the nominal charge

state of an extrinsic defect could differ from the charge added to the simulation cell, due to its (partial) localization on intrinsic defects. All these considerations indicate that the study of defects in an amorphous oxide requires particular care, which goes well beyond the trivial extension of the procedure generally applied to defects in crystalline materials. In particular, it also appears that it is recommended to have a deep understanding of the possible intrinsic defects before considering the investigation of extrinsic impurities.

## 1.2 Motivation for investigating defects in am-Al<sub>2</sub>O<sub>3</sub>

Amorphous alumina (am-Al<sub>2</sub>O<sub>3</sub>), an earth-abundant oxide with a wide electronic band gap, a low leakage current, and a modest value of dielectric constant. For these reasons, am-Al<sub>2</sub>O<sub>3</sub> is widely used in a variety of technological applications. These include gate dielectrics in metal-oxide-semiconductor (MOS) devices [16, 17, 18, 19, 20], coating layers for protecting cathodes in lithium-ion batteries from corrosion [21, 22, 23], overlayers on hematite photoanodes for reducing the overpotential of the water splitting reaction [24]. In these applications, the atomic layer deposition (ALD) technique is often used to deposit *a*-Al<sub>2</sub>O<sub>3</sub> [25, 26, 27]. The ALD procedure features metal-organic precursors which always undergo incomplete decomposition, due to low-temperature growth conditions. This in turn leads to the incorporation of a sizable amount of impurities [28, 29]. Concentrations up to 0.2 at. % of carbon [8] and ~5.0 at. % of nitrogen [9] have been detected. ALD processes also make use of water, thus giving non-negligible concentrations of hydrogen in the amorphous material [30].

However, despite clear evidence for the occurrence of such extrinsic impurities in am-Al<sub>2</sub>O<sub>3</sub>, much less is known about the effects of these defects on the electronic properties of the material and in turn on its performance in applied systems. Besides extrinsic impurities, native defects such as the oxygen vacancy and interstitial in am-Al<sub>2</sub>O<sub>3</sub> may also affect the performance of MOS devices through leakage channels generated by deep levels in the band gap of the channel materials. The experimental characterization of oxygen-related defect states in am-Al<sub>2</sub>O<sub>3</sub> has led to conflicting interpretations. Perevalov *et al.* [31] proposed oxygen vacancies acting as electron traps in oxygen-deficient am-Al<sub>2</sub>O<sub>3</sub> films produced via ALD on the basis of electron energy loss, photoluminescence measurements, and density functional theory (DFT) calculations. At variance, Århammar *et al.* [32] synthesized am-Al<sub>2</sub>O<sub>3</sub> through physical vapour deposition and investigated the defect states in the gap using X-ray absorption and resonant inelastic scattering techniques. Supplementing their experimental results with computational studies, they assigned the observed defect states to peroxy linkages between two oxygen atoms (O-O) rather than to oxygen vacancies. Furthermore, the role of am-Al<sub>2</sub>O<sub>3</sub> as an overlayer of hematite photoanodes has been debated. In fact, given the large band gap of am-Al<sub>2</sub>O<sub>3</sub> (6.1–7.0 eV [33, 34, 35]), photogenerated holes in the valence band of hematite should not be able to migrate across the amorphous overlayer. A tunneling mechanism has been invoked in Ref. [24]. Nevertheless, the interpretation of the experiments is still debated and a possible role of defects in am-Al<sub>2</sub>O<sub>3</sub>, favoring or hindering the working mechanism of these water splitting devices should be clarified.

Up to now, extensive theoretical investigations of defects in am- $\text{Al}_2\text{O}_3$  have been performed [36, 37, 38, 39, 40, 41, 42, 43, 44, 45, 46, 47, 48, 49, 50, 51], but the vast majority of these studies focused on crystalline phases of  $\text{Al}_2\text{O}_3$ . In particular, this applies to the impurities of carbon and nitrogen in am- $\text{Al}_2\text{O}_3$ . Given the significant difference in structure, density, and bandgap between amorphous and crystalline  $\text{Al}_2\text{O}_3$  [52], results concerning point defects in crystalline  $\text{Al}_2\text{O}_3$  cannot trivially be generalized to am- $\text{Al}_2\text{O}_3$ . Therefore, a direct investigation of intrinsic (e.g. oxygen vacancy and interstitial) and extrinsic defects (e.g. H, C and N impurities) in am- $\text{Al}_2\text{O}_3$  is of great importance.

### 1.3 Motivation for investigating hole transport in am- $\text{TiO}_2$

Titanium dioxide has been widely studied in the last decades due to its promising performance in a variety of novel technologies, such as dye-sensitized solar cells [53], hydrogen storage [54], photocatalytic water splitting [55], and sensors [56]. In this context, most of the ongoing theoretical research has mainly focused on crystalline phases of  $\text{TiO}_2$ , such as rutile, anatase, and brookite, with a particular focus on the electronic structure [57, 58, 59, 60, 61], the surface chemistry [62, 63], and the  $\text{TiO}_2$ -water interface [64, 65, 66]. However, more recently amorphous  $\text{TiO}_2$  (am- $\text{TiO}_2$ ) has attracted the interest of a growing scientific community, due to its possible application as switching material in resistive memory devices [67], blocking layer in bulk heterojunction solar cells [68], and surface passivation layer in biosensors [69]. A deep interest in the electronic properties of am- $\text{TiO}_2$  has arisen by recent unexpected observations [70, 71] of the performance of this material as a coating layer for photoanodes in photocatalytic water splitting [70, 72, 73, 74, 75]. In particular, an am- $\text{TiO}_2$  overlayer has been used to stabilize Si, GaAs, GaP, and  $\text{Fe}_2\text{O}_3$  photoanodes [70, 71]. Surprisingly, the insulating overlayer of am- $\text{TiO}_2$  does not only protect the photocatalyst from degradation, but it also allows the photogenerated holes to diffuse through the amorphous layer showing a thickness ranging from 4 to 143 nm and to reach the interface with liquid water [Fig. 1.1], thus behaving as a leaky channel rather than as an insulating layer [70]. An attempt to explain this leaky behavior in terms of oxygen vacancy hopping has recently been put forward [76], while a possible role of extrinsic defects has been excluded due to the low estimated mobility of charge carriers [77, 78]. However, the nature of intrinsic defects in amorphous materials has recently been questioned and it has been proposed that oxygen vacancies may actually not occur in amorphous oxides [15]. Therefore, it is of interest to investigate in more detail the possible transport mechanisms of holes in a technologically relevant material, such as am- $\text{TiO}_2$ .

### 1.4 Water-splitting photocatalysts

Since the pioneering work of Fujishima and Honda in 1972 [55], large efforts have been devoted to the study of photocatalytic water splitting, a promising and eco-friendly technology for fuel production [79, 80, 81, 82, 83]. A key component of a photocatalytic system for water splitting is the photocatalyst, a semiconducting material that harvests the artificial or natural light,

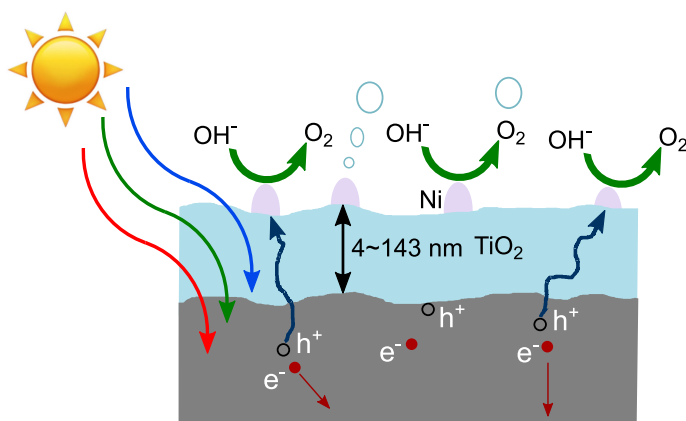


Figure 1.1 – Cross-sectional schematic of a photoanode stabilized against corrosion in a 1.0 M KOH(aq) by a thick electronically defective layer of unannealed TiO<sub>2</sub> deposited by ALD. Instead of corroding the anode, the photogenerated holes are conducted through the TiO<sub>2</sub> to Ni electrocatalysts, where the holes are used to oxidize water to O<sub>2</sub>. [adapted from Ref. [70]]

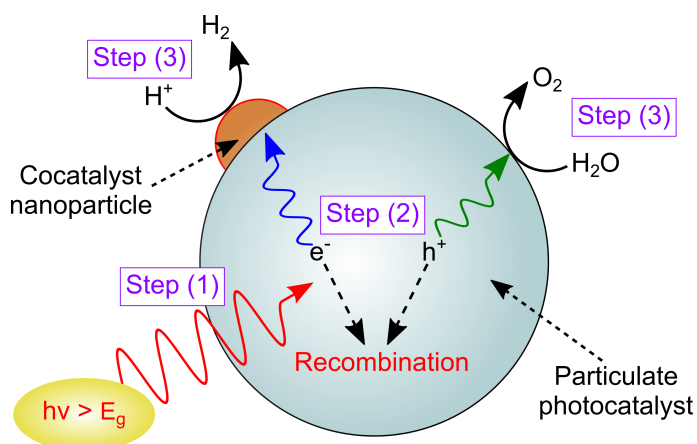


Figure 1.2 – A schematic illustration of the photocatalysts and main processes in photocatalytic water splitting. Step (1): photon adsorption and electron-hole excitation; step (2): electron-hole separation and migration to the surface; step (3): hydrogen and oxygen evolution reactions.

thus generating excited holes and electrons for the oxygen and hydrogen evolution reactions respectively [Fig. 1.2], which take place at the interface with water [84]. An ideal photocatalyst should have (i) a band gap  $E_g \geq 1.23$  eV, in order to straddle the hydrogen reduction and the water oxidation redox levels in water, and (ii)  $E_g \leq 3$  eV to be able to capture the largest part of the visible spectrum [85]. Moreover, a favorable alignment of the band edges with respect to the redox levels of liquid water is crucial for the design of an efficient device. In particular, the conduction band edge should be higher than the hydrogen reduction potential ( $H^+/H_2$ ), while the valence band edge should be lower than the water oxidation potential ( $H_2O/O_2$ ), for the overall reaction to be thermodynamically favorable [Fig. 1.3].

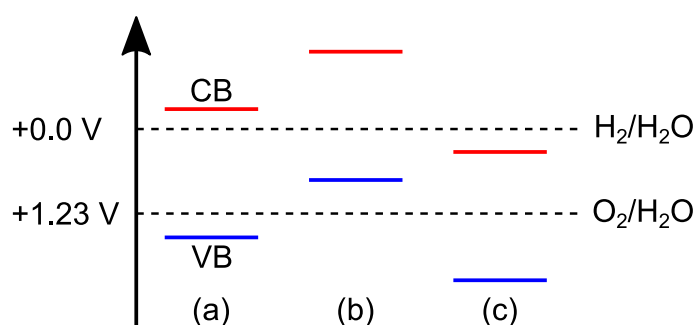


Figure 1.3 – A diagram of the energetic requirements for the band edge positions of the photocatalyst at the solid-water interface. Blue and red lines represent the valence band maximum (VBM) and conduction band minimum (CBM), respectively. (a) Favorable band-edge alignment with respect to redox levels; (b) unfavorable VBM position; (c) unfavorable CBM position.

The search for the ideal photocatalyst has motivated the screening of candidate materials, based on their physical properties [86, 87, 88, 89, 90]. In this context, electronic-structure calculations have been deployed mainly for identifying materials with an adequate band gap [86, 87]. Notwithstanding their general underestimation of the band gap [91, 92], density-functional-theory (DFT) calculations have enabled the high-throughput screening of a large number of candidate materials [86, 87]. Moreover, the recent development of advanced electronic-structure methods going beyond DFT has largely improved the accuracy of calculated band gaps [93, 94], thus allowing also a more refined screening.

## 1.5 Current research status of band alignment at semiconductor-water interfaces

The alignment of semiconductor band edges at the interface with liquid water has been less studied. Most of the computational studies have been performed either neglecting the interactions at the semiconductor-water interface or adopting various approximations to cope with them. This has led to results of different levels of accuracy [95, 96, 97, 86, 87, 98, 99, 100, 88, 101, 102, 103, 104]. Castelli *et al.* calculated the band gap of semiconductors with DFT calculations and used an empirical formula for connecting the position of the band edges with the electronegativity of the material under consideration. This simple scheme was employed to screen ~19000 perovskites [86, 87]. Stevanović *et al.* considered the band edges at the semiconductor-water interface to be approximately equivalent to the ionization potential and the electron affinity, which were then calculated at the *GW* level [98]. The same method was employed to estimate the band alignment for monochalcogenides through the use of both hybrid functionals and *GW* calculations [88].

The neglect of the atomic and electronic structure at the semiconductor-water interface may lead to large errors and can affect the accuracy of oversimplified screening protocols [100].



In particular, the orientation of the interfacial dipoles can only be accounted for through a proper atomistic model of the semiconductor-water system. For this reason, a few studies have recently incorporated such an atomistic description in the calculation of the band alignment. Cheng *et al.* aligned the band edges of rutile  $\text{TiO}_2$  and of  $\text{In}_x\text{Ga}_{1-x}\text{N}$  with respect to the standard hydrogen electrode, by combining *ab initio* molecular dynamics (MD) simulations and the thermodynamic integration method [101]. In Refs. [100] and [89], the band alignments were determined through the calculation of the electrostatic potential across the semiconductor-water interface. Atomistic interface models were constructed by placing several layers of water molecules on a semiconductor slab. However, the structures of these interface models were not equilibrated. Therefore, the calculated band offsets may still suffer from the incorrect orientation of the dipoles at the interface. At variance, Kharche *et al.* aligned the band edges of ZnO and GaN with respect to the vacuum level by combining MD simulations of atomistic interfaces with self-consistent *GW* calculations of the band gap [96]. However, it remained unclear whether the observed differences with respect to experimental values should be assigned to the modelling of the interface structure or to the electronic-structure method adopted for the calculation of the band gap and the band edges. A similar alignment scheme was used to determine the band alignment of functionalized Si surfaces in aqueous environment [105, 106].

As an outcome, available studies of the band alignment at semiconductor-water interfaces have either screened a large set of materials through computational schemes of low accuracy or focussed on few interface models at the atomistic level but subject to approximations, of which the effect has yet to be fully understood. In this context, various electronic-structure methods have been used but their accuracy in determining the band alignment has so far not been assessed. However, this knowledge is fundamental to achieve band alignments in a predictive way, especially when searching for novel materials with suitable electronic properties.

## 1.6 Outline of the thesis

The present thesis is organized as follows. In Chapter 2, we give a description of the computational approaches used in this work. First, we introduce hybrid functionals such as PBE0 and HSE adopted in this research. We then discuss the formulation of defect charge transition levels and defect formation energies, and describe the employed finite-size correction scheme. After that, we introduce the thermodynamic integration (TI) method, which is used to calculate the free energy difference between two given states. Subsequently, the theory behind the computational standard hydrogen electrode (SHE) is presented. Finally, the computational details in this work are reported.

In Chapter 3, we first study the electronic properties of the oxygen vacancy and interstitial in am- $\text{Al}_2\text{O}_3$  and demonstrate that these defects do not occur, due to structural rearrangements which assimilate the defect structures. The imbalance of oxygen is found to result in a nonstoi-

chiometric compound in which the oxygen occurs in the form of  $O^{2-}$  ions. Intrinsic oxygen defects are concluded to be unable to trap excess electrons. Next, electronic properties of carbon, nitrogen, and hydrogen impurities in am- $Al_2O_3$  are investigated. Hydrogen is found to be amphoteric with a thermodynamic  $+1/ - 1$  charge transition level lying at  $\sim 4.6$  eV above the VBM. Hydroxyl groups are further shown to lead to the same defect states as observed for hydrogen. Stable defect configurations related to carbon and nitrogen impurities are identified through *ab initio* molecular dynamics and found to depend on the total charge set in the simulation cell. Through the electron counting rule based on maximally localized Wannier functions, we assess that carbon and nitrogen impurities are only found in neutral and in singly positive charge states, respectively, which indicates that neither carbon nor nitrogen give charge transition levels in the band gap. Moreover, the defect core units are shown to incorporate a varying number of oxygen atoms, by which their formation energy depends on the oxygen chemical potential  $\mu_O$ . In oxygen poor conditions, both the carbon and the nitrogen impurity favor bonding to Al atoms, while they tend to form single or double bonds with oxygen atoms as  $\mu_O$  increases.

In Chapter 4, an atomistic model of am- $TiO_2$  consistent with the experimental characterization is first constructed. We then demonstrate that the oxygen vacancies do not occur in am- $TiO_2$ , as they can be assimilated by the amorphous structure upon structural rearrangement. Hence, their role in hole diffusion is ruled out. Subsequently, it is found that O-O peroxy linkages are formed in pristine am- $TiO_2$  upon injection of excess holes. Finally, we show that such linkages can provide a viable mechanism for hole diffusion in am- $TiO_2$ , as illustrated by a diffusion path of 1.2 nm with energy barriers lower than 0.5 eV in our atomistic model of am- $TiO_2$ .

In Chapter 5, we first report the details of the electronic-structure calculations and present the scheme used for the band alignment. Then, we determine the relative position of the calculated SHE level versus vacuum by modeling the water-vacuum interface. The comparison with the well-known experimental value (4.44 eV) allows us to assess the accuracy of the obtained SHE level. Next, we discuss band gaps, ionization potentials, and electron affinities, as achieved with the electronic-structure methods considered in this work, including various *GW* methods and hybrid functionals. Then, we describe the protocol used to generate the semiconductor-water interface models, to study their structural properties, and to determine the relative stability of molecular and dissociated models. In the end, we present the calculated band offsets, assess the overall accuracy of the employed methods, and compare our results with previous work.

In Chapter 6, we study the acid-base chemistry and reactivity of eight different semiconductors at the interface with liquid water: GaAs, GaP, GaN, CdS, ZnO,  $SnO_2$ , rutile  $TiO_2$  (r- $TiO_2$ ), and anatase  $TiO_2$  (a- $TiO_2$ ). By combining extensive *ab initio* molecular dynamics (MD) simulations with a grand-canonical formulation of adsorbates at the semiconductor water interface, we determine the pH at the point of zero charge ( $pH_{PZC}$ ) and find excellent agreement with the available experimental characterization for all considered semiconductors. Through calculating the acidity constant ( $pK_a$ ) of the individual adsorption sites at the interface, we

are capable of investigating for each material the stability of adsorbed protons, hydroxyl ions, and water molecules at different values of pH. Furthermore, we align the band edges of the considered semiconductors at the interface with water by applying a scheme based on the use of potential offsets and of a computational standard hydrogen electron. Therefore, we combine the acid-base chemistry with the alignment of the band edges with respect to the redox levels pertaining to the water splitting reactions. This allows us to get fundamental insights into the reactivity of potential photocatalysts, which would otherwise be inaccessible with approximated computational schemes.

In Chapter 7, the conclusions of this thesis are drawn.



## 2 Methodology

In Section 2.1, the hybrid functional approximations to density functional theory are discussed focusing on PBE0 and HSE functionals. In Section 2.2, the methodology used to calculate defect formation energies and charge transition levels as well as the adopted finite-size correction scheme are described. In Section 2.3, we introduce the thermodynamic integration (TI) methods. In Section 2.4, the theory behind the calculated standard hydrogen electrode (SHE) is presented. Finally, the basic settings for DFT calculations performed with the CP2K package in this research work are described in Section 2.5.

### 2.1 Hybrid density functional theory

Density functional theory (DFT) is a widely used method for computing properties of materials in many fields. This method is based on the Hohenberg-Kohn theorem [107] and on the Kohn-Sham ansatz [108]. Although DFT is exact, the functional form of the exchange-correlation (XC) functional is still unknown and thus has to be approximated. As the simplest class of approximations to the XC functional, the local density approximation (LDA), in which the exchange-correlation functional only depends locally on the electronic density, achieves noticeable success in predicting properties of a wide range of systems, especially the ones possessing slowly varying density, but generally fails in accurately describing the energetics of chemical reactions. The generalized gradient approximation (GGA), in which the XC functional depends on both the electronic density and its gradient, has been demonstrated to overcome such deficiencies to a considerable extent. The GGA functional proposed by Perdew, Burke, and Ernzerhof (PBE) is widely used due to its simplicity and accuracy [109]. However, it suffers from significant band gap underestimations, as other local and semilocal functionals. Generally, local and semilocal functionals underestimate the band gap of semiconductors by 40% or even more [110], and tend to delocalize electronic states (including defects states). Hybrid functionals [111], which combine the exchange of the GGA functional with a fraction of exact-exchange derived from the Hartree-Fock (HF) method, overcome this problem to some extent. They represent the forefront of density functional methods but are computationally expensive. The most used hybrid functionals are the so called PBE0 and HSE functionals.

### 2.1.1 PBE0 functional

The PBE0 functional [112, 113] mixes the Perdew–Burke–Ernzerhof (PBE) exchange energy and the Hartree-Fock exchange energy along with the full PBE correlation energy, and is generally written as:

$$E_{xc}^{\text{PBE0}} = \alpha E_x^{\text{HF}} + (1 - \alpha) E_x^{\text{PBE}} + E_c^{\text{PBE}}. \quad (2.1)$$

In this thesis, the range separated hybrid functional PBE0-TC-LRC [114, 115] is adopted with a tuned cutoff radius. This functional has been implemented to allow for an efficient calculation of exact exchange in CP2K. In this context, the PBE0-TC-LRC functional not only provides a dramatical speedup of the calculations but also leads to no loss of accuracy. The exchange-correlation part of this functional takes the following form:

$$E_{xc}^{\text{PBE0}} = \alpha E_x^{\text{HF,TC}} + \alpha E_x^{\text{PBE,LRC}} + (1 - \alpha) E_x^{\text{PBE}} + E_c^{\text{PBE}}, \quad (2.2)$$

where  $E_x^{\text{HF,TC}}$  is the truncated Hartree-Fock exchange,  $E_x^{\text{PBE,LRC}}$  is the long range PBE exchange with a truncated Coulomb potential,  $E_x^{\text{PBE}}$  is the PBE exchange and  $E_c^{\text{PBE}}$  is the PBE correlation. The truncated Coulomb (TC) version of the Hartree-Fock exchange has the form:

$$E_x^{\text{HF,TC}} = -\frac{1}{2} \sum_{i,j} \iint \psi_i(r_1) \psi_j(r_1) g_{tc}(r_{12}) \psi_i(r_2) \psi_j(r_2) d^3 r_1 d^3 r_2, \quad (2.3)$$

where the operator

$$g_{tc}(r_{12}) = \begin{cases} \frac{1}{r_{12}} & \text{for } r_{12} < R \\ 0 & \text{for } r_{12} > R \end{cases}. \quad (2.4)$$

Here,  $R$  is the cutoff parameter. The long-range correction (LRC) is based on the PBE exchange hole [114]. This functional is similar to HSE06 [116, 117] in that, unlike many other range-separated hybrid functionals, it uses short-range exact exchange and a long-range semi-local functional. In this work, the cutoff radius  $R$  is set to be less than but quite close to half of the smallest lattice parameter of the supercell.

### 2.1.2 HSE functional

The HSE functional proposed by Heyd, Scuseria, and Ernzerhof [116], introduces a range separation of the Fock integral by re-writing:

$$\frac{1}{r} = \underbrace{\frac{\text{erfc}(\omega r)}{r}}_{\text{SR}} + \underbrace{\frac{\text{erf}(\omega r)}{r}}_{\text{LR}}, \quad (2.5)$$

where  $r$  is the electron–electron distance,  $\text{erfc}(\omega r) = 1 - \text{erf}(\omega r)$ , and the parameter  $\omega$  corresponds to an inverse screening length and defines the extent of the exchange kernel in real

space. In this way, only the short-range of the Fock-integral is added to the semilocal exchange:

$$E_x^{\text{HSE}} = \alpha E_x^{\text{Fock,SR}}(\omega) + (1 - \alpha) E_x^{\text{GGA,SR}}(\omega) + E_x^{\text{GGA,LR}}(\omega). \quad (2.6)$$

In this context, the HSE functional reads as:

$$E_{\text{xc}}^{\text{HSE}} = E_x^{\text{HSE}} + E_c^{\text{PBE}} = \alpha E_x^{\text{Fock,SR}}(\omega) + (1 - \alpha) E_x^{\text{GGA,SR}}(\omega) + E_x^{\text{GGA,LR}}(\omega) + E_c^{\text{PBE}}. \quad (2.7)$$

It has been verified that the default setting of  $\omega = 0.11 \text{ bohr}^{-1}$  not only allows for a significant speedup of the calculations but also preserves the accuracy of the HSE functional [116, 118].

As mentioned above, the parameter  $\alpha$  is material dependent and can be tuned to reproduce some properties of the material, such as the band gap in the case of a semiconductor. It has been found that a linear dependence exists between the band-edge positions and the parameter  $\alpha$  [119]. In this thesis, all calculations within the hybrid functional scheme are carried out with the freely available CP2K/QUICKSTEP package [120], with the auxiliary density matrix method (ADMM) implemented [121, 114, 122]. This method, which features the calculation of exchange integrals in a small auxiliary basis set, largely speeds up the otherwise computationally expensive calculations at the hybrid functional level.

## 2.2 Defect study

In this thesis, defects in amorphous oxides are investigated by mainly focusing on the formation energy and on possible thermodynamic charge transition levels.

### 2.2.1 Defect formation energy

The formation energy  $E_f[X^q]$  of a defect  $X$  in its charge state  $q$  as a function of Fermi energy ( $\epsilon_F$ ) referred to the valence band maximum ( $\epsilon_v$ ) is given by the following equation [119, 13]:

$$E_f[X^q] = E_{\text{tot}}[X^q] + E_{\text{corr}}^q - E_{\text{tot}}[\text{bulk}] - \sum_i n_i \mu_i + q(\epsilon_F + \epsilon_v + \Delta v_{0/b}), \quad (2.8)$$

where  $E_{\text{tot}}[X^q]$  is the total energy of the supercell containing a defect  $X$  in the charge state  $q$ ,  $E_{\text{tot}}[\text{bulk}]$  is the total energy of the pristine bulk supercell,  $n_i$  is the number of added or subtracted atoms of the species  $i$  needed to create the defect  $X$ , and  $\mu_i$  is the respective chemical potential.  $\epsilon_v$  is the valence band maximum (VBM) of the bulk model. In this thesis, unless specified otherwise, the chemical potentials of hydrogen ( $\mu_H$ ), nitrogen ( $\mu_N$ ), and oxygen ( $\mu_O$ ) are set to half the energy of an isolated hydrogen, nitrogen, and oxygen molecule, respectively. The chemical potential of carbon is defined as  $\mu_C = E_{\text{tot}}[\text{CO}_2] - 2\mu_O$ . Here,  $E_{\text{tot}}[\text{CO}_2]$  represents the energy of an isolated carbon dioxide molecule. The potential alignment term  $\Delta v_{0/b}$  accounts for the potential shift between the bulk and the neutral defect calculation. Fi-

nally,  $E_{\text{corr}}^q$  corrects finite-size effects due to the long-range nature of the Coulomb interaction which affects charged systems under periodic boundary conditions (PBC). In this thesis, the total energy of a charged system is corrected according to the scheme proposed by Freysoldt, Neugebauer, and Van de Walle [123]. When studying defects in a solid-state system, a crucial quantity is the charge transition level. This is defined as the specific value of the electron chemical potential  $\epsilon_F$  for which the formation energies of a defect in the charge states  $q$  and  $q'$  are equal:  $E_f[X^q] = E_f[X^{q'}]$ . The expression of the corresponding charge transition level reads as follows:

$$\epsilon(q/q') = \frac{(E_{\text{tot}}[X^q] - E_{\text{tot}}[X^{q'}]) + (E_{\text{corr}}^q - E_{\text{corr}}^{q'})}{q' - q} - (\epsilon_v + \Delta v_{0/b}). \quad (2.9)$$

### 2.2.2 Finite-size corrections

In the study of defects, it is often of interest to investigate the properties of an isolated defect in an otherwise pristine crystal, due to the typically low concentration of defects reported in experiments. Periodic boundary conditions (PBC) are ideal for the description of pristine crystals and are thus often employed in density-functional-theory (DFT) calculations. Under PBC, when defects are introduced in the computational cell, the cell should be sufficiently large to eliminate the interactions of the defect with its periodic images. However, due to technical constraints, the supercells are usually restricted to a limited number of atoms, resulting in the impossible neglect of this unphysical interaction. In addition, supercell calculations for systems containing charged defects must include a compensating background charge, since the electrostatic energy of a system with a net charge in the unit cell diverges [124, 125]. The occurrence of unphysical electrostatic interactions of the defect with its periodic images and the background charge causes the defect energy to converge only slowly with respect to the supercell lattice constant  $L$  and to contain some spurious parts, which must be removed. In this thesis, the finite-size correction scheme proposed by Freysoldt, Neugebauer, and Van de Walle (FNV) [123] is adopted to eliminate these spurious energy contributions. This scheme is shown to be robust and applicable to a large set of defects [13]. In the FNV framework, the electrostatic finite-size correction energy ( $E_{\text{corr}}^q$ ) is expressed as follows:

$$E_{\text{corr}}^q = E_{\text{iso}} - E_{\text{per}} - q\Delta V_{q/0}, \quad (2.10)$$

where  $E_{\text{iso}}$  is the self-energy of the isolated charge distribution  $\rho_c$ , and  $E_{\text{per}}$  represents the electrostatic energy of the system subject to periodic boundary conditions, including both the self-energy of  $\rho_c$  as well as the interaction with the periodic images and with the background charge. Here,

$$E_{\text{iso}} = \frac{1}{2} \int_{\Omega} V_{\text{iso}}(\mathbf{r}) \rho_c(\mathbf{r}) d\mathbf{r}, \quad (2.11)$$



and

$$E_{\text{per}} = \frac{1}{2} \int_{\Omega} V_{\text{per}}(\mathbf{r}) \rho_c(\mathbf{r}) d\mathbf{r}. \quad (2.12)$$

The integrals in eqs. 2.11 and 2.12 are carried out over the simulation cell  $\Omega$ . The prefactor  $\frac{1}{2}$  is required to remove the double counting. The potential  $V_{\text{iso}}$  is determined by solving the Poisson equation for the isolated defect charge distribution  $\rho_c$ , while  $V_{\text{per}}$  is obtained by solving the Poisson equation for the defect charge distribution  $\rho_c$  and the background charge density  $n$  subject to periodic boundary conditions (the average of  $V_{\text{per}}$  is set to zero). The potential alignment term  $q\Delta V_{q/0}$  in eq. 2.10 is obtained by comparing the potential from the model charge to the potential difference (charged vs neutral) in the DFT calculation:

$$\Delta V_{q/0} = (V_q^{\text{DFT}} - V_0^{\text{DFT}})|_{\text{far}} - V^{\text{model}}|_{\text{far}}. \quad (2.13)$$

### 2.3 Thermodynamic integration

Thermodynamic integration (TI) is a widely used method to calculate the free energy difference between two given states (e.g.,  $A$  and  $B$ ), whose potential energies  $U_A$  and  $U_B$  show different dependences on the spatial coordinates. Since the free energy of a system is a function of the Boltzmann-weighted integral over phase space (i.e. partition function) rather than simply a function of the phase space coordinates of this system, it is impossible to directly calculate the free energy difference between states  $A$  and  $B$ . In the thermodynamic integration method, a thermodynamic path between states  $A$  and  $B$  is defined first, which either corresponds to a real chemical process or to an alchemical processes. An example alchemical process is the Kirkwood's coupling parameter method [126]. The free energy difference is then estimated by integrating over ensemble-averaged enthalpy changes along this path.

It is known that the potential energy in either system  $A$  or  $B$  can be calculated as an ensemble average over configurations sampled from a molecular dynamics or Monte Carlo simulation with proper Boltzmann weighting. Here, we define a new potential energy function  $U(\lambda)$  as:

$$U(\lambda) = U_A + \lambda(U_B - U_A). \quad (2.14)$$

where  $\lambda$  is a coupling parameter with a value ranging from 0 to 1. Therefore, the potential energy  $U(\lambda)$  as a function of  $\lambda$  can vary from the potential energy of system  $A$  with  $\lambda = 0$  to that of system  $B$  with  $\lambda = 1$ . In the canonical ensemble, the partition function of the system can be written as:

$$Q(N, V, T, \lambda) = \sum_s \exp[-U_s(\lambda)/k_B T], \quad (2.15)$$

where  $U_s(\lambda)$  is the potential energy of state  $s$  in the ensemble with potential energy function

$U(\lambda)$  as defined above. The free energy of this system can be given by

$$F(N, V, T, \lambda) = -k_B T \ln Q(N, V, T, \lambda). \quad (2.16)$$

When we take the derivative of  $F$  with respect to  $\lambda$ , we will find that it equals the ensemble average of the derivative of potential energy with respect to  $\lambda$ .

$$\begin{aligned} \Delta F(A \rightarrow B) &= \int_0^1 \frac{\partial F(\lambda)}{\partial \lambda} d\lambda = - \int_0^1 \frac{k_B T}{Q} \frac{\partial Q}{\partial \lambda} d\lambda \\ &= \int_0^1 \frac{k_B T}{Q} \sum_s \frac{1}{k_B T} \exp[-U_s(\lambda)/k_B T] \frac{\partial U_s(\lambda)}{\partial \lambda} d\lambda \\ &= \int_0^1 \left\langle \frac{\partial U(\lambda)}{\partial \lambda} \right\rangle_\lambda d\lambda = \int_0^1 \langle U_B(\lambda) - U_A(\lambda) \rangle_\lambda d\lambda \end{aligned} \quad (2.17)$$

The free energy change between states  $A$  and  $B$  can thus be calculated from the integral of the ensemble averaged derivatives of potential energy over the coupling parameter  $\lambda$  [127]. In practice, this calculation is carried out through the following four steps: (i) defining a potential energy function  $U(\lambda)$ , (ii) sampling the ensemble of equilibrium configurations at a series of  $\lambda$  values, (iii) calculating the ensemble-averaged derivative of  $U(\lambda)$  with respect to  $\lambda$  at each  $\lambda$  value, and (iv) computing the integral over the ensemble-averaged derivatives.

## 2.4 Computational standard hydrogen electrode

In this section, the theory behind the computational standard hydrogen electrode (SHE) is presented [128]. Firstly, we express redox levels by developing a formulation based on the grand-canonical approach [129], in analogy to that used for charge transition levels in crystalline materials [12]. Then, the computational version of the SHE based on the reduction of the hydronium ion ( $\text{H}_3\text{O}^+$ ) into the  $\text{H}_2$  and  $\text{H}_2\text{O}$  molecules is demonstrated.

### 2.4.1 Free energy of formation of solutes

We define the Gibbs free energy of formation of a solute  $X$  in the charged state  $q$ ,  $G_f^q[X]$ , as follows [128]:

$$G_f^q[X] = G^q[X] - G[\text{bulk}] - \sum n_i \mu_i + q(\epsilon_v + \mu) + E_{\text{corr}}^q, \quad (2.18)$$

where  $G^q[X]$  is the Gibbs free energy of the solute  $X$  in the charged state  $q$ ,  $G[\text{bulk}]$  is the Gibbs free energy of the pristine system,  $\mu_i$  is the chemical potential of the added/subtracted species  $i$ ,  $\epsilon_v$  is the VBM of the bulk system,  $\mu$  is the electron chemical potential, and  $E_{\text{corr}}^q$  is the correction term taking into account electrostatic finite-size effects in periodic DFT calculations, which is also estimated within Freysoldt-Neugebauer-Van de Walle (FNV) scheme, exactly the same scheme as that used to study defects in crystalline materials [13, 123].

## 2.4. Computational standard hydrogen electrode

The free energy difference associated to the reaction from the reactants (R) in charge state  $q$  to the products (P) in charge state  $q'$  is given by the following expression:

$$\Delta G(q/q') = G^{q'}[\text{P}] - G^q[\text{R}] + (\epsilon_v + \mu)(q - q') + E_{\text{corr}}^{q'} - E_{\text{corr}}^q. \quad (2.19)$$

The redox level can then be defined as the electron chemical potential for which the free energies of formation of  $X$  in the two charge states are equal,  $G_f^q[\text{R}] = G_f^{q'}[\text{P}]$ , which corresponds to

$$\Delta G(q/q') = 0, \quad (2.20)$$

$$\mu(q/q') = \frac{G^q[\text{R}] - G^{q'}[\text{P}]}{q' - q} + \frac{E_{\text{corr}}^q - E_{\text{corr}}^{q'}}{q' - q} - \epsilon_v. \quad (2.21)$$

### 2.4.2 Standard hydrogen electrode (SHE)

The standard hydrogen electrode (SHE), which is defined as a platinum electrode in a theoretical solution where aqueous protons have no interactions with other ions, is based on the following half-reaction [128]:



In this thesis, a computational version of the SHE proposed by Sprik et al. [101] is adopted, which corresponds to the following modified half-reaction:



Therefore, in the DFT-MD simulations, the solvated proton is approximated with the hydronium ion. In this approximation, the transfer of protons from one water molecule to another is neglected. The half-reaction associated with eq. 2.23 can be divided into the following two consecutive reactions:



and



The respective free energies corresponding to these two reactions are expressed as:

$$\Delta G_1(\text{SHE}) = G^{q'+1}[\text{H}^+(\text{g})] + G^{q=0}[\text{H}_2\text{O}(\text{l})] - G^{q'+1}[\text{H}_3\text{O}^+(\text{aq})] - E_{\text{corr}}^{q'+1}, \quad (2.26)$$

$$\Delta G_2(\text{SHE}) = G^{q=0} \left[ \frac{1}{2} \text{H}_2(\text{g}) \right] - G^{q=+1} [\text{H}^+(\text{g})] - \epsilon_v - \mu. \quad (2.27)$$

Here, the free energy difference  $G^{q=0}[\text{H}_2\text{O}(\text{l})] - G^{q=+1}[\text{H}_3\text{O}^+(\text{aq})]$  can be calculated from the deprotonation reaction of the hydronium cation via a thermodynamic integral  $\Delta_{\text{dp}}A_{\text{H}_3\text{O}^+}$  of vertical deprotonation energies  $\Delta_{\text{dp}}E_{\text{H}_3\text{O}^+}$ ,

$$\begin{aligned} G^{q=0}[\text{H}_2\text{O}(\text{l})] - G^{q=+1}[\text{H}_3\text{O}^+(\text{aq})] &= \int_0^1 \langle \Delta_{\text{dp}}E_{\text{H}_3\text{O}^+} \rangle_{\eta} d\eta - \Delta_{\text{zp}}E_{\text{H}_3\text{O}^+} \\ &= \Delta_{\text{dp}}A_{\text{H}_3\text{O}^+} - \Delta_{\text{zp}}E_{\text{H}_3\text{O}^+}, \end{aligned} \quad (2.28)$$

where  $\Delta_{\text{dp}}E_{\text{H}_3\text{O}^+}$  is a zero-point motion correction, which accounts for the error due to the classical treatment of the nuclei in DFT-MD simulations. This quantity  $\Delta_{\text{zp}}E_{\text{H}_3\text{O}^+} = \sum_{i=1}^3 \frac{h\nu_i}{2}$  can be estimated by calculating the vibrational frequencies ( $\nu_i$ ) of the related normal modes associated with a proton in the hydronium ion. The free energies of the gas-phase hydrogen ( $G^{q=0}[\frac{1}{2}\text{H}_2(\text{g})]$ ) and proton ( $G^{q=+1}[\text{H}^+(\text{g})]$ ) are calculated as follows:

$$G^{q=0} \left[ \frac{1}{2} \text{H}_2(\text{g}) \right] = \frac{1}{2} (E_{\text{H}_2} + \mu_{\text{H}_2}^{\text{trans}} + \mu_{\text{H}_2}^{\text{rot}} + \mu_{\text{H}_2}^{\text{vib}}) = \mu_{\text{H}}, \quad (2.29)$$

$$G^{q=+1} [\text{H}^+(\text{g})] = E_{\text{H}^+} + \mu_{\text{H}^+}^{\text{trans}} = \mu_{\text{H}^+}, \quad (2.30)$$

where  $E_{\text{H}_2}$  is the total energy of the hydrogen molecule in vacuum, evaluated from a DFT calculation of an isolated hydrogen molecule.  $E_{\text{H}^+}$  is the total energy of the proton in vacuum and vanishes ( $E_{\text{H}^+} = 0$ ).  $\mu_{\text{H}_2}^{\text{trans}}$ ,  $\mu_{\text{H}_2}^{\text{rot}}$ , and  $\mu_{\text{H}_2}^{\text{vib}}$  represent the translational, rotational, and vibrational contributions to the free energy of  $\text{H}_2(\text{g})$ , respectively.  $\mu_{\text{H}^+}^{\text{trans}}$  represents the translational contribution to the free energy of  $\text{H}^+(\text{g})$ . The translational, rotational, and vibrational contributions to the free energy can be calculated from the respective partition functions,  $Z_{\text{trans}}$ ,  $Z_{\text{rot}}$ , and  $Z_{\text{vib}}$  [130]. In the calculations, we adopt the standard state of concentration, corresponding to a temperature of  $T = 298$  K and pressure of  $p = 24.46$  atm (1 mol/l).

The free energy associated to the overall SHE reaction (eq. 2.23) is given by the sum of the free energies expressed by eqs. 2.26 and 2.27,

$$\begin{aligned} \Delta G(\text{SHE}) &= \Delta G_1(\text{SHE}) + \Delta G_2(\text{SHE}) \\ &= \Delta_{\text{dp}}A_{\text{H}_3\text{O}^+} - \Delta_{\text{zp}}E_{\text{H}_3\text{O}^+} - E_{\text{corr}}^{q=+1} + \mu_{\text{H}} - \epsilon_v - \mu. \end{aligned} \quad (2.31)$$

From  $\Delta G(\text{SHE}) = 0$  [cf. eq. 2.20], we obtain

$$\mu(\text{SHE}) = \Delta_{\text{dp}} A_{\text{H}_3\text{O}^+} - \Delta_{\text{zp}} E_{\text{H}_3\text{O}^+} - E_{\text{corr}}^{q=+1} + \mu_{\text{H}} - \epsilon_{\text{v}}. \quad (2.32)$$

## 2.5 Computational details

In this research, all the calculations are carried out with the freely available CP2K suite of codes, except the *GW* calculations of band gaps of semiconductors, which are performed with the ABINIT code [131]. The CP2K code features a combined atomic basis set/plane-wave approach: atom-centered Gaussian-type basis functions are used to describe the orbitals and an auxiliary plane-wave basis set is employed to re-expand the electron density. Here, analytical Goedecker-Teter-Hutter pseudopotentials [132, 133] are used to account for core-valence interactions. We use a triple- $\zeta$  correlation-consistent polarized basis set (cc-pVTZ) [134] for O, H, C, P, N, and S atoms, and the shorter range molecularly optimized double- $\zeta$  basis set with one polarization function [135] for Al, Ti, Ga, As, Cd, Zn, and Sn atoms. For the plane-waves, a cutoff of 500 Ry is employed. The Brillouin zone is sampled at the sole  $\Gamma$  point. In this thesis, all structural relaxations are carried out with the PBE functional under a force tolerance of  $10^{-4}$  hartree/bohr. All molecular dynamics (MD) simulations are performed in the NVT ensemble with the rVV10 functional [136] for systems containing  $\text{H}_2\text{O}$  water molecules and the PBE functional for the other systems. The temperature is controlled by a Nosé–Hoover thermostat [137, 138]. In order to overcome the band gap underestimation associated with the use of the PBE, the electronic properties of various defects in am- $\text{Al}_2\text{O}_3$  are finally evaluated at the HSE level [116, 118] with the fraction of Fock exchange  $\alpha = 0.44$  and the range-separation parameter  $\omega = 0.11 \text{ bohr}^{-1}$ .

### 2.5.1 Molecular dynamics simulations of semiconductor-water interfaces

Molecular dynamics (MD) simulations of the semiconductor-water interfaces are performed with the rVV10 functional, which accounts for nonlocal van der Waals interactions [139, 140]. The parameter  $b$  of the rVV10 functional is set to the value of 9.3, in order to correctly reproduce the density and the structural properties of liquid water [136]. The MD simulations are carried out in the NVT ensemble with a time step of 0.5 fs. The temperature is set at 350 K to ensure a frank diffusive motion of liquid water and is controlled by a Nosé–Hoover thermostat [137, 138].



## 3 Defects in amorphous $\text{Al}_2\text{O}_3$

This chapter first introduces the method for generating model structures of the defects of interest in Section 3.1. Then, intrinsic (e.g. oxygen vacancy and interstitial) and extrinsic defects (e.g. interstitial hydrogen, carbon and nitrogen) in am- $\text{Al}_2\text{O}_3$  are discussed in Sections 3.2 and 3.3, respectively. Next, the possible electrical activity of the defect levels identified in this work is discussed in Section 3.4. The conclusions of this chapter are drawn in Section 3.5.

### 3.1 Model generation

We use the model of am- $\text{Al}_2\text{O}_3$  generated in Ref. [52], which features an orthorhombic supercell containing 64 Al and 96 O atoms, with lattice constants of 11.47, 11.24, and 12.78 Å, corresponding to a mass density of  $3.29 \text{ g/cm}^3$  in accord with the experimental range ( $3.05\text{--}3.65 \text{ g/cm}^3$ ) [141, 142, 143]. This bulk model was produced via *ab initio* MD simulations through a quench from the melt. The obtained structure shows good agreement with neutron diffraction experiments [52, 141]. With the setting of the fraction of Fock exchange  $\alpha = 0.44$  and the short-range parameter  $\omega = 0.11 \text{ bohr}^{-1}$ , the HSE functional reproduces well the experimental band gap of 9.13 eV of  $\alpha\text{-Al}_2\text{O}_3$  and also gives a bandgap of 6.63 eV for this am- $\text{Al}_2\text{O}_3$  model in accord with the experimental range 6.1–7.0 eV [33, 34, 35]. For the native defects (e.g. interstitial oxygen) and the extrinsic impurities (e.g. hydrogen, carbon and nitrogen), defect structures are generated by a two-step procedure. First, we identify available voids in the amorphous structure, in which the defect atom (O, H, C, and N) is placed. For this, we carry out a Voronoi analysis, which determines the position and the size of the available voids. For each defect atom and for each considered charge state, ten such voids with radii between 1.7 and 2.5 Å are selected and ten different initial configurations are generated by placing the defect atom at their center. Next, each initial configuration is allowed to evolve through *ab initio* MD simulations in the NVT ensemble for a duration of 3 ps. The temperature is set at 1000 K through a Nosé-Hoover thermostat [138, 137]. In this way, the defect atom can optimize its structural configuration on an affordable time scale. It should be noted that the barriers that can be overcome with such a temperature are just of the order of 0.1 eV. In our simulations, these barriers are overcome in a couple of picoseconds. Hence, on the macroscopic time

scales of typical experimental conditions, the system would easily undergo such structural rearrangements, independently of the adopted growth method. We then sample structural configurations at simulation times of 1, 1.5, 2, 2.5, and 3 ps of every MD trajectory and fully relax the structures, until the forces are smaller than  $10^{-4}$  Ha/bohr. Among these 5 relaxed configurations, only the lowest-energy one is kept for further investigation, resulting in 10 models for each defect atom in a given charge state. During the MD runs, the structural rearrangement induced by the defect is always accompanied by a general relaxation of the amorphous structure. To minimize the influence of this effect on the defect formation energy, we carry out a cycling procedure, as proposed earlier in the study of defects in amorphous  $\text{HfO}_2$  (Ref. [14]) and  $\text{Al}_2\text{O}_3$  (Ref. [15]). In this procedure, we first remove the inserted defect atom from its relaxed configuration and relax the resulting structure. Hence, we reinsert the defect atom and relax the structures again. The cycling is continued until the total energies of both the defective and the pristine bulk systems converge within  $10^{-3}$  eV. In this procedure, we only retain the model when the final configuration for the pristine amorphous system shows an energy that is lower than its initial energy and a band gap that does not differ by more than 0.2 eV from the initial one.

### 3.2 Intrinsic defects in amorphous $\text{Al}_2\text{O}_3$

#### 3.2.1 Oxygen vacancy

We first focus on the oxygen vacancy ( $V_{\text{O}}$ ), which is found to be an important defect in crystalline  $\text{Al}_2\text{O}_3$ , as well as in numerous other oxides [144, 145, 146, 147]. In our calculations,  $V_{\text{O}}$  is created by directly removing an O atom from the pristine bulk am- $\text{Al}_2\text{O}_3$  model. For removal, we consider five threefold and five fourfold coordinated O atoms [Fig. 3.1], yielding a distinct defect model for each case upon full structural relaxation. We do not find significant differences among these ten models. The relative energies of the various charge states are illustrated in Fig. 3.2(a) for the most stable  $V_{\text{O}}$  model. As for crystalline oxides [36, 37, 39, 40, 41], the neutral and the +2 charge states are the most stable ones with a +2/0 charge transition level occurring in the band gap of am- $\text{Al}_2\text{O}_3$  at  $\sim 5$  eV from the VBM.

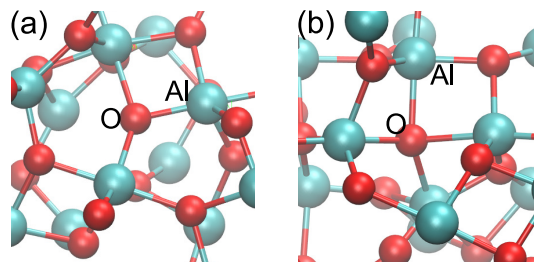


Figure 3.1 – Representation of (a) a threefold and (b) a fourfold O atom in am- $\text{Al}_2\text{O}_3$ , prior to vacancy formation.

To investigate the stability of the neutral oxygen vacancy ( $V_{\text{O}}^0$ ), we then carry out an annealing



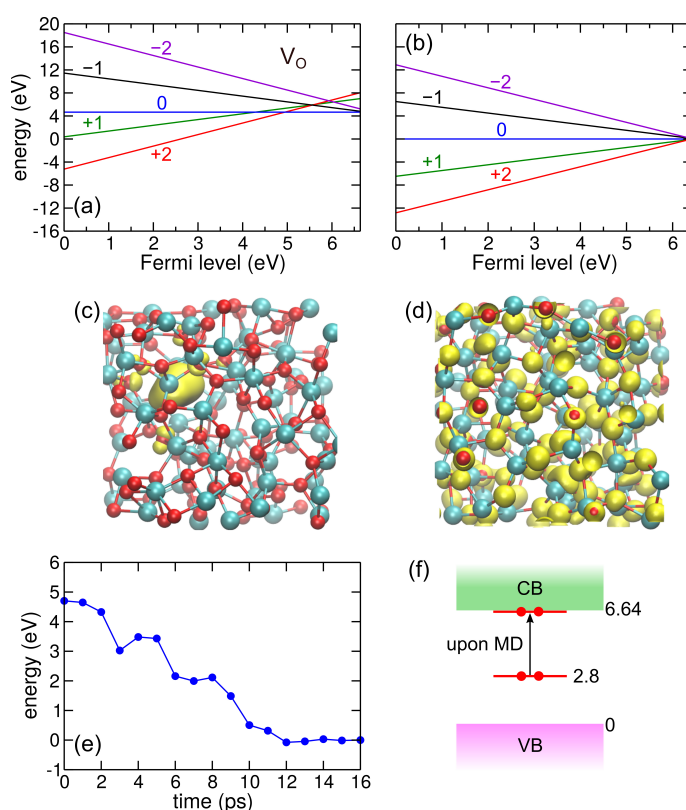


Figure 3.2 – Relative energies of am- $\text{Al}_2\text{O}_3$  upon removal of one O atom, (a) before and (b) after MD annealing. The energies are referred to the energy of the neutral defective system after MD simulation. The extent of the defect state upon the removal of one neutral O atom is illustrated (c) before and (d) after the MD simulation; (e) total energy during the annealing cycle of the neutral O vacancy, obtained by full structural relaxation from configurations occurring during the MD evolution; (f) corresponding evolution of the occupied single-particle energy level of the system upon MD annealing.

cycle using *ab initio* molecular dynamics. Through the use of a Nosé-Hoover thermostat [138, 137], the defect system is first equilibrated at 2000 K for 8 ps and then progressively cooled down to 800 K over a period of 8 ps, corresponding to a cooling rate of 150 K/ps. Other tested cooling rates (100, 200, 300 K/ps) produce final structures of equivalent total energy. We here use a high annealing temperature to accelerate the transition of energy barriers in the structural relaxation around the defect in order to restrain the process to time scales that can be afforded in MD simulations.

To monitor the total energy during the evolution, the system is fully relaxed from MD configurations at regular intervals showing that a stabilization of almost 5 eV is achieved through the annealing cycle [Fig. 3.2(e)]. The evolution is continued until the total energy has clearly reached a plateau value. Recalculation of the defect energies in the various charge states reveals that the charge state +2 now dominates throughout the band gap [Fig. 3.2(b)]. This stabilization is accompanied by a complete disappearance of the void resulting from O re-

removal. Interestingly, even the doubly occupied localized electronic state associated to the vacancy [Fig. 3.2(c)] has evolved to a delocalized state [Fig. 3.2(d)], with a concurrent shift of its single particle level from 2.8 eV above the VBM to the conduction band edge [Fig. 3.2(f)]. Starting the MD from the oxygen vacancy in the +2 charge state, we observe that the localized unoccupied single particle level similarly disappears upon annealing. These results indicate that the vacancy is completely assimilated by the amorphous structure, a property which has previously also been observed for O vacancies in amorphous  $\text{HfO}_2$  [146]. Since any signature of defect localization has vanished, the use of defect formation energies as defined in Eq. 2.8 is inappropriate and the energies in Fig. 3.2 have been referred to the neutral configuration after annealing. The stability of the +2 charge state and the occurrence of delocalized electrons in the neutral charge state indicate that oxygen removal corresponds to the removal of an  $\text{O}^{2-}$  ion, whereby the amorphous is turned into a defect-free substoichiometric oxide,  $\text{am-Al}_2\text{O}_{3-\delta}$ . Thus, unlike in crystalline phases, the oxygen vacancy cannot serve as an electron trap in  $\text{am-Al}_2\text{O}_3$ . The oxygen deficiency results in a release of electrons, which extra charge are likely to be compensated by the formation of defect cores related to N and C impurities, especially under the oxygen poor conditions [cf. Section 3.3].

### 3.2.2 Interstitial oxygen

Next, we investigate the interstitial oxygen ( $\text{O}_i$ ) in  $\text{am-Al}_2\text{O}_3$ , with 3 different charge states: 0,  $-1$ , and  $-2$  considered. For the charge state  $-2$ , the inserted  $\text{O}^{2-}$  ion is found to be either threefold or fourfold coordinated [Fig. 3.1], being thus indistinguishable from regular oxygen configurations in pristine  $\text{am-Al}_2\text{O}_3$ . The same structural configurations are encountered for  $\text{O}^-$ . In the neutral charge state, we systematically observe the formation of an O–O peroxy linkage with an average bond length of 1.51 Å. Here, two bonding patterns for this peroxy linkage are observed: (i) the two O atoms in the peroxy linkage are bonded to different Al atoms [Fig. 3.3(a)] and (ii) the O atoms form one bond to the same Al atom [Fig. 3.3(b)], which are marked as  $(\text{O}-\text{O})_{\text{I}}$  and  $(\text{O}-\text{O})_{\text{II}}$ , respectively. We verify that the formation of this linkage is robust against further structural relaxation at the HSE level. The occurrence of O–O linkages is consistent with NEXAFS and EELS experiments [32].

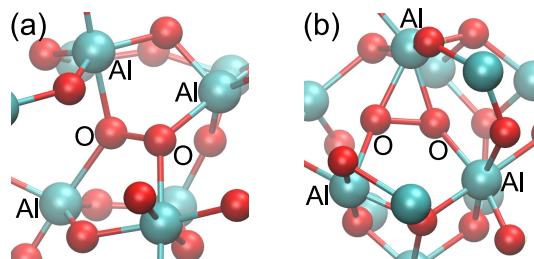


Figure 3.3 – Representation of the O–O peroxy linkages formed upon the insertion of a neutral oxygen in  $\text{am-Al}_2\text{O}_3$ .

The formation energy diagram of  $\text{O}_i$  in  $\text{am-Al}_2\text{O}_3$  are shown in Fig. 3.4. The neutral and  $-2$

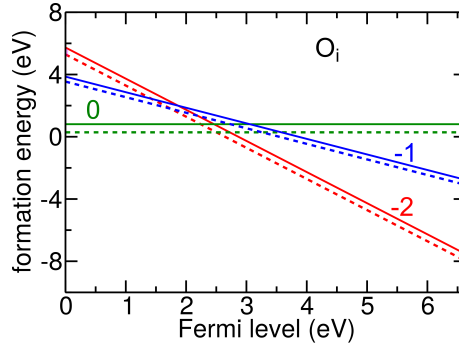


Figure 3.4 – Formation energy of  $\text{O}_i$  in various charge states as a function of Fermi energy. The chemical potential of oxygen is set to half the energy of an oxygen molecule. Solid and dashed lines correspond to the average and minimum values, respectively.

charge states are the most stable charge states with a  $0/-2$  charge transition level at  $\sim 2.5$  eV above the VBM. The charge state  $-1$  is metastable. A statistical analysis of formation energies related to various configurations of  $\text{O}^0$  and  $\text{O}^{2-}$  are summarized in Table 3.1. It is noticed that the  $\text{O}^{2-}$  ion bonding to four Al atoms is energetically more favorable (by  $\sim 0.6$  eV) than the one bonding to 3 Al atoms, which can be attributed to the significant stabilization of the  $\text{O}^{2-}$  ion resulting from the extra Al–O bond. In addition, the  $(\text{O}-\text{O})_{\text{I}}$  configuration is found to be more stable than the  $(\text{O}-\text{O})_{\text{II}}$  one by 0.56 eV, because of the significant distortion of the O–Al–O angle occurring in the latter configuration.

Since extra or missing of O atoms in am- $\text{Al}_2\text{O}_3$  generally appear in the form of  $\text{O}^{2-}$  ions, we investigate whether the formation of an O–O peroxy linkage observed in the case of the neutral  $\text{O}_i$  could be induced by electron depletion. To this aim, we introduce one or two holes ( $\text{h}^+$ ) in the pristine am- $\text{Al}_2\text{O}_3$  model, and apply the same computational procedure employed for  $\text{O}_i$ . Formation energies of holes in am- $\text{Al}_2\text{O}_3$  obtained before and after MD simulations are comparatively shown in Fig. 3.5. Here, only the formation energies corresponding to the most stable model structures are considered, given that they differ by less than 0.5 eV from the average achieved over the set of ten model structures we have kept for each defect. Before

Table 3.1 – Formation energies (in eV) with standard deviations ( $\sigma$ ) for various  $\text{O}_i$  defects in am- $\text{Al}_2\text{O}_3$ . The electron chemical potential is taken at the top of the valence band.  $\text{Al}_{3-n}-\text{O}^{2-}-\text{Al}_n$  and  $\text{Al}_{4-n}-\text{O}^{2-}-\text{Al}_n$  configurations correspond to  $\text{O}^{2-}$  threefold and fourfold coordinated with Al atoms, respectively.  $(\text{O}-\text{O})_{\text{I}}$  and  $(\text{O}-\text{O})_{\text{II}}$  correspond to the peroxy configurations shown in Fig. 3.3 (a) and (b), respectively.

Configuration	formation energy		$\sigma$
	avg.	min.	
$\text{Al}_{3-n}-\text{O}^{2-}-\text{Al}_n$	7.01	5.70	0.33
$\text{Al}_{4-n}-\text{O}^{2-}-\text{Al}_n$	5.42	5.29	0.16
$(\text{O}-\text{O})_{\text{I}}$	0.53	0.26	0.28
$(\text{O}-\text{O})_{\text{II}}$	1.09	0.88	0.23

MD simulation [Fig. 3.5(a)], the single hole is found to be bound with a binding energy of  $\sim 2$  eV, while the system with two holes does not lead to any localized state. However, upon MD simulations, the energy diagram changes considerably [Fig. 3.5(b)]. In particular, the system with two holes undergoes significant stabilization [Fig. 3.5(c)] with its unoccupied single particle state moving from the valence band all the way to the conduction band [Fig. 3.5(d)]. These changes result from the rearrangement of the amorphous structure leading to the formation of an O–O peroxy linkage. In view of these observations, the neutral state of  $\text{O}_i$  should be interpreted as the occurrence of an  $\text{O}^{2-}$  ion with two independent holes. Indeed, this interpretation is also supported by the calculated formation energies. As illustrated in Fig. 3.5(b), we find that the stabilization energy upon the formation of the peroxy linkage is the same when the holes are introduced in the pristine am- $\text{Al}_2\text{O}_3$  or in am- $\text{Al}_2\text{O}_3$  with an additional  $\text{O}^{2-}$  ion, i.e.  $E_f[\text{O}_i^0] - E_f[\text{O}_i^{2-}] = E_f[2\text{h}^+]$ . We remark that the formation of a O–O linkage is a reversible process. When the two missing electrons are returned, they first go into the conduction band but eventually their energy level returns to the valence band upon structural rearrangements which break the O–O bond. Hence, we conclude that the formation of the peroxy linkage is a direct consequence of electron depletion and that the associated charge transition level at 2.5 eV corresponds to the binding of two holes in pristine am- $\text{Al}_2\text{O}_3$ .

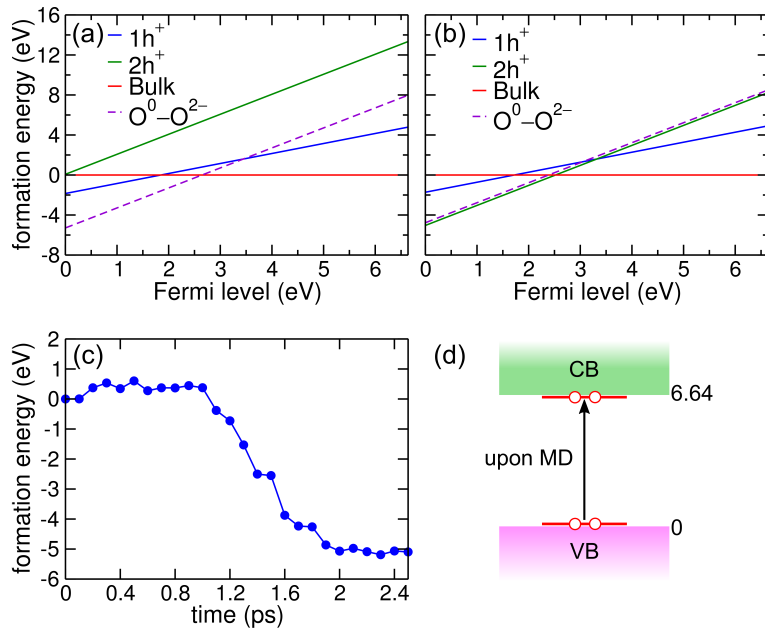


Figure 3.5 – Formation energies of one and two holes in am- $\text{Al}_2\text{O}_3$  as a function of  $\epsilon_F$  with respect to VBM, (a) before and (b) after MD simulations. The formation energy difference between the charge states 0 and  $-2$  for the  $\text{O}_i$ ,  $E_f[\text{O}_i^0] - E_f[\text{O}_i^{2-}]$ , is reported for comparison; (c) total energy during the annealing cycle of the amorphous system with two holes, obtained by full structural relaxation from configurations occurring during the MD evolution; (f) corresponding evolution of the unoccupied single-particle energy level of the system upon MD annealing.

### 3.3 Extrinsic impurities in amorphous $\text{Al}_2\text{O}_3$

#### 3.3.1 Hydrogen

We first focus on hydrogen, which has been extensively investigated in crystalline  $\text{Al}_2\text{O}_3$  [40, 39, 45, 42], as well as in numerous other oxides [45, 42, 148, 149, 14, 150, 151, 152, 153, 154]. In our calculation, three charge states are considered: +1, 0, and -1. Upon MD, the  $\text{H}^+$  is found to bond either to a twofold [Fig. 3.6(a)] or to a threefold coordinated O atom [Fig. 3.6(b)]. On average, configurations with attachments to twofold coordinated O atoms are found to be 0.75 eV more stable than those involving threefold coordinated O atoms. Similarly,  $\text{H}^-$  can form single bonds to Al atoms [Fig. 3.6(d)], but it can also bridge two Al atoms [Fig. 3.6(c)], with the latter configuration being  $\sim 0.9$  eV more stable.

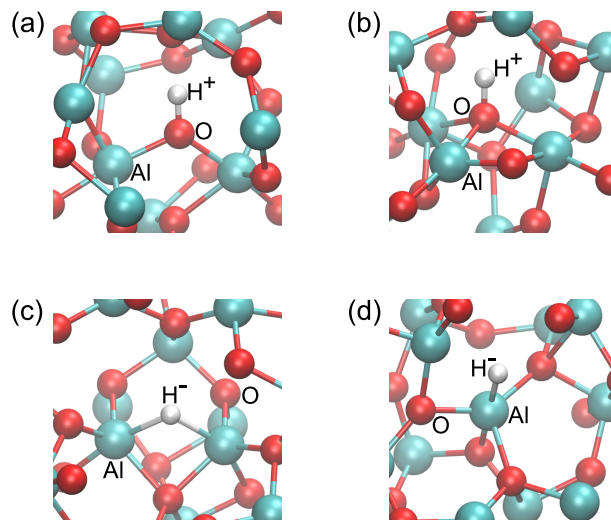


Figure 3.6 – Relaxed atomic configurations of  $\text{H}^+$ , bonding (a) to a twofold coordinated O atom and (b) to a threefold coordinated O atom, and of  $\text{H}^-$  (c) bridging two Al atoms and (d) bonding to a single Al atom. Al atoms are shown in cyan, O atoms in red, and H atoms in white.

In order to investigate the stabilization effect resulting from the MD simulations, the configurations achieved by MD and by structural relaxation only are compared. For  $\text{H}^+$  and  $\text{H}^-$ , the achieved structural configurations show a similar first-neighbor coordination shell. However, a different description applies to the case of the neutral hydrogen atom ( $\text{H}^0$ ). After structural relaxation without performing any MD,  $\text{H}^0$  stays at the center of the void, minimizing the interactions with the surrounding atoms, as previously found in other oxides [42, 45, 14].

At variance, upon MD, the H atom bonds to an oxygen atom [Fig. 3.6(a) and (b)]. This implies that the neutral H atom undergoes oxidation and becomes positively charged ( $\text{H}^+$ ). The missing electron has been donated to the conduction band (CB) of am- $\text{Al}_2\text{O}_3$ , as attested by the delocalized nature of the highest occupied Kohn-Sham orbital (HOMO). In experiments, the detached electron may give rise to the formation of negatively charged defects. In any

event, the present results clearly indicate that neutral H cannot occur in am- $\text{Al}_2\text{O}_3$ .

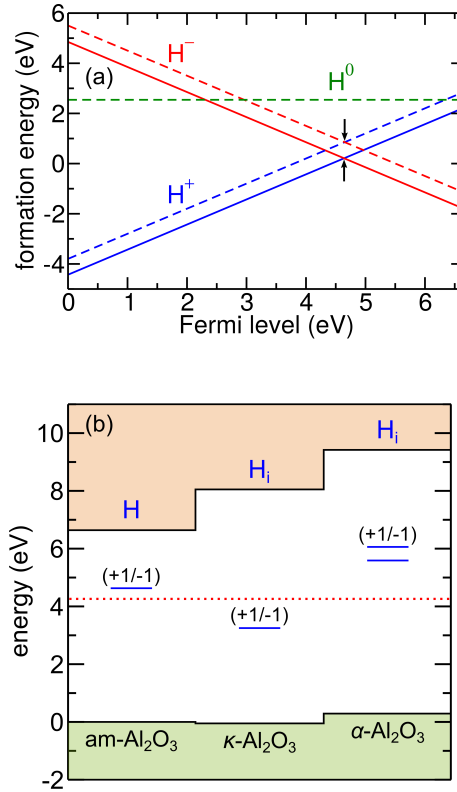


Figure 3.7 – (a) Average formation energies of hydrogen in am- $\text{Al}_2\text{O}_3$  as a function of the Fermi energy ( $\epsilon_F$ ) referred to the VBM, obtained with (solid) and without (dashed) MD simulations. The +1/−1 charge transition level is marked by black arrows. (b) The calculated defect level is compared with corresponding ones in  $\kappa$ - $\text{Al}_2\text{O}_3$  (Ref. [40]) and in  $\alpha$ - $\text{Al}_2\text{O}_3$  (Refs. [42, 51]). The band structures of the three phases of alumina are aligned through the 2s level of twofold coordinated O atoms following Ref. [52]. The universal hydrogen level (red dotted) of Ref. [102] is included through the alignment between GaAs and am- $\text{Al}_2\text{O}_3$  measured in Refs. [33, 34, 35].

The formation energies of H in am- $\text{Al}_2\text{O}_3$  are shown in Fig. 3.7(a) as a function of Fermi level for the charge states +1, −1, and 0. For each charge state, we find that the average formation energies upon MD are lower than those achieved without MD by  $\sim 0.6$  eV, indicating that the MD runs significantly contribute to the stabilization of hydrogen impurities in amorphous oxide models. As found in numerous semiconductors and oxides [102, 42], the stable states correspond to the charge states +1 and −1. We also remark that when the Fermi level is in the CB, the energy of  $\text{H}^0$  is higher than that of  $\text{H}^+$  upon MD, further supporting that  $\text{H}^0$  is unstable. Upon MD, the +1/−1 charge transition level is found in the gap of am- $\text{Al}_2\text{O}_3$  at 4.63 eV above the VBM. Otherwise, when only structural relaxations are performed, this level is found at 4.65 eV, barely different from the case with MD. For both  $\text{H}^+$  and  $\text{H}^-$ , we also examine the density of states (DOS) and do not observe any single-particle energy level in the band gap of am- $\text{Al}_2\text{O}_3$ . In Fig. 3.7(b), the calculated defect level due to hydrogen is compared with previous calculations for crystalline phases of  $\text{Al}_2\text{O}_3$  [40, 42, 51]. One notices that the level

found in the amorphous oxide differs noticeably from both results obtained with crystalline models. Interestingly, the former falls within 0.4 eV from the universal hydrogen level of Van de Walle and Neugebauer [102], while the latter differ from this level by more than 1 eV.

Experimental work has revealed that an ultrathin layer of am- $\text{Al}_2\text{O}_3$  deposited on hematite can greatly enhance its performance in splitting water [24]. However, hydroxyl ions in water may penetrate into the voids of am- $\text{Al}_2\text{O}_3$ , and corrode the overlayer. With the aim of clarifying the nature and the potential impact of hydroxyl ions, we include this impurity in our study and consider two charge states ( $\text{OH}^-$  and  $\text{OH}^0$ ). Upon MD simulations, the interstitial  $\text{OH}^-$  in am- $\text{Al}_2\text{O}_3$  is found to merge with the amorphous network, the inserted O atom bonding to two or three Al atoms. The obtained configurations precisely correspond to those of  $\text{H}^+$  in am- $\text{Al}_2\text{O}_3$  [Figs. 3.6(a) and (b)]. The full assimilation of the  $\text{OH}^-$  into the amorphous structure is also supported by the energetics. Indeed, Fig. 3.8 shows that the formation energy of  $\text{OH}^-$  barely differs from the sum of the formation energies of  $\text{O}^{2-}$  and  $\text{H}^+$ . Insofar  $\text{OH}^-$  is equivalent to the combination of  $\text{H}^+$  and  $\text{O}^{2-}$ , there are no single-particle energy levels in the band gap associated with  $\text{OH}^-$ . As far as  $\text{OH}^0$  is concerned, the same behavior is observed as for  $\text{OH}^-$ . The extra hole is found in a valence-band-like state in which it is shared by two O atoms of the amorphous oxide, as can be inferred through the inspection of the lowest unoccupied molecular orbital (LUMO).

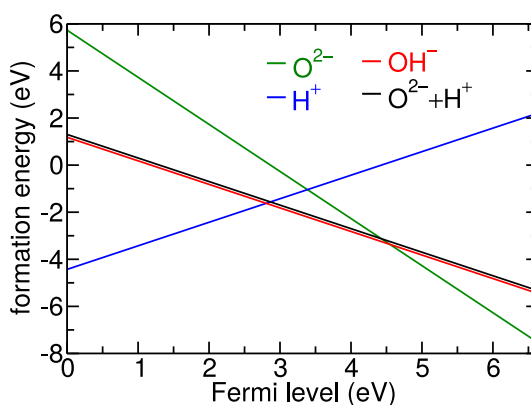


Figure 3.8 – Average formation energies of interstitial  $\text{OH}^-$ ,  $\text{H}^+$ , and  $\text{O}^{2-}$  in am- $\text{Al}_2\text{O}_3$  as a function of Fermi level referred to the VBM, as obtained upon MD runs. The sum of the formation energies of  $\text{H}^+$  and  $\text{O}^{2-}$  is also given (black) to be compared with that of  $\text{OH}^-$  (red).

### 3.3.2 Carbon

We investigate carbon as a possible impurity in am- $\text{Al}_2\text{O}_3$ , as metal-organic precursors are often used in the ALD technique when growing this oxide [155, 30, 156]. In monoclinic  $\text{HfO}_2$ , carbon has been suggested to occur in various configurations with the charge imbalance being compensated by an additional defect, such as an oxygen vacancy [157]. In order to explore carbon-related configurations in am- $\text{Al}_2\text{O}_3$  broadly, the carbon impurity is positioned at the centers of ten different voids after which the geometry is optimized by performing MD. This



procedure is repeated for different total charges  $Q$  of the simulation cell. Since carbon atoms assume even oxidation states in their oxide (e.g. CO and  $\text{CO}_2$ ) and hydride (e.g.  $\text{CH}_4$  and  $\text{C}_2\text{H}_4$ ) molecules, we start our investigation by first considering the total charge  $Q = +4, +2, 0, -2,$  and  $-4$ . It is important to realize that the nominal charge  $q$  carried by the carbon impurity and appearing in the definition of the formation energy in Eq. (2.8) does not necessarily correspond to the total charge  $Q$ , as the added charge could localize elsewhere in the simulation cell.

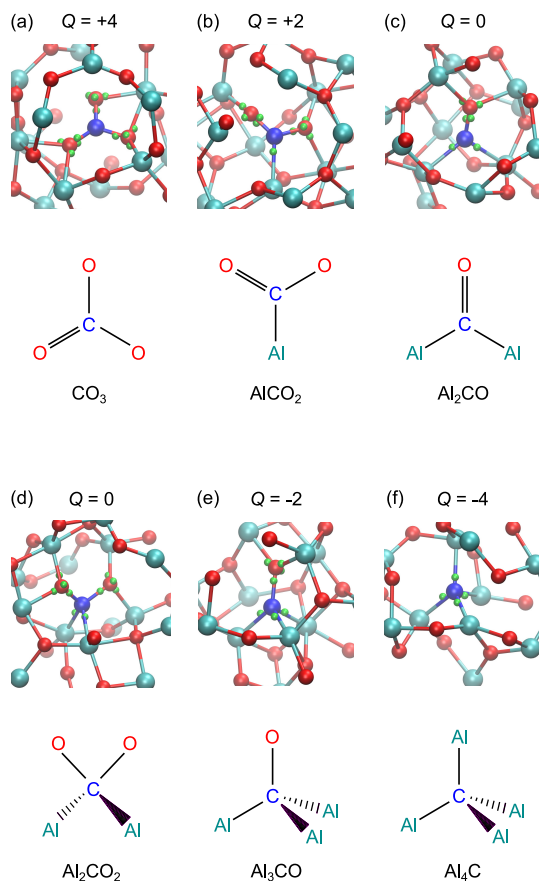


Figure 3.9 – Carbon related defect configurations and their skeletal formulas, as obtained with total charge  $Q = +4, +2, 0, -2,$  and  $-4$ . In the atomic configurations, Al, O, and C atoms are shown in cyan, red, and blue, respectively. In addition, the centers of the relevant maximally localized Wannier functions are indicated by small green spheres.

The configurations of the carbon impurity resulting from our investigation for each total charge  $Q$  are shown in Fig. 3.9. For  $Q = 0$ , we identify two kinds of structures. In one of them, the C impurity shows  $sp^3$  hybridization and bonds to two oxygen atoms and two aluminum atoms [Fig. 3.9(d)]. In the other one, the C impurity is  $sp^2$  hybridized and shows a first-neighbor shell with one double-bonded O atom and two single-bonded Al atoms [Fig. 3.9(c)]. For  $Q = -2$  and  $Q = -4$ , we find carbon in  $sp^3$  configurations, with either three Al atoms and one O oxygen atom or four Al atoms in the first-neighbor shell, respectively. For  $Q = +2$  and  $Q = +4$ , the carbon impurity is  $sp^2$  hybridized. In the case  $Q = +2$ , the first-neighbor shell of the carbon



atom consists of one aluminum atom and two oxygen atoms, one of the latter being double bonded, i.e. showing a  $\pi$  bond in addition to a  $\sigma$  bond. For  $Q = +4$ , the defect configuration corresponds to a planar  $\text{CO}_3$  structure, in which one of the O atoms is double bonded.

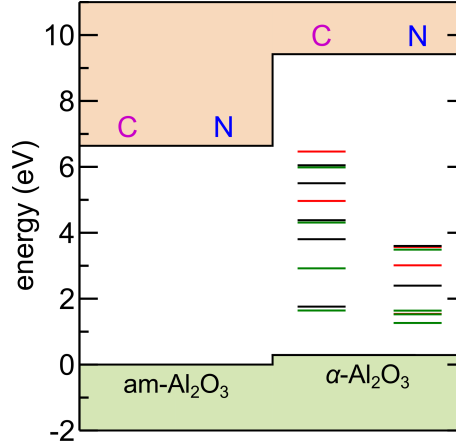


Figure 3.10 – Absence of charge transition levels of carbon and nitrogen impurities in am- $\text{Al}_2\text{O}_3$  compared with the levels for the same impurities in  $\alpha$ - $\text{Al}_2\text{O}_3$  reported in Ref. [38]. The latter include defect levels from substitutional sites to Al (red), substitutional sites to O (green), and interstitial sites (black). The alignment between am- $\text{Al}_2\text{O}_3$  and  $\alpha$ - $\text{Al}_2\text{O}_3$  is taken from Ref. [52].

In order to rationalize the electronic structure of these defect configurations, we adopt an analysis based on maximally localized Wannier functions (WF) [158], which yields a real-space representation of the electron localization. The centers of these WFs are indicated by small green spheres in Fig. 3.9. Such a WF analysis allows us to distinguish the nature of the chemical bonds (single vs. double bonds) and hence to determine the nominal charge state of the C impurity. The WF analysis enables electron counting, which reveals that four electrons can be assigned to the carbon impurity in all defect configurations [Fig. 3.9], corresponding to a nominally neutral defect state with  $q = 0$ . Since all the identified defect states are locally neutral, there are no thermodynamic charge transition levels in the band gap. This important result is illustrated in Fig. 3.10, where the absence of any charge transition level in am- $\text{Al}_2\text{O}_3$  is contrasted with the multitude of charge transition levels found for the carbon impurity in crystalline  $\alpha$ - $\text{Al}_2\text{O}_3$  [38]. These differences highlight that the properties of defects in an amorphous oxide cannot be inferred relying on the study of crystalline counterparts.

From the configurations found in Fig. 3.9, we remark that the number of O atoms in the first-neighbor shell reduces with  $Q$  decreasing from  $+4$  to  $-4$ , suggesting a connection between total charge and available O atoms. This is consistent with our results in Section 3.2 on intrinsic defects in am- $\text{Al}_2\text{O}_3$ , in which it was found that adding or removing  $\text{O}^{2-}$  just produces a defect-free nonstoichiometric oxide (am- $\text{Al}_2\text{O}_{3\pm\delta}$ ) [15]. Following these lines, the charge imbalance resulting from  $Q \neq q$  can be associated to the addition or removal of  $\text{O}^{2-}$  ions to the core of the defect, similar in spirit to the dopant compensation found in  $\text{HfO}_2$  [157].

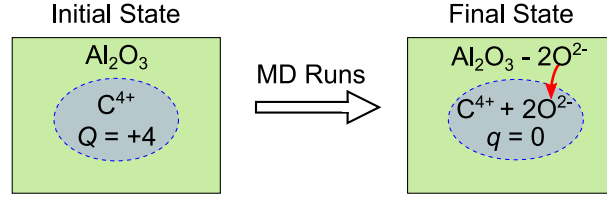


Figure 3.11 – Schematic representation of charge compensation induced by the insertion of carbon in the simulation cell under the condition of total charge  $Q = +4$ .

Table 3.2 – Charge in the simulation cell  $Q$ , nominal defect charge  $q$ , inferred defect core unit, and observed atomic structure for the carbon impurity in am-Al<sub>2</sub>O<sub>3</sub>.

$Q$	$q$	Core unit	Atomic structure
+4	0	$C^{4+} \oplus 2O^{2-}$	CO <sub>3</sub>
+2	0	$C^{2+} \oplus O^{2-}$	AlCO <sub>2</sub>
0	0	$C^0$	Al <sub>2</sub> CO <sub>2</sub> and Al <sub>2</sub> CO
-2	0	$C^{2-} \ominus O^{2-}$	Al <sub>3</sub> CO
-4	0	$C^{4-} \ominus 2O^{2-}$	Al <sub>4</sub> C

Let us focus for instance on the case  $Q = +4$ . In this case, a neutral defect with  $q = 0$  is obtained by considering that two  $O^{2-}$  ions of the amorphous structure should actually be considered as an inherent part of the defect, as illustrated graphically in Fig. 3.11. We therefore effectively focus on a neutral defect core unit composed of  $C^{4+}$  and two  $O^{2-}$ . The formation energy of such a neutral defect unit can then be expressed with respect to a host consisting of Al<sub>2</sub>O<sub>3</sub> with two missing  $O^{2-}$  ions:

$$E_f[C^{4+} \oplus 2O^{2-}] = E_{\text{tot}}[\text{Al}_2\text{O}_3 \oplus C^{4+}] - \mu_C - 2\mu_O - E_{\text{tot}}[\text{Al}_2\text{O}_3 \ominus 2O^{2-}], \quad (3.1)$$

where  $E_{\text{tot}}[\text{Al}_2\text{O}_3 \oplus C^{4+}]$  refers to the total energy of the simulation cell with the carbon impurity and  $Q = +4$ , and  $E_{\text{tot}}[\text{Al}_2\text{O}_3 \ominus 2O^{2-}]$  to the total energy of a pristine amorphous system of the same size from which two  $O^{2-}$  ions have been removed. Following the same rationale, defect core units can be established for the other values of  $Q$  and have been summarized in Table 3.2. We give the corresponding formation energies explicitly:

$$E_f[C^{2+} \oplus O^{2-}] = E_{\text{tot}}[\text{Al}_2\text{O}_3 \oplus C^{2+}] - \mu_C - \mu_O - E_{\text{tot}}[\text{Al}_2\text{O}_3 \ominus O^{2-}], \quad (3.2)$$

$$E_f[C^0] = E_{\text{tot}}[\text{Al}_2\text{O}_3 \oplus C^0] - \mu_C - E_{\text{tot}}[\text{Al}_2\text{O}_3], \quad (3.3)$$

$$E_f[C^{2-} \ominus O^{2-}] = E_{\text{tot}}[\text{Al}_2\text{O}_3 \oplus C^{2-}] - \mu_C + \mu_O - E_{\text{tot}}[\text{Al}_2\text{O}_3 \oplus O^{2-}], \quad (3.4)$$

$$E_f[\text{C}^{4-} \ominus 2\text{O}^{2-}] = E_{\text{tot}}[\text{Al}_2\text{O}_3 \oplus \text{C}^{4-}] - \mu_{\text{C}} + 2\mu_{\text{O}} - E_{\text{tot}}[\text{Al}_2\text{O}_3 \oplus 2\text{O}^{2-}]. \quad (3.5)$$

A general expression for Eqs. 3.1–3.5 can be cast in the form:

$$E_f[\text{C}^Q \ominus n\text{O}^{2-}] = E_{\text{tot}}[\text{Al}_2\text{O}_3 \oplus \text{C}^Q] - \mu_{\text{C}} + n\mu_{\text{O}} - E_{\text{tot}}[\text{Al}_2\text{O}_3 \oplus n\text{O}^{2-}], \quad (3.6)$$

where  $n = -(Q - q)/2$ , with  $q = 0$  and  $Q = +4, +2, 0, -2$  and  $-4$ . In Eq. 3.6, all quantities are known except the last term,  $E_{\text{tot}}[\text{Al}_2\text{O}_3 \oplus n\text{O}^{2-}]$ , with  $n = -2, -1, 0, +1$ , and  $+2$ . Such terms can be related to the formation energy of  $n \text{O}^{2-}$  ions:

$$E_f[n\text{O}^{2-}] = E_{\text{tot}}[\text{Al}_2\text{O}_3 \oplus n\text{O}^{2-}] - n\mu_{\text{O}} - E_{\text{tot}}[\text{Al}_2\text{O}_3] - 2n(\epsilon_{\text{F}} + \epsilon_{\text{V}}), \quad (3.7)$$

where finite-size corrections and alignment terms have been omitted for clarity. Assuming linearity, we further express the formation energy of  $n \text{O}^{2-}$  ions in terms of that of a single  $\text{O}^{2-}$  ion:

$$E_f[n\text{O}^{2-}] = n \cdot E_f[\text{O}^{2-}], \quad (3.8)$$

where the formation of a single  $\text{O}^{2-}$  ion can be expressed as [15]:

$$E_f[\text{O}^{2-}] = E_{\text{tot}}[\text{Al}_2\text{O}_3 \oplus \text{O}^{2-}] - \mu_{\text{O}} - E_{\text{tot}}[\text{Al}_2\text{O}_3] - 2(\epsilon_{\text{F}} + \epsilon_{\text{V}}). \quad (3.9)$$

Combining Eqs. 3.7, 3.8, and 3.9, we obtain the following expression in terms of total energies that can explicitly be calculated:

$$E_{\text{tot}}[\text{Al}_2\text{O}_3 \oplus n\text{O}^{2-}] = n \cdot E_{\text{tot}}[\text{Al}_2\text{O}_3 \oplus \text{O}^{2-}] - (n - 1) \cdot E_{\text{tot}}[\text{Al}_2\text{O}_3]. \quad (3.10)$$

Our analysis shows that the defect core units contain a variable amount of oxygen atoms. Therefore, their defect formation energies show a different dependence on the oxygen chemical potential  $\mu_{\text{O}}$ , as can be seen from Eqs. 3.1–3.5. To study this dependence, we allow the oxygen chemical potential to vary from oxygen-rich conditions to oxygen-poor conditions. In oxygen-rich conditions, the chemical potential is set to half the total energy of an isolated O<sub>2</sub> molecule:  $\mu_{\text{O}}^{\text{rich}} = \frac{1}{2} E_{\text{tot}}[\text{O}_2]$ . In oxygen-poor conditions,  $\mu_{\text{O}}$  is set by taking  $\mu_{\text{Al}}$  from Al metal and by imposing the equilibrium condition between  $\mu_{\text{O}}$  and  $\mu_{\text{Al}}$  in Al<sub>2</sub>O<sub>3</sub>. This gives:

$$\mu_{\text{O}}^{\text{poor}} = \frac{E_{\text{tot}}^{\text{fu}}[\text{Al}_2\text{O}_3] - 2E_{\text{tot}}^{\text{at}}[\text{Al}]}{3}, \quad (3.11)$$

where  $E_{\text{tot}}^{\text{fu}}[\text{Al}_2\text{O}_3]$  is the total energy per formula unit for our bulk am-Al<sub>2</sub>O<sub>3</sub> model and  $E_{\text{tot}}^{\text{at}}[\text{Al}]$  the total energy per atom for Al metal, which we calculate using a face-centered cubic bulk. Taking  $\mu_{\text{O}}^{\text{rich}}$  as reference, we determine  $\mu_{\text{O}}^{\text{poor}}$  to be  $-5.33$  eV.

In Fig. 3.12, we display the formation energies of C-related defects in am-Al<sub>2</sub>O<sub>3</sub> as a function

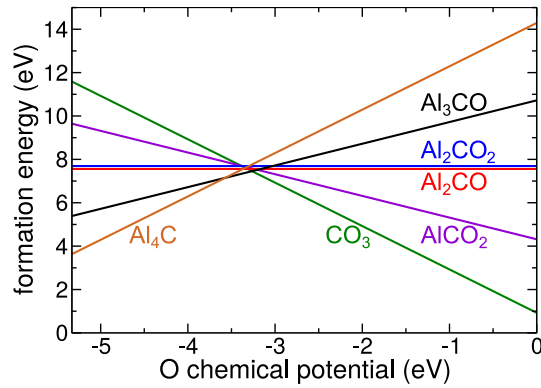


Figure 3.12 – Formation energies of various defect configurations related to the carbon impurity as a function of oxygen chemical potential. The latter is referred to its value in oxygen-rich conditions.

of oxygen chemical potential. As  $\mu_{\text{O}}$  decreases from 0 to  $-5.33$  eV, the most stable defect configurations sequentially change from  $\text{CO}_3$  to  $\text{Al}_3\text{CO}$  and  $\text{Al}_4\text{C}$ . In particular, we remark that the two configurations found for  $Q = 0$ , i.e.  $\text{Al}_2\text{CO}$  and  $\text{Al}_2\text{CO}_2$ , which differ in formation energy by only 0.18 eV, are both metastable. This result is consistent with experimental FT-IR observations, which have identified the coexistence of C=O and O–C–O moieties [159].

For the carbon-related defects identified here, we further investigate the DOS to determine the occurrence of single-electron energy levels in the band gap, which could be active on short time scales. For the  $\text{CO}_3$  and  $\text{AlCO}_2$  configurations, there are no such energy levels in the gap, in analogy to the  $\text{CO}_3$  defect in  $\text{HfO}_2$  [157]. At variance, the  $\text{Al}_2\text{CO}$  and  $\text{Al}_2\text{CO}_2$  structures give rise to an occupied defect state at  $\sim 2.0$  eV above the VBM. Similarly, two and three occupied defect states occur in the range from 1.5 to 3.0 eV above the VBM for  $\text{Al}_3\text{CO}$  and  $\text{Al}_4\text{C}$ , respectively. The occurrence of such states is consistent with the experimental finding that photocurrents are induced by sub-band-gap photons in amorphous samples of anodic-barrier  $\text{Al}_2\text{O}_3$ , which contain a sizable concentration of carbon impurities [159].

To complete our investigating of carbon-related defects, we finally also consider the case of odd values of total charge  $Q$ . Upon MD, we find for all odd values of  $Q$  carbon defect states showing an unpaired electron. Next, we investigate a double-sized simulation cell containing two such carbon defects and perform further MD. In all cases, we observe disproportionation with the two odd- $Q$ -valued defects transforming to the carbon defect configurations found above for  $Q-1$  and  $Q+1$  [Fig. 3.9]. This transition is accompanied by a significant decrease in total energy certifying that  $2E_{\text{tot}}^Q > E_{\text{tot}}^{Q-1} + E_{\text{tot}}^{Q+1}$  for odd values of  $Q$ . On this basis, the carbon configurations resulting from odd values of  $Q$  can conclusively be ruled out as thermodynamically stable defect configurations.

### 3.3.3 Nitrogen

Nitrogen is often incorporated into am-Al<sub>2</sub>O<sub>3</sub> either intentionally or unintentionally due to the use of metal-organic precursors during growth. Therefore, we study this impurity in am-Al<sub>2</sub>O<sub>3</sub> following the same protocol adopted for carbon. However, unlike carbon, the isolated N atom carries five valence electrons and we thus start our investigation by considering odd values of  $Q$ , i.e.  $Q = +5, +3, +1, -1$ , and  $-3$ . The nitrogen related configurations that are identified as  $Q$  is varied are shown in Fig. 3.13. In particular, we find AlNO<sub>2</sub>, Al<sub>2</sub>NO<sub>2</sub>, Al<sub>3</sub>NO, and Al<sub>4</sub>N for  $Q = +3, +1, -1$ , and  $-3$ , respectively. We remark that the nitrate-like NO<sub>3</sub> configuration does not occur. For  $Q = +5$ , we find the same AlNO<sub>2</sub> defect configuration obtained for  $Q = +3$  [Fig. 3.13(a)], the two extra holes being trapped through the formation of a peroxy linkage [15]. More generally, one can note that the nitrogen defect configurations identified for a total charge  $Q$  correspond to the carbon ones for  $Q' = Q - 1$ , accounting in this way for the fact that N possesses one extra valence electron compared to C. In the AlNO<sub>2</sub> configuration, the N impurity shows a  $sp^2$  hybridization, with a double bond between N and one of the O atoms [see skeletal formula in Fig. 3.13(a)]. At variance, the nitrogen impurity is  $sp^3$  hybridized in the other configurations. Inspection of the DOS reveals that the AlNO<sub>2</sub> configuration shows an unoccupied single-particle energy level at 4.8 eV above the VBM, corresponding to an antibonding  $\pi$  orbital. The Al<sub>2</sub>NO<sub>2</sub>, Al<sub>3</sub>NO, and Al<sub>4</sub>N configurations give rise to occupied single-particle energy levels in the lower part of the band gap, within 1 eV from the VBM.

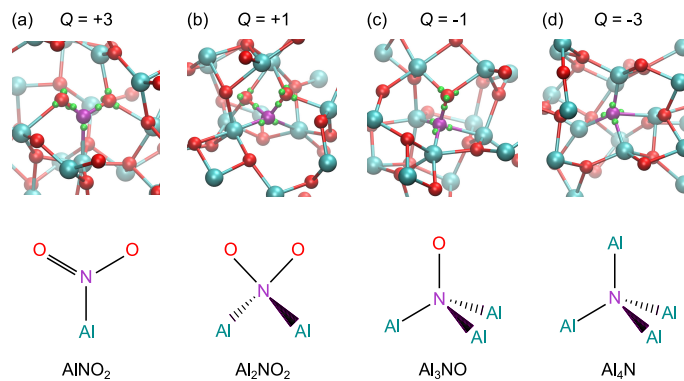


Figure 3.13 – Nitrogen defect related configurations and their skeletal formulas, as obtained with total charge  $Q = +3, +1, -1$ , and  $-3$ . In the atomic configurations, Al, O, and N atoms are shown in cyan, red, and purple, respectively. In addition, the centers of the relevant maximally localized Wannier functions are indicated by small green spheres.

Adopting the electron counting rule based on a WF analysis, we find that in all configurations four electrons are associated with the nitrogen impurity. This implies that the nominal charge state of the impurity is always  $q = +1$ , and consequently no thermodynamic charge transition level associated with the nitrogen impurity occurs in am-Al<sub>2</sub>O<sub>3</sub>. As for carbon, this conclusion contrasts with results found for crystalline phases [Fig. 3.10] [38].

To account for the local defect charge  $q = +1$ , we define defect core units by including a suitable

Table 3.3 – Charge in the simulation cell  $Q$ , nominal defect charge  $q$ , inferred defect core unit, and observed atomic structure for the nitrogen impurity in am-Al<sub>2</sub>O<sub>3</sub>.

$Q$	$q$	Core unit	Atomic structure
+3	+1	N <sup>3+</sup> ⊕ O <sup>2-</sup>	AlNO <sub>2</sub>
+1	+1	N <sup>1+</sup>	Al <sub>2</sub> NO <sub>2</sub>
-1	+1	N <sup>1-</sup> ⊖ O <sup>2-</sup>	Al <sub>3</sub> NO
-3	+1	N <sup>3-</sup> ⊖ 2O <sup>2-</sup>	Al <sub>4</sub> N

number of O<sup>2-</sup> atoms [Table 3.3]. Their formation energies are then calculated following the same rationale used for the carbon impurity, through the following general expression:

$$E_f(\text{N}^Q \ominus n\text{O}^{2-}) = E_{\text{tot}}[\text{Al}_2\text{O}_3 \oplus \text{N}^Q] - \mu_{\text{N}} + n\mu_{\text{O}} - E_{\text{tot}}[\text{Al}_2\text{O}_3 \oplus n\text{O}^{2-}] + \epsilon_{\text{F}} + \epsilon_{\text{v}}, \quad (3.12)$$

where  $n = -(Q - q)/2$  with  $q = +1$  and  $Q = +3, +1, -1$  and  $-3$ . In Eq. 3.12, finite-size corrections and alignment terms have been omitted for clarity. Fixing the Fermi level at the VBM, we display these formation energies as a function of oxygen chemical potential in Fig. 3.14. It is seen that the most stable defect configurations rapidly loose O atoms from their first-neighbor shell as the oxygen chemical potential moves away from oxygen-rich conditions. In particular, for  $\mu_{\text{O}} < -1.3$  eV, the prevalent defect structure in am-Al<sub>2</sub>O<sub>3</sub> is Al<sub>4</sub>N. This observation is quite consistent with the conclusion reported in Ref. [38] that nitrogen incorporates into the oxide by replacing O atoms (N<sub>O</sub>).

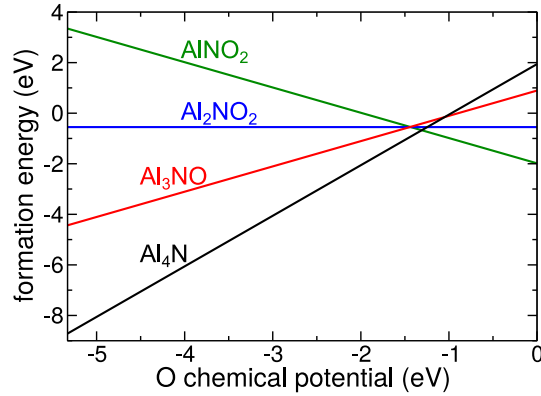


Figure 3.14 – Formation energies of various defect configurations related to the nitrogen impurity as a function of oxygen chemical potential. The latter is referred to its value in oxygen-rich conditions. The formation energies are determined for the Fermi level fixed at the VBM.

We also investigate the nitrogen impurity in our model of am-Al<sub>2</sub>O<sub>3</sub> by setting the total charge  $Q$  to even values, i.e.  $Q = +4, +2, 0$ , and  $-2$ . For  $Q = +4$ , we find the same defect configuration AlNO<sub>2</sub> found in the case of  $Q = +3$ , but with an extra hole in the valence band. For  $Q = +2, 0$ , and  $-2$ , we find defect structures with unpaired electrons on the nitrogen impurity, but all of them undergo disproportionation to structures pertaining to  $Q + 1$  and  $Q - 1$  when

doubling the simulation cell, in an analogous way as seen for odd values of  $Q$  in the case of the carbon impurity. Hence, we conclude that no other nitrogen defect structures occur than those reported in Fig. 3.13.

### 3.4 Alignment to semiconductor band edges

In this section, we discuss the possible electrical activity of the defect levels identified in this work. For this purpose, we first align the band structure of am- $\text{Al}_2\text{O}_3$  to the band edges of three semiconductors (GaAs, GaN, and  $\alpha\text{-Fe}_2\text{O}_3$ ), which are relevant for technological applications. The Fermi level is bound to the range that encompasses the band gap and its position determines the stable charge states that can be found in the oxide. For GaAs and GaN, we take the band alignment with respect to am- $\text{Al}_2\text{O}_3$  from photoemission experiments [33, 34, 35, 160], which propose valence band offsets of 3.8 and 1.1 eV, respectively. For  $\alpha\text{-Fe}_2\text{O}_3$ , we rely on the band alignment put forward in Ref. [161]. The band alignment obtained in this way is illustrated in Fig. 3.15.

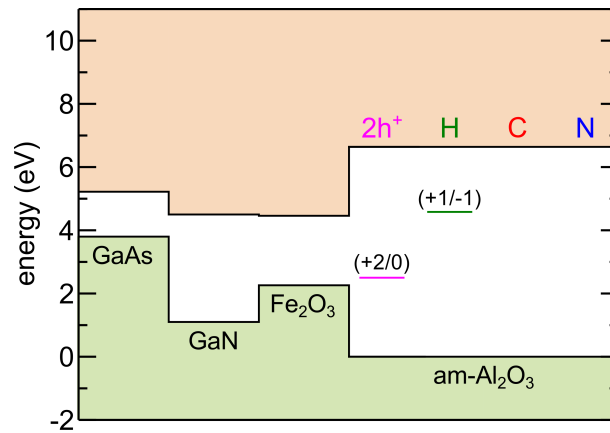


Figure 3.15 – Band alignment between three different semiconductors, i.e. GaAs, GaN, and  $\alpha\text{-Fe}_2\text{O}_3$ , and am- $\text{Al}_2\text{O}_3$ . The charge transition levels for hydrogen, carbon, and nitrogen, found in this work, are indicated together with the double hole polaron ( $2h^+$ ), corresponding to the formation of a peroxy linkage (Ref. [15]). The band alignment is taken from experiment (Refs. [33, 34, 35, 160, 161]).

Additionally, we include the charge transition levels determined for hydrogen, carbon, and nitrogen impurities in am- $\text{Al}_2\text{O}_3$ . Since carbon and nitrogen do not give any defect level in the band gap, this sums up considering only the  $-1/+1$  charge transition level of hydrogen. To complete the picture, we also include the  $+2/0$  charge transition level associated with the self-trapped double polaron, as inferred in Section 3.2 from the study of intrinsic defects in am- $\text{Al}_2\text{O}_3$  [15].

For GaAs, only the  $-1/+1$  charge transition level of hydrogen lies in the range of the band gap. Hence, hydrogen impurities in am- $\text{Al}_2\text{O}_3$  may contribute to gate leakage currents and degrade

the performance of MOS devices based on GaAs. For GaN and  $\alpha\text{-Fe}_2\text{O}_3$ , the hydrogen defect level in am- $\text{Al}_2\text{O}_3$  is found in the proximity of the conduction band minimum, and might constitute a trap for free electron carriers. Furthermore, this suggests that hydrogen is in a positively charged state for most Fermi levels in the band gaps of these materials.

Also, the +2/0 charge transition level associated with the peroxy linkage falls in the range of the band gap for GaN and  $\alpha\text{-Fe}_2\text{O}_3$ . This level might thus constitute a conduction channel for hole leakage in p-type doping conditions for these materials. In particular, in the case of  $\alpha\text{-Fe}_2\text{O}_3$ , this level could explain the observations in Ref. [24], in which hole conduction was observed across an overlayer of am- $\text{Al}_2\text{O}_3$  on hematite. The +2/0 level of the double polaron lies at only 0.25 eV from the VBM of  $\alpha\text{-Fe}_2\text{O}_3$ . This alignment favors the injection of holes from  $\alpha\text{-Fe}_2\text{O}_3$  into am- $\text{Al}_2\text{O}_3$ , which could diffuse across the oxide through the sequential formation and breaking of O–O pairs, as proposed for hole diffusion in am- $\text{TiO}_2$  [cf. Chapter 4]. Furthermore, the small offset between the VBM of  $\alpha\text{-Fe}_2\text{O}_3$  and the +2/0 level would not affect significantly the energy of photogenerated holes and thus preserve the catalytic properties of  $\alpha\text{-Fe}_2\text{O}_3$  in the oxidation of water.

### 3.5 Conclusion

In conclusion, we investigated the structural and electronic properties of native defects (e.g. oxygen vacancy and interstitial) and extrinsic impurities (e.g. hydrogen, carbon, and nitrogen) in am- $\text{Al}_2\text{O}_3$ . We devoted particular attention to finding the most stable structural configurations through extensive *ab initio* molecular dynamics in various charge states. It is found that the structure of am- $\text{Al}_2\text{O}_3$  rearranges in such a way that the excess or deficiency of isolated  $\text{O}^{2-}$  ions shows electronic properties which do not differ from those of the pristine material. The oxygen vacancy leads to a substoichiometric oxide in which excess electrons are released. Analogously, the presence of excess oxygen induces the generation of holes, which can be trapped in the amorphous structure through the formation of peroxy linkages. In the case of hydrogen, our approach did not lead to qualitative differences with respect to calculations based on straight structural relaxations. Hydrogen was found to be amphoteric with a +1/–1 charge transition level lying at  $\sim 4.6$  eV above the VBM. Hydroxyl groups incorporated in am- $\text{Al}_2\text{O}_3$  were shown to give rise to defect states equivalent to those of the hydrogen impurity. At variance, in the case of carbon and nitrogen impurities, we found a series of structural configurations which varied depending on the total charge set in the simulation cell. To identify the nominal charge on the defect, we adopted an electron counting scheme based on maximally localized Wannier functions. In this way, we inferred that carbon and nitrogen impurities in am- $\text{Al}_2\text{O}_3$  only give rise to neutral and singly positive charge states, respectively. This leads to the astonishing observation that these impurities do not give any charge transition level in am- $\text{Al}_2\text{O}_3$ , in stark contrast with studies on crystalline models predicting a multitude of levels. To account for the local charge of the impurity, we then redefined the core unit of the defect, by which the obtained configurations naturally depend on the oxygen chemical potential. In oxygen-poor conditions, both the carbon and the nitrogen favor bonding to Al



atoms, while they tend to form single and double bonds with oxygen atoms as the oxygen chemical potential increases.

From our study, a picture emerges by which only two significant charge transition levels occur in am- $\text{Al}_2\text{O}_3$ , namely the  $+1/-1$  level of hydrogen and the intrinsic  $+2/0$  level related to the peroxy linkage. Relying on the experimental band alignment, we could position these levels with respect to the band edges of three semiconductors of technological relevance (GaAs, GaN, and  $\alpha\text{-Fe}_2\text{O}_3$ ). The  $+1/-1$  and  $+2/0$  levels fall in the band-gap range of GaAs and GaN, respectively, and could thus degrade the electronic properties in MOS devices or trap free carriers. On the other hand, the intrinsic  $+2/0$  level is suitably positioned with respect to the valence band maximum of  $\alpha\text{-Fe}_2\text{O}_3$  for favoring hole transport across am- $\text{Al}_2\text{O}_3$  overlayers, thereby providing a rationale for experimental observations [24].

Overall, the present approach has revealed the importance of identifying the most stable structural configurations when studying defects in amorphous oxides. Furthermore, our study highlights the importance of defining properly the nominal charge of the defect and its core unit. We expect the procedure outlined in this work to be transferable to other defects as well as to other amorphous oxides.

The results presented in this chapter have been published in Ref. [15].



## 4 Transport of holes in amorphous $\text{TiO}_2$

In this chapter, we combine electronic-structure calculations, molecular dynamics simulations (MD) and nudge elastic band (NEB) calculations to study the mechanism of hole diffusion across amorphous  $\text{TiO}_2$  layers. We first build an atomistic model of am- $\text{TiO}_2$  of which the structural and electronic properties are consistent with available experiments [Section 4.1]. Next, we investigate the stability of the oxygen vacancy and find that structural rearrangements in the amorphous can assimilate oxygen vacancies, thus excluding them as a possible channel for hole diffusion across the material [Section 4.2.1]. At variance, we find that excess holes in the material lead to the formation of O–O peroxy linkages with a defect level at  $1.25 \pm 0.15$  eV above the valence band [Section 4.2.2]. Considering that an O–O peroxy linkage can store two holes and that these holes are released when the O–O pair is broken, we propose an exchange mechanism for hole conduction in am- $\text{TiO}_2$ , which is based on the simultaneous breaking and forming of O–O peroxy linkages that share one O atom. Through NEB calculations, we demonstrate a hopping path as long as 1.2 nm with barriers of 0.3–0.5 eV, thus indicating that hole diffusion through O–O peroxy linkages is viable in am- $\text{TiO}_2$  [Section 4.3].

### 4.1 Model of amorphous $\text{TiO}_2$

MD simulations within the NVT ensemble are used to generate an atomistic model for am- $\text{TiO}_2$  through the melt-and-quench method. This technique has proved successful in generating atomistic models of amorphous oxides [162, 163, 146, 164, 52, 76]. In these MD simulations, the temperature is controlled by a Nosé-Hoover thermostat [137, 138]. A  $3 \times 3 \times 4$  supercell of rutile  $\text{TiO}_2$  containing 216 atoms is taken as initial configuration. Through uniform elongation along the three Cartesian directions, the starting configuration is fixed at a density of  $\rho = 3.82$  g/cm<sup>3</sup>, in order to stay within the experimental range (3.80–3.85 g/cm<sup>3</sup>) [165, 166]. The prepared system undergoes molecular dynamics for a duration of 12 ps at a temperature of 4000 K, much higher than the melting point of  $\text{TiO}_2$  [167]. This ensures that there is no memory from the initial crystalline structure upon MD. Then, we carry out a slow cooling procedure in which the temperature is decreased at a rate of 75 K/ps (Model 1), until the final temperature of 300 K is reached. The lattice parameters of the model are then relaxed and we

obtain a final structure with  $\rho = 3.85 \text{ g/cm}^3$  [Fig. 4.1], still consistent with the experimental range [165, 166]. In order to clarify the effect of the cooling rate on the structural and electronic properties of atomistic models of am-TiO<sub>2</sub>, we generated two additional models following the same protocol but with cooling rates of 300 K/ps (Model 2) and 600 K/ps (Model 3).

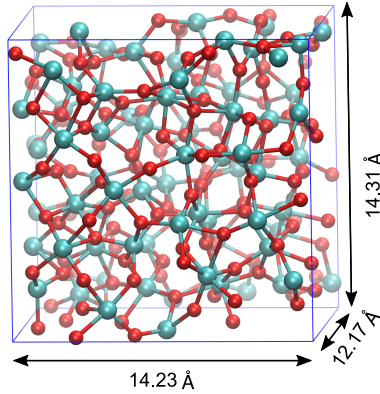


Figure 4.1 – Atomistic representation of the am-TiO<sub>2</sub> model achieved in this work. The lattice parameters of the supercell are also reported. O atoms in red, Ti atoms in cyan.

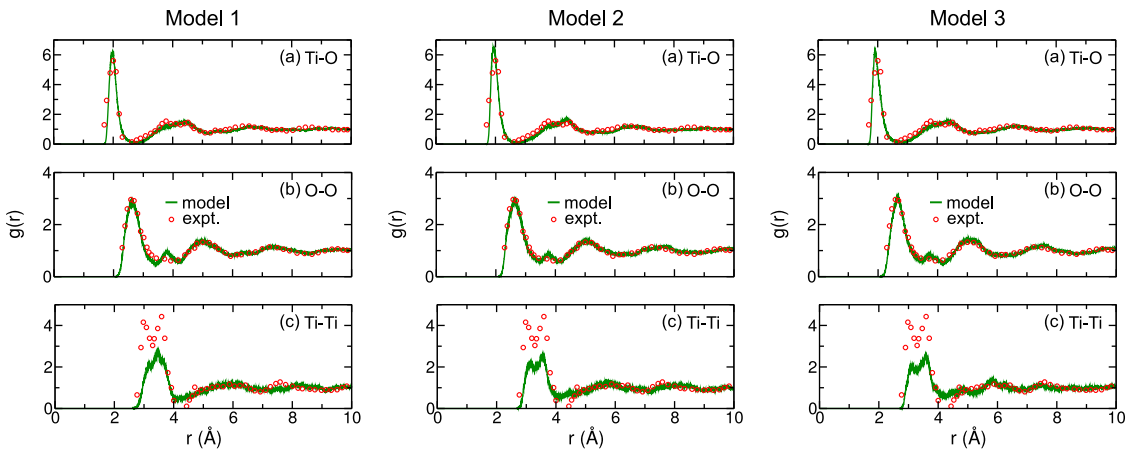


Figure 4.2 – Comparison of the radial distribution functions  $g(r)$  for Ti-O, O-O, and Ti-Ti, as achieved from 3-ps-long molecular dynamics of three am-TiO<sub>2</sub> models generated with cooling rates of 75 K/ps (Model 1), 300 K/ps (Model 2), and 600 K/ps (Model 3). RDFs as obtained from X-ray diffraction for sputtered TiO<sub>2</sub> amorphous layers [168] are shown for comparison.

We test the structure of the achieved am-TiO<sub>2</sub> model by comparing the calculated radial distribution functions (RDF) with their experimental counterparts [168] measured for sputtered amorphous TiO<sub>2</sub> layers [Fig. 4.2]. The positions of the main peaks and the shapes of the curves for O-O, Ti-O, and Ti-Ti RDFs as achieved from MD simulations of three models are all in fair agreement with the experiment. It is noticed that the RDFs generally differ negligibly among the generated models. Nevertheless, we note that the double-peak structure observed in the experimental Ti-Ti RDF is slightly better reproduced with the faster cooling rates. The

calculated mass density of the three models is found to increase by only 2% when going from Model 1 to Model 3 [Table 4.1]. Similarly, the electronic properties are barely affected by the adopted cooling rate, with band gap differences amounting to at most 0.05 eV [Table 4.1]. Overall, our analysis indicates that melt-and-quench procedures with cooling rates varying between 75 K/ps and 600 K/ps lead to equivalent atomistic models of the amorphous oxide. Given the fact that the experimental cooling rate is much lower than that adopted in the melt-and-quench method, the model constructed with the lowest cooling rate is kept for the following investigation, i.e. Model 1.

Table 4.1 – Calculated lattice parameters and mass density  $\rho$  at the PBE level for various am-TiO<sub>2</sub> models generated with cooling rates of 75 K/ps (Model 1), 300 K/ps (Model 2), and 600 K/ps (Model 3). The band gaps  $E_g$  are calculated at the PBE0 level with  $\alpha = 0.15$ , on structural configurations relaxed at the PBE level. Experimental values for both structural and electronic properties are reported for comparison.

	$a$ (Å)	$b$ (Å)	$c$ (Å)	$\rho$ (g/cm <sup>3</sup> )	$E_g$ (eV)
Model 1	14.31	14.23	12.17	3.85	3.42
Model 2	14.07	14.73	12.20	3.78	3.47
Model 3	14.40	14.26	12.32	3.77	3.48
Expt.				3.80–3.85 <sup>a-d</sup>	3.20–3.40 <sup>e,f</sup>

<sup>a</sup> Ref. [169]. <sup>b</sup> Ref. [170]. <sup>c</sup> Ref. [171]. <sup>d</sup> Ref. [172]. <sup>e</sup> Ref. [165]. <sup>f</sup> Ref. [166].

Table 4.2 – Calculated lattice parameters and mass density  $\rho$  at the PBE level for am-TiO<sub>2</sub>, r-TiO<sub>2</sub>, and a-TiO<sub>2</sub>. The band gaps  $E_g$  are calculated at the PBE0 level with  $\alpha = 0.15$ , on structural configurations achieved at the PBE level. Experimental values for both structural and electronic properties are reported for comparison.

	$a$ (Å)	$b$ (Å)	$c$ (Å)	$\rho$ (g/cm <sup>3</sup> )	$E_g$ (eV)
am-TiO <sub>2</sub>					
Present theory	14.31	14.23	12.17	3.85	3.42
Expt.				3.80–3.85 <sup>a-d</sup>	3.20–3.40 <sup>e,f</sup>
r-TiO <sub>2</sub>					
Present theory	4.66		3.00	4.07	3.02
Expt.	4.59		2.96	4.25	3.00 <sup>g</sup>
a-TiO <sub>2</sub>					
Present theory	3.81		9.67	3.79	3.35
Expt.	3.79		9.51	3.89	3.36 <sup>h,i</sup>

<sup>a</sup> Ref. [169]. <sup>b</sup> Ref. [170]. <sup>c</sup> Ref. [171]. <sup>d</sup> Ref. [172]. <sup>e</sup> Ref. [165].

<sup>f</sup> Ref. [166]. <sup>g</sup> Ref. [173]. <sup>h</sup> Ref. [174]. <sup>i</sup> Ref. [175].

We calculate the coordination number for oxygen and titanium atoms, considering a Ti-O cutoff distance of 2.4 Å, which corresponds to the position of the first minimum in the Ti-O RDF. We find that the majority of Ti atoms are sixfold coordinated (70%), but sevenfold

(23%) and fivefold (7%) coordinations are also relevant. Threefold coordination is found to be prevalent for O atoms (80%), with only a small fraction of O atoms showing either twofold (14%) or fourfold (6%) coordination.

The electronic properties of am-TiO<sub>2</sub> are evaluated at the hybrid functional level, in order to overcome the band gap underestimation associated with semilocal functionals. In particular, we use the PBE0 functional [113, 114], in which we set the fraction of Fock exchange  $\alpha$  to 0.15, as this value reproduces the experimental band gap of both r-TiO<sub>2</sub> and a-TiO<sub>2</sub> [Table 4.2]. We refer to this level of theory as to PBE0( $\alpha$ ). Hybrid-functional calculations are performed using the auxiliary density matrix method [121, 114, 122] available in CP2K. The am-TiO<sub>2</sub> model constructed in this work has a band gap of 3.42 eV, close to the experimental range (3.20–3.40 eV) [169, 170, 171, 172].

### 4.2 Intrinsic defects in amorphous TiO<sub>2</sub>

In this research, we investigate charge transport through defect states. Extrinsic charge carriers are ruled out by their low mobilities [77, 78]. Furthermore, the hopping through extrinsic impurities would require excessively high defect concentrations. Therefore, we focus in this study on intrinsic defects, such as vacancies and interstitials, which result from stoichiometric imbalance. For am-TiO<sub>2</sub>, it is sufficient to focus on oxygen related defects as the concentration imbalance due to missing or excess Ti atoms would lead to equivalent defects in the relaxed amorphous oxide [15]. Hence, the study of oxygen vacancies and interstitials is expected to give a comprehensive account of the defects states relevant to charge transport.

#### 4.2.1 Oxygen vacancy

First, we analyze the stability of the oxygen vacancy in am-TiO<sub>2</sub>. We create an oxygen vacancy by removing a single O atom from the am-TiO<sub>2</sub> model and relax the structure of the neutral defect at the PBE level. This procedure is carried out for ten different oxygen atoms, which show variations in their local chemical environment. The electronic structure of the system is carried out at the hybrid functional level before and after the structural relaxation of the neutral vacancy. The wave function corresponding to the occupied defect state is always found to localize within the vacancy prior to relaxation [Fig. 4.3(a)]. However, upon structural relaxation, the vacancy is completely assimilated by the amorphous structure in all the studied cases, and the associated wave function is found to be delocalized [Fig. 4.3(b)]. This corresponds to a shift of the defect level towards the conduction band edge [Fig. 4.3(c)], which has been further verified by the DOS of V<sub>O</sub> shown in Fig. 4.4(a) and (b). In the +2 charge state, barely removing an O atom leads to several empty states in the gap [Fig. 4.4(c)], but these defect states completely disappear after structural relaxation, with the DOS becoming identical to that of the bulk model [Fig. 4.4(d)]. Overall, the removal of an O atom has produced a defect-free substoichiometric oxide, am-TiO<sub>2- $\delta$</sub> , similarly to what has been observed previously for oxygen-deficient amorphous HfO<sub>2</sub> [146] and amorphous Al<sub>2</sub>O<sub>3</sub> [cf. Chapter 3]. Hence, unlike

for the crystalline phases of  $\text{TiO}_2$ , oxygen vacancies do not occur in the amorphous material. By consequence, the hopping of holes in am- $\text{TiO}_2$  through defect states associated with this kind of defect cannot be supported. Equivalent results are achieved when a Ti atom is removed from the atomistic model of am- $\text{TiO}_2$ .

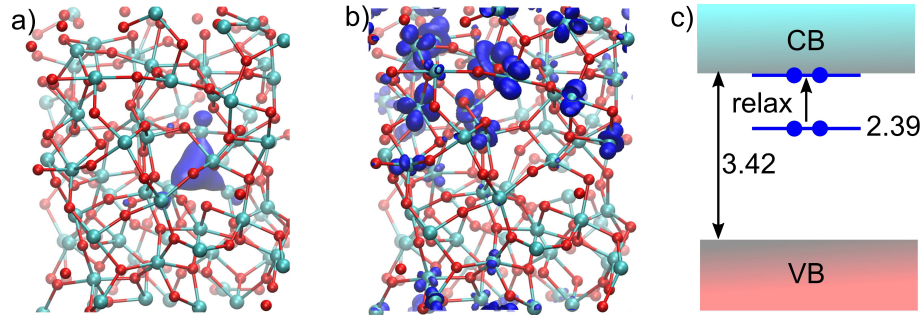


Figure 4.3 – Isosurface representation (blue) of the wave function corresponding to the highest occupied single-particle energy level associated with the neutral oxygen vacancy (a) before and (b) after structural relaxation; O atoms in red, Ti atoms in cyan. (c) Evolution of the Kohn-Sham energy level associated with the defect state upon structural relaxation. Energies are given in eV and are referred to the VBM of pristine am- $\text{TiO}_2$ .

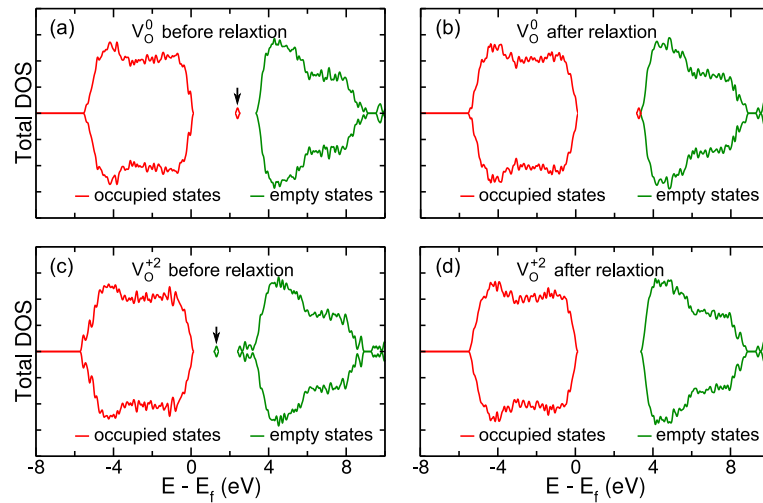


Figure 4.4 – Density of states (DOS) for am- $\text{TiO}_2$  with an O atom removed in the charge states  $q = 0$  (a-b) and  $q = +2$  (c-d). For each charge state, the DOS before and after relaxation are comparatively shown.

#### 4.2.2 Double hole polaron

Next, considering an oxygen interstitial is equivalent to introducing two extra holes, as the oxygen atom only takes the  $-2$  charge state [15]. Hence, we address the case of excess oxygen by adding two holes to the system and by carrying out MD simulations with the PBE functional. We use a temperature of 1000 K to accelerate the crossing of energy barriers. After 3 ps

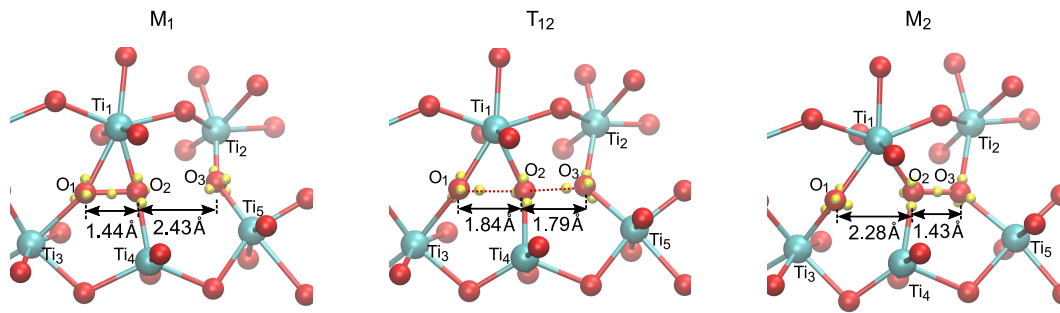


Figure 4.5 – Representation of am- $\text{TiO}_2$  with an O–O peroxy linkage in a configuration in which the O atoms involved in the O–O bond (a) are linked to the same Ti atom or (c) are bonded to different Ti atoms. The structures in (a) and (c) correspond to local minima denoted  $M_1$  and  $M_2$  (cf. main text). In (b), we illustrate the transition state denoted  $T_{12}$ , which connects  $M_1$  and  $M_2$ , as achieved from NEB calculations. The yellow spheres represent the centers of maximally localized Wannier functions associated with the relevant O atoms. The atoms denoted  $\text{Ti}_2$ ,  $\text{Ti}_3$ , and  $\text{Ti}_5$  are sixfold coordinated, whereas  $\text{Ti}_1$  and  $\text{Ti}_4$  are sevenfold and fivefold coordinated, respectively.

of simulation, the system has relaxed and its energy has undergone a decrease of  $\sim 2$  eV. The stabilization results from the rearrangement of the amorphous structure leading to the formation of an O–O peroxy linkage with a bond length of  $1.44 \text{ \AA}$  [Fig. 4.5(a)]. To examine the stability of the O–O peroxy bond in am- $\text{TiO}_2$ , we carry out MD simulations at a higher temperature of 1500 K for 5 ps and find that this feature is preserved. The O–O moiety is found to disappear upon injection of two electrons in the system. We repeat this computational procedure using 30 different starting configurations, as achieved from the MD of the uncharged am- $\text{TiO}_2$ , and the O–O pair is systematically recovered. In particular, we can distinguish two bonding patterns for the peroxy linkage: (i) the two O atoms in the peroxy linkage form one bond to the same Ti atom [Fig. 4.5(a)] and (ii) the O atoms are bound to different Ti atoms [Fig. 4.5(c)]. The former is generally found to be less stable than the latter by 0.2 eV, because of the significant distortion of the O–Ti–O angle. In our analysis, the bonding between O and Ti atoms is assigned according to a Ti–O cutoff distance of  $2.4 \text{ \AA}$ , which corresponds to the first minimum of the Ti–O radial distribution function [Fig. 4.2]. The O–O peroxy linkages are easily recognized as their average bond length ( $1.46 \text{ \AA}$ ) is much lower than distances between second-neighbor O atoms, which exceed  $2 \text{ \AA}$ , as can be inferred from the O–O RDF in Fig. 4.2.

In Fig. 4.6, we give the calculated (+2/0) charge transition levels vs. the O–O bond length for the 30 different peroxy configurations investigated. The distribution of the calculated energy levels shows an average value of 1.25 eV referred to the valence band edge and a standard deviation of 0.15 eV. The bond length distribution has an average of  $1.46 \text{ \AA}$  and a standard deviation of  $0.014 \text{ \AA}$ .

The distribution of calculated (+2/0) defect levels is also illustrated by the blue Gaussian-shaped curve in Fig. 4.7 with respect to the band alignments [70, 176, 177, 178] between am- $\text{TiO}_2$  and the three semiconductors considered in the experiment of Ref. [70], namely



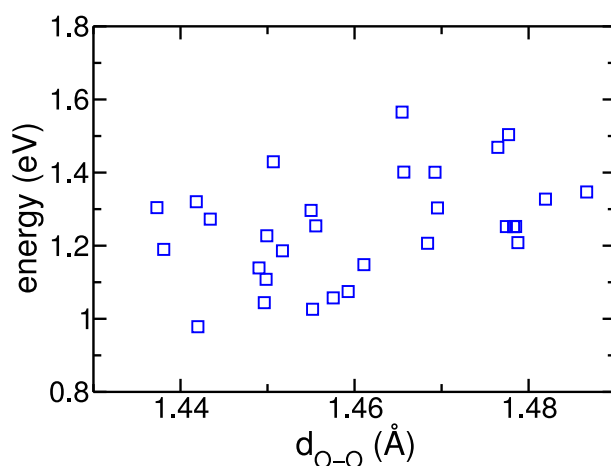


Figure 4.6 – Calculated (+2/0) charge transition levels vs. O–O bond length for 30 different peroxy configurations.

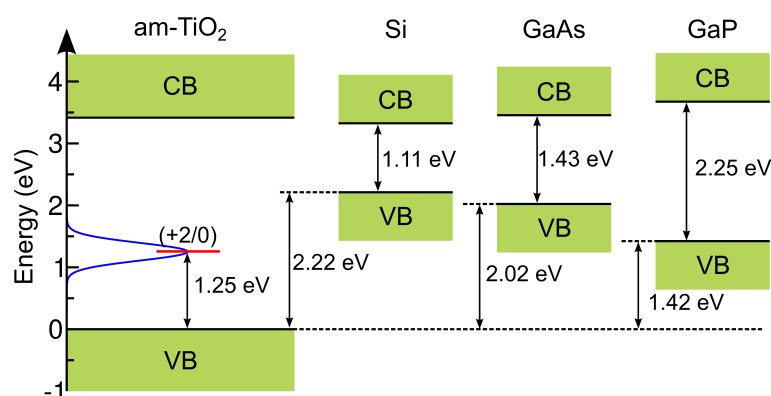


Figure 4.7 – Energy diagram illustrating the distribution of (+2/0) charge transition levels associated with O–O defects in am-TiO<sub>2</sub>. The band edges of Si, GaAs, and GaP are aligned with those of am-TiO<sub>2</sub> using the measured results of Refs. [70, 176, 177, 178]. All energies are given in eV and referred to the VBM of the pristine am-TiO<sub>2</sub> model.

Si, GaAs, and GaP. In this experiment, holes in the *p*-type semiconductor reach the catalytic surface by conduction through a thin layer of am-TiO<sub>2</sub> deposited on the semiconductor [70]. The large currents observed in the experiment preclude conduction of holes through the valence band of am-TiO<sub>2</sub>, which involves barriers corresponding to the valence band offsets, i.e. 2.22, 2.02, and 1.42 eV for Si, GaAs, and GaP, respectively [Fig. 4.7]. We here suggest that the conduction occurs through charge hopping associated with the (+2/0) level of the O–O defect. This conduction channel lowers the barrier for charge injection into am-TiO<sub>2</sub> by ~1.25 eV for the three semiconductors, providing a rationale for the large currents observed in the experiment [70].

### 4.3 Hopping of holes in amorphous TiO<sub>2</sub>

To reveal the hole transport mechanism through O–O peroxy linkages upon injection in am-TiO<sub>2</sub>, we investigate the breaking of an O–O pair followed by its simultaneous formation in a neighbouring location. We first consider a mechanism in which the initial and final O–O peroxy linkages do not share a common O atom. We add two extra holes and observe the formation of a second O–O pair within the same model at a distance of  $\sim 4$  Å from the initial O–O pair. We then construct initial and final configurations in the +2 charge state, both of which contain a single O–O pair, but in different locations. To determine the transition barrier, we perform NEB calculations at the PBE level with the improved tangent (IT) method [179], considering nine replicas between the initial and final configurations. In this way, we obtain a transition barrier of 1.0 eV resulting from the high energy cost for breaking the O–O bond at the transition state.

We then investigate a second transport mechanism, in which the O–O peroxy linkages of the initial and final states share an O atom. This mechanism relies on the fact that all oxygen atoms can be involved in the formation of at least two different O–O pairs by relatively minor structural adjustments. The oxygen atoms do not diffuse across the material and they recover their original positions once the positive charge has passed. In this case, we have been able to construct a minimum energy path involving four subsequent steps by which the charge associated with an O–O pair diffuses over a distance of 1.2 nm, with barriers ranging between 0.3 and 0.5 eV [Fig. 4.8]. The lower barriers found in this second mechanism can be explained by analyzing the structure of the transition states  $T_{ij}$  between two consecutive energy minima  $M_i$  and  $M_j$ . In fact, in the transition state  $T_{ij}$ , the O atom which is shared by the initial and final O–O pairs is found to be almost equidistant from the O atoms involved in the O–O linkages in  $M_i$  and  $M_j$  [Fig. 4.5(b)], with average bond lengths of about 1.8 Å, longer by 0.36 Å than those observed in an isolated peroxy bond. Hence, the diffusion proceeds without ever completely breaking the O–O bond and the transition barriers are lower. This behavior can further be illustrated in terms of maximally localized Wannier functions [158], which give a real-space representation of the electron localization. In Fig. 4.5, we show the evolution of the centers of such Wannier functions for the relevant O atoms as the hopping proceeds. In the initial state, the Wannier center representing the O<sub>1</sub>–O<sub>2</sub> bond is located centrally, but moves closer to O<sub>1</sub> in the transition state, where O<sub>2</sub> attracts one of the lone pairs of O<sub>3</sub>, in view of forming a regular O<sub>2</sub>–O<sub>3</sub> bond in the final state. This process gives a diffusion mechanism by which the holes leak through the am-TiO<sub>2</sub> layer, despite the presence of a well defined band gap that supports its insulating character. The energy barriers are found to be only marginally affected by the density functional as IT-NEB calculations at the PBE0( $\alpha$ ) level are found to give differences smaller than 0.07 eV.

It should be noted that the energy barriers calculated in this work may represent an upper-bound limit. In fact, given the disordered environment and the possibility of forming O–O pairs anywhere in the oxide, the diffusion is expected to proceed through percolation, generally resulting in overall lower transition barriers than the ones encountered in the present study.

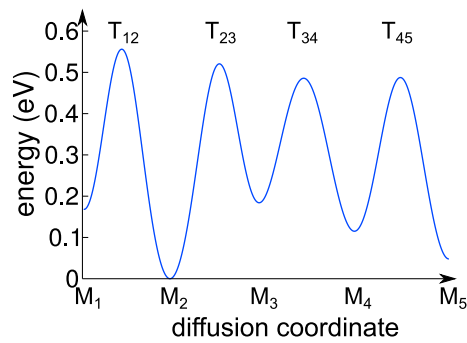


Figure 4.8 – (a) Energy diagram illustrating the hole diffusion through O–O peroxy linkages in am-TiO<sub>2</sub> along a diffusion coordinate visiting several minima  $M_i$  in sequence ( $i = 1, 2, \dots, 5$ ). Transition states  $T_{ij}$  connect sequential minima  $M_i$  and  $M_j$ , where  $j = i + 1$ . The minima  $M_1$  and  $M_5$  are separated by a distance of 1.2 nm.

Furthermore, the barrier is related to the distance between O atoms, which in turn depends on the concentration of oxygen in the material. Therefore, lower barriers are expected to occur in oxygen-rich conditions or in amorphous layers of higher density.

#### 4.4 Conclusion

In conclusion, we studied hole diffusion across amorphous TiO<sub>2</sub> layers through O–O peroxy linkages. We generated a model for amorphous TiO<sub>2</sub> through *ab initio* molecular dynamics simulations, and found good agreement with the experimental characterization. Then, we demonstrated that oxygen vacancies cannot contribute to hole transport, as these intrinsic defects do not occur in am-TiO<sub>2</sub>. In contrast, O–O peroxy linkages are formed in pristine am-TiO<sub>2</sub> upon injection of excess holes, and give a defect distribution centered at 1.25 eV above the valence band. The hole diffusion in am-TiO<sub>2</sub> through an exchange mechanism involving such O–O pairs is viable and proceeds with energy barriers lower than 0.5 eV.

The results presented in this chapter have been published in Ref. [180].



## 5 Alignment of energy levels at semiconductor-water interfaces

In this chapter, we present an *ab initio* study of the band alignment at the pH corresponding to the point of zero charge for various semiconductor-water interfaces. The employed protocol combines molecular dynamics simulations of atomistic semiconductor-water interfaces, advanced electronic-structure calculations, and a computational standard hydrogen electrode. Considered semiconductors are GaAs, GaP, GaN, CdS, ZnO, SnO<sub>2</sub>, rutile TiO<sub>2</sub>, and anatase TiO<sub>2</sub>. Through extensive *ab initio* molecular dynamics simulations, we determine the most stable interface structures, in which the water molecules are adsorbed either molecularly, dissociatively, or in a mixed fashion. Advanced electronic-structure calculations, including hybrid functional and various *GW* schemes are used to determine the band edges of the bulk materials. These are then aligned with respect to the standard hydrogen electrode level, which is defined as a redox level in the band gap of liquid water [128], through the line-up of the electrostatic potential at the solid-liquid interface. By defining a mean average error (MAE) with respect to the experimental offsets, we finally assess the accuracy of the electronic-structure methods employed in this work for the calculation of band alignments. This work emphasizes that both the proper atomistic description of the interface structure and the use of electronic-structure methods producing accurate band gaps of semiconductors are ineluctable for accurately determining the band alignment.

This chapter is organized as follows. In Section 5.1, we report the details of the electronic-structure calculations and present the scheme used for the band alignment. In Section 5.2, we calculate the SHE level relative to the vacuum level by modeling the water-vacuum interface, and compare our result with the well-known experimental value (4.44 eV). In Section 5.3, we discuss band gaps, ionization potentials, and electron affinities, as achieved with the electronic-structure methods considered in this work. In Section 5.4, we describe the protocol used to generate the semiconductor-water interface models, their structural properties, and the relative stability of molecular and dissociated models. In Section 5.5, we present the calculated band offsets, assess the overall accuracy of the employed methods, and compare our results with previous work. The conclusions are drawn in the last Section 5.6.

## 5.1 Methods

We investigate the interface with liquid water for the following materials: GaAs and GaP with the zinc blende structure, GaN, ZnO, and CdS with the wurtzite structure, SnO<sub>2</sub> and TiO<sub>2</sub> in both the rutile (r-TiO<sub>2</sub>) and anatase (a-TiO<sub>2</sub>) polymorphs. For these materials, experimental data for the band alignment at the interface with liquid water are available [181, 182, 80, 183]. Since they have different chemical compositions, structural properties, and band gaps, they represent an appropriate benchmark set. In the following, we report the computational details of the electronic-structure calculations, and describe the method used for the band alignment at the semiconductor-water interface.

### 5.1.1 Electronic-structure calculations

The lattice parameters of GaP, GaN, CdS, ZnO, and TiO<sub>2</sub> [Table 5.1] are achieved through structural relaxation with the density functional developed by Perdew, Burke, and Ernzerhof (PBE) [109] and are converged with respect to the size of the supercells. These calculations are performed with the CP2K code. Following Ref. [94], we use experimental lattice parameters for GaAs and SnO<sub>2</sub>. This choice is motivated by the fact that small deviations of the calculated lattice parameters with respect to the experimental values would lead to a large effect on the energy levels, due to the high absolute deformation potentials of these materials [184].

Table 5.1 – Crystal lattice parameters  $a$  and  $c$  used in this work. The lattice parameters correspond to the relaxed values obtained with the PBE functional, except in the case of GaAs and SnO<sub>2</sub>, for which the experimental values are used. Experimental values are given in parentheses for comparison. The dimensions of the supercells employed in the MD simulations of bulk semiconductors at 300 K are also given.

semiconductor	$a$ (Å)	$c$ (Å)	supercell for MD
GaAs	5.653 (5.653)		$3 \times 3 \times 3$
GaP	5.536 (5.451)		$3 \times 3 \times 3$
GaN	3.235 (3.189)	5.264 (5.185)	$3 \times 4 \times 2$
CdS	4.214 (4.137)	6.863 (6.714)	$3 \times 4 \times 2$
ZnO	3.294 (3.249)	5.301 (5.207)	$3 \times 4 \times 2$
SnO <sub>2</sub>	4.737 (4.737)	3.185 (3.185)	$3 \times 3 \times 4$
r-TiO <sub>2</sub>	4.662 (4.593)	3.002 (2.958)	$3 \times 3 \times 4$
a-TiO <sub>2</sub>	3.805 (3.785)	9.673 (9.514)	$4 \times 4 \times 2$

The theoretical band gap of a semiconductor at 0 K is defined as follows:

$$E_g^{\text{theory}}(0) = \varepsilon_c^{\text{theory}}(0) - \varepsilon_v^{\text{theory}}(0), \quad (5.1)$$

where  $\varepsilon_c^{\text{theory}}(0)$  and  $\varepsilon_v^{\text{theory}}(0)$  are the calculated positions of the conduction and valence band at 0 K, respectively. The band gaps of the semiconductors at 0 K are calculated using the ABINIT

code [131]. For all the materials studied, core-valence interactions are described through norm-conserving pseudopotentials [Table 5.2]. The  $\mathbf{k}$ -point mesh [185] used for each semiconductor is given in Table 5.3. We carry out hybrid functional calculations with the PBE0 functional [112, 113], in which the fraction of Fock exchange  $\alpha$  is set to 0.25. In the following, this scheme is denoted as PBE0(0.25). Among the calculations of the band gap at the  $GW$  level, we first consider single-shot  $G_0W_0$  schemes [Table 5.4]. In particular, we perform  $G_0W_0$  calculations on top of starting points achieved at (i) the PBE level [ $G_0W_0(0)$ ] and (ii) the PBE0 level with  $\alpha = 0.25$  [ $G_0W_0(0.25)$ ], where  $W_0$  is described within the random phase approximation. For both these  $GW$  schemes, the calculations are also repeated including vertex corrections in the screened interaction  $\widetilde{W}$  [ $G_0\widetilde{W}_0(0)$  and  $G_0\widetilde{W}_0(0.25)$ ]. Next, we complement our  $GW$  calculations with quasi-particle self-consistent schemes [186]. In particular, these schemes include (i) the  $QSGW_0^{\text{PBE}}$  method, where the screened potential  $W$  is fixed at the PBE level, and (ii)  $QSGW$  and  $QSG\widetilde{W}$ , where the screened interactions  $W$  and  $\widetilde{W}$  are both iterated to self-consistency [94]. We also perform hybrid functional and  $GW$  calculations, which are empirically tuned to reproduce the experimental band gap, in order to evaluate the relative accuracies of PBE0

Table 5.2 – Setup of the norm-conserving pseudopotentials used in this work. The angular momentum  $l$  of the local channel, the cutoff radii  $r_s$ ,  $r_p$ , and  $r_d$  (in bohr) in the various waves of angular momentum, and the kinetic energy cutoff  $E_{\text{cut}}$  (in Ry) are listed.

	Valence	$l(\text{local})$	$r_s$	$r_p$	$r_d$	$E_{\text{cut}}$
N	$2s2p$	0	1.35	1.54		65
O	$2s2p$	2	1.15	1.25		80
P	$3s3p$	0	1.40	1.45		50
S	$3s3p$	4	1.45	1.45		60
As	$4s4p$	0	1.58	1.75		100
Zn	$3s3p4s4p3d$	1	0.80	0.80	0.80	330
Ga	$3s3p4s4p3d$	1	0.80	0.80	0.80	330
Cd	$4s4p4d5s$	4	1.25	1.30	1.35	100
Sn	$4s4p4d5s5p$	4	1.30	1.30	1.30	100
Ti	$3s3p4s4p3d$	0	1.28	1.28	1.70	100

Table 5.3 –  $\mathbf{k}$ -point samplings ( $\Gamma$  centered), the number of unoccupied bands  $n_b$ , and the cutoff  $E_{\text{cut}}^{\text{d}}$  (in Ry) for the dielectric matrix used in the  $GW$  calculations.

Compound	$\mathbf{k}$ points	$n_b$	$E_{\text{cut}}^{\text{d}}$
GaAs	$6 \times 6 \times 6$	768	25
GaP	$6 \times 6 \times 6$	768	25
GaN	$6 \times 6 \times 4$	768	25
CdS	$6 \times 6 \times 4$	768	25
ZnO	$6 \times 6 \times 4$	1000	25
SnO <sub>2</sub>	$5 \times 5 \times 7$	1000	25
r-TiO <sub>2</sub>	$5 \times 5 \times 7$	750	25
a-TiO <sub>2</sub>	$5 \times 5 \times 5$	768	25

## Chapter 5. Alignment of energy levels at semiconductor-water interfaces

Table 5.4 – Notation for the  $GW$  schemes used in this work. All the schemes are fully *ab initio* except the last two, in which the fraction of Fock exchange  $\alpha$  is tuned to reproduce the experimental band gap.

Notation	Type	Starting point	Correction
$G_0W_0(0)$	One-shot	PBE	
$G_0\widetilde{W}_0(0)$	One-shot	PBE	vertex
$G_0W_0(0.25)$	One-shot	PBE0(0.25)	
$G_0\widetilde{W}_0(0.25)$	One-shot	PBE0(0.25)	vertex
QSGW	Self-consistent		
$QSGW_0^{\text{PBE}}$	Self-consistent	$W$ fixed at the PBE level	
$QSG\widetilde{W}$	Self-consistent		vertex
$G_0W_0(\alpha)$	One-shot	PBE0( $\alpha$ )	
$G_0\widetilde{W}_0(\alpha)$	One-shot	PBE0( $\alpha$ )	vertex

and  $GW$  calculations beyond the error in the calculated band gap. In particular, we perform (i) PBE0 calculations with the fraction  $\alpha$  of Fock exchange set to reproduce the band gap [PBE0( $\alpha$ )] and (ii) one-shot  $G_0W_0$  and  $G_0\widetilde{W}_0$  calculations on top of starting points obtained with PBE0( $\alpha$ ), in which  $\alpha$  is tuned to obtain calculated band gaps matching the experimental ones [ $G_0W_0(\alpha)$  and  $G_0\widetilde{W}_0(\alpha)$ ]. The notation for the various  $GW$  schemes used in this work is given in Table 5.4. For r-TiO<sub>2</sub> and a-TiO<sub>2</sub>, the band gap at the  $G_0W_0(0)$  level already exceeds the experimental value and the empirical tuning of the band gap by varying  $\alpha$  in  $G_0W_0(\alpha)$  can thus not be achieved.

In the  $GW$  calculations, the contour deformation method [187] is used to evaluate the frequency dependence of the dielectric matrices  $\epsilon^{-1}(\omega)$ . The cutoff energy  $E_{\text{cut}}^{\text{d}}$  used for the dielectric matrices is 25 Ry. A large number of unoccupied bands  $n_{\text{b}}$  (usually 764 to 1000) is included in the  $GW$  calculations [Table 5.3] [93, 94]. In order to verify the convergence of these calculations, we analyze the results achieved at the  $G_0W_0$  level by systematically varying  $E_{\text{cut}}^{\text{d}}$  and  $n_{\text{b}}$  for the eight materials under investigation. To extrapolate the dependence on  $n_{\text{b}}$ , the  $G_0W_0$  band edges are fitted using the following hyperbolic function [188]:

$$f(n_{\text{b}}) = \frac{a}{n_{\text{b}} - b} + c, \quad (5.2)$$

where  $f(n_{\text{b}})$  is either the valence or the conduction band edge at a given  $n_{\text{b}}$ , and where  $a$ ,  $b$ , and  $c$  are fitting parameters. These convergence tests are illustrated in Fig. 5.1 for ZnO<sub>2</sub> and a-TiO<sub>2</sub>. The band edges obtained with various  $GW$  methods are modified by adding a correction term ( $\Delta_{\text{v}}^{\text{GW}}$  and  $\Delta_{\text{c}}^{\text{GW}}$ ) calculated as the difference between the  $G_0W_0$  results achieved with the setup of Table 5.3 and the extrapolated value for  $n_{\text{b}} \rightarrow \infty$ . The correction terms reported in Table 5.5 indicate that for most of the semiconductors the results achieved with the setup listed in Table 5.3 are within 0.05 eV from the extrapolated values. However, the convergence is found to be slower in some cases, such as for ZnO, SnO<sub>2</sub>, and TiO<sub>2</sub>, for which the correction terms are larger than 0.1 eV. A slower convergence for ZnO has already been reported in Refs.



[189] and [190].

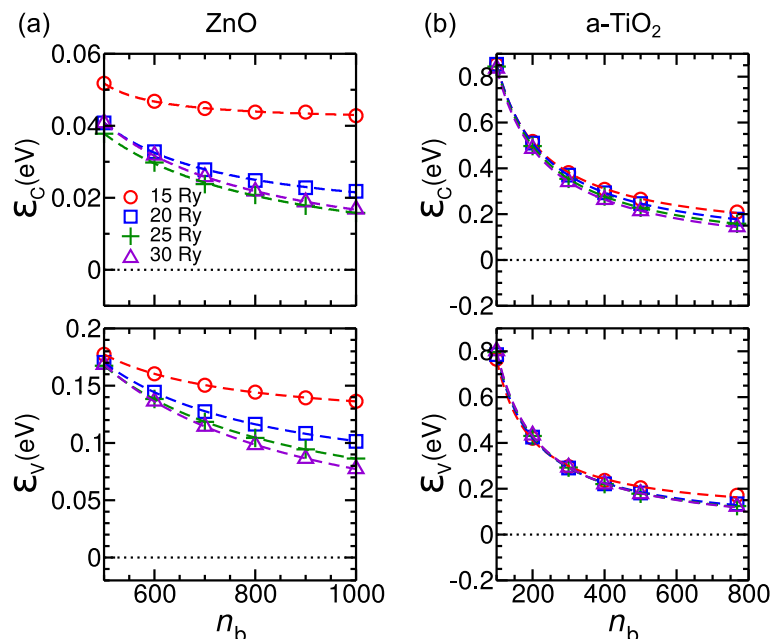


Figure 5.1 – Valence and conduction band edges calculated at the  $G_0 W_0(0)$  level for (a) ZnO<sub>2</sub> and (b) a-TiO<sub>2</sub>, as a function of  $n_b$  for different values of  $E_{\text{cut}}^d$ . Dashed lines represent fitted hyperbolic functions. Energies are referred to the position of the band edges extrapolated to  $n_b \rightarrow \infty$  (black dotted lines).

Our hybrid functional and GW calculations do not include effects of spin-orbit coupling (SOC). The corrections in the calculated band edges induced by SOC effects,  $\Delta\varepsilon_v^{\text{SOC}}$  and  $\Delta\varepsilon_c^{\text{SOC}}$ , are taken from the values reported in Ref. [191] for GaP, GaN, CdS, and ZnO, and are explicitly calculated for GaAs, SnO<sub>2</sub>, r-TiO<sub>2</sub>, and a-TiO<sub>2</sub>. We carried out the latter calculations at the PBE level with the code QUANTUM ESPRESSO [192], using fully relativistic optimized norm-conserving pseudopotentials [193]. Apart from GaAs, for which SOC effects are known to be relevant [194], the correction terms for the other materials are negligibly small [Table 5.5].

Table 5.5 – Corrections to the calculated band edges (in eV) due to SOC effects, thermal effects at 300 K, and convergence of the GW results.

	$\Delta\varepsilon_v^{\text{SOC}}$	$\Delta\varepsilon_c^{\text{SOC}}$	$\Delta\varepsilon_v^T$	$\Delta\varepsilon_c^T$	$\Delta\varepsilon_v^{\text{GW}}$	$\Delta\varepsilon_c^{\text{GW}}$
GaAs	0.11	0.00	0.05	-0.04	-0.02	-0.02
GaP	0.03	0.00	0.05	-0.05	-0.02	-0.02
GaN	0.00	0.00	0.05	-0.05	-0.08	-0.05
CdS	0.03	0.00	0.04	-0.04	-0.09	-0.05
ZnO	0.00	0.00	0.03	-0.03	-0.06	-0.02
SnO <sub>2</sub>	0.00	0.00	0.07	-0.03	-0.11	-0.07
r-TiO <sub>2</sub>	0.00	0.00	0.06	-0.07	-0.13	-0.15
a-TiO <sub>2</sub>	0.00	0.00	0.17	0.08	-0.12	-0.14

## Chapter 5. Alignment of energy levels at semiconductor-water interfaces

---

The fundamental band gaps, the ionization potentials, the band alignments at semiconductor-water interfaces considered in this work are all measured at room temperature. In order to make contact with experiment, we define the theoretical band gap of a semiconductor at a given temperature  $T$  as follows:

$$E_g^{\text{theory}}(T) = \varepsilon_c^{\text{theory}}(T) - \varepsilon_v^{\text{theory}}(T), \quad (5.3)$$

where

$$\varepsilon_v^{\text{theory}}(T) = \varepsilon_v^{\text{theory}}(0) + \Delta\varepsilon_v^T, \quad (5.4)$$

and

$$\varepsilon_c^{\text{theory}}(T) = \varepsilon_c^{\text{theory}}(0) + \Delta\varepsilon_c^T, \quad (5.5)$$

where  $\Delta\varepsilon_v^T$  and  $\Delta\varepsilon_c^T$  are the  $T$ -dependent corrections of the band edges. These quantities are obtained by performing molecular dynamics simulations at 300 K. We use the CP2K code at the PBE level, with pseudopotentials and basis sets reported above. The simulation periods range between 2 and 4 ps. The supercells employed in these calculations are reported in Table 5.1. The corrections  $\Delta\varepsilon_v^T$  and  $\Delta\varepsilon_c^T$  of the band edges given in Table 5.5 are obtained from the linear extrapolation of the wings of the averaged electronic density of states (DOS), as described in Refs. [128] and [195].

To verify that the method employed to evaluate  $\Delta\varepsilon_v^T$  and  $\Delta\varepsilon_c^T$  is consistent with available temperature-dependent band-gap measurements, we compare the experimental renormalization of the band gap between 0 and 300 K,  $\Delta E_g(\text{expt.})$ , with the calculated one,  $\Delta E_g(\text{theory}) = \Delta\varepsilon_c^T - \Delta\varepsilon_v^T$ . The results collected in Table 5.6 indicate that our MD simulations reproduce well the experimental band-gap renormalization induced by thermal effects. Electron-phonon coupling has been neglected in the calculation of band gaps.

Table 5.6 – Experimental and calculated band-gap renormalization between 0 and 300 K for various semiconductors.

Semiconductor	$\Delta E_g(\text{expt.})$	$\Delta E_g(\text{theory})$
GaAs	-0.10 <sup>a</sup>	-0.09
GaP	-0.08 <sup>b</sup>	-0.10
GaN	-0.09 <sup>c</sup>	-0.10
CdS	-0.09 <sup>d,e</sup>	-0.08
ZnO	-0.07 <sup>f,g,h</sup>	-0.07
SnO <sub>2</sub>	-0.17 <sup>i,j</sup>	-0.12
r-TiO <sub>2</sub>	-0.06 <sup>k,l</sup>	-0.08
a-TiO <sub>2</sub>	-0.10 <sup>m,n</sup>	-0.09

<sup>a</sup> Ref. [196]. <sup>b</sup> Ref. [197]. <sup>c</sup> Ref. [198]. <sup>d</sup> Ref. [199]. <sup>e</sup> Ref. [200]. <sup>f</sup> Ref. [201]. <sup>g</sup> Ref. [202].

<sup>h</sup> Ref. [203]. <sup>i</sup> Ref. [204]. <sup>j</sup> Ref. [205]. <sup>k</sup> Ref. [173]. <sup>l</sup> Ref. [206]. <sup>m</sup> Ref. [174]. <sup>n</sup> Ref. [175].

## 5.1.2 Band alignment at semiconductor-water interfaces

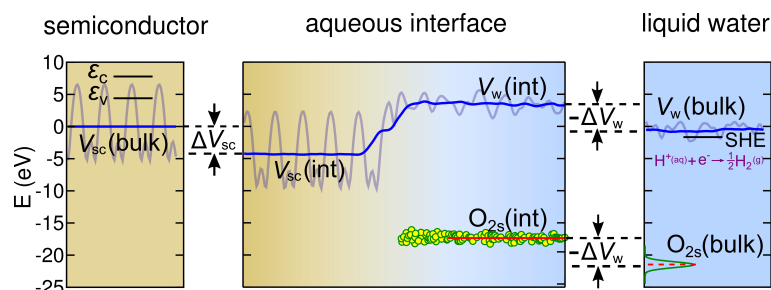


Figure 5.2 – Schematic representation of the band alignment at the semiconductor-water interface. In the left panel, the conduction and valence band edges ( $\epsilon_c$  and  $\epsilon_v$ ) of the semiconductor are shown with respect to the electrostatic potential (grey) and its average  $V_{sc}(\text{bulk})$ . Similarly, on the right, the SHE level is given with respect to the electrostatic potential (grey) and its average  $V_w(\text{bulk})$  in liquid water. The line-up between the electrostatic potentials  $V_{sc}(\text{int})$  and  $V_w(\text{int})$  is illustrated in the middle panel. The figure also illustrates the alternative but equivalent alignment in liquid water through the average O 2s level.

The band alignment at the semiconductor-water interface requires three steps [207, 208, 209, 96, 105]: (i) the calculation of the SHE redox level, (ii) the calculation of the band gap of the semiconductor, and (iii) the calculation of the line-up of the average electrostatic potential across the semiconductor-water interface. We employ a computational version of the SHE level, which is defined by the reduction of the hydronium ion to gaseous hydrogen [128, 101]. The redox level associated to this reaction  $\mu_{\text{SHE}}$  has been calculated by combining *ab initio* MD simulations, a grand-canonical formulation of solutes in aqueous solution, and the thermodynamic integration method [128]. This redox level is referred to the average electrostatic potential of liquid water,  $V_w(\text{bulk})$ . The band gaps of the semiconductors under consideration are calculated with various electronic-structure methods, and the valence band edges  $\epsilon_v$  are referred to the average electrostatic potential. The band edges of the semiconductor and the SHE level are aligned at the semiconductor-water interface through the line-up of the plane-averaged electrostatic potential [Fig. 5.2]. In particular, we define the potential shift of the semiconductor  $\Delta V_{sc}$  and of liquid water  $\Delta V_w$ , as follows:

$$\Delta V_{sc} = V_{sc}(\text{bulk}) - V_{sc}(\text{int}), \quad (5.6)$$

and

$$\Delta V_w = V_w(\text{bulk}) - V_w(\text{int}), \quad (5.7)$$

where  $V_{sc}(\text{int})$  and  $V_w(\text{int})$  are the averaged electrostatic potentials in the bulk-like region of the interface for the semiconductor and for liquid water, respectively.  $\Delta V_w$  can equivalently be calculated through the shift of the O 2s core levels, the difference being at most 0.05 eV. Moreover, we verify that the line-up of the average electrostatic potential across the interface does not depend on the employed level of theory, with PBE, rVV10, and PBE0(0.25) functionals

all providing the same potential profiles within 0.01 eV when using the structural configurations generated in the MD simulations. This result is consistent with previous calculations for solid-solid interfaces [209, 210, 211].

It should be noted that special attention in the alignment has been devoted to the cases of GaAs and SnO<sub>2</sub>. For these materials, the exposed surface area of the semiconductor in the MD simulations is based on the experimental lattice parameters, effectively leading to the application of in-plane strain. This effect in turn leads to interlayer relaxation in the direction perpendicular to the interface, which needs to be accounted for in the overall alignment. We determine the resulting shift by considering an interface between a relaxed and a nonrelaxed layer of the same semiconductor [212]. This extra shift amounts to at most 0.06 eV and is included in  $\Delta V_{sc}$ .

All the interfaces studied in this work are neutral by construction. Hence, the semiconductors are modelled in aqueous environment at a pH value corresponding to the point of zero charge (pH<sub>PZC</sub>). The alignment of the valence band edge at pH<sub>PZC</sub> reads as follows [Fig. 5.2]:

$$\varepsilon_v^{\text{SHE}}(\text{PZC}) = \varepsilon_v^{\text{theory}}(T) - \mu_{\text{SHE}} - \Delta V_{sc} + \Delta V_w. \quad (5.8)$$

Consequently, the conduction band edge  $\varepsilon_c^{\text{SHE}}(\text{PZC})$  is obtained as follows:

$$\varepsilon_c^{\text{SHE}}(\text{PZC}) = \varepsilon_v^{\text{SHE}}(\text{PZC}) + E_g^{\text{theory}}(T). \quad (5.9)$$

The use of the computational SHE [128] allows one to calculate the band alignment with respect to an energy level that is defined in a similar way to a charge transition level of a defect in a wide band-gap insulator (liquid water in the present case). We have also verified that  $\mu_{\text{SHE}}$  is constant with respect to the average electrostatic potential when varying the fraction of Fock exchange  $\alpha$  introduced in the density functional from 0 to 60% [128]. Such a robust definition of  $\mu_{\text{SHE}}$  with respect to  $\alpha$  mirrors the analogous behavior observed for charge transition levels of defects in crystalline materials [209, 119, 213]. The robustness of the correspondence also holds at the *GW* level [214, 215]. Therefore, it is meaningful to employ the value of  $\mu_{\text{SHE}}$  calculated at the rVV10 level to align band edges calculated at the hybrid-functional and *GW* level.

Furthermore, the proposed method does not require the calculation of potential offsets at the water-vacuum interface, which implies long MD simulations, is subject to large uncertainties due to the slow convergence of surface dipoles, and depends upon the computational setup (i.e. pseudopotentials, classic or ab initio MD) [216, 217]. For the purpose of our work, defining the accuracy of the computational SHE with respect to the experimental SHE is unnecessary. In fact, within the employed formulation, the computational SHE represents a reference for other redox levels (or charge transition levels) to be compared with. The energy separations between the computational SHE level and calculated redox levels are indeed comparable with the experiment. It has been shown that the overall accuracy of the method is within 0.1-0.2 eV

[128, 218, 99, 101, 219].

## 5.2 Absolute energy levels of liquid water

In this work, a value of 0.87 eV corresponding to the computational SHE level versus the average electrostatic potential in bulk water is adopted [220]. This value has been reported to be almost constant with the fraction  $\alpha$  of Fock exchange in the PBE0 functional [128]. In order to avoid confusion, we define that a positive value for an energy level vs. SHE means that this level is farther away from the vacuum level than the SHE reference, while a negative value means this level is closer to the vacuum.

To get an estimate of the computational SHE with respect to the vacuum level, we model the water-vacuum interface by carrying out *ab initio* molecular dynamics (MD) simulations of liquid water with classical nuclei in the NVT ensemble. We use an orthorhombic periodic supercell ( $a = 12.42$  and  $c = 24.48$  Å) containing 128 water molecules at the experimental density of liquid water ( $1 \text{ g/cm}^3$ ). Then, we enlarge the simulation cell in the  $c$  direction to accommodate 40 Å of vacuum ( $a = 12.42$  and  $c = 64.48$  Å) and evolve the MD further for 60 ps. This computational setup has been shown to be sufficient for achieving proper potential offsets, when compared to simulations with larger supercells and with quantum nuclei [221]. We use the rVV10 functional that has been designed to reproduce the experimental density of bulk liquid water [136]. In the MD simulation of the slab, the averaged mass density of water in the bulk region amounts to  $0.995 \text{ g/cm}^3$  [Fig. 5.3], thus differing from the target value by only  $0.005 \text{ g/cm}^3$ . Such a difference leads to negligible differences in the potential offset, as can be inferred from the calculated deformation potential of liquid water [222].

During the MD simulation, we monitor the electric field in the vacuum region finding oscillations without any drifting behavior around an average value of only  $0.004 \text{ eV/Å}$  [Fig. 5.4] to be compared with the average value of  $0.005 \text{ eV/Å}$  achieved in Ref. [217] for a classical simulation lasting 1 ns. In the calculation of the potential offset  $\Delta V$  between the bulk region of the water slab and the vacuum level, the potential profile is symmetrized, thereby effectively eliminating the bias due to a residual electric field. Upon MD evolution,  $\Delta V$  converges to a value of  $3.69 \pm 0.04 \text{ eV}$ , where the error is calculated by performing a blocking analysis [Fig. 5.3(b)] [223]. This value appears to have converged, as time averages over the duration of 1 ps are found to oscillate around the average value, without showing any drifting behavior [Fig. 5.5]. We also notice that recalculation of  $\Delta V$  at the hybrid functional level produces an almost negligible difference (0.06 eV), in line with previous observations [209, 211, 224]. The present value of  $\Delta V$  is similar to other calculations in the literature (3.63–3.97 eV) [221, 217], but it should be noted that it depends in principle on the functional and the pseudopotentials and can thus be used only for internal alignments within a given computational setup.

To achieve a water-vacuum interface at which the water molecules are randomly oriented, we also construct water slabs from structural configurations obtained with simulations of bulk liquid water. In particular, we take a cubic 64-water-molecule supercell, double it along

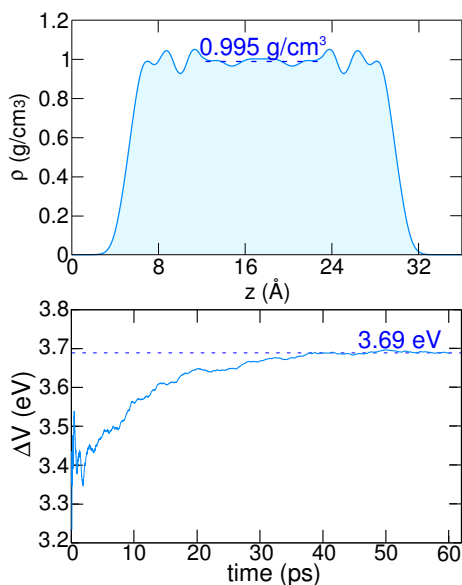


Figure 5.3 – (a) Planar averaged mass density of liquid water at the interface with vacuum. (b) Cumulative running average of the potential offset  $\Delta V$  across the water-vacuum interface. The dashed line indicates the converged value.

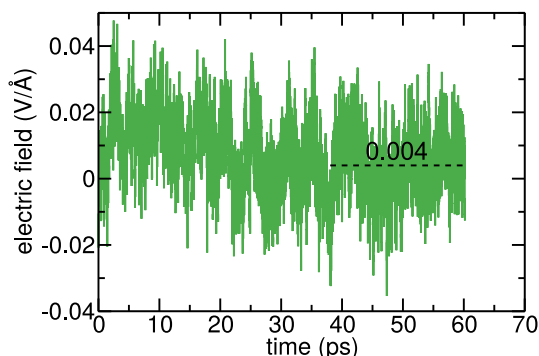


Figure 5.4 – Time evolution of the electric field in the slab simulation.

one direction, cut it on both sides avoiding the formation of dangling bonds, and add a vacuum layer. This procedure allows us to produce slabs of the same size as those achieved in the MD simulation of the water-vacuum interface, but in which the water dipoles at the interface are oriented randomly. Considering a set of 2400 structures constructed in this way, we calculate a potential offset of  $\Delta V_{\text{random}} = 3.54$  eV for such an interface. The availability of  $\Delta V$  and  $\Delta V_{\text{random}}$  allows us to distinguish between quadrupolar and dipolar contributions to the potential offset. In particular, we find that  $\Delta V$  is dominated by quadrupolar contributions, which do not depend on the interface structure, as also observed in Ref. [217]. The calculated dipolar contribution of 0.15 eV is consistent with a previous theoretical study [217] and agrees well with available estimates for the dipolar surface potential of water (0.14–0.17 eV) [101, 225].

## 5.2. Absolute energy levels of liquid water

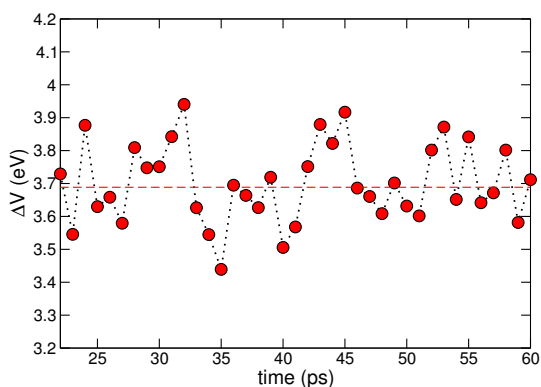


Figure 5.5 – Average values of  $\Delta V$  calculated at each ps of the MD simulation. The overall average is reported as a dashed red line.

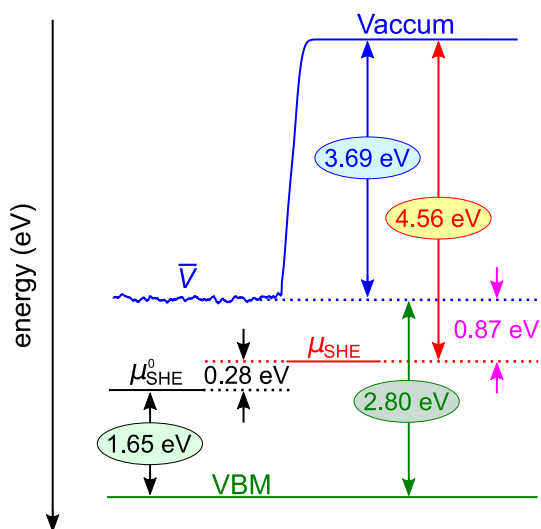


Figure 5.6 – Schematic representation of the alignment of the standard hydrogen electrode level  $\mu_{\text{SHE}}$  at the water-vacuum interface.

To achieve a physically meaningful reference level of bulk liquid water, we focus on the computational SHE level [101, 128]. The level  $\mu_{\text{SHE}}$  can be aligned with respect to the average electrostatic potential of liquid water by using the grand-canonical formulation of solutes in aqueous solution and the thermodynamic integration method [128]. Hence, by combining this result with the potential offset at the water-vacuum interface, we place  $\mu_{\text{SHE}}$  at 4.56 eV below the vacuum level [Fig. 5.6], very close to the value of 4.44 eV proposed by Trasatti [226]. This agreement therefore allows one to align in a reliable way the band structure of bulk water to the vacuum level as well as the redox levels at semiconductor-water interfaces.

It should be noted that in our paper “Alignment of Redox Levels at Semiconductor-Water Interfaces” (*Chem. Mater.* 2018, 30, 94-111), the SHE level ( $\mu_{\text{SHE}}^0$ ) had been located at 0.28 eV below the present SHE level ( $\mu_{\text{SHE}}$ ) [Fig. 5.6]. Therefore, the relative positions of the band edges of the semiconductors versus the standard hydrogen electrode reported here have been

corrected accordingly. Because the  $\mu_{\text{SHE}}$  is a redox level, the calculated alignment is expected to be robust and to depend only very weakly on the adopted density functional [128], in perfect analogy with defect levels in semiconductors and insulators [209, 119].

### 5.3 Electronic properties of semiconductors

Table 5.7 – Experimental and calculated band gaps (in eV) at 300 K of the semiconductors studied in the present work. Mean absolute errors (MAEs) are given for each electronic-structure scheme.

	Expt.	PBE	PBE0(0.25)	$G_0W_0(0)$	$G_0\widetilde{W}_0(0)$	$G_0W_0(0.25)$	$G_0\widetilde{W}_0(0.25)$	$\text{QSGW}_0^{\text{PBE}}$	QSGW	$\text{QSGW}^{\widetilde{}}$
GaAs	1.42 <sup>a</sup>	0.35	1.76	1.01	0.91	1.65	1.49	1.17	1.66	1.42
GaP	2.26 <sup>b</sup>	1.31	2.88	2.02	1.91	2.71	2.52	2.20	2.65	2.35
GaN	3.42 <sup>c</sup>	1.57	3.46	2.54	2.30	3.43	3.05	2.94	3.68	3.04
CdS	2.49 <sup>d</sup>	0.97	2.66	2.03	1.88	2.93	2.56	2.39	3.14	2.55
ZnO	3.37 <sup>e</sup>	0.71	3.04	2.01	1.59	3.40	2.71	3.07	4.32	3.35
SnO <sub>2</sub>	3.49 <sup>f,g</sup>	1.17	3.57	2.70	2.28	3.87	3.24	3.44	4.44	3.51
r-TiO <sub>2</sub>	3.00 <sup>h</sup>	1.72	3.89	3.07	2.84	3.75	3.33	3.17	4.02	3.51
a-TiO <sub>2</sub>	3.36 <sup>i,j</sup>	2.05	4.22	3.48	3.21	3.48	3.00	3.20	4.19	3.52
MAE		1.62	0.42	0.54	0.74	0.30	0.29	0.20	0.66	0.16

<sup>a</sup> Ref. [196]. <sup>b</sup> Ref. [197]. <sup>c</sup> Ref. [198]. <sup>d</sup> Ref. [199]. <sup>e</sup> Ref. [201]. <sup>f</sup> Ref. [204]. <sup>g</sup> Ref. [205]. <sup>h</sup> Ref. [173]. <sup>i</sup> Ref. [174]. <sup>j</sup> Ref. [175].

Table 5.8 – Simulation cell and semiconductor slabs used in the semiconductor-vacuum and semiconductor-water calculations. The repeat units of the orthorhombic supercells employed ( $L_x$ ,  $L_y$ , and  $L_z$ ) and the number of atomic layers  $n_l$  in the semiconductor slab are given. The parameter  $t_z$  indicates the thickness of the vacuum (water) layer at the semiconductor-vacuum (semiconductor-water) interface. For illustration of the semiconductor-water interface models, refer to Fig. 5.9.

	$L_x$ (Å)	$L_y$ (Å)	$L_z$ (Å)	$t_z$ (Å)	$n_l$
GaAs(110)	11.99	11.31	34.62	16.45	9
GaP(110)	11.74	11.07	34.56	17.27	9
GaN(10 $\bar{1}$ 0)	10.53	9.71	38.18	21.26	6
CdS(10 $\bar{1}$ 0)	13.73	12.64	35.23	13.52	6
ZnO(10 $\bar{1}$ 0)	10.60	9.88	38.50	21.19	6
SnO <sub>2</sub> (110)	13.40	12.74	30.04	14.03	5
r-TiO <sub>2</sub> (110)	13.19	12.01	30.62	15.20	5
a-TiO <sub>2</sub> (101)	10.39	11.41	35.00	18.68	5

The calculated fundamental band gaps are reported in Table 5.7, where they are compared with experimental reference values at room temperature. The mean absolute error (MAE) calculated for each electronic-structure method, allows one to evaluate the accuracy, by which the band gaps are reproduced. The methods PBE0(0.25),  $G_0W_0(0)$ , and  $G_0\widetilde{W}_0(0)$  generally produce considerable band-gap errors, with MAEs larger than 0.40 eV. The band-gap estimations are noticeably improved when the one-shot  $GW$  calculations are performed on top of a hybrid-functional starting point, as manifested by the MAE of 0.30 and 0.29 eV obtained with the



### 5.3. Electronic properties of semiconductors

Table 5.9 –  $\Delta\Delta V$  (in eV) for  $\text{SnO}_2(110)$  and  $\text{r-TiO}_2(110)$  at the interface with vacuum and liquid water, respectively, for  $n_l = 5, 9, 7, 11$ .

		$n_l = 5$	$n_l = 7$	$n_l = 9$	$n_l = 11$
$\text{SnO}_2(110)$	vacuum	0	0.03	0.04	0.05
$\text{r-TiO}_2(110)$	vacuum	0	0.02	0.04	0.05
	water	0	–	0.05	–

Table 5.10 – Experimental reference values for IP, EA,  $\text{pH}_{\text{PZC}}$ ,  $\epsilon_{\text{v}}^{\text{SHE}}(\text{PZC})$ , and  $\epsilon_{\text{c}}^{\text{SHE}}(\text{PZC})$ . IP, EA,  $\epsilon_{\text{v}}^{\text{SHE}}(\text{PZC})$ , and  $\epsilon_{\text{c}}^{\text{SHE}}(\text{PZC})$  are given in eV. See the text for a detailed description of the compilation.

	IP	EA	$\text{pH}_{\text{PZC}}$	$\epsilon_{\text{v}}^{\text{SHE}}(\text{PZC})$	$\epsilon_{\text{c}}^{\text{SHE}}(\text{PZC})$
GaAs	5.47	4.09	5.9	0.42	–1.00
GaP	6.01	3.75	4.9	0.91	–1.35
GaN			7.0	2.51	–0.91
CdS	7.26	4.77	7.5	1.35	–1.14
ZnO	7.80	4.43	9.0	2.96	–0.41
$\text{SnO}_2$			4.3	3.63	0.14
$\text{r-TiO}_2$	7.70	4.70	5.9	2.64	–0.36
$\text{a-TiO}_2$			5.9	2.93	–0.43

$G_0W_0(0.25)$  and  $G_0\widetilde{W}_0(0.25)$  methods, respectively. To improve the accuracy, it is necessary to include self-consistency as in QSGW schemes. In fact, while a very good agreement is obtained within the  $\text{QSGW}_0^{\text{PBE}}$  scheme (MAE = 0.20 eV), in which the  $W$  interaction is calculated at the level of the PBE starting point, this scheme is conceptually not satisfying and the good agreement results from error cancellations [227, 94]. This can be inferred from the large band-gap overestimations achieved with the QSGW method (MAE = 0.66 eV), in which the  $W$  interaction is evaluated in a fully self-consistent way [94, 228]. The screening in  $W$  can be improved through the account of vertex corrections, as in the  $\text{QSGW}\widetilde{W}$  method [94]. For the present set of semiconductors, this leads to a MAE of 0.16 eV, thus providing the best agreement with the experiment, in accord with previous work [94].

We now focus on the accuracy by which the band-edge positions are calculated. We construct symmetric pristine slabs which expose stable low-index surfaces. More specifically, we model the (110) surface for GaAs, GaP,  $\text{SnO}_2$  and  $\text{r-TiO}_2$ , the (10 $\bar{1}$ 0) surface for GaN, CdS, and ZnO, and the (101) surface for  $\text{a-TiO}_2$ . These surfaces are fully relaxed at the PBE level to achieve the interface with vacuum. We determine the electrostatic-potential line-ups across the surfaces with the PBE functional. In this way, the band edges of the semiconductor can be positioned with respect to the vacuum level, and the ionization potentials (IP) and electron affinities (EA) determined. In order to verify the convergence of ionization potentials and electron affinities with respect to the thickness of the employed slabs, we recalculate this quantity using thicker slabs for  $\text{SnO}_2(110)$  and  $\text{r-TiO}_2(110)$  (i.e. the thinnest ones occurring in Table 5.8) and evaluate

Table 5.11 – Ionization potentials (IP) and electron affinities (EA) of the semiconductors considered in this work, referred to the vacuum level, as obtained at various levels of theory. Mean absolute errors (MAEs) with respect to experiment are also given. All energies are in eV.

	PBE	PBE0(0.25)	$G_0W_0(0)$	$G_0\widetilde{W}_0(0)$	$G_0W_0(0)$	$G_0\widetilde{W}_0(0.25)$	$QSGW_0^{PBE}$	QSGW	$QSG\widetilde{W}$	PBE0( $\alpha$ )	$G_0W_0(\alpha)$	$G_0\widetilde{W}_0(\alpha)$
GaAs(110)	IP	4.45	5.17	5.08	5.09	5.35	5.24	5.41	5.38	5.00	5.26	5.32
	EA	4.10	3.40	4.07	4.17	3.70	4.06	3.75	3.96	3.58	3.84	3.90
GaP(110)	IP	5.20	5.99	6.02	6.02	6.30	6.17	6.35	6.31	5.68	6.11	6.17
	EA	3.89	3.11	3.99	4.11	3.59	3.98	3.70	3.96	3.42	3.85	3.91
GaN(10 $\bar{1}$ 0)	IP	5.72	6.91	6.64	6.54	7.11	7.11	7.49	7.25	6.89	7.11	7.16
	EA	4.15	3.45	4.09	4.24	3.68	4.17	3.81	4.20	3.47	3.69	3.74
CdS(10 $\bar{1}$ 0)	IP	6.00	7.22	7.09	7.06	7.55	7.42	7.78	7.58	7.09	7.33	7.43
	EA	5.03	4.56	5.06	5.18	4.62	5.03	4.65	5.02	4.60	4.84	4.94
ZnO(10 $\bar{1}$ 0)	IP	5.99	7.62	7.16	6.90	7.90	8.16	8.73	8.34	7.84	7.89	7.88
	EA	5.28	4.57	5.15	5.32	4.50	5.09	4.42	5.00	4.47	4.52	4.51
SnO <sub>2</sub> (110)	IP	7.83	9.53	9.09	8.85	9.82	9.94	10.52	10.06	9.47	9.59	9.63
	EA	6.66	5.96	6.39	6.57	5.95	6.49	6.08	6.55	5.98	6.10	6.14
r-TiO <sub>2</sub> (110)	IP	7.19	8.42	7.65	7.57	8.18	8.26	8.62	8.42	7.92		7.71
	EA	5.46	4.53	4.58	4.72	4.43	5.09	4.59	4.91	4.92		4.71
a-TiO <sub>2</sub> (101)	IP	7.25	8.53	7.81	7.70	8.82	7.88	8.53	8.24	8.03		
	EA	5.19	4.32	4.33	4.49	5.35	4.68	4.34	4.71	4.67		
MAE	IP	1.08	0.25	0.25	0.32	0.26	0.29	0.55	0.39	0.24	0.12	0.11
	EA	0.41	0.36	0.28	0.36	0.20	0.31	0.12	0.27	0.24	0.12	0.11

the shift in the calculated potential offset,  $\Delta\Delta V$ . When increasing  $n_l$  from 5 to 11 for SnO<sub>2</sub>(110) and r-TiO<sub>2</sub>(110), we observe a shift in the calculated offset as small as 0.05 eV [Table 5.9]. This is included in the calculation of the respective IPs and EAs.

The calculated results are compared with the available IPs at room temperature measured for the surfaces considered in this work: 5.47 eV for GaAs(110) [229], 6.01 eV for GaP(110) [230], 7.26 eV for CdS(10 $\bar{1}$ 0) [231], 7.80 eV for ZnO(10 $\bar{1}$ 0) [232], and 7.70 eV for TiO<sub>2</sub>(110) [233]. For the EA, our experimental reference is set by subtracting the measured fundamental gap reported in Table 5.7 from the respective IP [Table 5.10].

The calculated IPs and EAs are given in Table 5.11. We calculate mean average errors (MAEs) with respect to experimental measurements only using data referring to well characterized surfaces. Both hybrid functionals and one-shot  $GW$  methods perform well despite the error in the calculated band gap, with MAEs ranging between 0.15 and 0.36. However, it should be noted that the maximum error for PBE0(0.25),  $G_0W_0(0)$ , and  $G_0\widetilde{W}_0(0)$  exceeds 0.6 eV. Better results are achieved when using the  $G_0W_0$  scheme based on PBE0(0.25) as starting point, either with [ $G_0\widetilde{W}_0(0.25)$ ] or without [ $G_0W_0(0.25)$ ] vertex corrections. In particular, with the [ $G_0\widetilde{W}_0(0.25)$ ] method, we not only achieve low MAEs (0.24 and 0.15 eV for IP and EA, respectively) but also the maximum error does not exceed 0.28 eV.

Next, we analyze the results achieved through self-consistent  $GW$  schemes. At the  $QSGW_0^{PBE}$  level, we obtain overall a good accuracy with MAE values of 0.29 and 0.31 eV, with maximum errors below 0.4 eV. However, this agreement is partly fortuitous and results from a cancellation effect, by which the enhanced screening due to the use of the PBE compensates for the lack of vertex corrections [227, 94]. Indeed, the use of the  $QSGW$  method, which restores self-consistent screening, deteriorates the agreement with experiment (with errors larger than 0.8 eV for ZnO and r-TiO<sub>2</sub>), due to the systematic overestimation of the band gap [94, 228] and to the ensuing underestimation of the screening. When vertex corrections are accounted for as in the  $QSG\widetilde{W}$  scheme, MAE values of 0.39 and 0.27 eV are found. This scheme is strongly recommended for the study of novel materials, which have not priorly been characterized, both for its fully *ab initio* nature and for its accuracy. However, we remark that the  $QSG\widetilde{W}$  scheme does not improve upon the computationally less demanding  $G_0\widetilde{W}_0(0.25)$ , in which the self-consistency is taken care of at the hybrid functional level.

The importance of accurately describing the band gap is highlighted by focussing on the results obtained with hybrid-functional and one-shot  $G_0W_0$  schemes, which have been empirically tuned to reproduce the experimental band gap. In fact, these schemes yield the best agreement with experiment, with MAEs ranging between 0.11 and 0.24 eV. In particular, the tuned  $G_0W_0$  schemes are found to produce the most accurate IPs and EAs, with MAE as small as 0.11 eV and maximum errors smaller than 0.2 eV.

## 5.4 Interface models

### 5.4.1 Generation protocol

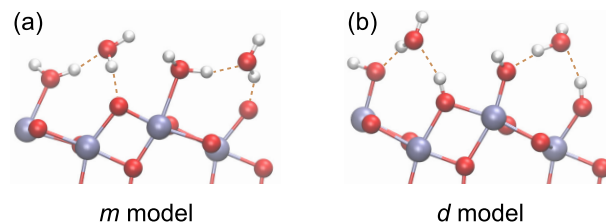


Figure 5.7 – Representation of (a) the molecular (*m*) model and of (b) the dissociative (*d*) model for the  $\alpha$ -TiO<sub>2</sub>(101)/H<sub>2</sub>O interface. Ti, O, and H atoms are shown in blue, red, and white, respectively.

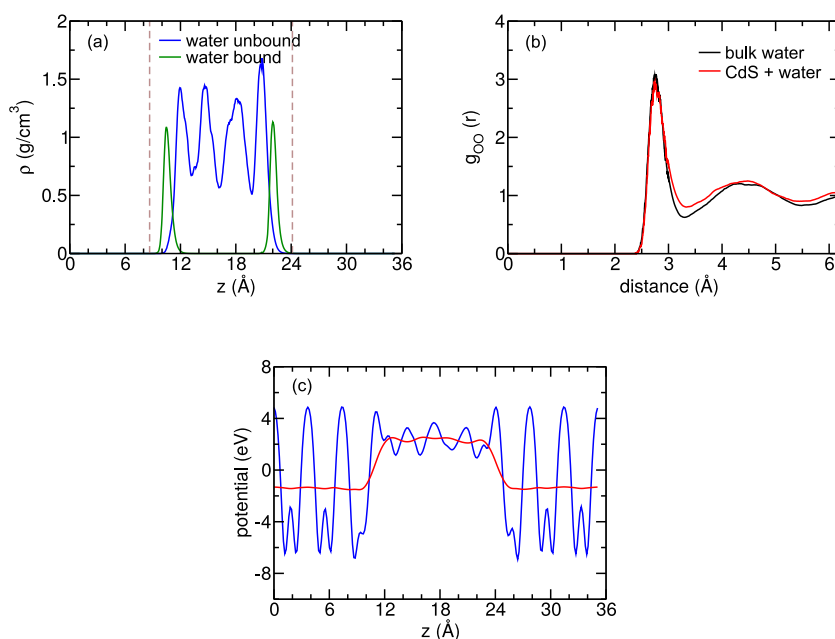


Figure 5.8 – (a) Planar averaged mass density of water (blue) at the CdS-water interface. The density resulting from the water molecules attached to the CdS surface molecules are indicated separately (green). The position of the terminating atomic layers of the semiconductor are shown by vertical lines (dashed brown); (b) O-O radial distribution functions for the bulk-like region of liquid water at the CdS-water interface (red) compared with the one for bulk liquid water (black); (c) electrostatic potential across the  $z$  direction (blue) for the CdS-water interface. The average value (red) is obtained through a Gaussian broadening with a width equal to the interlayer distance of the CdS(10 $\bar{1}$ 0) slab.

In order to generate semiconductor-water interfaces, we employ the minimum number of layers in the semiconductor slab required for achieving convergence of the calculated ionization potential within 0.05 eV [Table 5.8]. Two neutral interface models are constructed: (i) a molecular (*m*) model [Fig. 5.7(a)], in which the water molecules are molecularly adsorbed

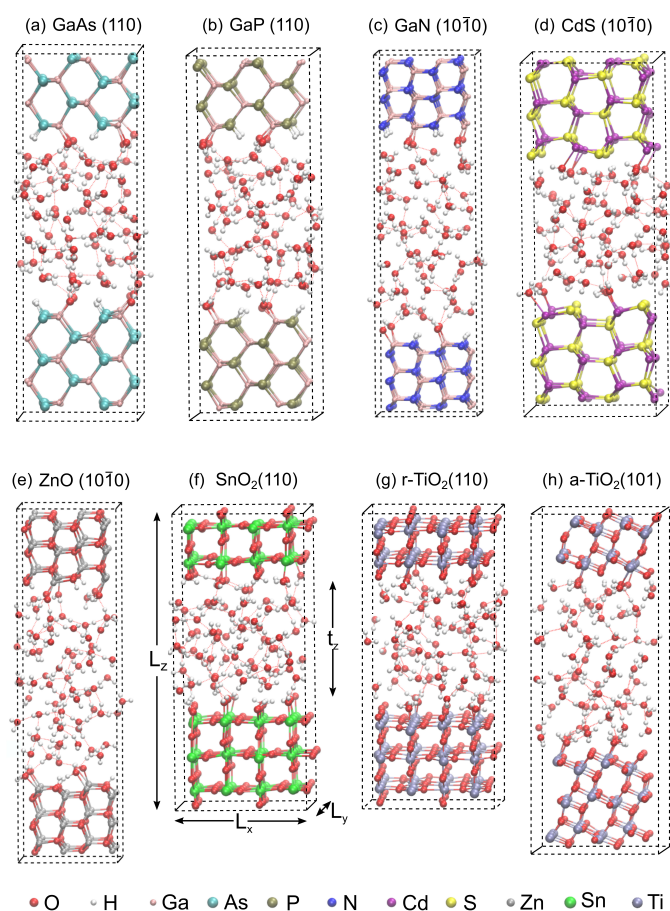


Figure 5.9 – Structural configurations of equilibrated aqueous interfaces for (a) GaAs(110), (b) GaP(110), (c) GaN( $10\bar{1}0$ ), (d) CdS( $10\bar{1}0$ ), (e) ZnO( $10\bar{1}0$ ), (f) SnO<sub>2</sub>(110), (g) r-TiO<sub>2</sub>(110), and (h) a-TiO<sub>2</sub>(101). For GaAs and GaP, the *d* model is shown. For a-TiO<sub>2</sub>, the *m* model is shown. In panel (f), the parameters  $L_x$ ,  $L_y$ ,  $L_z$ , and  $t_z$ , given in Table 5.8, are illustrated.

on the semiconductor interface through an oxygen-metal bond; (ii) a dissociative (*d*) model [Fig. 5.7(b)], in which the water molecules are dissociated on the semiconductor surface, with a hydroxyl group attached to the metal atom and a proton bound to a non-metal surface site (O for the oxide, N of GaN, and S for CdS). For both *m* and *d* models, we first add one monolayer (1 ML) of H<sub>2</sub>O molecules on both sides of the slab. We then place an orthorhombic box containing 64 H<sub>2</sub>O molecules with a surface area that matches that of the semiconductor slab. The length of the box along the *z* direction perpendicular to the interface is chosen in order to give the appropriate mass density and radial distribution functions of liquid water in the bulk-like region of the system. As illustrated in Fig. 5.8(a) for the CdS-water interface, one can see that the density of non-adsorbed H<sub>2</sub>O molecules shows a typical oscillatory behaviour, due to a layering effect caused by the hard-wall boundary conditions at the semiconductor surface [95, 96, 234, 235]. Fig. 5.8(b) shows that the O-O radial distribution function for the same interface agrees well with the one calculated for the bulk liquid. The radial distribution

function at the interface is obtained through the scheme outlined in Ref. [236] and refers to H<sub>2</sub>O molecules showing a distance from the surface larger than 3 Å. Moreover, we verify that the average electrostatic potential in the bulk-like region of liquid water is converged [Fig. 5.8(c)], even for the system with the thinnest water layer  $t_z$  [Table 5.8]. Atomic configurations of equilibrated interfaces are illustrated in Fig. 5.9.

### 5.4.2 Structural properties of semiconductor-water interfaces

We perform molecular dynamics simulations starting from both  $m$  and  $d$  models. In order to monitor the dynamics of the semiconductor-water interface, it is convenient to define the ratio  $\eta$  of dissociated H<sub>2</sub>O molecules at the semiconductor surface:

$$\eta = \frac{n_d}{n_{\text{ads}}}, \quad (5.10)$$

where  $n_d$  is the number of dissociated water molecules and  $n_{\text{ads}}$  the total number of water molecules adsorbed in either the molecular or the dissociative mode. Water molecules and

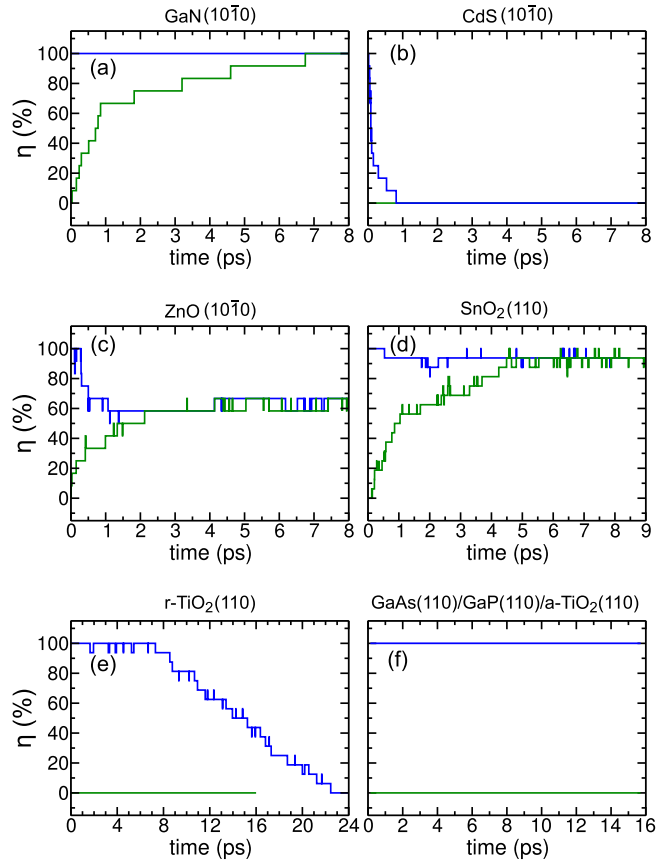


Figure 5.10 – Time evolution of the parameter  $\eta$  indicating the ratio of dissociated molecules at the interface for all the semiconductor-water models studied in this work. The MD simulations are started either from model  $m$  (green) or from model  $d$  (blue).

hydroxyl ions are considered to be bound to the semiconductor surface when the distance between the O atom and a cationic surface site is smaller than a given cutoff radius (2.5 Å for Ga and Zn sites; 2.8 Å for Cd, Sn, and Ti sites). In Fig. 5.10, we show the time-dependent evolution of the parameter  $\eta$ . For GaN, CdS, ZnO, SnO<sub>2</sub>, and r-TiO<sub>2</sub>, we observe that the interface converges to the same structure regardless of whether  $m$  or  $d$  models are used as starting points. More specifically, GaN favors dissociative adsorption, whereas molecular adsorption is observed for CdS and r-TiO<sub>2</sub>. In the case of GaN, the dissociation of the H<sub>2</sub>O molecules occurs within a few picoseconds, consistent with the results of Ref. [237], where the energy barrier for the dissociation of a H<sub>2</sub>O monolayer on the GaN(10 $\bar{1}$ 0) surface was found to be negligible. In the case of r-TiO<sub>2</sub>, the simulation starting from the  $d$  model requires as much as 24 ps of MD simulation to convert to the  $m$  one. For ZnO and SnO<sub>2</sub>, we find that both  $m$  and  $d$  models lead to a surface with mixed adsorption modes, described by  $\eta = 58-67\%$  and  $\eta = 87-94\%$ , respectively. For GaAs, GaP, and a-TiO<sub>2</sub> interfaces, no sign of change in the adsorption mode of H<sub>2</sub>O molecules is observed after MD simulations as long as 16 ps, when starting from either of the models. This indicates that the activation barrier for the dissociation/recombination process at these interfaces is higher than the thermal energy.

Table 5.12 – Average energy difference in eV per adsorbed water molecule between  $m$  and  $d$  models as derived from the MD simulations,  $\Delta E_{\text{MD}} = E_{\text{MD}}(m) - E_{\text{MD}}(d)$ ; difference in vibrational zero point motion (ZPM) energies of the adsorbed water molecule between  $m$  and  $d$  models,  $\Delta E_{\text{ZPM}} = E_{\text{ZPM}}(m) - E_{\text{ZPM}}(d)$ ; and corrected energy differences,  $\Delta E_{\text{corr}} = \Delta E_{\text{MD}} + \Delta E_{\text{ZPM}}$ .

surface	$\Delta E_{\text{MD}}$	$\Delta E_{\text{ZPM}}$	$\Delta E_{\text{corr}}$
GaAs(110)	-0.15	0.12	-0.03
GaP(110)	0.07	0.08	0.15
a-TiO <sub>2</sub> (101)	-0.07	0.08	0.01

For the systems that do not converge to a unique interfacial structure, we further investigate the relative stability of  $m$  and  $d$  models. We derive the average energy difference per water molecule adsorbed from the MD simulations and adopt a harmonic model to include entropic and quantum effects. To estimate the relevant vibrational frequencies, we consider a model, which consists of a semiconductor slab with a single water molecule attached, either in dissociated or in molecular mode. The displacement matrix is constructed by only considering the displacements of the water molecule, leading to a total amount of nine frequencies for both  $m$  and  $d$  models. These frequencies are used to obtain zero-point motion contributions, which correct for the classical treatment of the nuclei in our simulations. Vibrational entropy contributions are found to be very small and are neglected. For GaP, the  $d$  model is found to be more stable by 0.15 eV per adsorbed H<sub>2</sub>O molecule [Table 5.12]. In contrast, for a-TiO<sub>2</sub> and GaAs, the resulting energy differences between  $m$  and  $d$  models are found to be 0.01 and -0.03 eV per adsorbed water molecule [Table 5.12], too small to allow us to favor either model, as such energy differences are below the accuracy of the employed methodology. We notice

that it has been reported for GaAs and a-TiO<sub>2</sub> that surface defects and synthesis conditions may play a major role in the reactivity of H<sub>2</sub>O molecules on the semiconductor surface, thus possibly favouring dissociative adsorption [238, 239]. In the following, we nevertheless address the band alignment for both *m* and *d* models in these ambiguous cases.

## 5.5 Band alignment

In Fig. 5.11, we report the time evolution of the potential offset  $\Delta V = \Delta V_{sc} - \Delta V_w$  for each of the studied interfaces. For GaN, CdS, ZnO, SnO<sub>2</sub>, and r-TiO<sub>2</sub>, we report the values calculated

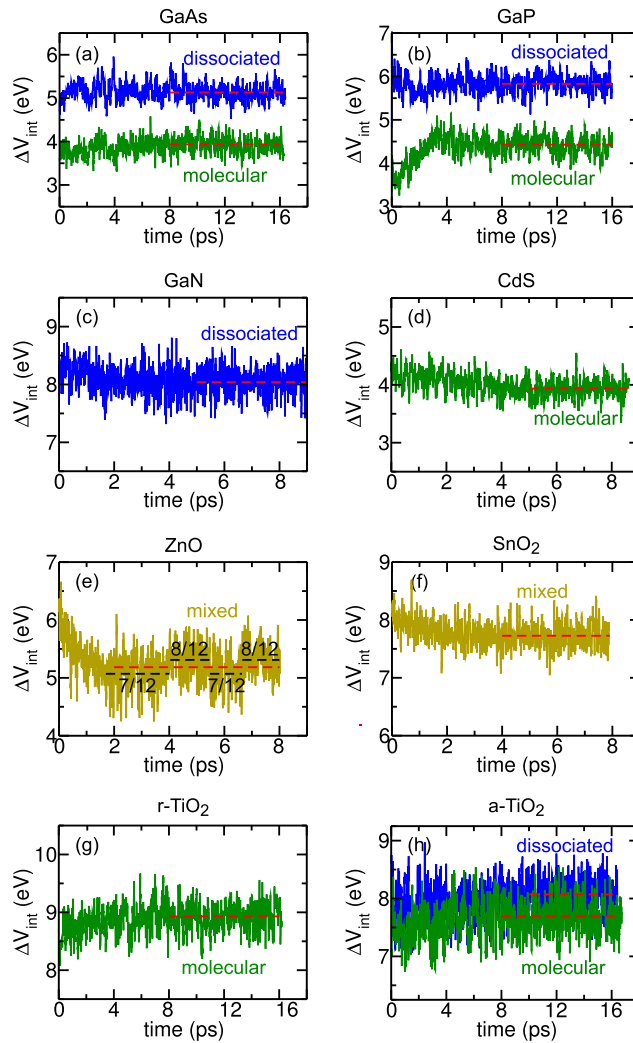


Figure 5.11 – Time evolution of  $\Delta V$  for the interfaces studied. The red dashed lines indicate the average values of  $\Delta V$ . Blue, green, and brown lines correspond to  $\Delta V$  calculated for molecular, dissociative, and mixed models, respectively. In panel (e), discrete variations of  $\Delta V$  (dashed black) are observed depending on the indicated ratio between the number of dissociated H<sub>2</sub>O molecules and the total number of adsorbed H<sub>2</sub>O molecules.



for the equilibrated final models. For GaAs, GaP, and a-TiO<sub>2</sub>, we discuss results achieved with both the *m* and *d* models. For all the studied interfaces,  $\Delta V$  is converged within a few ps of MD simulations. The fluctuations observed for the ZnO interface are due to the dynamical rearrangements of the H<sub>2</sub>O molecules on the surface by which the number of dissociated molecules varies over time [Fig. 5.11(e)]. The noticeably different values of  $\Delta V$  calculated for *m* and *d* models in the case of GaAs and GaP [Fig. 5.11(a) and (b)] clearly indicate the large effect of the interface structure on the band alignment. For a-TiO<sub>2</sub>, the difference between *m* and *d* models is less impressive.

When a 9-layer slab of r-TiO<sub>2</sub>(110) is employed in the MD simulations of the semiconductor-water interface, we find a change in the electrostatic potential of  $\Delta\Delta V = 0.05$  eV with respect to our MD simulation with a 5-layer slab. This value is very close to that calculated for the r-TiO<sub>2</sub>(110)-vacuum interface [Table 5.9]. Therefore, we applied the same  $\Delta\Delta V$  correction calculated for semiconductor-vacuum interfaces to the band alignment of both r-TiO<sub>2</sub> and SnO<sub>2</sub> at their interfaces with water.

### 5.5.1 Assignment of semiconductor-water interfaces

For GaN, CdS, ZnO, SnO<sub>2</sub>, and r-TiO<sub>2</sub>, the MD simulations are found to produce a unique interfacial structure. For GaP, the *d* model is found to be favored from calculations of adsorption energies. For GaAs and a-TiO<sub>2</sub>, neither the MD simulations nor the calculated adsorption energies allow us to clearly discern which interfacial structure should be the most stable. In this section, we analyze the band-alignment pertaining to GaAs, GaP, and a-TiO<sub>2</sub>, i.e. the materials for which our MD simulations have not provided a single final model. In order to focus on the effect of the underlying structural model, we carry out our analysis through the electronic-structure methods that are expected to be most accurate, as they are designed to reproduce the semiconductor band gap [209], i.e. PBE0( $\alpha$ ),  $G_0W_0(\alpha)$ , and  $G_0\widetilde{W}_0(\alpha)$ . In Fig. 5.12, the comparison between calculated and measured values of the band edges of GaAs, GaP, and a-TiO<sub>2</sub> at their interfaces with water is illustrated. All three electronic-structure methods favor *d* models for the structure at the semiconductor-water interface of these three materials. In the case of GaP, the assignment to the *d* model is consistent with our analysis of the relative stability of *m* and *d* models. The differences between *m* and *d* models are smaller in the case of a-TiO<sub>2</sub>, but the dissociative adsorption mode systematically yields the closest agreement with experiment also in this case. Our assignment of interfacial structures to be used in the benchmark of the electronic structure methods is given in Table 5.13.

As a further verification of the calculated alignments of GaAs, GaP, and a-TiO<sub>2</sub>, we take under consideration a simple interface model consisting of the relaxed semiconductor surface with a single monolayer of adsorbed water molecules. Such a simple model reproduces well all the qualitative trends found for the fully hydrated surfaces. The numerical differences do not exceed 0.4 eV and can be easily accounted for by the effect of the more distant water layers.

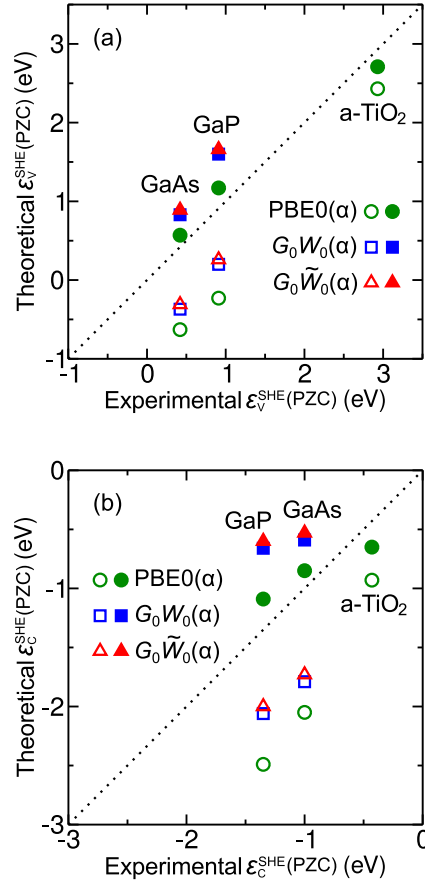


Figure 5.12 – (a) Valence [ $e_v^{SHE}(PZC)$ ] and (b) conduction [ $e_c^{SHE}(PZC)$ ] band edges at semiconductor-water interfaces calculated with various electronic-structure schemes compared to experimental values, for GaAs, GaP, and a-TiO<sub>2</sub>. All the electronic-structure schemes considered here reproduce the experimental band gap of the semiconductor. Full and empty symbols correspond to  $d$  and  $m$  models, respectively. The dashed diagonal lines represent the ideal accord between calculated and measured values.

Table 5.13 – Assignment of the interfacial structure with water for the semiconductors under consideration. We also give the basis for the adopted assignment.

semiconductor	reference structure	basis of assignment
GaAs(110)	$d$	band alignment
GaP(110)	$d$	$\Delta E_{corr}$ , band alignment
GaN(10 $\bar{1}$ 0)	$d$	MD
CdS(10 $\bar{1}$ 0)	$m$	MD
ZnO(10 $\bar{1}$ 0)	mixed ( $\eta=58-67\%$ )	MD
SnO <sub>2</sub> (110)	mixed ( $\eta=87-94\%$ )	MD
r-TiO <sub>2</sub> (110)	$m$	MD
a-TiO <sub>2</sub> (101)	$d$	$\Delta E_{corr}$ , band alignment

### 5.5.2 Experimental reference values

The band edges determined through Eqs. 5.8 and 5.9 can directly be compared with experimental values provided the latter are measured at  $\text{pH}_{\text{PZC}}$ . In fact, band edges at semiconductor-water interfaces show a Nernstian dependence on pH [240, 183, 241, 242], i.e. the band edges are shifted by 0.059 eV closer to the vacuum level as the pH is increased by one unit. However, while the  $\text{pH}_{\text{PZC}}$  of a semiconductor immersed in an aqueous solution can be determined by acid-base titration, the band offsets are not necessarily measured at the same value of pH. Therefore, in order to compare the calculated results with experiment, the conduction band edge measured at a given pH is shifted to its value at  $\text{pH}_{\text{PZC}}$  through the following expression:

$$\epsilon_c^{\text{SHE}}(\text{PZC}) = \epsilon_c^{\text{SHE}}(\text{pH}) + (0.059 \text{ eV}) \times (\text{pH}_{\text{PZC}} - \text{pH}), \quad (5.11)$$

where  $\epsilon_c^{\text{SHE}}(\text{pH})$  is the conduction band edge at a given pH. In the following, Eq. 5.11 is employed to shift conduction band edges measured at a given pH to their position at  $\text{pH}_{\text{PZC}}$ , prior to the comparison with their theoretical counterparts. We use experimental values for  $\text{pH}_{\text{PZC}}$ . In order to identify reliable experimental results to be compared with our calculations, the complex and rich literature of electrochemical measurements at semiconductor-water interfaces has been thoroughly investigated for each material.

For GaAs, the  $\text{pH}_{\text{PZC}}$  was determined to be  $\sim 5.9$  from measurements performed on powdered material [243]. Benard and Handler [244] studied the capacitance-voltage behavior of n- and p-type GaAs on the  $(\bar{1}\bar{1}\bar{1})$  surface, and observed that the flat-band potentials of n- and p-type GaAs differed by  $\sim 1.42$  eV (i.e. the band gap), thus indicating that the band-edge positions are the same for both types of doping. Impedance measurements of  $(\bar{1}\bar{1}\bar{1})$  and (100) surfaces give  $\epsilon_c^{\text{SHE}}(\text{PZC}) = -1.22$  eV [245, 246] and  $\epsilon_c^{\text{SHE}}(\text{PZC}) = -1.19$  eV [247], respectively. Photocurrent measurements on p-type GaAs with the (100) facet exposed in a 0.5 M  $\text{H}_2\text{SO}_4$  solution give  $\epsilon_c^{\text{SHE}}(\text{PZC}) = -1.08$  eV [248], in substantial agreement with the impedance experiments. However, photoelectrochemical measurements of n-type GaAs with the (100) and (111) facets exposed in alkaline solutions provide the significantly different value of  $-0.78$  eV for  $\epsilon_c^{\text{SHE}}(\text{PZC})$  [249]. The latter agrees with the value of  $\epsilon_c^{\text{SHE}}(\text{PZC}) = -0.70$  eV reported by Wrighton *et al.* [250]. The experimental large spread appears to be unresolved at present. Therefore, we consider in the present work the average value  $\epsilon_c^{\text{SHE}}(\text{PZC}) = -1.00$  eV, which is expected to be accurate within  $\pm 0.3$  eV for GaAs.

For GaP, we have not been able to find any measurement of  $\text{pH}_{\text{PZC}}$ . However, Butler and Ginley [251] have shown that the  $\text{pH}_{\text{PZC}}$  of semiconductors depends linearly upon their electronegativity. By calculating the electronegativities of the compounds from those of the constituent atoms for both GaAs and GaP, and considering the  $\text{pH}_{\text{PZC}} = 5.9$  for GaAs, we infer a value of the  $\text{pH}_{\text{PZC}}$  of 4.9 for GaP. From photoelectrochemical measurements of n-type GaP at  $\text{pH}=0$ ,  $\epsilon_c^{\text{SHE}}(\text{PZC}) = -1.42$  eV [250]. This value is slightly different from that inferred from impedance measurements [ $\epsilon_c^{\text{SHE}}(\text{PZC}) = -1.30, -1.45$  eV [252]]. Gomes and Cardon [253] summarized various electrochemical measurements on n- and p-type GaP

[247, 252, 250, 254, 255], and found that the conduction band edge of both types of GaP satisfied the expression  $\epsilon_c^{\text{SHE}} = -1.05 - 0.06 \cdot \text{pH}$  (in eV). Furthermore, this expression appears to be independent of the exposed semiconductor surface. According to this expression,  $\epsilon_c^{\text{SHE}}(\text{PZC}) = -1.35$  eV, and this value is used as our experimental reference for GaP. We estimate an error of  $\pm 0.1$  eV on the basis of the spread of the experimental data.

For GaN,  $\text{pH}_{\text{PZC}} = 7$  is inferred from an indirect estimate based on a model [256] used to fit the measurements of Ref. [257]. Electrochemical capacitance measurements on n-type GaN give  $\epsilon_c^{\text{SHE}}(\text{PZC}) = -0.91$  eV [241], in substantial agreement with earlier measurements of the same group giving  $\epsilon_c^{\text{SHE}}(\text{PZC}) = -0.86$  eV [183]. At variance, the interpolation of the values reported by Huygens and co-workers [242] lead to  $\epsilon_c^{\text{SHE}}(\text{PZC}) = -0.96$  eV. Hence, we here adopt the average value of the reported data,  $\epsilon_c^{\text{SHE}}(\text{PZC}) = -0.91$  eV. This value is expected to be accurate within  $\pm 0.05$  eV.

The  $\text{pH}_{\text{PZC}}$  of CdS is reported to be 7.5 from measurements of the zeta potential on hydrous CdS at various pH [258]. Numerous electrochemical measurements on CdS have been performed and very different values for the flat-band potential have been reported [259, 260, 261, 262, 263, 264, 265, 250]. In particular, it has been observed that the flat-band potential of CdS(0001) shifts dramatically when the measurements are performed on Cd and S surfaces [263]. In our work, the exposed face of CdS is (10 $\bar{1}$ 0), a nonpolar surface with 1:1 ratio of Cd and S at the surface. Therefore, we consider as our experimental reference the average of the values measured for S and Cd surfaces in Ref. [263]. This leads to  $\epsilon_c^{\text{SHE}}(\text{PZC}) = -1.14$  eV.

The  $\text{pH}_{\text{PZC}}$  of ZnO is reported to lie in an interval between 8 and 10, depending on the experimental setup [266]. Therefore, we considered the average value of 9 in this work. From capacitance-voltage measurements of n-type ZnO(11 $\bar{2}$ 0) electrodes, we infer  $\epsilon_c^{\text{SHE}}(\text{PZC}) = -0.46$  eV [267, 268]. The experimental characterization of (0001) and (000 $\bar{1}$ ) surfaces did not show any significant difference, yielding  $\epsilon_c^{\text{SHE}}(\text{PZC}) = -0.41$  eV in Ref. [269] and  $\epsilon_c^{\text{SHE}}(\text{PZC}) = -0.36$  eV in Ref. [270]. We here adopt the average of the reported data, i.e.  $\epsilon_c^{\text{SHE}}(\text{PZC}) = -0.41$  eV. The adopted value is consistent within  $\pm 0.05$  eV with all the available experimental data.

A value of 4.3 for the  $\text{pH}_{\text{PZC}}$  of SnO<sub>2</sub> has been reported in Refs. [251] and [271]. Photocurrent measurements on n-type SnO<sub>2</sub> give  $\epsilon_c^{\text{SHE}}(\text{PZC}) = 0.11$  eV [272], in accord with more recent electrochemical experiments in Refs. [273] and [274], giving 0.15 and 0.16 eV for  $\epsilon_c^{\text{SHE}}(\text{PZC})$ , respectively. Again, we here adopt the average value of the reported measurements,  $\epsilon_c^{\text{SHE}}(\text{PZC}) = 0.14$  eV. With this assignment, all measurements are accounted for within  $\pm 0.03$  eV.

As far as TiO<sub>2</sub> is concerned, the  $\text{pH}_{\text{PZC}}$  is reported to lie in the interval ranging from 5.8 to 6.0 [251, 275], and to be independent of the crystal structure [275]. Thus, we set  $\text{pH}_{\text{PZC}} = 5.9$  for both rutile and anatase in this work. The literature of electrochemical measurements on rutile and anatase TiO<sub>2</sub> is extremely rich and the relative position of the band edges of the two polymorphs is still debated [276]. However, electrochemical measurements for both types of TiO<sub>2</sub> agree within 0.1 eV or less, generally with the conduction band edge of a-TiO<sub>2</sub> lying slightly higher than that of r-TiO<sub>2</sub>. In the following, we give a compilation of various

experimental results. Early measurements performed on rutile and anatase powders yield  $-0.36$  and  $-0.40$  eV, respectively [277]. We infer  $\epsilon_c^{\text{SHE}}(\text{PZC})$  values of  $-0.32$  and  $-0.52$  eV for r-TiO<sub>2</sub>(001) and a-TiO<sub>2</sub>(101) from Ref. [278]. For rutile, a value of  $\epsilon_c^{\text{SHE}}(\text{PZC}) = -0.41$  eV is inferred from the pH-dependent band bending of TiO<sub>2</sub>(110) [279]. Values of  $-0.31$  eV and  $-0.39$  eV for the same material have been reported in Refs. [280] and [272], respectively. For a-TiO<sub>2</sub>(101), Refs. [281] and [282] lead to  $\epsilon_c^{\text{SHE}}(\text{PZC})$  at  $-0.41$  and  $-0.36$  eV, respectively. For the purpose of this work, we take as reference for each material the average of the measured values. This gives  $\epsilon_c^{\text{SHE}}(\text{PZC}) = -0.36$  eV for r-TiO<sub>2</sub> and  $-0.43$  eV for a-TiO<sub>2</sub>. These values account for all the experimental data within  $\pm 0.05$  and  $\pm 0.09$  eV, respectively.

The compilation of experimental  $\epsilon_c^{\text{SHE}}(\text{PZC})$  used in this work is summarized in Table 5.10. Reference values for  $\epsilon_v^{\text{SHE}}(\text{PZC})$  are achieved by adding the measured fundamental gap listed in Table 5.7 to the pertinent  $\epsilon_c^{\text{SHE}}(\text{PZC})$ .

### 5.5.3 Benchmark of electronic-structure methods

In this section, we only retain the adsorption models which correspond to our assignment, as reported in Table 5.13. We investigate the full set of electronic-structure methods considered in this work in order to assess their accuracy in reproducing the experimental band alignment. The energy levels of the valence and conduction band edges,  $\epsilon_v^{\text{SHE}}(\text{PZC})$  and  $\epsilon_c^{\text{SHE}}(\text{PZC})$ , are given in Table 5.14 and are illustrated graphically in Fig. 5.13. In addition, from the comparison with experimental band-edge levels (summarized in Table 5.10), we give in Table 5.14 the mean average error (MAE) for each of electronic-structure method adopted. The MAEs are also summarized graphically in Fig. 5.14.

We first consider the performance of the hybrid functional and the one-shot *GW* methods [Fig. 5.13(a)]. Again, for these electronic-structure methods, it should be realized that the discrepancies on the band alignments partially stem from the error in the calculated band gap. At the PBE0(0.25) level, the calculated values for the valence band edges yield a sizeable MAE of 0.35 eV, but the MAE pertaining to the conduction band edges is only 0.22 eV. The latter value suggests that PBE0(0.25) could represent a computational fast and accurate method for the screening of photoanode materials suitable for oxygen evolution in the water splitting process. At the  $G_0W_0(0)$  level, we find a moderate MAE (0.29 eV) for  $\epsilon_v^{\text{SHE}}(\text{PZC})$  but a rather large MAE (0.66 eV) for  $\epsilon_c^{\text{SHE}}(\text{PZC})$ . When the initial state is kept at the PBE level and vertex corrections are included, the agreement is found to worsen as can be inferred from the  $G_0\widetilde{W}_0(0)$  results, with MAEs of 0.39 and 0.73 eV for  $\epsilon_v^{\text{SHE}}(\text{PZC})$  and  $\epsilon_c^{\text{SHE}}(\text{PZC})$ , respectively. For the  $G_0W_0$  scheme using a starting point based on PBE0(0.25), either without [ $G_0W_0(0.25)$ ] or with [ $G_0\widetilde{W}_0(0.25)$ ] vertex corrections, a noticeable improvement of MAEs by at least 0.22 eV for  $\epsilon_c^{\text{SHE}}(\text{PZC})$  is observed, compared to that obtained with the  $G_0W_0(0)$  and  $G_0\widetilde{W}_0(0)$  methods. But the band alignment pertaining to the valence band edges becomes worse, with MAEs of 0.50 and 0.41 eV, respectively.

Table 5.14 – Band edge positions  $\varepsilon_v^{\text{SHE}}$  (PZC) (denoted v) and  $\varepsilon_c^{\text{SHE}}$  (PZC) (denoted c) of the semiconductors considered in this work referred to the SHE at  $\text{pH}_{\text{PZC}}$ , as obtained at various levels of theory. The mean absolute errors (MAEs) with respect to the experimental values in Table 5.10 are also given. All energies are in eV.

	PBE	PBE0(0.25)	$G_0W_0(0)$	$G_0\widetilde{W}_0(0)$	$G_0W_0(0.25)$	$G_0\widetilde{W}_0(0.25)$	$QSGW_0^{\text{PBE}}$	QSGW	$QSG\widetilde{W}$	PBE0( $\alpha$ )	$G_0W_0(\alpha)$	$G_0\widetilde{W}_0(\alpha)$
GaAs	v	0.02	0.74	0.65	0.66	0.92	0.81	0.98	0.96	0.57	0.83	0.89
	c	-0.32	-1.02	-0.36	-0.26	-0.72	-0.36	-0.68	-0.46	-0.85	-0.59	-0.53
GaP	v	0.69	1.48	1.50	1.50	1.79	1.66	1.84	1.80	1.17	1.60	1.66
	c	-0.63	-1.40	-0.52	-0.40	-0.92	-0.54	-0.81	-0.55	-1.09	-0.66	-0.60
GaN	v	1.60	2.78	2.52	2.42	2.99	2.99	3.36	3.12	2.76	2.98	3.04
	c	0.03	-0.67	-0.03	0.12	-0.44	0.05	-0.32	0.08	-0.66	-0.44	-0.38
CdS	v	0.34	1.56	1.43	1.40	1.89	1.76	2.12	1.92	1.43	1.67	1.77
	c	-0.63	-1.11	-0.60	-0.48	-1.04	-0.63	-1.02	-0.64	-1.06	-0.82	-0.72
ZnO	v	1.11	2.73	2.28	2.02	3.02	3.28	3.85	3.46	2.96	3.00	2.99
	c	0.39	-0.31	0.27	0.43	-0.39	0.20	-0.47	0.11	-0.41	-0.37	-0.38
SnO <sub>2</sub>	v	2.35	4.06	3.62	3.38	4.35	4.46	5.04	4.59	3.99	4.12	4.15
	c	1.18	0.49	0.91	1.09	0.47	1.02	0.60	1.07	0.50	0.63	0.66
r-TiO <sub>2</sub>	v	1.86	3.10	2.32	2.24	2.86	2.93	3.29	3.10	2.59		2.38
	c	0.13	-0.80	-0.75	-0.60	-0.89	-0.24	-0.73	-0.41	-0.41		-0.62
a-TiO <sub>2</sub>	v	1.93	3.22	2.49	2.39	3.51	2.56	3.21	2.92	2.71		
	c	-0.12	-1.00	-0.99	-0.83	0.03	-0.64	-0.98	-0.61	-0.65		
MAE	v	0.93	0.35	0.29	0.39	0.50	0.48	0.79	0.57	0.17	0.40	0.42
	c	0.69	0.22	0.66	0.73	0.33	0.59	0.38	0.56	0.17	0.40	0.42

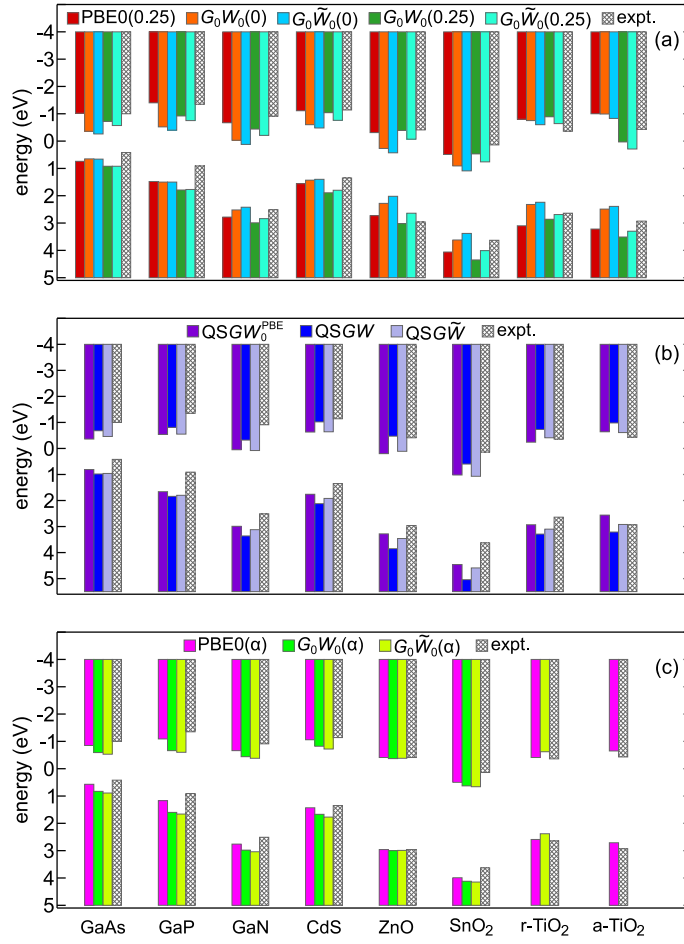


Figure 5.13 – Valence band edge  $\varepsilon_v^{\text{SHE}}(\text{PZC})$  and conduction band edge  $\varepsilon_c^{\text{SHE}}(\text{PZC})$  calculated with various electronic-structure schemes and referred to the SHE level in liquid water for the set of semiconductor-water interfaces considered in this work: (a) PBE0(0.25) and non-empirical one-shot  $GW$  calculations, (b) quasi-particle self-consistent  $GW$  schemes, and (c) hybrid functional and  $G_0W_0$  calculations tuned to reproduce the band gap of the semiconductors.

Next, we consider the results obtained through self-consistent  $GW$  schemes, as illustrated in Fig. 5.13(b). When the band edges are calculated at the  $\text{QSGW}_0^{\text{PBE}}$  level, we obtain unsatisfactory accuracy for both the valence band (MAE = 0.48 eV) and the conduction band (MAE = 0.59 eV). The use of the QSGW method, which restores self-consistent screening, remarkably deteriorates the overall agreement with experiment as the MAE of  $\varepsilon_v^{\text{SHE}}(\text{PZC})$  is up to 0.79 eV and that of  $\varepsilon_c^{\text{SHE}}(\text{PZC})$  (0.38 eV) is still sizeable. In this regard, it should be noted that our results at the QSGW level for GaN and ZnO are close to those obtained by Kharche *et al.* with a similar methodology. The study of a large set of interfaces in our work, clearly conveys that the discrepancies with the experiment found in Ref. [96] should be assigned to the use of the QSGW method, rather than to a model deficiency of the interface structure. When vertex corrections are accounted for as in the  $\text{QSGW}\tilde{}$  scheme, the agreement with the

experiment is still not satisfactory, with MAE values of 0.57 and 0.56 eV. Again, we find that the self-consistent  $QSG\tilde{W}$  scheme does not improve upon the  $G_0W_0(0.25)$ , thus providing a strong preference for the latter method when a fast screening is performed.

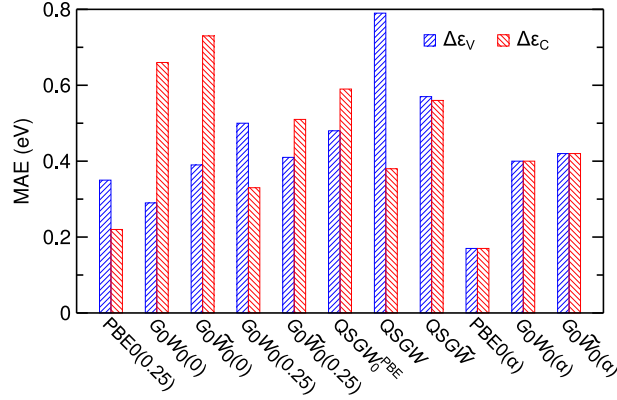


Figure 5.14 – Mean absolute errors (MAEs) for the valence band edge  $\epsilon_v^{SHE}$  (PZC) (blue) and for the conduction band edge  $\epsilon_c^{SHE}$  (PZC) (red), calculated with various electronic-structure schemes and referred to the SHE level in liquid water, for the set of semiconductor-water interfaces considered in this work. Experimental references correspond to the pH at the point of zero charge given in Table 5.10.

We conclude our analysis by considering hybrid-functional and one-shot  $G_0W_0$  schemes which have empirically been tuned to reproduce the experimental band gap [Fig. 5.13(c)]. The importance of reproducing the band gap is conveyed by the fact that the scheme of PBE0( $\alpha$ ) yields the best agreement with experiment, with MAE of 0.17 eV, noticeably better than all the nonempirical schemes. When the tuning procedure is combined with a  $G_0W_0$  method, as in the  $G_0W_0(\alpha)$  and  $G_0\tilde{W}_0(\alpha)$  schemes, the overall agreement with experiment is also improved with respect to nonempirical schemes, resulting in MAEs of 0.40 and 0.42 eV, respectively. From the comparison between  $G_0W_0(\alpha)$  and  $G_0\tilde{W}_0(\alpha)$ , one infers that the inclusion of vertex corrections in such tuning procedures is not beneficial, despite the conceptual advance.

#### 5.5.4 Comparison with previous work

It is of interest to compare the results calculated in this work with those of previous computational studies. Stevanović *et al.* derived the band alignment from ionization potentials and electron affinities of semiconductor-vacuum interfaces calculated at the  $GW$  level [98]. Hence, the structure at the semiconductor-water interface was not explicitly considered. The large discrepancy with the experiment ( $> 0.6$  eV) for the majority of the studied semiconductors was then justified by invoking a systematic correction of  $\sim 0.5$  eV, which was meant to account for the effect of the aqueous environment at  $pH_{PZC}$ . However, the results in our work indicate that the specific interface structure strongly affects the band alignment, with molecular and dissociative models of water adsorption leading to energy differences exceeding 1 eV in some cases. To further examine the validity of the approach proposed in Ref. [98], we evaluate



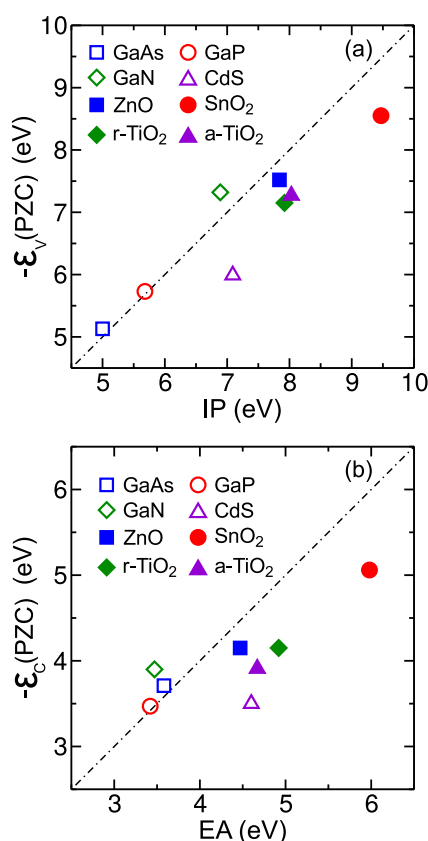


Figure 5.15 – (a)  $\epsilon_v(\text{PZC})$  vs. IP and (b)  $\epsilon_c(\text{PZC})$  vs. EA. All quantities shown here are consistently obtained at the PBE0( $\alpha$ ) level of theory and are referred to the vacuum level.

the ionization potentials (IPs) and electron affinities (EAs) for semiconductor-vacuum interfaces at the PBE0( $\alpha$ ) level of theory and compare the calculated values with  $\epsilon_v^{\text{SHE}}(\text{PZC})$  and  $\epsilon_c^{\text{SHE}}(\text{PZC})$  determined at the same level of theory [Fig. 5.15]. The connection between the SHE and the vacuum level is established according to Fig. 5.6, in which the SHE level is placed at 4.56 eV below the vacuum level. The comparison in Fig. 5.15 shows differences ranging from  $-0.43$  to  $1.10$  eV, thereby indicating that the implicit account of the semiconductor-water interface structure through a fixed correction is subject to large errors.

Wu, Chan, and Ceder used a simplified interface model and obtained a MAE of 0.19 eV from the band alignment calculated at the PBE level for six different semiconductors. However, the level of agreement in Ref. [100] arises from a fortuitous cancellation of errors. In fact, the results in their computational study are achieved at  $\text{pH}_{\text{PZC}}$ , but are compared with measurements carried out at different values of pH. The authors argue that their simulation cells containing 127  $\text{H}_2\text{O}$  molecules and one hydronium ion closely correspond to  $\text{pH}=1$ . However, it has recently been shown that proper account of the pH effect should be included in simulations of aqueous solutions through the connection with the electron chemical potential [128]. Furthermore, this effect adds up to the errors resulting from the use of PBE for the band edge calculation (up to 1 eV depending on the material) and from the use of non-equilibrated interface models,

which do not account for the specific adsorption mode of the water molecules.

### 5.6 Conclusion

In this work, we assessed the accuracy of hybrid functionals and *GW* calculations for the prediction of the band alignment at semiconductor-water interfaces. We considered a set of eight semiconductors, namely GaAs, GaP, GaN, CdS, ZnO, SnO<sub>2</sub>, rutile TiO<sub>2</sub> (r-TiO<sub>2</sub>), and anatase TiO<sub>2</sub> (a-TiO<sub>2</sub>), for all of which the band-edge levels in aqueous environment have been measured [181, 182, 80, 183]. For each material, we calculated the electronic band gap through hybrid functional calculations at the PBE0 level [112, 113] and with various *GW* schemes [283]. For both hybrid functional and *GW* calculations, the intrinsic error in the description of the band edges was disentangled from the error due to the difference between experimental and calculated band gaps. In fact, the electronic-structure methods employed include both nonempirical schemes with no input parameter taken from experiment, and empirical schemes, which were designed to reproduce the experimental band gap. More specifically, we carried out PBE0 hybrid functional calculations, in which the fraction of Fock exchange (i) was fixed to its original value of  $\alpha = 0.25$  or (ii) tuned to reproduce the experimental band gap of the semiconductor under investigation. Similarly, we performed one-shot *GW* calculations based on starting points from (i) PBE and PBE0(0.25) or from (ii) tuned PBE0( $\alpha$ ) functionals. Additionally, we also examined the performance of quasi-particle self-consistent *GW* schemes [186] and the role of vertex corrections [94].

We modelled semiconductor-water interfaces at the atomistic level. For each semiconductor surface, two neutral interfaces were built: (i) a molecular (*m*) model, in which all the adsorbed water molecules are bound molecularly through a bond between the O atom of the water molecule and an undercoordinated metal site of the semiconductor; (ii) a dissociative (*d*) model, in which the water molecules are dissociated on the surface, with the hydroxyl group adsorbed at a metal site and the proton attached to a non-metal atom of the surface. Taking either of these models as initial structures, we performed molecular dynamics simulations to reach equilibrated structures. For GaN, CdS, ZnO, SnO<sub>2</sub>, and r-TiO<sub>2</sub>, this led to a unique model with either a fully molecular, a fully dissociative or a mixed adsorption mode, which does not depend on the initial structural configuration. In contrast, for GaAs, GaP, and a-TiO<sub>2</sub>, we did not observe an evolution of the starting models to a unique structure during the time period of our simulations, due to the slow kinetics of water dissociation/recombination processes at the surfaces of these semiconductors. An energetic analysis including the effect of zero-point motion of the adsorbed H<sub>2</sub>O molecules allowed us to clearly favor the *d* model in the case of GaP. However, for GaAs and a-TiO<sub>2</sub>, such an analysis proved insufficient to discriminate between *m* and *d* models. Hence, for these ambiguous cases, the structural model was inferred from the band alignment.

The band edges of the semiconductors at the interface with liquid water were referred to the standard hydrogen electrode (SHE) via the following three-step procedure [207, 208, 209, 96]:

(i) the SHE level was calculated using the computational scheme proposed in Ref. [128] and referred to the average electrostatic potential of liquid water; (ii) for each semiconductor the band edges were calculated and referred to its average electrostatic potential; (iii) the electrostatic potential line-up across the semiconductor-water interface was extracted from the structural configurations achieved with MD simulations. All the comparisons with experiment were made at the pH corresponding to the point of zero charge. As experimental band edges are generally determined at a different pH, we applied a Nernstian shift before the comparison with their calculated counterparts. We first addressed the remaining ambiguity concerning the interface structures of GaP, GaAs, and a-TiO<sub>2</sub>. For GaP, the *d* model, which was clearly identified as the most stable one, was found to provide a band alignment in close agreement with the experiment, while the *m* model gave discrepancies exceeding 1 eV. For GaAs and a-TiO<sub>2</sub>, the alignments associated to *m* and *d* models were also found to be significantly different, with a clear preference for the dissociative adsorption mode when comparing with experiment.

At this stage, we were ready to assess the accuracy of a variety of advanced electronic-structure methods, including both hybrid functionals and *GW* methods. We defined mean absolute errors (MAEs) for the valence-band and conduction-band edges, by comparing our calculated results with the experiment. First, we focussed on PBE0(0.25) and one-shot *GW* methods. The PBE0(0.25) functional yields a high MAE for the valence band edge (0.35 eV), while the MAE for the conduction band edge is relatively low (0.22 eV). However, while the latter level of agreement appears very promising, especially in view of the low computational cost of hybrid functionals, the investigation of a larger set of semiconductor-water interfaces appears advisable before drawing definite conclusions. The one-shot *GW* methods based on a starting point determined at the PBE level produce large MAEs (0.29-0.73 eV), and a minor improvement of the agreement with experiment is observed when the starting point is determined at the PBE0(0.25) level (MAEs between 0.33 and 0.51 eV).

Next, we investigated various quasi-particle self-consistent *GW* schemes. When the screening interaction *W* is kept fixed at the PBE level, the achieved accuracy is unsatisfactory with MAEs of 0.48 and 0.59 eV for valence and conduction band edges, respectively. A comparable accuracy with slightly higher MAEs (0.57 and 0.56 eV) is obtained with the QSGW scheme, which includes vertex corrections [94]. The latter method is fully *ab initio* and corresponds to the state of the art as far as band-gap calculations are concerned [94], and should thus generally be preferred in predictive approaches. Instead, the QSGW without vertex corrections is found to perform worse (0.79 and 0.38 eV), due to the overestimation of the band gaps. It should be remarked that the inclusion of self-consistency at the *GW* level does not generally lead to higher accuracies for the band alignment, while it entails a higher computational cost. In this respect, the one-shot *GW* methods based on a starting point at the PBE0(0.25) level appear as a better choice, with MAEs ranging between 0.33 and 0.51 eV.

We completed our investigation through a series of electronic-structure schemes that rely on the knowledge of the semiconductor band gap. In hybrid functionals, one can take advantage

## Chapter 5. Alignment of energy levels at semiconductor-water interfaces

---

of this knowledge by adjusting the fraction of exchange such that the calculated band gap reproduces the experimental one. A similar adjustment can be introduced in one-shot *GW* schemes based on a starting point calculated at the hybrid functional level. As a general remark, we observe that such tuned schemes outperform the fully *ab initio* ones as far as the band alignment is concerned, with the highest accuracy corresponding to a MAE as low as 0.17 eV for the PBE0( $\alpha$ ) method. This result indicates that the correct description of the band gap is an important preliminary criterion for such alignments.

In conclusion, the present work addresses the band alignment at semiconductor-water interfaces taking under consideration advanced state-of-the-art electronic-structure methods and an extensive set of semiconductors. Our study not only defines a computational protocol but also provides an assessment of the accuracy that can be achieved in this type of investigation, setting a benchmark for high-throughput material searches in large data bases.

The results presented in this chapter have been published in Refs. [66] and [220].

## 6 Evaluation of photocatalysts for water splitting through combined analysis of surface coverage and energy-level alignment

In this chapter, we determine surface concentrations of water molecules, protons, and hydroxyl ions adsorbed at the interface with liquid water as a function of pH for a series of eight semiconductors, including GaAs, GaP, GaN, CdS, ZnO, SnO<sub>2</sub>, rutile TiO<sub>2</sub>, and anatase TiO<sub>2</sub>. This is achieved through the calculation of the acidity constants at the surface sites, which are derived from *ab initio* molecular dynamics simulations and a grand-canonical formulation of adsorbates. This method is validated by the excellent agreement of the resulting pH values at the point of zero charge with experimental data. By combining the nature of the surface coverage and the alignment of the band edges to the relevant redox levels, the potential of the studied semiconductors as photocatalysts for water splitting is examined.

This chapter is organized as follows. In Section 6.1, we introduce the general motivation for the research conducted in this chapter. The theoretical formulation for calculating acidity constants of adsorbates (H<sup>+</sup> and H<sub>2</sub>O) on surface sites is given in Section 6.2. In Section 6.3, we report the methods to calculate (i) the free energies associated with the deprotonation of adsorbates (e.g. H<sup>+</sup> and H<sub>2</sub>O), (ii) the electrostatic finite-size corrections accounting for a hydronium cation in liquid water and for an extra proton at semiconductor-water interfaces, and (iii) the zero-point energies of protons. The pK<sub>a</sub> and pH<sub>ZPC</sub> for the investigated semiconductor surfaces achieved with semilocal and hybrid functionals are compared in Section 6.4. The acid-base properties of semiconductor-water interfaces are reported in Section 6.5. In Section 6.6, the band alignments of semiconductor-water interfaces are studied as a function of pH including the consideration of the surface adsorbates. Finally, a discussion concluding this chapter is given in Section 6.7.

## **6.1 General motivation**

Despite the extensive attention from the scientific community [284, 285, 80, 286, 84, 287, 288, 289, 81, 290] and the tremendous efforts devoted [55, 82, 83, 79, 291, 292, 293], the efficiency of heterogeneous photocatalytic water splitting is still and by large unsatisfactory [284, 294]. This precludes any large-scale application of this otherwise promising technology for the production of clean fuel [294]. One of the key features currently hindering any perspective use of this process is the lack of an efficient photocatalyst material [89].

In principle, any semiconductor that is stable in aqueous environment and capable of harvesting solar light could be a photocatalyst for the water splitting reaction, thus providing a plethora of candidate materials. This enormous set might be reduced by considering several supplementary requirements, such as (i) a favorable alignment of the band edges of the semiconductor with respect to the redox levels of hydrogen reduction and water oxidation [100] and (ii) beneficial surface effects which might lower the overpotentials associated to the four proton-coupled electron transfers of the water oxidation reaction [295, 296, 297, 24, 298]. However, in practice, these properties cannot be tested experimentally for so many candidate materials.

Therefore, since the first investigations of heterogeneous water splitting [55], computational chemistry and physics have been used to disentangle some of the phenomena that are relevant to the efficiency of this process and to introduce an element of design in the systematic exploration of candidate materials [66, 299, 300, 295, 86, 87, 88, 89, 90, 301]. Excellent results have been achieved in the calculation of the band gap of semiconductors [93, 94, 302, 303, 304] as well as in the alignment of the band edges at water-semiconductor interfaces [66, 299, 100]. Based on simplified computational protocols, theoretical screenings of candidate materials have been deployed [86, 87, 88, 89, 90] in order to define smaller sets of possibly promising photocatalysts with band edges favorably aligned to the redox levels of hydrogen reduction and water oxidation [100]. Furthermore, the calculation of the overpotentials associated to the water oxidation reaction has been made possible both by means of simplified interface models [305, 295, 306, 307, 308, 309], and more recently, by means of more realistic semiconductor-water interfaces in a few cases [309, 310].

In this framework, the theoretical description of physical processes occurring at semiconductor-water interfaces is complicated by their multi-faceted nature, which depends upon various factors, e.g. the pH of the aqueous solution in which the material is immersed and possible reconstructions and defects at the surface [300, 311]. Therefore, simplified computational protocols in which such effects are completely ignored are likely to miss important physical aspects, thus affecting and possibly invalidating the achieved results. While the simultaneous inclusion of all effects in a single simulation is currently beyond reach, it has recently been shown that theory is at least capable of describing the acid-base chemistry and reactivity of pristine semiconductor-water interfaces [299, 300]. However, in order to identify the characteristics of the ideal photocatalyst, it is necessary to enable a more extensive screening, in which

several semiconductors are compared. In this chapter, we try to evaluate photocatalysts for water splitting through the combined analysis of surface coverage and energy-level alignment.

## 6.2 Theoretical formulation

Considering an ideal semiconductor surface  $M_xA_y$ , we assume that protons are adsorbed only on surface anion sites A, while water molecules and hydroxyl ions are adsorbed on surface metal sites M, all M and A sites being equivalent. For the calculation of the  $pK_a$  of individual adsorption sites, we consider the following acid-base equilibria:



and



where  $H_A^+$  and  $A_{\text{emp}}$  represent a proton adsorbed on a surface site A and an empty site A, respectively.  $w_M$  and  $OH_M^-$  represent a water molecule and a hydroxyl ion adsorbed on a surface site M, respectively. The acid-base constants  $K_a$  of the proton adsorbed on a site A ( $H_A^+$ ) and of the water molecule adsorbed on a site M ( $w_M$ ) read as:

$$K_a(H_A^+) = \frac{[H_3O^+(\text{aq})][A_{\text{emp}}]}{[H_A^+]}, \quad (6.3)$$

and

$$K_a(w_M) = \frac{[H_3O^+(\text{aq})][OH_M^-]}{[w_M]}. \quad (6.4)$$

Given the definition of  $pK_a$  of an acid as the pH value for which the concentration of the adsorbed acid is equal to that of its conjugated base, at  $\text{pH} = pK_a(H_A^+)$ , the concentration of protons adsorbed on sites A ( $c_{H_A^+}$ ) should be equal to that of empty sites A ( $c_{A_{\text{emp}}}$ ):

$$c_{H_A^+} = c_{A_{\text{emp}}}. \quad (6.5)$$

Similarly, at  $\text{pH} = pK_a(w_M)$ , the concentration of water molecules ( $c_{w_M}$ ) and hydroxyl ions ( $c_{OH_M^-}$ ) adsorbed on sites M should be equal to each other:

$$c_{w_M} = c_{OH_M^-}. \quad (6.6)$$

In analogy to the definition of defect concentrations in crystalline materials,  $c_{H_A^+}$  and  $c_{A_{\text{emp}}}$  can be expressed in terms of the formation free energies of a proton adsorbed on a site A ( $G_f[H_A^+]$ ) and of an empty site A ( $G_f[A_{\text{emp}}]$ ), and read as [300]:

$$c_{H_A^+} = c_A e^{-G_f[H_A^+]/k_B T}, \quad (6.7)$$

## Chapter 6. Evaluation of photocatalysts for water splitting through combined analysis of surface coverage and energy-level alignment

---

and

$$c_{A_{\text{emp}}} = c_A e^{-G_f[A_{\text{emp}}]/k_B T}, \quad (6.8)$$

where  $c_A$  is the surface concentration of sites A,  $T$  the temperature, and  $k_B$  the Boltzmann constant. Similarly,  $c_{w_M}$  and  $c_{OH_M^-}$  can also be expressed in terms of the formation free energies of a water molecule ( $G_f[w_M]$ ) and a hydroxyl ion ( $G_f[OH_M^-]$ ) adsorbed on a site M. They read as follows:

$$c_{w_M} = c_M e^{-G_f[w_M]/k_B T}, \quad (6.9)$$

and

$$c_{OH_M^-} = c_M e^{-G_f[OH_M^-]/k_B T}, \quad (6.10)$$

where  $c_M$  is the surface concentration of sites M. From eqs. 6.5–6.10, one obtains:

$$G_f[H_A^+] = G_f[A_{\text{emp}}], \quad (6.11)$$

at  $\text{pH} = \text{p}K_a(H_A^+)$ , and

$$G_f[OH_M^-] = G_f[w_M], \quad (6.12)$$

at  $\text{pH} = \text{p}K_a(w_M)$ .

The formation free energies  $G_f[H_A^+]$ ,  $G_f[A_{\text{emp}}]$ ,  $G_f[OH_M^-]$ , and  $G_f[w_M]$  can be expressed using a grand-canonical formulation of adsorbates at the interface, analogous to that of solutes in aqueous solution [128, 300]. Following Ref. [300], the formation free energy of an adsorbate Y in the charged state  $q$  is defined as follows:

$$G_f^q[Y] = G^q[Y] - G[\text{ref}] - \sum_i n_i \mu_i + q(\varepsilon_{v_w} - \Delta V_w + \mu_e) + E_{\text{corr}}^q(\text{int}), \quad (6.13)$$

where  $G^q[Y]$  is the Gibbs free energy of the adsorbate Y in the charged state  $q$ , and  $G[\text{ref}]$  the Gibbs free energy of the reference interface system. In this work, we take as reference neutral semiconductor-water interfaces achieved from molecular dynamics (MD) simulations showing a water adsorption mode that can either be molecular, dissociative, or mixed [66].  $\mu_i$  is the chemical potential of the added/subtracted species  $i$ ,  $n_i$  is the number of added/subtracted atoms of the  $i$ -th atomic species (positive for added species, negative for subtracted species).  $\varepsilon_{v_w}$  is the valence band edge of bulk liquid water.  $\Delta V_w$  is the difference between the electrostatic potential of liquid water in a model of bulk water and in the respective bulk component of the semiconductor-water interface model [Fig. 6.1] [300].  $\mu_e$  is the electron chemical potential, and  $E_{\text{corr}}^q(\text{int})$  is a correction term taking into account electrostatic finite-size effects induced by the presence of a charge close to the interface.

In the following subsections, we give the expressions to be used for  $G_f[H_A^+]$ ,  $G_f[A_{\text{emp}}]$ ,  $G_f[OH_M^-]$ ,



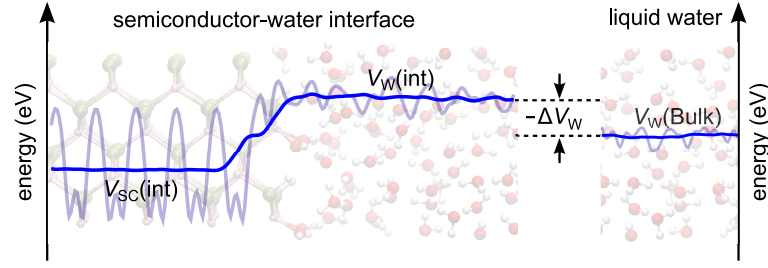


Figure 6.1 – Schematic representation of the alignment scheme. The lineup between the average electrostatic potential in bulk liquid water  $V_w(\text{bulk})$  and at the semiconductor-water interface  $V_w(\text{int})$  is achieved through  $\Delta V_w = V_w(\text{bulk}) - V_w(\text{int})$ .

and  $G_f[\text{w}_M]$  as derived depending on the water adsorption mode occurring in the reference models.

### Molecular Mode

For a reference interface showing a molecular adsorption mode of water, all surface anion sites A are empty, while all surface metal sites M are occupied by water molecules. In this case, we can write:

$$G_f[\text{A}_{\text{emp}}] = 0 \quad (6.14)$$

and

$$G_f[\text{w}_M] = 0. \quad (6.15)$$

According to eq. 6.13, the formation free energies of an adsorbed  $\text{H}^+$  on a site A ( $G_f[\text{H}_A^+]$ ) and of an  $\text{OH}^-$  on a site M ( $G_f[\text{OH}_M^-]$ ) read as follows:

$$G_f[\text{H}_A^+] = G[\text{H}_A^+] - G[\text{ref}] - \mu_{\text{H}} + \varepsilon_{\text{v}_w} - \Delta V_w + \mu_e + E_{\text{corr}}^{+1}(\text{int}) \quad (6.16)$$

and

$$G_f[\text{OH}_M^-] = G[\text{OH}_M^-] - G[\text{ref}] + \mu_{\text{H}} - \varepsilon_{\text{v}_w} + \Delta V_w - \mu_e + E_{\text{corr}}^{-1}(\text{int}). \quad (6.17)$$

The free-energy differences appearing in eqs. 6.16 and 6.17 can be calculated by employing the thermodynamic integration (TI) method [128, 219], and read as follows:

$$G[\text{H}_A^+] - G[\text{ref}] = \Delta_{\text{p}} A_{\text{A}_{\text{emp}}} + \Delta_{\text{zp}} E_{\text{H}_A^+} \quad (6.18)$$

and

$$G[\text{OH}_M^-] - G[\text{ref}] = \Delta_{\text{dp}} A_{\text{w}_M} - \Delta_{\text{zp}} E_{\text{w}_M}, \quad (6.19)$$

## Chapter 6. Evaluation of photocatalysts for water splitting through combined analysis of surface coverage and energy-level alignment

---

where  $\Delta_p A_{A_{\text{emp}}}$  and  $\Delta_{\text{dp}} A_{W_M}$  are the thermodynamic integrals associated with the protonation reaction occurring on an empty site A and the deprotonation reaction of a water molecule adsorbed on a site M, respectively.  $\Delta_{\text{zp}} E_{H_A^+}$  and  $\Delta_{\text{zp}} E_{W_M}$  are the zero-point motions of a proton adsorbed on a site A and of a proton belonging to a water molecule adsorbed on a site M, respectively. These are correction terms that account for the fact that the nuclei are treated classically in our simulations.

At  $\text{pH} = \text{p}K_a(H_A^+)$ , from eqs. 6.11, 6.14, 6.16, and 6.18, we obtain the following expression for the electron chemical potential  $\mu_e$ :

$$\mu_e = -\Delta_p A_{A_{\text{emp}}} - \Delta_{\text{zp}} E_{H_A^+} + \mu_H - \varepsilon_{v_w} + \Delta V_w - E_{\text{corr}}^{+1}(\text{int}). \quad (6.20)$$

At  $\text{pH} = \text{p}K_a(W_M)$ , from eqs. 6.12, 6.15, 6.17, and 6.19, we also achieve the expression for the electron chemical potential  $\mu_e$ :

$$\mu_e = \Delta_{\text{dp}} A_{W_M} - \Delta_{\text{zp}} E_{W_M} + \mu_H - \varepsilon_{v_w} + \Delta V_w + E_{\text{corr}}^{-1}(\text{int}). \quad (6.21)$$

### Dissociative Mode

For the reference interface showing a dissociative adsorption mode of water, all surface anion sites A and metal sites M are occupied by protons ( $H^+$ ) and hydroxyl ions ( $OH^-$ ), respectively. Therefore, we have in this case:

$$G_f[H_A^+] = 0 \quad (6.22)$$

and

$$G_f[OH_M^-] = 0. \quad (6.23)$$

According to eq. 6.13, the formation free energies of an empty site A and an adsorbed water molecule on the site M are given by:

$$G_f[A_{\text{emp}}] = G[A_{\text{emp}}] - G[\text{ref}] + \mu_H - \varepsilon_{v_w} + \Delta V_w - \mu_e + E_{\text{corr}}^{-1}(\text{int}) \quad (6.24)$$

and

$$G_f[W_M] = G[W_M] - G[\text{ref}] - \mu_H + \varepsilon_{v_w} - \Delta V_w + \mu_e + E_{\text{corr}}^{+1}(\text{int}). \quad (6.25)$$

Here, the free-energy differences appearing in eqs. 6.24 and 6.25 read as follows:

$$G[A_{\text{emp}}] - G[\text{ref}] = \Delta_{\text{dp}} A_{H_A^+} - \Delta_{\text{zp}} E_{H_A^+} \quad (6.26)$$

and

$$G[W_M] - G[\text{ref}] = \Delta_p A_{OH_M^-} + \Delta_{\text{zp}} E_{W_M}, \quad (6.27)$$

where  $\Delta_{\text{dp}}A_{\text{H}_\text{A}^+}$  and  $\Delta_{\text{p}}A_{\text{OH}_\text{M}^-}$  are the thermodynamic integrals associated with the deprotonation reaction of a  $\text{H}^+$  adsorbed on a site A and the protonation reaction of a  $\text{OH}^-$  adsorbed on a site M, respectively.

At  $\text{pH} = \text{p}K_{\text{a}}(\text{H}_\text{A}^+)$ , from eqs. 6.11, 6.22, 6.24, and 6.26, we derive the following expression for the electron chemical potential  $\mu_{\text{e}}$ :

$$\mu_{\text{e}} = \Delta_{\text{dp}}A_{\text{H}_\text{A}^+} - \Delta_{\text{zp}}E_{\text{H}_\text{A}^+} + \mu_{\text{H}} - \varepsilon_{\text{v}_\text{w}} + \Delta V_{\text{w}} + E_{\text{corr}}^{-1}(\text{int}). \quad (6.28)$$

At  $\text{pH} = \text{p}K_{\text{a}}(\text{w}_\text{M})$ , using eqs. 6.12, 6.23, 6.25, and 6.27, we obtain the following expression for the electron chemical potential  $\mu_{\text{e}}$ :

$$\mu_{\text{e}} = -\Delta_{\text{p}}A_{\text{OH}_\text{M}^-} - \Delta_{\text{zp}}E_{\text{w}_\text{M}} + \mu_{\text{H}} - \varepsilon_{\text{v}_\text{w}} + \Delta V_{\text{w}} - E_{\text{corr}}^{+1}(\text{int}). \quad (6.29)$$

### Mixed Mode

For the reference interface with the mixed adsorption mode of water, surface anion sites A are partially protonated, while metal sites M are occupied by either  $\text{H}_2\text{O}$  molecules or hydroxyl ions ( $\text{OH}^-$ ). In this case, following eq. 6.13, the formation free energies associated with the protonation of an empty site  $\text{A}_1$  ( $G_{\text{f}}[\text{H}_{\text{A}_1}^+]$ ) is expressed as:

$$G_{\text{f}}[\text{H}_{\text{A}_1}^+] = G[\text{H}_{\text{A}_1}^+] - G[\text{ref}] - \mu_{\text{H}} + \varepsilon_{\text{v}_\text{w}} - \Delta V_{\text{w}} + \mu_{\text{e}} + E_{\text{corr}}^{+1}(\text{int}). \quad (6.30)$$

Similarly, the formation free energy of an empty site  $\text{A}_2$  ( $G_{\text{f}}[\text{A}_{2\text{emp}}]$ ) obtained through deprotonation reads:

$$G_{\text{f}}[\text{A}_{2\text{emp}}] = G[\text{A}_{2\text{emp}}] - G[\text{ref}] + \mu_{\text{H}} - \varepsilon_{\text{v}_\text{w}} + \Delta V_{\text{w}} - \mu_{\text{e}} + E_{\text{corr}}^{-1}(\text{int}). \quad (6.31)$$

The free-energy differences contained in eqs. 6.30 and 6.31 can also be expressed as:

$$G[\text{H}_{\text{A}_1}^+] - G[\text{ref}] = \Delta_{\text{p}}A_{\text{A}_1\text{emp}} + \Delta_{\text{zp}}E_{\text{H}_\text{A}^+} \quad (6.32)$$

and

$$G[\text{A}_{2\text{emp}}] - G[\text{ref}] = \Delta_{\text{dp}}A_{\text{H}_{\text{A}_2}^+} - \Delta_{\text{zp}}E_{\text{H}_\text{A}^+}, \quad (6.33)$$

where  $\Delta_{\text{p}}A_{\text{A}_1\text{emp}}$  and  $\Delta_{\text{dp}}A_{\text{H}_{\text{A}_2}^+}$  are the thermodynamic integrals associated with the protonation at site  $\text{A}_1$  and the deprotonation of site  $\text{A}_2$ . At  $\text{pH} = \text{p}K_{\text{a}}(\text{H}_\text{A}^+)$ , through eqs. 6.11 and 6.30–6.33, we achieve the following expression for the electron chemical potential  $\mu_{\text{e}}$ :

$$\mu_{\text{e}} = \frac{1}{2}(\Delta_{\text{dp}}A_{\text{H}_{\text{A}_2}^+} - \Delta_{\text{p}}A_{\text{A}_1\text{emp}}) - \Delta_{\text{zp}}E_{\text{H}_\text{A}^+} + \mu_{\text{H}} - \varepsilon_{\text{v}_\text{w}} + \Delta V_{\text{w}} + \frac{1}{2}[E_{\text{corr}}^{-1}(\text{int}) - E_{\text{corr}}^{+1}(\text{int})]. \quad (6.34)$$

Proceeding in an analogous way, we derive through eq. 6.13 the formation free energies of an adsorbed  $\text{OH}^-$  ion resulting from the deprotonation of an adsorbed water molecule on site

## Chapter 6. Evaluation of photocatalysts for water splitting through combined analysis of surface coverage and energy-level alignment

---

$M_1$  ( $G_f[\text{OH}_{M_1}^-]$ ) and of a water molecule resulting from the protonation of an adsorbed  $\text{OH}^-$  on site  $M_2$  ( $G_f[\text{w}_{M_2}]$ ):

$$G_f[\text{OH}_{M_1}^-] = G[\text{OH}_{M_1}^-] - G[\text{ref}] + \mu_{\text{H}} - \varepsilon_{\text{v}_w} + \Delta V_{\text{w}} - \mu_{\text{e}} + E_{\text{corr}}^{-1}(\text{int}) \quad (6.35)$$

and

$$G_f[\text{w}_{M_2}] = G[\text{w}_{M_2}] - G[\text{ref}] - \mu_{\text{H}} + \varepsilon_{\text{v}_w} - \Delta V_{\text{w}} + \mu_{\text{e}} + E_{\text{corr}}^{+1}(\text{int}). \quad (6.36)$$

The free-energy differences appearing in eqs. 6.35 and 6.36 read as:

$$G[\text{OH}_{M_1}^-] - G[\text{ref}] = \Delta_{\text{dp}} A_{\text{w}_{M_1}} - \Delta_{\text{zp}} E_{\text{w}_M} \quad (6.37)$$

and

$$G[\text{w}_{M_2}] - G[\text{ref}] = \Delta_{\text{p}} A_{\text{OH}_{M_2}^-} + \Delta_{\text{zp}} E_{\text{w}_M}, \quad (6.38)$$

where  $\Delta_{\text{dp}} A_{\text{w}_{M_1}}$  and  $\Delta_{\text{p}} A_{\text{OH}_{M_2}^-}$  are the thermodynamic integrals associated with the deprotonation of a water molecule adsorbed on site  $M_1$  and the protonation of an adsorbed  $\text{OH}^-$  on site  $M_2$ , respectively. At  $\text{pH} = \text{p}K_{\text{a}}(\text{w}_M)$ , using eqs. 6.12 and 6.35–6.38, we obtain the following expression for the electron chemical potential  $\mu_{\text{e}}$ :

$$\mu_{\text{e}} = \frac{1}{2}(\Delta_{\text{dp}} A_{\text{w}_{M_1}} - \Delta_{\text{p}} A_{\text{OH}_{M_2}^-}) - \Delta_{\text{zp}} E_{\text{w}_M} + \mu_{\text{H}} - \varepsilon_{\text{v}_w} + \Delta V_{\text{w}} + \frac{1}{2}[E_{\text{corr}}^{-1}(\text{int}) - E_{\text{corr}}^{+1}(\text{int})]. \quad (6.39)$$

A more general expression can be put forward for  $\mu_{\text{e}}$  that encompasses all the interface models with the various absorption modes. The deprotonation reaction of the  $\text{H}^+$  adsorbed on site  $A$  is the reverse process of protonation of an empty site  $A$ . This leads to the equation  $\Delta_{\text{dp}} A_{\text{H}_A^+} = -\Delta_{\text{p}} A_{\text{A}_{\text{emp}}}$ . Together with the assumption that all  $A$  sites are equivalent, the expressions for the electron chemical potential  $\mu_{\text{e}}$  at  $\text{pH} = \text{p}K_{\text{a}}(\text{H}_A^+)$  derived in eqs. 6.20, 6.28, and 6.34 can be combined into a single expression:

$$\mu_{\text{e}} = \Delta_{\text{dp}} A_{\text{H}_A^+} - \Delta_{\text{zp}} E_{\text{H}_A^+} + \mu_{\text{H}} - \varepsilon_{\text{v}_w} + \Delta V_{\text{w}} + E_{\text{corr}}^{\text{A}}(\text{int}), \quad (6.40)$$

with

$$E_{\text{corr}}^{\text{A}}(\text{int}) = \begin{cases} -E_{\text{corr}}^{+1}(\text{int}) & \text{molecular mode} \\ E_{\text{corr}}^{-1}(\text{int}) & \text{dissociated mode} \\ [E_{\text{corr}}^{-1}(\text{int}) - E_{\text{corr}}^{+1}(\text{int})]/2 & \text{mixed mode} \end{cases}$$

Similarly, using  $\Delta_{\text{dp}} A_{\text{w}_M} = -\Delta_{\text{p}} A_{\text{OH}_M^-}$  and the assumption of equivalent  $M$  sites, we reformulate

## 6.2. Theoretical formulation

the expressions of  $\mu_e$  given in eqs. 6.21, 6.29, and 6.39. At  $\text{pH} = \text{p}K_a(w_M)$ , we thus obtain the following more general expression:

$$\mu_e = \Delta_{\text{dp}} A_{w_M} - \Delta_{\text{zp}} E_{w_M} + \mu_{\text{H}} - \varepsilon_{v_w} + \Delta V_w + E_{\text{corr}}^{\text{M}}(\text{int}), \quad (6.41)$$

with

$$E_{\text{corr}}^{\text{M}}(\text{int}) = \begin{cases} E_{\text{corr}}^{-1}(\text{int}) & \text{molecular mode} \\ -E_{\text{corr}}^{+1}(\text{int}) & \text{dissociated mode} \\ [E_{\text{corr}}^{-1}(\text{int}) - E_{\text{corr}}^{+1}(\text{int})]/2 & \text{mixed mode} \end{cases}$$

The electron chemical potential  $\mu_e$  given in eqs. 6.40 and 6.41 is instrumental to achieve the pH value of the solution. In fact,  $\mu_e$  and pH can be related through the formation free energy of the hydronium ion in aqueous solution [300]:

$$\mu_e = \Delta_{\text{dp}} A_{\text{H}_3\text{O}^+} - \Delta_{\text{zp}} E_{\text{H}_3\text{O}^+} + \mu_{\text{H}} - \varepsilon_{v_w} - E_{\text{corr}}^{+1}(\text{aq}) + k_{\text{B}} T [\ln c_0 + \ln 10 \cdot \text{pH}], \quad (6.42)$$

where  $\Delta_{\text{dp}} A_{\text{H}_3\text{O}^+}$  is the thermodynamic integral associated with the deprotonation reaction of the hydronium cation,  $\Delta_{\text{zp}} E_{\text{H}_3\text{O}^+}$  is the zero-point motion of a proton belonging to a hydronium cation, and  $\mu_{\text{H}}$  is the chemical potential of hydrogen.  $E_{\text{corr}}^{+1}(\text{aq})$  is the correction term taking into account electrostatic finite-size effects induced by the presence of the positive charge localized on the hydronium cation when using a simulation supercell for modelling liquid water.  $c_0$  is the number of water moles in 1 L of liquid water (55.5 mol/L).

We can now obtain the expression for the  $\text{p}K_a$  values associated with the surface sites. By combining eqs. 6.40 and 6.42, we achieve the  $\text{p}K_a$  of a proton attached to a site A:

$$\begin{aligned} \text{p}K_a(\text{H}_A^+) &= \frac{\Delta_{\text{dp}} A_{\text{H}_A^+} - \Delta_{\text{dp}} A_{\text{H}_3\text{O}^+} + \Delta V_w}{k_{\text{B}} T \ln 10} + \frac{-\Delta_{\text{zp}} E_{\text{H}_A^+} + \Delta_{\text{zp}} E_{\text{H}_3\text{O}^+}}{k_{\text{B}} T \ln 10} \\ &+ \frac{E_{\text{corr}}^{\text{A}}(\text{int}) + E_{\text{corr}}^{+1}(\text{aq})}{k_{\text{B}} T \ln 10} - \log c_0, \end{aligned} \quad (6.43)$$

By combining eqs. 6.41 and 6.42, we also obtain the  $\text{p}K_a$  of a water molecule attached to a site M:

$$\begin{aligned} \text{p}K_a(w_M) &= \frac{\Delta_{\text{dp}} A_{w_M} - \Delta_{\text{dp}} A_{\text{H}_3\text{O}^+} + \Delta V_w}{k_{\text{B}} T \ln 10} + \frac{-\Delta_{\text{zp}} E_{w_M} + \Delta_{\text{zp}} E_{\text{H}_3\text{O}^+}}{k_{\text{B}} T \ln 10} \\ &+ \frac{E_{\text{corr}}^{\text{M}}(\text{int}) + E_{\text{corr}}^{+1}(\text{aq})}{k_{\text{B}} T \ln 10} - \log c_0, \end{aligned} \quad (6.44)$$

The values of  $\text{p}K_a(\text{H}_A^+)$  and  $\text{p}K_a(w_M)$  directly give access to the pH value at the point of zero charge ( $\text{pH}_{\text{PZC}}$ ) and at the free energy of dissociation of a water molecule adsorbed on the

## Chapter 6. Evaluation of photocatalysts for water splitting through combined analysis of surface coverage and energy-level alignment

surface. The  $\text{pH}_{\text{PZC}}$  for a semiconductor surface  $\text{M}_x\text{A}_y$  at the interface with liquid water is defined as the pH for which the concentration of adsorbed protons  $c_{\text{H}_\text{A}^+}$  is equal to that of adsorbed hydroxyl ions  $c_{\text{OH}_\text{M}^-}$ . This has been demonstrated to be related to  $\text{p}K_\text{a}(\text{H}_\text{A}^+)$  and  $\text{p}K_\text{a}(\text{w}_\text{M})$  through the following expression [300]:

$$\text{pH}_{\text{PZC}} = \frac{\text{p}K_\text{a}(\text{H}_\text{A}^+) + \text{p}K_\text{a}(\text{w}_\text{M})}{2} - \frac{1}{2} \left[ \log \left( \frac{c_\text{M}}{c_\text{A}} \right) \right], \quad (6.45)$$

where  $c_\text{M}$  and  $c_\text{A}$  are the surface concentration of M and A sites, respectively. Furthermore, the free energy of dissociation of an adsorbed water is given by [300]:

$$\Delta A_\text{d}(\text{w}_\text{M}) = \ln 10 \cdot k_\text{B} T [\text{p}K_\text{a}(\text{w}_\text{M}) - \text{p}K_\text{a}(\text{H}_\text{A}^+)]. \quad (6.46)$$

### 6.3 Method

#### 6.3.1 Calculation of deprotonation energy

In this work, the thermodynamic integrals  $\Delta_\text{dp}A_{\text{H}_\text{A}^+}$  and  $\Delta_\text{dp}A_{\text{w}_\text{M}}$  are calculated for two values of the Kirkwood coupling parameter  $\eta$  (0 and 1), thus actually adopting the linear Marcus approximation, which has been found to produce a negligible error when applied to deprotonation integrals [128, 312, 300]. Therefore,  $\Delta_\text{dp}A_{\text{H}_\text{A}^+}$  and  $\Delta_\text{dp}A_{\text{w}_\text{M}}$  can be calculated as follows:

$$\int_0^1 \langle \Delta_\text{dp}E_{\text{H}_\text{A}^+} \rangle_\eta d\eta = \Delta_\text{dp}A_{\text{H}_\text{A}^+} = \frac{\langle \Delta_\text{dp}E_{\text{H}_\text{A}^+} \rangle_0 + \langle \Delta_\text{dp}E_{\text{H}_\text{A}^+} \rangle_1}{2} \quad (6.47)$$

and

$$\int_0^1 \langle \Delta_\text{dp}E_{\text{w}_\text{M}} \rangle_\eta d\eta = \Delta_\text{dp}A_{\text{w}_\text{M}} = \frac{\langle \Delta_\text{dp}E_{\text{w}_\text{M}} \rangle_0 + \langle \Delta_\text{dp}E_{\text{w}_\text{M}} \rangle_1}{2}. \quad (6.48)$$

$\langle \Delta_\text{dp}E_{\text{H}_\text{A}^+} \rangle_0$  and  $\langle \Delta_\text{dp}E_{\text{w}_\text{M}} \rangle_0$  are the average vertical deprotonation energies for an adsorbed proton and for a proton belonging to an adsorbed water molecule, respectively. At equilibrated neutral interfaces showing molecular water adsorption, there are no protons attached to sites A. Hence, we consider a configuration of the equilibrated interface and construct an initial configuration by inserting a proton close to an empty site A. MD simulations are then evolved for 7 ps including 2 ps for equilibration. This operation is carried out twice for two different proton insertions. In the case of equilibrated neutral interfaces showing the dissociative adsorption mode, there are no water molecules adsorbed on sites M. Hence, the proton is inserted in the vicinity of an hydroxyl ion, but otherwise the same procedure is followed as for the interface showing molecular adsorption. Then,  $\langle \Delta_\text{dp}E_{\text{H}_\text{A}^+} \rangle_0$  and  $\langle \Delta_\text{dp}E_{\text{w}_\text{M}} \rangle_0$  are calculated by vertically detaching the inserted proton from the surface and from the adsorbed water molecule, respectively. For each vertical detachment, we consider 100 configurations sampled at intervals of 50 fs during the last 5 ps of every MD trajectory.

$\langle \Delta_{\text{dp}} E_{\text{H}_\text{A}^+} \rangle_1$  and  $\langle \Delta_{\text{dp}} E_{\text{wM}} \rangle_1$  represent the energies associated to a vertical proton insertion and are evaluated following the scheme outlined in Ref. [300]. In this scheme, an extra proton is vertically inserted and relaxed in the proximity of the acidic site, while all other atoms are kept fixed. However, there are no empty sites at the equilibrated neutral interface showing a dissociative adsorption mode, and no adsorbed hydroxyl ions at the equilibrated neutral interface showing a molecular adsorption mode. In order to create acidic sites for the addition of a proton at these interfaces, we use initial configurations of the neutral interfaces and either remove a proton attached to a site A or a proton from an adsorbed water molecule. MD simulations are then evolved for 7 ps and the sampling is carried out on the last 5 ps.

The structural relaxations are here carried out with the rVV10 functional. To examine the validity of the rVV10 functional for the achieved structures, we also perform the structural relaxations at the h-rVV10 level in selected test calculations. The h-rVV10 functional combines the PBE0 hybrid functional with the rVV10 description of nonlocal van der Waals interactions. In this h-rVV10 functional, the fraction  $\alpha$  of Fock exchange is set to 0.40 and the  $b$  parameter of rVV10 to 5.3, as these parameters have been found to give a good description of the density and the structural properties of liquid water [312]. In the test calculations, it is found the rVV10 and h-rVV10 functionals give energy differences smaller than 0.05 eV upon the structural relaxations considered here. Hence, this supports the use of the rVV10 structures also when the vertical excitations are evaluated with the h-rVV10 functional.

### 6.3.2 Electrostatic finite-size corrections

Table 6.1 – The lattice parameters of the supercells used, the adopted dielectric constants of the semiconductors ( $\epsilon$ ), and the estimated values for  $E_{\text{corr}}^{+1}(\text{int})$  and  $E_{\text{corr}}^{-1}(\text{int})$  in eV.

	$L_x$ (Å)	$L_y$ (Å)	$L_z$ (Å)	$\epsilon$	$E_{\text{corr}}^{+1}(\text{int})$	$E_{\text{corr}}^{-1}(\text{int})$
GaAs/H <sub>2</sub> O	11.99	11.31	34.62	13.2	0.02	0.02
GaP/H <sub>2</sub> O	11.74	11.07	34.56	11.1	0.02	0.02
GaN/H <sub>2</sub> O	10.53	9.71	38.18	9.8	0.03	0.03
CdS/H <sub>2</sub> O	13.73	12.64	35.23	9.4	0.03	0.03
ZnO/H <sub>2</sub> O	10.60	9.88	38.50	8.8	0.03	0.03
SnO <sub>2</sub> /H <sub>2</sub> O	13.40	12.74	30.04	9.9	0.03	0.03
r-TiO <sub>2</sub> /H <sub>2</sub> O	13.19	12.01	30.62	85.0	0.01	0.01
a-TiO <sub>2</sub> /H <sub>2</sub> O	10.39	11.41	36.00	30.0	0.01	0.01

In this work, the FNV scheme [123, 13] is employed to estimate the correction term  $E_{\text{corr}}^{+1}(\text{aq})$  relative to a H<sub>3</sub>O<sup>+</sup> ion in liquid water. In this scheme a model charge distribution consisting of a Gaussian with a fixed width of 1 Å is adopted. Due to the high dielectric constant of liquid water ( $\epsilon_w = 78.3$ ), the alignment-like term contained in the FNV correction is vanishingly small [128]. Hence, only the Madelung term contributes and is determined to be 0.02 eV.

$E_{\text{corr}}^{-1}(\text{int})$  and  $E_{\text{corr}}^{+1}(\text{int})$  correspond to finite-size corrections for the semiconductor-water

## Chapter 6. Evaluation of photocatalysts for water splitting through combined analysis of surface coverage and energy-level alignment

Table 6.2 – Zero-point energies of bare protons adsorbed on surface sites A ( $\Delta_{\text{zp}}E_{\text{H}_\text{A}^+}$ ) and of protons belonging to water molecules adsorbed on surface sites M ( $\Delta_{\text{zp}}E_{\text{w}_\text{M}}$ ), calculated with the rVV10 and h-rVV10 functionals.

	rVV10		h-rVV10	
	$\Delta_{\text{zp}}E_{\text{H}_\text{A}^+}$	$\Delta_{\text{zp}}E_{\text{w}_\text{M}}$	$\Delta_{\text{zp}}E_{\text{H}_\text{A}^+}$	$\Delta_{\text{zp}}E_{\text{w}_\text{M}}$
GaAs/H <sub>2</sub> O	0.19	0.30	0.20	0.32
GaP/H <sub>2</sub> O	0.21	0.30	0.22	0.32
GaN/H <sub>2</sub> O	0.31	0.30	0.33	0.31
CdS/H <sub>2</sub> O	0.22	0.32	0.24	0.33
ZnO/H <sub>2</sub> O	0.30	0.31	0.32	0.32
SnO <sub>2</sub> /H <sub>2</sub> O	0.28	0.31	0.30	0.32
r-TiO <sub>2</sub> /H <sub>2</sub> O	0.30	0.31	0.32	0.33
a-TiO <sub>2</sub> /H <sub>2</sub> O	0.30	0.32	0.32	0.33

interfaces with either a proton removed or added. This correction does not depend on the sign of the charge and can be estimated through the scheme given in Ref. [313]. The estimated values for  $E_{\text{corr}}^{+1}(\text{int})$  and  $E_{\text{corr}}^{-1}(\text{int})$  are given in Table 6.1, together with the parameters defining the supercell and the adopted dielectric constant for the semiconductors.

### 6.3.3 Energy of zero-point motion

We need to evaluate the energy of zero-point motion associated with (i) one proton in the aqueous H<sub>3</sub>O<sup>+</sup> ion ( $\Delta_{\text{zp}}E_{\text{H}_3\text{O}^+}$ ), (ii) a bare proton attached to a surface A site ( $\Delta_{\text{zp}}E_{\text{H}_\text{A}^+}$ ), and (iii) a proton belonging to a water molecule attached to a surface M site ( $\Delta_{\text{zp}}E_{\text{w}_\text{M}}$ ). We estimate those energies by calculating the vibrational frequencies of the related normal modes. In particular, we construct the displacement matrix by only considering the displacements of the considered proton. Therefore, for each case we calculate three frequencies, and the zero-point energy is calculated as follows

$$\Delta_{\text{zp}}E = \sum_{n=1}^3 \frac{h\nu_n}{2}, \quad (6.49)$$

where  $h$  is the Planck constant and  $\nu_i$  the frequency of the  $i$ -th normal mode. Using this computational protocol, the zero point motion pertaining to the proton in the aqueous hydronium ion ( $\Delta_{\text{zp}}E_{\text{H}_3\text{O}^+}$ ) is found to 0.32 and 0.34 eV when using the rVV10 and h-rVV10 functionals, respectively. These estimates agree closely with those inferred from the experimental vibrational spectrum of the hydrated proton [128, 314]. The energies of zero-point motion pertaining to protons in adsorbates are given in Table 6.2.



#### 6.4. Comparison of $\text{pH}_{\text{PZC}}$ and $\text{p}K_{\text{a}}$ achieved with semilocal and hybrid functionals

Table 6.3 – Calculated values of  $\text{pH}_{\text{PZC}}$  as obtained with the semilocal rVV10 and hybrid h-rVV10 functionals for various semiconductor-water interfaces. Mean absolute errors (MAEs) of  $\text{pH}_{\text{PZC}}$  with respect to experimental values are also given. All values are given in pH units.

	$\text{pH}_{\text{PZC}}(\text{theory})$		$\text{pH}_{\text{PZC}}(\text{expt.})$
	rVV10	h-rVV10	
GaAs/H <sub>2</sub> O(m)	9.69	6.12	5.90
GaAs/H <sub>2</sub> O(d)	6.96	5.57	5.90
GaP/H <sub>2</sub> O(m)	8.94	5.65	4.90
GaP/H <sub>2</sub> O(d)	6.31	5.15	4.90
GaN/H <sub>2</sub> O	6.89	5.76	7.00
CdS/H <sub>2</sub> O	8.94	6.58	7.50
ZnO/H <sub>2</sub> O	6.47	7.48	9.00
SnO <sub>2</sub> /H <sub>2</sub> O	4.63	4.18	4.30
r-TiO <sub>2</sub> /H <sub>2</sub> O	6.61	6.73	5.90
a-TiO <sub>2</sub> /H <sub>2</sub> O(m)	6.90	7.03	5.90
a-TiO <sub>2</sub> /H <sub>2</sub> O(d)	6.81	6.87	5.90
MAE	1.58	0.75	

#### 6.4 Comparison of $\text{pH}_{\text{PZC}}$ and $\text{p}K_{\text{a}}$ achieved with semilocal and hybrid functionals

In Table 6.3, we report the values of  $\text{pH}_{\text{ZPC}}$  for various semiconductor-water interfaces as obtained with both the semilocal rVV10 and the hybrid h-rVV10 functionals. The comparison with experimental values shows that the hybrid functional provides much more accurate values of  $\text{pH}_{\text{ZPC}}$  than the semilocal one, with the MAE (0.75 pH units) for the former being less than half of that for the latter (1.58 pH units). Especially when referring to GaAs and GaP with molecular water adsorption, the rVV10 functional gives  $\text{pH}_{\text{PZC}}$  values that exceed their experimental counterparts by about 4 pH units. In addition, we notice that the rVV10 functional significantly underestimates the  $\text{pH}_{\text{ZPC}}$  for ZnO, leading to an error of 2.46 pH units respect to the experimental result. The size of the errors achieved by rVV10 should be contrasted with the maximum error of only 1.52 pH units achieved by h-rVV10 in the case of ZnO. As far as the other semiconductors are concerned, the rVV10 and h-rVV10 functionals yield relatively similar results, with the maximum difference being less than 1.4 pH units.

We give in Table 6.4 the  $\text{p}K_{\text{a}}(\text{H}_{\text{A}}^+)$ , the  $\text{p}K_{\text{a}}(\text{w}_{\text{M}})$ , and the dissociation free energy of an adsorbed water  $\Delta A_{\text{d}}(\text{w}_{\text{M}})$ , as calculated with rVV10 and h-rVV10 functionals. For GaAs and GaP with molecular water adsorption, the  $\text{p}K_{\text{a}}(\text{H}_{\text{A}}^+)$  calculated with the rVV10 functional is found to be very alkaline, i.e. 13.41 and 14.75, respectively, about 6 pH units higher than the values determined with the h-rVV10 functional. This effect appears to be the main origin of the errors of up to 4 pH units found for the corresponding  $\text{pH}_{\text{ZPC}}$  [Table 6.3]. For CdS, the  $\text{p}K_{\text{a}}(\text{H}_{\text{A}}^+)$  achieved with the rVV10 functional (5.70) is considerably higher than that determined at the h-rVV10 level (0.19). The rVV10 value of the  $\text{p}K_{\text{a}}(\text{H}_{\text{A}}^+)$  appears nevertheless to be sufficiently acid to turn the dissociative adsorption mode into a molecular one within 1 ps of MD evolution [66].

## Chapter 6. Evaluation of photocatalysts for water splitting through combined analysis of surface coverage and energy-level alignment

Table 6.4 –  $pK_a$  of protons adsorbed on surface sites A [ $pK_a(H_A^+)$ ] and of protons belonging to water molecules adsorbed on surface sites M [ $pK_a(w_M)$ ], together with the dissociation free energy of an adsorbed water molecule [ $\Delta A_d(w_M)$ ] at various semiconductor-water interfaces, as calculated with the rVV10 and h-rVV10 functionals. The label  $m$  ( $d$ ) specifies that the water adsorption mode is molecular (dissociative) in the considered model. A positive (negative) value of  $\Delta A_d(w_M)$  favors the  $m$  ( $d$ ) adsorption mode. The values of  $pK_a$  and  $\Delta A_d(w_M)$  are given in units of pH and eV, respectively.

	rVV10			h-rVV10		
	$pK_a(H_A^+)$	$pK_a(w_M)$	$\Delta A_d(w_M)$	$pK_a(H_A^+)$	$pK_a(w_M)$	$\Delta A_d(w_M)$
GaAs ( $m$ )	13.41	5.97	-0.52	7.42	4.81	-0.18
GaAs ( $d$ )	8.21	5.71	-0.17	7.03	4.10	-0.20
GaP ( $m$ )	14.75	3.12	-0.81	8.95	2.35	-0.46
GaP ( $d$ )	9.70	2.92	-0.47	8.47	1.83	-0.46
GaN ( $d$ )	12.12	1.65	-0.73	11.14	0.38	-0.75
CdS ( $m$ )	5.70	12.18	0.45	0.19	12.96	0.89
ZnO (mixed)	7.98	4.96	-0.21	8.42	6.54	-0.13
SnO <sub>2</sub> (mixed)	6.17	3.09	-0.21	5.20	3.16	-0.14
r-TiO <sub>2</sub> (m)	3.97	9.25	0.37	3.25	10.21	0.48
a-TiO <sub>2</sub> (m)	3.50	10.31	0.47	2.86	11.20	0.58
a-TiO <sub>2</sub> (d)	3.68	9.94	0.43	4.02	9.72	0.40

The failure of achieving accurate  $pK_a(H_A^+)$  with rVV10 at the aforementioned interfaces can be attributed to the improper description of the bare proton adsorbed on surface As, P, and S sites. For the other semiconductors, the rVV10 and h-rVV10 functionals provide similar results for both  $pK_a(H_A^+)$  and  $pK_a(w_M)$  with a difference of at most 1.61 pH units, corresponding to an energy error of 0.11 eV. In the following, we only focus on results achieved with the h-rVV10 functional.

The results in Table 6.4 also allow one to determine whether the water molecules adsorb in the molecular or dissociative mode. For GaAs, GaP, and a-TiO<sub>2</sub>, the adsorption mode could not be inferred from molecular dynamics simulation, as the initial adsorption modes were preserved during the time scale of the simulation [66]. For GaAs and GaP, the calculated acidity constants indicate that the protons attached to surface As and P sites are more alkaline than the water molecules adsorbed on Ga sites by over 2.6 and 6.6 pH units, respectively [Table 6.4]. For the corresponding dissociation free energy of an adsorbed water molecule [ $\Delta A_d(w_M)$ ], we find -0.20 and -0.46 eV, respectively, which support the dissociative adsorption mode. This result is consistent with the conclusion inferred from the alignment of the redox levels, for which the dissociative mode was found to yield a much better agreement with experiment than the molecular mode [66]. For a-TiO<sub>2</sub>, the protons on surface O sites are found to be more acidic than the water molecules on surface Ti sites by at least 5.70 pH units, and the corresponding  $\Delta A_d(w_M)$  is 0.40 eV or higher. These results clearly indicate that the molecular adsorption mode is preferred on the a-TiO<sub>2</sub> surface. We remark that this assessment could not be achieved on the basis of the alignment of redox levels as molecular and dissociative

adsorption modes yield too close results in this case [66]. In the following, we will only pay attention to the results achieved from the models with the dissociative adsorption mode for GaAs and GaP, and with the molecular mode for a-TiO<sub>2</sub>.

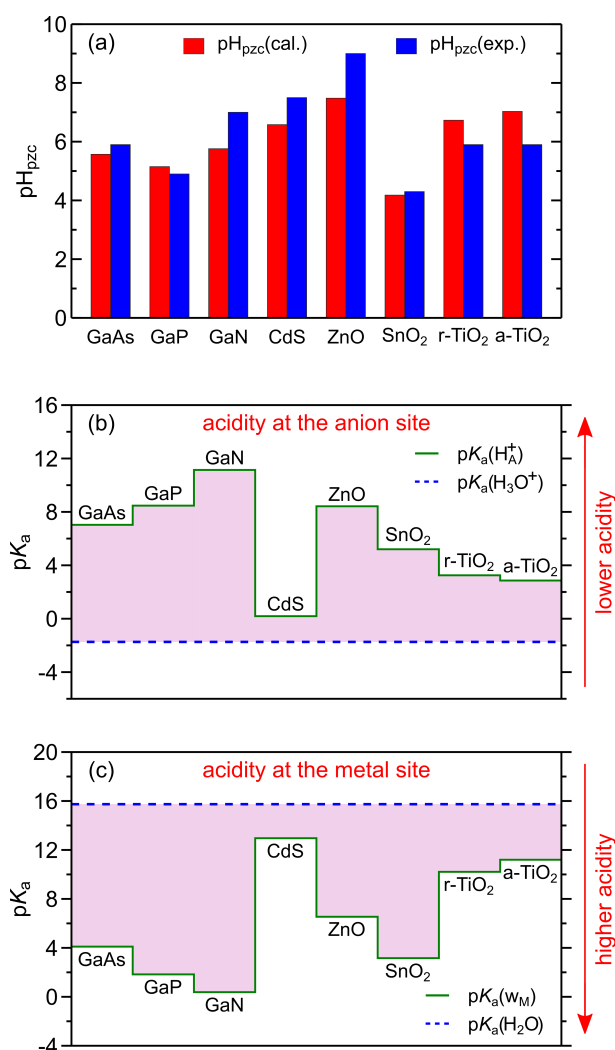


Figure 6.2 – (a) Calculated values of  $pH_{PZC}$  (red bars) at various semiconductor-water interfaces compared with experimental estimates taken from Ref. [66] (blue bars). (b)  $pK_a$  of the proton  $H_A^+$  adsorbed on a non-metal site A of the surface (e.g. As, P, N, S, and O atoms). (c)  $pK_a$  for a water molecule  $w_M$  adsorbed on a metal site M of the surface (e.g. Ga, Cd, Zn, Sn, and Ti atoms). In panel (b) and (c), the blue dashed lines indicate the  $pK_a$  for aqueous hydronium ions and water molecules, respectively. All values are reported in units of pH.

## **6.5 Acid-Base properties**

### **6.5.1 Acidity of semiconductor surfaces**

The values of  $\text{pH}_{\text{PZC}}$  calculated at the hybrid level of theory (h-rVV10) are reported in Fig. 6.2(a) for comparison with experimental estimates [66]. The agreement with the measured values is excellent as demonstrated by the mean average error (MAE) of only 0.79 pH unit, corresponding to an energy error of only about 0.05 eV. The remarkable accuracy achieved for the values of  $\text{pH}_{\text{PZC}}$  enables us to further analyze the acid-base chemistry of the water-semiconductor interfaces under consideration. In particular, we investigate the acidic constants of adsorbed protons on non-metal sites A [ $\text{p}K_{\text{a}}(\text{H}_{\text{A}}^+)$ ] and of adsorbed water molecules on metal sites M [ $\text{p}K_{\text{a}}(\text{w}_{\text{M}})$ ] for each semiconductor surface. The respective acidic constants from our calculations are illustrated in Figs. 6.2(b) and (c), where they are compared with the acidic constant of the aqueous hydronium cation [ $\text{p}K_{\text{a}}(\text{H}_3\text{O}^+) = -1.74$ , by definition] and with that of an aqueous water molecule [ $\text{p}K_{\text{a}}(\text{H}_2\text{O}) = 15.74$ ], respectively. For all the interfaces, we find that the acidity of the adsorbed proton is noticeably weaker than that of the aqueous hydronium cation. While the acidity of adsorbed water molecules is higher than that of an aqueous water molecule, which can be rationalized by the occurrence of electron transfer between the O atoms of the adsorbed water molecules and the metal atoms at the semiconductor surfaces, thereby enhancing the acidity of the O atoms and favoring their release of protons.

Concerning  $\text{p}K_{\text{a}}(\text{H}_{\text{A}}^+)$ , we can distinguish two different behaviors. Oxides and sulfides, with the exception of ZnO, show a moderately acidic adsorbed proton. In particular, a value of  $\text{p}K_{\text{a}}(\text{H}_{\text{A}}^+)$  as low as 0.19 is obtained for CdS. Anatase and rutile show similar properties with values of  $\text{p}K_{\text{a}}(\text{H}_{\text{A}}^+)$  close to 3, while a higher alkalinity is observed for  $\text{SnO}_2$  [ $\text{p}K_{\text{a}}(\text{H}_{\text{A}}^+) = 5.20$ ] and, more remarkably, for ZnO [ $\text{p}K_{\text{a}}(\text{H}_{\text{A}}^+) = 8.42$ ]. At variance, the non-metal sites A of the III-V semiconductors are rather alkaline with values of  $\text{p}K_{\text{a}}(\text{H}_{\text{A}}^+)$  up to 11.14 for GaN. It is interesting to point out that, comparing GaN, GaP, and GaAs, we observe an increasing acidity of the proton site going from N to As, in agreement with the decreasing electronegativity. For  $\text{p}K_{\text{a}}(\text{w}_{\text{M}})$ , III-V semiconductors show noticeable differences with calculated values ranging between 0.38 for GaN and 4.10 for GaAs. Since the water molecules are always adsorbed on a Ga surface site in these cases, it is evident that also the surrounding chemical environment as determined by the nearest neighbors and the surface structure (110 for GaAs and GaP, 10 $\bar{1}$ 0 for GaN) affect the acidity of the adsorbed water molecules. For oxides and sulfides, we observe alkaline values of  $\text{p}K_{\text{a}}(\text{w}_{\text{M}})$  for CdS and for the two polymorphs of  $\text{TiO}_2$ . By contrast, the acidity of adsorbed water molecules is noticeably increased for ZnO [ $\text{p}K_{\text{a}}(\text{w}_{\text{M}}) = 6.54$ ], and even more so for  $\text{SnO}_2$  [ $\text{p}K_{\text{a}}(\text{w}_{\text{M}}) = 3.16$ ]. We further remark that the acidic constants achieved for the two polymorphs of  $\text{TiO}_2$  fall rather close to each other, suggesting that the acid-base properties of their surfaces are weakly dependent on the underlying crystal structures. This observation is consistent with the experimental finding that the  $\text{pH}_{\text{PZC}}$  of  $\text{TiO}_2$  lies in a small interval ranging from 5.8 to 6.0 [251, 275], irrespective of the crystal structure [275].

Overall, the calculated data should be interpreted taking into account the different electroneg-

activities of the surface sites but also the chemical environment at the surface. For example, while CdS and ZnO have a very similar surface structure, the calculated values of both  $pK_a(H_A^+)$  and  $pK_a(w_M)$  are completely different, because of the intrinsic difference in reactivity of the surface sites. Similarly, we observe that surface O sites of different semiconductor surfaces can span a large range of  $pK_a(H_A^+)$  values. Hence, a clear role should be assigned to the chemical environment at the surface in modulating the acidity of chemically equivalent sites. It is important to underline that the complex interplay between intrinsic reactivity and chemical environment might not be captured by simplified models.

For the semiconductors under investigation, the free energy of dissociation ( $\Delta A_d$ ) for adsorbed water molecules as calculated from eq. 6.46 is illustrated in Fig. 6.3. Negative values of  $\Delta A_d$  indicate exothermic dissociation of the adsorbed water molecules at  $pH_{PZC}$ , while positive values make the process unfavorable, thus favoring adsorption of molecular water. Again, we can broadly distinguish two groups of semiconductors. III-V semiconductors favor the dissociation of the  $H_2O$  molecules with a clear trend towards more favorable dissociation as the electronegativity of the anion increases along the series GaAs, GaP, and GaN. At variance, oxides and sulfides appear to favor molecular adsorption of water molecules on their pristine surfaces, with the exception of  $SnO_2$  and ZnO, which show moderately negative values for  $\Delta A_d$  ( $\sim -0.15$  eV). This result is consistent with the outcome of molecular dynamics simulations for these two interfaces [66], for which we observe coexistence of molecular and dissociated water molecules. For GaN, the rather low  $\Delta A_d(w_M)$  of  $-0.75$  eV provides a clear motivation for the fast conversion of the molecular adsorption mode into the dissociative one during the MD simulations [66]. On the contrary, the extremely high  $\Delta A_d(w_M)$  of 0.89 eV for CdS supports the high stability of molecularly adsorbed water. For both a-TiO<sub>2</sub> and r-TiO<sub>2</sub>, we find  $\Delta A_d$  of  $\sim 0.5$  eV, indicating that the water molecules are molecularly adsorbed on their pristine surfaces.

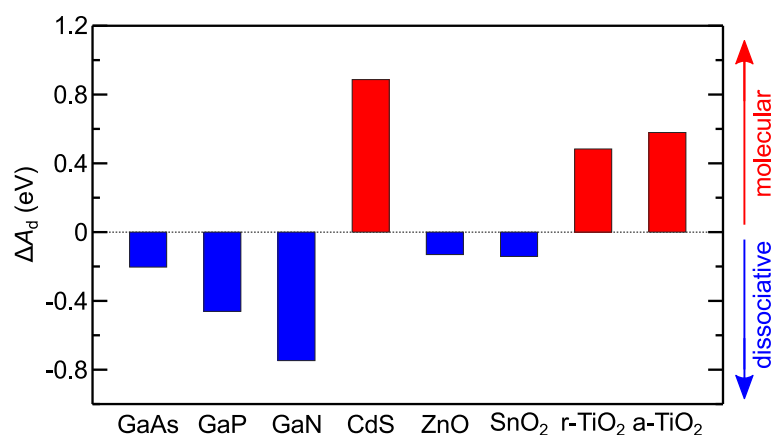


Figure 6.3 – Calculated free energy of dissociation for adsorbed water molecules on various semiconductor surfaces. Red (blue) bars indicate that the molecular (dissociative) adsorption mode is favored.

### **6.5.2 Surface concentration of adsorbates vs. pH**

The calculated acidity constants do not only provide insights into the physico-chemical properties of the semiconductor-water interfaces, but they also allow for a detailed description of the pH-dependent surface chemistry of such interfaces. This is achieved by constructing logarithmic diagrams of concentration, commonly employed for weak acids in aqueous solution, and recently extended to semiconductor-water interfaces [300]. In Fig. 6.4, we illustrate this powerful instrument to visualize the acid-base properties of the studied interfaces. First, we focus on III-V semiconductors. The diagram for GaN [Fig. 6.4(c)] clearly shows that the adsorption of protons and hydroxyl ions is dominant for a wide range of pH values comprised between 2 and 10. This feature is particularly desirable for the overall photocatalytic water splitting, for which we need adsorption of both these species, without having to enforce extremely acidic (for protons) or alkaline (for hydroxyl ions) conditions. Similar concentration diagrams are observed for GaAs and GaP [Figs. 6.4(a) and (b)]. In the case of GaAs, the ratio between the concentrations of dissociatively and molecularly adsorbed water is found to be close to 30:1 at  $\text{pH} = \text{pH}_{\text{PZC}}$ , implying that only  $\sim 3\%$  of the adsorbed water retains its molecular form. This is consistent with in-situ near-ambient pressure XPS studies revealing dissociative adsorption of water at GaAs-H<sub>2</sub>O interfaces [315]. For GaP, the concentration of ionic species dominates that of molecular adsorption by over three orders of magnitude, indicating that the model showing complete dissociation is representative of the real interface [66]. In near-neutral pH conditions, at which an ideal water-splitting plant should operate [284], almost 100% of the surface Ga sites are passivated by hydroxyl ions for both GaAs and GaP. Hence, at  $\text{pH} \cong 7$ , the water oxidation reaction on these surfaces will proceed through the reaction mechanism occurring under alkaline conditions (i.e. the oxidation of the adsorbed hydroxyl ions) [316], which is kinetically more favorable and faster than the reaction mechanism occurring under acidic conditions (i.e. the dehydrogenation of the adsorbed water molecules) [316]. At  $\text{pH} \cong 7$ , roughly 52% of the surface As sites are found to be protonated in the case of GaAs, while the corresponding fraction of surface P sites is as high as  $\sim 97\%$  in the case of GaP. Furthermore, concerning GaAs, we observe a narrow pH window ( $4.1 < \text{pH} < 7.0$ ), within which protons and hydroxyl ions are the dominant adsorbed species. The corresponding pH range is wider for GaP, where it extends from 1.8 to 8.5. For  $\text{pH} < 4.1$  in the case of GaAs and  $\text{pH} < 1.8$  in the case of GaP, molecular water becomes the dominant adsorbate. At these pH values, the water splitting reaction would mainly proceed through the kinetically unfavorable mechanism occurring under acidic conditions.

Next, we turn to ZnO and SnO<sub>2</sub>. The diagram for ZnO [Fig. 6.4(e)] clearly highlights its peculiar surface coverage, indicating that ions, vacant surface O sites, and molecularly adsorbed water molecules coexist in similar ratios in near-neutral conditions. The concentration diagram for SnO<sub>2</sub> is overall similar, although the pH range for the coexistence of the various adsorbates is found to be shifted towards more acidic pH values [Fig. 6.4(f)]. For SnO<sub>2</sub>, the fraction of dissociatively adsorbed water is  $\sim 91\%$  at  $\text{pH}_{\text{PZC}}$ , consistent with previous MD simulations indicating a mixed adsorption mode with a fraction of dissociated molecules of 87 – 94% [66]. At  $\text{pH} \cong 7$ , all surface Sn sites are passivated by hydroxyl ions, but the percentage of protonated

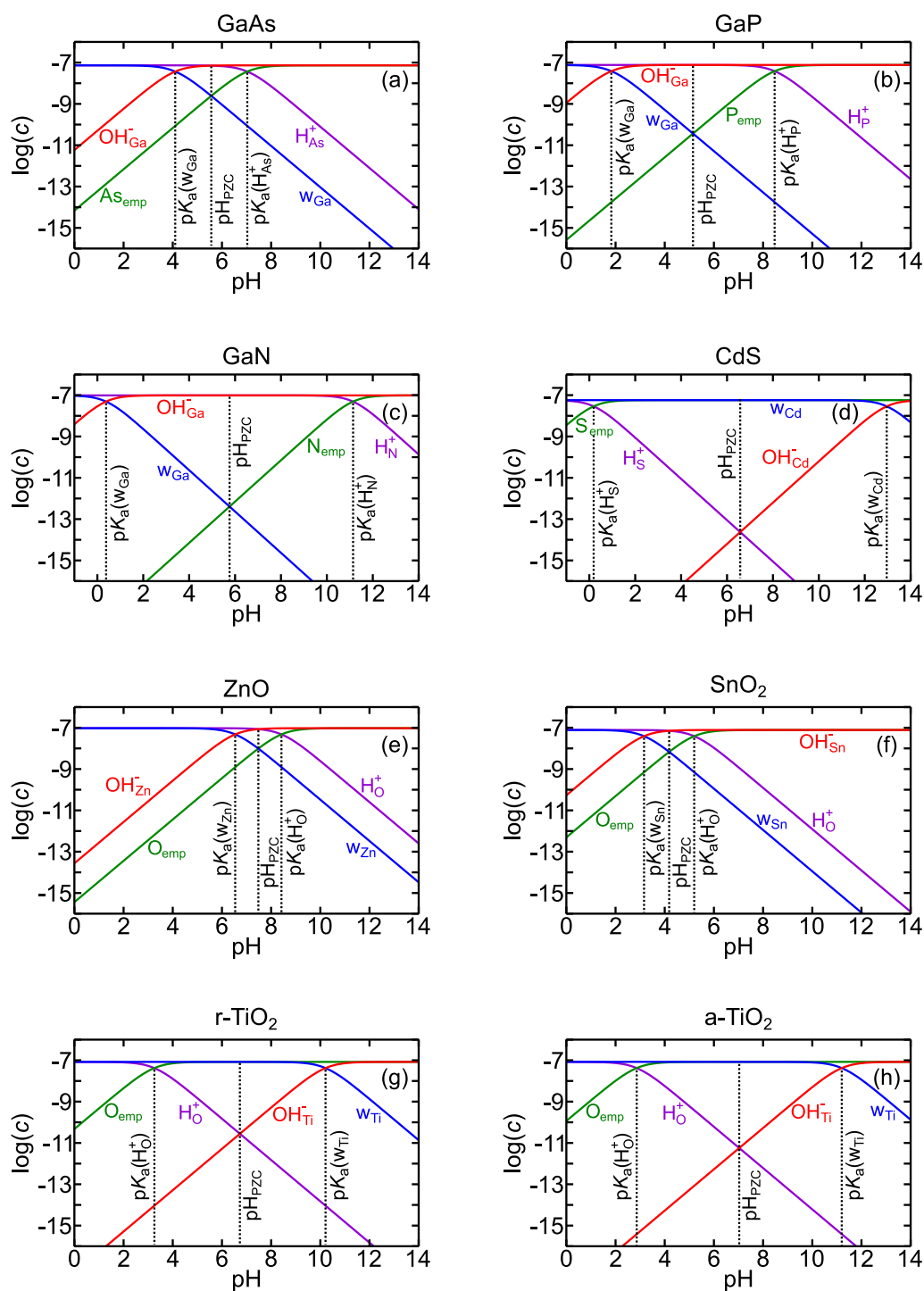


Figure 6.4 – Acid-base logarithmic diagrams for the coverages of (a) GaAs(110), (b) GaP(110), (c) GaN(10 $\bar{1}$ 0), (d) CdS(10 $\bar{1}$ 0), (e) ZnO(10 $\bar{1}$ 0), (f) SnO<sub>2</sub>(110), (g) r-TiO<sub>2</sub>(110), and (h) a-TiO<sub>2</sub>(101) surfaces in aqueous environment, as calculated at the hybrid rVV10 level. Concentrations are given in mol/dm<sup>2</sup>.

## Chapter 6. Evaluation of photocatalysts for water splitting through combined analysis of surface coverage and energy-level alignment

---

surface O sites is nevertheless lower than 2%. Hence, when using SnO<sub>2</sub> as a photocatalyst for the overall water splitting reaction, it would be preferable to operate in slightly acidic conditions, with a pH ranging between 3.2 and 5.2, for which protons and hydroxyl ions are the main adsorbates on the surface.

Finally, we focus on CdS, r-TiO<sub>2</sub> and a-TiO<sub>2</sub>, which favor the molecular adsorption mode throughout a large range of pH values. Among these semiconductors, the diagram for r-TiO<sub>2</sub> reported in Fig. 6.4(g) is discussed firstly as a representative example. In this case, H<sup>+</sup> and OH<sup>-</sup> ions are found in significative concentrations only at acidic and alkaline conditions, respectively. Such interfaces are not convenient for the operation of a photocatalytic water splitting device because the hydrogen evolution would be hindered by the absence of adsorbed protons in near-neutral conditions. Furthermore, the oxygen evolution reaction would occur through the slow mechanism associated with the dehydrogenation of water molecules [316], while the kinetically more favorable mechanism involving oxidation of adsorbed hydroxyl ions [316] would be inhibited. The latter tendency could be reversed only at highly alkaline values of pH, where one would however face the issue of surface degradation. The concentration diagrams for CdS [Fig. 6.4(d)] and a-TiO<sub>2</sub> [Fig. 6.4(h)] are similar to that of r-TiO<sub>2</sub>. For CdS, the concentration of ionic adsorbates at pH<sub>PZC</sub> is ~6 orders of magnitude lower than that of molecularly adsorbed water. This result is fully consistent with the outcome of previous MD simulations, in which the molecular adsorption mode was found to realize spontaneously [66]. The fraction of adsorbed protons and hydroxyl ions is negligible over the pH interval ranging from 1.2 to 12. Therefore, water oxidation can only proceed through the slow and kinetically unfavorable mechanism occurring under acidic conditions. Furthermore, the reduction of protons would be largely adsorption limited, suggesting that the pristine surface of CdS may be a poor photocatalyst. Selective oxygen evolution by oxidizing OH<sup>-</sup> ions or hydrogen reduction may only be achieved in extreme pH conditions. The hydroxylation of the surface only occurs for pH > 13, while the pH has to be lower than 0.2 to achieve protonation of the majority of the S sites. As far as a-TiO<sub>2</sub> is concerned, the concentrations of ionic species at pH<sub>PZC</sub> are at least 4 orders of magnitude lower than that of molecularly adsorbed water, revealing that the molecular model should be preferred to represent the real interfacial structures. In near-neutral pH conditions, the water oxidation reaction therefore proceeds through the slow and kinetically unfavorable reaction mechanism occurring under acidic conditions. For pH < 2, all surface O and Ti sites are passivated by protons and water molecules, respectively. In this case, a-TiO<sub>2</sub> can be used as photocatalyst for simultaneously reducing protons and oxidizing water molecules. At variance, for pH > 12, the hydroxyl ions are the dominant adsorbates and the water splitting reaction then proceeds through the reaction mechanism occurring under alkaline conditions [316].

### 6.6 Band alignment vs. pH

The adsorption of suitable reactants is surely a precondition for heterogeneous photocatalytic water splitting, but is not sufficient to ensure the efficiency of the process. In fact, a desirable



acid-base chemistry of the semiconductor-water interface must also rely on a favorable alignment between the electrochemical energy levels involved in the proton-coupled electron transfer reactions [305], namely the band edges of the semiconductors, which provide the charge carriers, and the redox levels associated with hydrogen reduction and water oxidation. By combining the band alignment at the semiconductor-water interface with the description of the surface chemistry, one can infer whether the photocatalytic reactions run efficiently [299]. Hence, for each semiconductor, we consider an energy level scheme that includes the band edges and the relevant redox levels. In particular, we consider the  $\text{H}^+/\text{H}_2$  redox level for the hydrogen evolution, the  $\text{H}_2\text{O}/\text{OH}^\bullet$  redox level for the dehydrogenation of the water molecule, and the  $\text{OH}^-/\text{OH}^\bullet$  redox level for the oxidation of the hydroxyl anion. The latter two energy levels represent the first step of the water oxidation process in acidic and alkaline conditions, respectively [316]. The dominating mechanism is expected to be dependent on the availability of the required adsorbates at the pH value of operation. In the ideal conditions considered in the present work, the band edges of the semiconductor and the  $\text{H}^+/\text{H}_2$  and  $\text{H}_2\text{O}/\text{OH}^\bullet$  redox levels follow a Nernstian behaviour, i.e. they move closer to the vacuum level with increasing pH at the rate of 0.059 eV per pH unit. At variance, the redox level of the  $\text{OH}^-/\text{OH}^\bullet$  couple does not depend on the pH of the solution, as this redox reaction does not imply any proton transfer.

All the energy levels are included in a pH-dependent energy diagram [Fig. 6.5]. We adopt the band edges as calculated in Ref. [66] and revised according to the improved estimate of the SHE level proposed in Ref. [220]. We assume the  $\text{H}^+/\text{H}_2$  redox level to correspond to the SHE level at pH = 0, thus neglecting possible catalytic effects at the semiconductor surfaces. For the oxidation of water molecules, the dehydrogenation reaction can be realized by two steps, involving sequentially the deprotonation of the water molecule and the oxidation of the hydroxyl ion. For the former, we use the free-energy difference calculated in this work, for the latter we consider the value achieved in Ref. [128] for the aqueous anion. Furthermore, the lines in the diagram corresponding to the  $\text{H}^+/\text{H}_2$ ,  $\text{H}_2\text{O}/\text{OH}^\bullet$ , and  $\text{OH}^-/\text{OH}^\bullet$  levels are drawn only in the range of pH values for which the concentrations of the involved species are non-negligible, corresponding to fractions of 10% or more.

First, we focus on III-V semiconductors. The energy diagram for GaN [Fig. 6.5(c)] immediately illustrates that the energy levels are all favorably aligned for the water-splitting reaction and that the reduction of protons and the oxidation of hydroxyl ions can take place simultaneously in a wide range of pH values [100]. However, the use of GaN as photocatalyst material is hindered, on the one hand, by its band gap of 3.4 eV, which is too large for efficient adsorption of visible light and, on the other hand, by the large energy difference between the  $\text{OH}^-/\text{OH}^\bullet$  level and the valence band edge, which lowers the rate of the reaction according to Marcus' theory [317]. In comparison, the other III-V semiconductors show a smaller band gap, but the alignment of the energy levels is found to worsen. In the case of GaAs [Fig. 6.5(a)] and GaP [Fig. 6.5(b)], the conduction band edge is favorably aligned with respect to the redox levels associated with the hydrogen reduction, but the valence band lies too high with respect to the redox levels associated with the first step of the water oxidation reaction. The conduction band

## Chapter 6. Evaluation of photocatalysts for water splitting through combined analysis of surface coverage and energy-level alignment

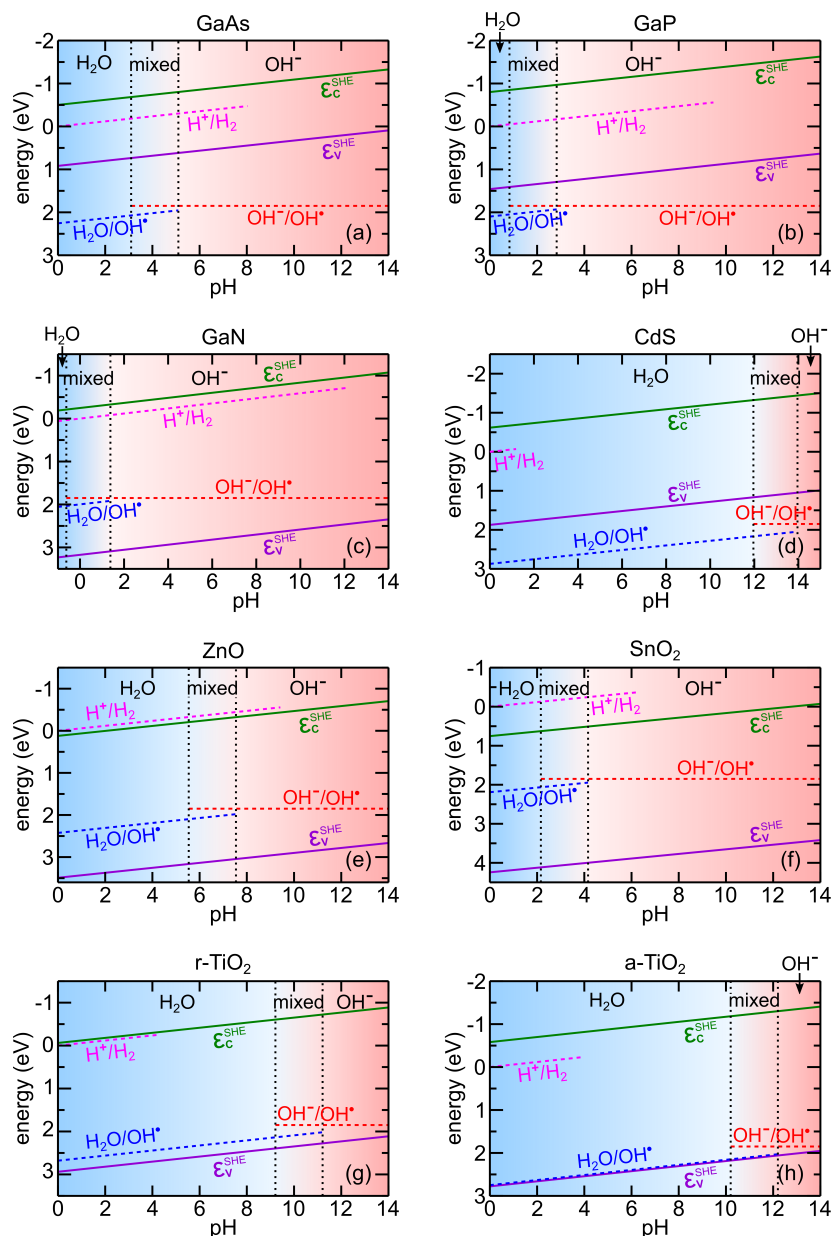


Figure 6.5 – Energy level diagram as a function of pH for (a) GaAs, (b) GaP, (c) GaN, (d) CdS, (e) ZnO, (f) SnO<sub>2</sub>, (g) r-TiO<sub>2</sub>, and (h) a-TiO<sub>2</sub> including the valence band edge ( $\epsilon_v^{SHE}$ , purple solid), the conduction band edge ( $\epsilon_c^{SHE}$ , green solid), and the relevant redox levels, namely those corresponding to the reduction of the protons ( $H^+/H_2$ , pink dashed), the dehydrogenation of the water molecule ( $H_2O/OH^*$ , blue dashed), and the oxidation of the hydroxyl ion ( $OH^-/OH^*$ , red dashed). All the levels are given versus the computational SHE, which is located at 0 eV at pH = 0. The vertical black dotted lines indicate the pH intervals where adsorbed water molecules and hydroxyl ions coexist. The dashed lines used for the redox levels illustrate the pH ranges, where more than 10% of the corresponding adsorbates can undergo the reaction.

of CdS lies higher than the  $H^+/H_2$  level by 0.62 eV, corresponding to a favorable alignment for the reduction of protons. However, the rather low  $pK_a$  for surface S sites prevents protons from being adsorbed unless the pH is lower than 1.2. Therefore, CdS can only be employed for  $H_2$  evolution in extremely acidic conditions. The valence band of CdS is unfavorably positioned by about 1.0 eV with respect to the  $H_2O/OH^\bullet$  redox level and by at least 0.68 eV with respect to  $OH^-/OH^\bullet$  redox level, making this material a poor photocatalyst for  $O_2$  evolution. For ZnO, the energy diagram [Fig. 6.5(e)] shows that the valence band edge is positioned similarly to the case of GaN, but the alignment of the energy levels for the hydrogen reduction reaction is worse. For  $SnO_2$  [Fig. 6.5(f)], the conduction band is much lower than the  $H^+/H_2$  level, making this material unsuitable for photocatalytic  $H_2$  evolution. The valence band of  $SnO_2$  is favorably positioned with respect to the redox levels, but the large energy separation is nevertheless expected to severely hamper the rate of the water oxidation reaction. Concerning r- $TiO_2$  [Fig. 6.5(g)], both the hydrogen reduction and the hydroxyl oxidation can be achieved due to the very favorable alignment of the energy levels. However, an all-in-one water splitting device based on r- $TiO_2$  would be possible only in acidic conditions with  $pH \leq 4.2$ , by which the oxygen oxidation would take place through the rather slow dehydrogenation of water molecules. For  $pH \geq 9$ , the more efficient oxygen oxidation reaction starting from  $OH^-$  adsorbates could be realized provided the semiconductor remains stable in such alkaline conditions. A similar band alignment is observed for a- $TiO_2$ , for which the conduction and the valence band are favorably positioned with respect to their respective redox levels. More specifically, our calculations indicate that the valence band edge lies within 0.03 eV from the  $H_2O/OH^\bullet$  level for a wide range of pH values, which is indeed a quite favorable condition for nonadiabatic charge transfer, and suggests that a- $TiO_2$  could be a promising photocatalyst for water oxidation. For pH values larger than 10, both water molecules and hydroxyl ions are adsorbed on the surface. Hence, both the mechanism pertaining to acidic conditions and the one pertaining to alkaline condition could be operative. MD simulations and  $pK_a$  calculations indicate that molecular water adsorption should prevail at pristine  $TiO_2$  surfaces in near-neutral conditions. However, experimental and theoretical studies have demonstrated that the appearance of surface defects, such as oxygen vacancies, might significantly promote the dissociation of adsorbed water on  $TiO_2$  surfaces [318, 319]. It remains therefore unclear whether the water oxidation reaction in near-neutral conditions proceeds through the majority water molecules or through the minority hydroxyl ions. Since the energy separation between the valence band edge and the  $OH^-/OH^\bullet$  level decreases with increasing pH, we expect that the more favorable mechanism involving the oxidation of hydroxyl ions should progressively become more significant. Hence, it is concluded that the efficiency of  $TiO_2$  as photocatalyst for the water oxidation reaction should improve in highly alkaline conditions.

We provide an overview of the photocatalytic potential of the semiconductors studied in this work by combining in Fig. 6.6 information concerning the surface coverage and the energy separation between the band edges and the relevant redox levels. For each adsorbate, the bars indicate the pH range where their coverage rate exceeds 10%. The color code refers to the alignment, with the blue (red) color specifying a favorable (unfavorable) level ordering. The

## Chapter 6. Evaluation of photocatalysts for water splitting through combined analysis of surface coverage and energy-level alignment

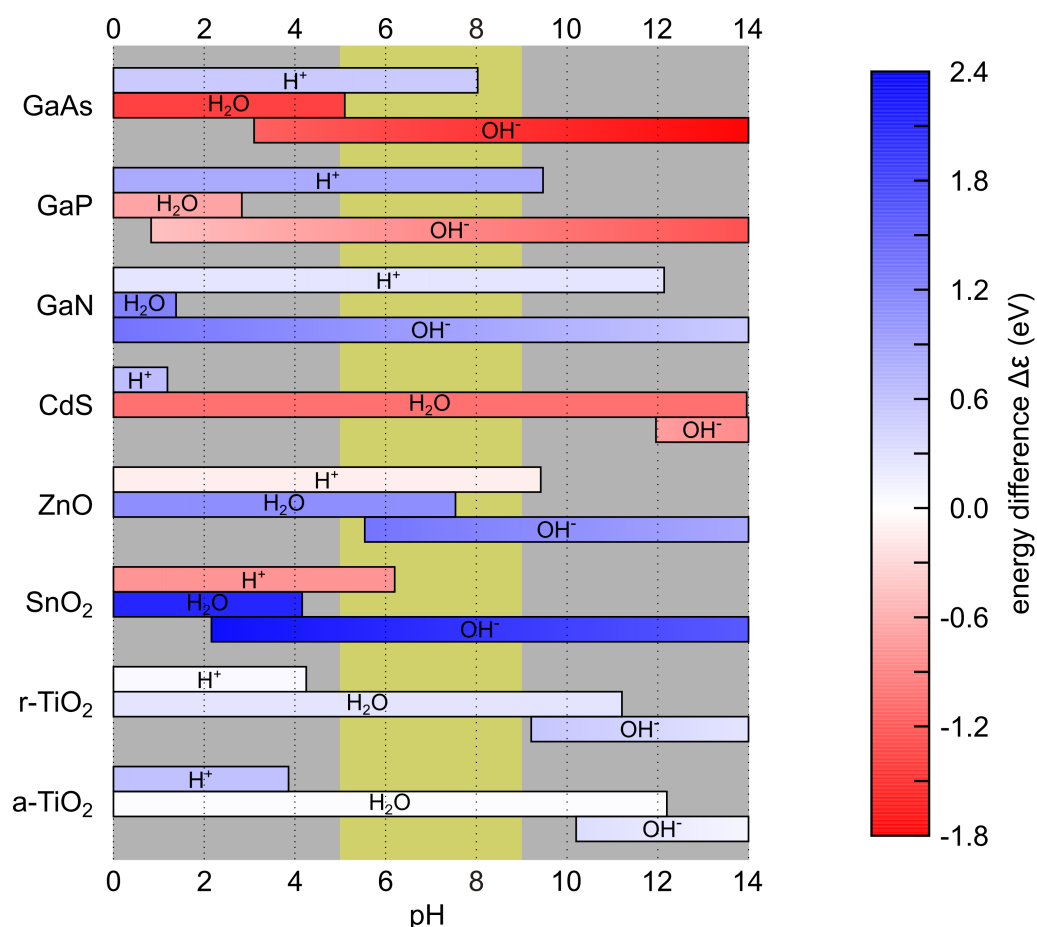


Figure 6.6 – Combined view on the surface coverage and alignment for the various semiconductors. For each adsorbate, the bars indicate the pH range where its surface coverage corresponds to a fraction of 10% or more. The energy separation ( $\Delta\epsilon$ ) between the band edges and the corresponding redox levels is given by a color code: the lighter the color used, the more favorable the alignment for the evolution of the reaction. For H<sup>+</sup>,  $\Delta\epsilon = \epsilon(\text{H}^+/\text{H}_2) - \epsilon_{\text{C}}^{\text{SHE}}$ . For H<sub>2</sub>O,  $\Delta\epsilon = \epsilon_{\text{V}}^{\text{SHE}} - \epsilon(\text{H}_2\text{O}/\text{OH}^{\bullet})$ . For OH<sup>-</sup>,  $\Delta\epsilon = \epsilon_{\text{V}}^{\text{SHE}} - \epsilon(\text{OH}^-/\text{OH}^{\bullet})$ . The vertical yellow stripe emphasizes near-neutral conditions with  $5 \leq \text{pH} \leq 9$ .

lighter the color, the closer the relevant energy levels and therefore the higher the reaction rate [317]. Focusing on the Ga-based semiconductors, one notices that the adsorbates are mostly ionic in near-neutral pH conditions, with the most favorable alignment encountered for GaN. CdS shows molecular adsorption over a very large pH range, with an unsuitable alignment. The coverage and the alignment for ZnO resemble those found for GaN, although a higher coverage rate of molecular water is seen in this case. For SnO<sub>2</sub>, there is a convenient pH range in which both protons and hydroxyls ions are found on the surface, but the redox level for the hydrogen evolution is unsuitably located with respect to the conduction band edge. In the case of the two polymorphs of TiO<sub>2</sub>, all the alignments are favorable, but there is no pH range in which protons and hydroxyl ions occur simultaneously on the surface.

## 6.7 Discussion and conclusion

The present results suggest that none of the materials studied here possesses at a given pH the desirable surface coverage and the ideal alignment of energy levels for the all-in-one reaction. Nevertheless, GaN shows several good properties and may represent a promising starting point for the design of new materials. Indeed, a few attempts have been made to design alloys based on GaN. Meng *et al.* [320] have used *ab initio* calculations to define the ideal fraction of In to be included in  $\text{In}_x\text{Ga}_{1-x}\text{N}$  alloys in order to tune the band gap and to achieve optimal alignment of the electrochemical energy levels. Similarly, Zn-doped GaN has been investigated with some success [321]. Our work suggests an alternative alloying strategy that could consist in partially substituting N with either As or P. In fact, the valence band edges of GaP and GaAs lie higher than in the case of GaN. Hence, a suitable concentration of P and As might push up the valence band of the alloyed GaN, bringing its edge in close correspondence with the redox levels, thereby kinetically favoring the course of the reaction. Our work shows that the acidity of the Ga surface sites only moderately varies among GaN, GaP, and GaAs. Furthermore, despite the slightly different acidity at the N, P, and As sites, their  $\text{p}K_a(\text{H}^+)$  values allow for a large fraction of protons to be adsorbed in near-neutral conditions.

Among the oxides, ZnO appears to be the most viable candidate. It is of interest to remark that N-doped ZnO [322] and GaN-ZnO alloys [323, 324, 325, 326, 327] have experimentally been found to possess enhanced photocatalytic properties compared to ZnO. This can be understood by the reduction of the band gap through an upwards shift of the valence band edge. Our results show that such a shift reduces the energy separation between the valence band edge and the  $\text{OH}^-/\text{OH}^\bullet$  redox level, thereby favoring the hole injection process [317].

As for  $\text{TiO}_2$ , the reaction rate remains unsatisfactory [328] and appears to be hindered by the low concentration of adsorbed ionic species in near-neutral conditions. The water dissociation due to active defect sites at the r- $\text{TiO}_2$  surface is apparently insufficient to make the reaction viable at sustained rates [329, 330, 319]. Furthermore, the design of new materials based on  $\text{TiO}_2$  seems to be more complicated than other cases, as it would require a substantial modification of the surface coverage without deteriorating the good alignment of the energy levels. In this context, N-doping has been extensively deployed for  $\text{TiO}_2$  with the motivation of simultaneously shifting the valence band closer to the  $\text{OH}^-/\text{OH}^\bullet$  level and inducing a higher surface coverage of ionic species [331, 332, 333, 334]. In an alternative approach, one could turn to nanoparticles of  $\text{TiO}_2$  which expose higher-energy surfaces [335, 336, 337, 338, 339, 340, 341, 342]. Such surfaces have been demonstrated to be more reactive and to favor electron-transfer processes in dye-sensitized solar cells [343], thus deserving a more in-depth investigation for water splitting.

In this thesis, the explicit dependence of the  $\text{p}K_a$  values on the pH of the solution has not been included in the analysis. The consideration of this effect will be the objective of future work.

To conclude, we have developed a theoretical tool for examining the suitability of semiconductor materials as photocatalysts of the water splitting reaction. For any value of pH, our analysis

## **Chapter 6. Evaluation of photocatalysts for water splitting through combined analysis of surface coverage and energy-level alignment**

---

informs us simultaneously about the kind of species adsorbed at the semiconductor-interface and the alignment of the band edges with respect to the relevant redox levels. These pieces of information represent invaluable descriptors for identifying the optimal photocatalyst in the high-throughput screening of candidate photocatalysts.

## 7 Conclusion

In this work, we first study the electronic properties of the oxygen vacancy and interstitial in am- $\text{Al}_2\text{O}_3$ . Hybrid functionals are adopted to overcome the significant underestimation of the band gap induced by the use of the PBE functional. In order to investigate the stability of each defect, we carry out an annealing process by running MD simulations for at least 3 ps with the temperature set at 1000 K or even higher. It is observed that oxygen vacancy and oxygen interstitial defects do not occur in am- $\text{Al}_2\text{O}_3$ , due to structural rearrangements which assimilate the defect structure and cause a delocalization of the associated defect levels. The imbalance of oxygen leads to a nonstoichiometric compound in which the oxygen occurs in the form of  $\text{O}^{2-}$  ions. Therefore, intrinsic oxygen defects are unable to trap excess electrons. However, extra holes can be captured in the amorphous structure through the formation of peroxy linkages, which correspond to a +2/0 defect level lying at 2.5 eV above the valence band of am- $\text{Al}_2\text{O}_3$  and may lead to the performance degradation of MOS devices when this level falls within the band gap of the channel semiconductor. Then, we present a procedure for investigating extrinsic defects in amorphous oxides, in which the most stable defect configurations are identified through *ab initio* molecular dynamics in various charge states. This protocol is further complemented with an electron counting scheme based on maximally localized Wannier functions, which allows one to identify the nominal charge state and the composition of the defect core unit. We apply this approach to the study of hydrogen, carbon, and nitrogen impurities in am- $\text{Al}_2\text{O}_3$ . Hydrogen is found to be amphoteric with a thermodynamic +1/−1 charge transition level lying at ~4.6 eV above the valence band maximum, in qualitative agreement with results obtained with crystalline models but at a substantially different energy level. Hydroxyl groups are further shown to lead to the same defect states as observed for hydrogen. Application of our procedure to carbon and nitrogen impurities leads to structural configurations that are found to depend on the total charge set in the simulation cell. Through the adopted electron counting rule, we assess that carbon and nitrogen impurities are only found in neutral and in singly positive charge states, respectively. This indicates that neither carbon nor nitrogen give charge transition levels in the band gap, in strong contrast with results achieved for crystalline models. In addition, the defect core units are shown to incorporate a varying number of oxygen atoms, by which their formation energy

depends on the oxygen chemical potential  $\mu_{\text{O}}$ . In oxygen poor conditions, both the carbon and the nitrogen impurity favor bonding to Al atoms, while they tend to form single or double bonds with oxygen atoms as  $\mu_{\text{O}}$  increases. Based on the band alignment of am- $\text{Al}_2\text{O}_3$  with three technologically relevant semiconductors (GaAs, GaN,  $\alpha$ - $\text{Fe}_2\text{O}_3$ ), we discuss the possible role of point defects in degrading the performance of electronic devices and in favoring hole transport across the oxide in water-splitting set-ups.

We also address the mechanism of hole diffusion across leaky am- $\text{TiO}_2$  layers. We construct an atomistic model of am- $\text{TiO}_2$  in accord with the experimental characterization through the melt-and-quench method. Like in am- $\text{Al}_2\text{O}_3$ , oxygen vacancies in am- $\text{TiO}_2$  are also found to disappear upon MD-induced structural relaxations. Hence, the role of this defect in hole diffusion is ruled out. By contrast, O-O peroxy linkages are observed to form in pristine am- $\text{TiO}_2$  upon injection of excess holes and to be robust against MD simulations. The associated +2/0 defect level locates at  $1.25 \pm 0.15$  eV above the valence band. Based on the finding that an O-O peroxy linkage can store two holes and that these holes are released when the O-O pair is broken, we propose an exchange mechanism for hole transport in am- $\text{TiO}_2$ , which relies on the simultaneous breaking and forming of O-O peroxy linkages that share one O atom. Using NEB calculations, we demonstrated a hopping path as long as 1.2 nm with barriers of 0.3-0.5 eV, suggesting that hole diffusion through O-O peroxy linkages is viable in am- $\text{TiO}_2$ .

Next, we develop a first-principles approach to determine the band alignment at various semiconductor-water interfaces by combining molecular dynamics (MD) simulations of atomistic interface models, electronic-structure calculations at the hybrid-functional and *GW* levels, and a computational standard hydrogen electrode. Eight semiconductors with different chemical compositions, structural properties and band gaps, namely GaAs, GaP, GaN, CdS, ZnO,  $\text{SnO}_2$ , rutile and anatase  $\text{TiO}_2$ , are selected to make a benchmark study. For each semiconductor, atomistic interface models with liquid water at the pH corresponding to the point of zero charge are obtained by performing MD simulations, which are started from two kinds of initial configurations, in which the water molecules are either molecularly (*m*) or dissociatively (*d*) adsorbed on the semiconductor surface, and continued until converged interfacial structures are achieved. But for GaAs, GaP, and a- $\text{TiO}_2$ , the interfacial structures were not found to converge towards a unique adsorption model within the time scale of our simulations, which lasted for at least 20 ps. This ambiguity arises from the slow kinetics of water dissociation/recombination processes at these semiconductor surfaces. The calculated band offsets are found to be strongly dependent on the adsorption mode at the semiconductor-water interface, giving differences larger than 1 eV between *m* and *d* models of the same semiconductor. Then, the accuracy of various ab initio electronic-structure schemes is assessed. The use of a standard hybrid functional leads to sizeable errors for the valence band edge but nevertheless accounts accurately for the position of the conduction band edge. One-shot *GW* calculations with a starting point at the semilocal density functional level yield quite inaccurate predictions for the position of the conduction band edge with respect to the SHE, with mean average errors (MAEs) up to 0.66 eV or larger. When turning to one-shot *GW* calculations based on a hybrid-functional starting point, an improvement of the overall



---

agreement with experiment is observed, with MAEs ranging between 0.33 and 0.51 eV. The use of state-of-the-art quasiparticle self-consistent *GW* schemes does not lead to any further improvement for the set of semiconductors under investigation. A noticeable improvement with the MAE of 0.17 eV is obtained when tuned hybrid-functionals are used, in which the experimental band gap of the semiconductor is enforced by construction. The present work sets a benchmark for the accuracy by which band edges at semiconductor-water interfaces can be obtained with current advanced electronic-structure methods.

Finally, we evaluate photocatalysts for water-splitting through the combined analysis of the surface coverage and energy-level alignment. We determine surface concentrations of water molecules, protons, and hydroxyl ions adsorbed at the interface with liquid water as a function of pH for a series of eight semiconductors, including GaAs, GaP, GaN, CdS, ZnO, SnO<sub>2</sub>, rutile TiO<sub>2</sub>, and anatase TiO<sub>2</sub>. This was achieved through the calculation of the acidity constants at surface sites, which are derived from *ab initio* molecular dynamics simulations and a grand-canonical formulation of adsorbates. The method is validated by the excellent agreement of the resulting pH values at the point of zero charge with experimental data. By combining our results for the surface coverage with the alignment of the band edges with respect to the relevant redox levels, we establish whether suitable pH conditions occur for hydrogen reduction, water oxidation, or for both reactions simultaneously. More specifically, we find that GaN and ZnO fulfill the conditions for the overall reaction, even though further improvement could be achieved by a closer level alignment. TiO<sub>2</sub> does not show ideal surface adsorbates for the overall reaction, but appears effective for hydrogen and oxygen evolution in acid and alkaline environments, respectively. In this way, our analysis allows us to discriminate among candidate photocatalysts through a characterization that is at present beyond experimental reach.



# A An appendix

<b>Abbreviation</b>	<b>Definition</b>
<b>ALD</b>	atomic layer deposition
<b>am-Al<sub>2</sub>O<sub>3</sub></b>	amorphous Al <sub>2</sub> O <sub>3</sub>
<b>am-TiO<sub>2</sub></b>	amorphous TiO <sub>2</sub>
<b>r-TiO<sub>2</sub></b>	rutile TiO <sub>2</sub>
<b>a-TiO<sub>2</sub></b>	anatase TiO <sub>2</sub>
<b>NEB</b>	nudged-elastic band
<b>DFT</b>	density functional theory
<b>XC</b>	exchange-correlation
<b>LDA</b>	local density approximation
<b>GGA</b>	generalized gradient approximation
<b>PBE</b>	Perdew, Burke, and Ernzerhof
<b>TI</b>	thermodynamic integration
<b>HF</b>	Hartree-Fock
<b>TC</b>	truncated Coulomb
<b>LRC</b>	long-range correction
<b>ADMM</b>	auxiliary density matrix method
<b>VBM</b>	valence band maximum
<b>CBM</b>	conduction band minimum
<b>PBC</b>	periodic boundary conditions
<b>FNV</b>	Freysoldt, Neugebauer, and Van deWalle
<b>MEP</b>	minimum energy path
<b>TS</b>	transition state
<b>SHE</b>	standard hydrogen electrode
<b>MD</b>	molecular dynamics
<b>MOS</b>	metal-oxide-semiconductor
<b>ALD</b>	atomic layer deposition
<b>RDF</b>	radial distribution functions
<b>DOS</b>	density of states
<b>IT</b>	improved tangent

## Appendix A. An appendix

---

<b>Abbreviation</b>	<b>Definition</b>
<b>MAE</b>	mean average error
<b>SOC</b>	spin-orbit coupling
<b>IP</b>	ionization potentials
<b>EA</b>	electron affinities
<b>ZPM</b>	zero point motion

## Bibliography

- [1] T. Kuwabara, T. Nakayama, K. Uozumi, T. Yamaguchi, and K. Takahashi, "Highly durable inverted-type organic solar cell using amorphous titanium oxide as electron collection electrode inserted between ITO and organic layer," *Sol. Energy Mater. Sol. Cells*, vol. 92, no. 11, pp. 1476 – 1482, 2008.
- [2] H. Chiang, J. Wager, R. Hoffman, J. Jeong, and D. A. Keszler, "High mobility transparent thin-film transistors with amorphous zinc tin oxide channel layer," *Appl. Phys. Lett.*, vol. 86, no. 1, p. 013503, 2005.
- [3] K. Nomura, H. Ohta, A. Takagi, T. Kamiya, M. Hirano, and H. Hosono, "Room-temperature fabrication of transparent flexible thin-film transistors using amorphous oxide semiconductors," *Nature*, vol. 432, no. 7016, p. 488, 2004.
- [4] D. Guyomard, C. Sigala, A. de Gal La Salle, and Y. Piffard, "New amorphous oxides as high capacity negative electrodes for lithium batteries: the  $\text{Li}_x\text{MVO}_4$  ( $\text{M} = \text{Ni}, \text{Co}, \text{Cd}, \text{Zn}; 1 < x \leq 8$ ) series," *J. Power Sources*, vol. 68, no. 2, pp. 692 – 697, 1997.
- [5] Y. Piffard, F. Leroux, D. Guyomard, J.-L. Mansot, and M. Tournoux, "The amorphous oxides  $\text{MnV}_2\text{O}_{6+\delta}$  ( $0 < \delta < 1$ ) as high capacity negative electrode materials for lithium batteries," *J. Power Sources*, vol. 68, no. 2, pp. 698 – 703, 1997.
- [6] A. Mehonic, M. Munde, W. Ng, M. Buckwell, L. Montesi, M. Bosman, A. Shluger, and A. Kenyon, "Intrinsic resistance switching in amorphous silicon oxide for high performance  $\text{SiO}_x$  ReRAM devices," *Microelectron. Eng.*, vol. 178, pp. 98 – 103, 2017.
- [7] M. Cho, J. H. Kim, C. S. Hwang, H.-S. Ahn, S. Han, and J. Y. Won, "Effects of carbon residue in atomic layer deposited  $\text{HfO}_2$  films on their time-dependent dielectric breakdown reliability," *Appl. Phys. Lett.*, vol. 90, no. 18, p. 182907, 2007.
- [8] K. Kukli, M. Ritala, M. Leskelä, and J. Jokinen, "Atomic layer epitaxy growth of aluminum oxide thin films from a novel  $\text{Al}(\text{CH}_3)_2\text{Cl}$  precursor and  $\text{H}_2\text{O}$ ," *J. Vac. Sci. Technol. A*, vol. 15, no. 4, pp. 2214–2218, 1997.
- [9] S. Lee and H. Jeon, "Characteristics of an  $\text{Al}_2\text{O}_3$  thin film deposited by a plasma enhanced atomic layer deposition method using  $\text{N}_2\text{O}$  plasma," *Electron. Mater. Lett.*, vol. 3, pp. 17–21, 2007.

## Bibliography

---

- [10] W. G. Lee, S. I. Woo, J. C. Kim, S. H. Choi, and K. H. Oh, "Preparation and properties of amorphous TiO<sub>2</sub> thin films by plasma enhanced chemical vapor deposition," *Thin Solid Films*, vol. 237, no. 1, pp. 105 – 111, 1994.
- [11] C. Wenger, M. Lukosius, I. Costina, R. Sorge, J. Dabrowski, H.-J. Müssig, S. Pasko, and C. Lohe, "Investigation of atomic vapour deposited TiN/HfO<sub>2</sub>/SiO<sub>2</sub> gate stacks for MOSFET devices," *Microelectron. Eng.*, vol. 85, no. 8, pp. 1762 – 1765, 2008.
- [12] C. Freysoldt, B. Grabowski, T. Hickel, J. Neugebauer, G. Kresse, A. Janotti, and C. G. Van de Walle, "First-principles calculations for point defects in solids," *Rev. Mod. Phys.*, vol. 86, pp. 253–305, Mar 2014.
- [13] H.-P. Komsa, T. T. Rantala, and A. Pasquarello, "Finite-size supercell correction schemes for charged defect calculations," *Phys. Rev. B*, vol. 86, p. 045112, Jul 2012.
- [14] J. Godet, P. Broqvist, and A. Pasquarello, "Hydrogen in Si(100)–SiO<sub>2</sub>–HfO<sub>2</sub> gate stacks: Relevant charge states and their location," *Appl. Phys. Lett.*, vol. 91, no. 26, p. 262901, 2007.
- [15] Z. Guo, F. Ambrosio, and A. Pasquarello, "Oxygen defects in amorphous Al<sub>2</sub>O<sub>3</sub>: A hybrid functional study," *Appl. Phys. Lett.*, vol. 109, no. 6, p. 062903, 2016.
- [16] P. Ye, G. Wilk, J. Kwo, B. Yang, H.-J. Gossmann, M. Frei, S. Chu, J. Mannaerts, M. Sergent, M. Hong, K. Ng, and J. Bude, "GaAs MOSFET with oxide gate dielectric grown by atomic layer deposition," *IEEE Electron Device Lett.*, vol. 24, pp. 209–211, April 2003.
- [17] P. D. Ye, B. Yang, K. K. Ng, J. Bude, G. D. Wilk, S. Halder, and J. C. M. Hwang, "GaN metal-oxide-semiconductor high-electron-mobility-transistor with atomic layer deposited Al<sub>2</sub>O<sub>3</sub> as gate dielectric," *Appl. Phys. Lett.*, vol. 86, no. 6, p. 063501, 2005.
- [18] H. Zhao, D. Shahrjerdi, F. Zhu, M. Zhang, H.-S. Kim, I. OK, J. H. Yum, S. I. Park, S. K. Banerjee, and J. C. Lee, "Gate-first inversion-type InP metal-oxide-semiconductor field-effect transistors with atomic-layer-deposited Al<sub>2</sub>O<sub>3</sub> gate dielectric," *Appl. Phys. Lett.*, vol. 92, no. 23, p. 233508, 2008.
- [19] Y. Xuan, Y. Wu, H. Lin, T. Shen, and P. Ye, "Submicrometer Inversion-Type Enhancement-Mode InGaAs MOSFET With Atomic-Layer-Deposited Al<sub>2</sub>O<sub>3</sub> as Gate Dielectric," *IEEE Electron Device Lett.*, vol. 28, pp. 935–938, Nov 2007.
- [20] P. Kordoš, D. Gregušová, R. Stoklas, K. Čičo, and J. Novák, "Improved transport properties of Al<sub>2</sub>O<sub>3</sub>/AlGaIn/GaN metal-oxide-semiconductor heterostructure field-effect transistor," *Appl. Phys. Lett.*, vol. 90, no. 12, p. 123513, 2007.
- [21] X. Zhang, I. Belharouak, L. Li, Y. Lei, J. W. Elam, A. Nie, X. Chen, R. S. Yassar, and R. L. Axelbaum, "Structural and electrochemical study of Al<sub>2</sub>O<sub>3</sub> and TiO<sub>2</sub> coated Li<sub>1.2</sub>Ni<sub>0.13</sub>Mn<sub>0.54</sub>Co<sub>0.13</sub>O<sub>2</sub> cathode material using ALD," *Adv. Energy Mater.*, vol. 3, no. 10, pp. 1299–1307, 2013.

- [22] J. W. Kim, D. H. Kim, D. Y. Oh, H. Lee, J. H. Kim, J. H. Lee, and Y. S. Jung, "Surface chemistry of  $\text{LiNi}_{0.5}\text{Mn}_{1.5}\text{O}_4$  particles coated by  $\text{Al}_2\text{O}_3$  using atomic layer deposition for lithium-ion batteries," *J. Power Sources*, vol. 274, pp. 1254–1262, 2015.
- [23] J.-T. Lee, F.-M. Wang, C.-S. Cheng, C.-C. Li, and C.-H. Lin, "Low-temperature atomic layer deposited  $\text{Al}_2\text{O}_3$  thin film on layer structure cathode for enhanced cycleability in lithium-ion batteries," *Electrochim. Acta*, vol. 55, no. 12, pp. 4002–4006, 2010.
- [24] F. Le Formal, N. Tetreault, M. Cornuz, T. Moehl, M. Gratzel, and K. Sivula, "Passivating surface states on water splitting hematite photoanodes with alumina overlayers," *Chem. Sci.*, vol. 2, pp. 737–743, 2011.
- [25] Y. Chang, F. Ducroquet, E. Gautier, O. Renault, J. Legrand, J. Damlencourt, and F. Martin, "Surface preparation and post thermal treatment effects on interface properties of thin  $\text{Al}_2\text{O}_3$  films deposited by ALD," *Microelectron. Eng.*, vol. 72, no. 1-4, pp. 326–331, 2004.
- [26] H. Lin, P. Ye, and G. Wilk, "Current-transport properties of atomic-layer-deposited ultrathin  $\text{Al}_2\text{O}_3$  on GaAs," *Solid-State Electron.*, vol. 50, no. 6, pp. 1012–1015, 2006.
- [27] B. Shin, D. Choi, J. S. Harris, and P. C. McIntyre, "Pre-atomic layer deposition surface cleaning and chemical passivation of (100)  $\text{In}_{0.2}\text{Ga}_{0.8}\text{As}$  and deposition of ultrathin  $\text{Al}_2\text{O}_3$  gate insulators," *Appl. Phys. Lett.*, vol. 93, no. 5, p. 052911, 2008.
- [28] R. L. Puurunen, "Surface chemistry of atomic layer deposition: A case study for the trimethylaluminum/water process," *J. Appl. Phys.*, vol. 97, no. 12, p. 9, 2005.
- [29] M. J. Young, C. B. Musgrave, and S. M. George, "Growth and Characterization of  $\text{Al}_2\text{O}_3$  Atomic Layer Deposition Films on sp<sup>2</sup>-Graphitic Carbon Substrates Using  $\text{NO}_2$ /Trimethylaluminum Pretreatment," *ACS Appl. Mater. Interfaces*, vol. 7, no. 22, pp. 12030–12037, 2015.
- [30] M. Groner, F. Fabreguette, J. Elam, and S. George, "Low-temperature  $\text{Al}_2\text{O}_3$  atomic layer deposition," *Chem. Mater.*, vol. 16, no. 4, pp. 639–645, 2004.
- [31] T. V. Perevalov, O. E. Tereshenko, V. A. Gritsenko, V. A. Pustovarov, A. P. Yelisseyev, C. Park, J. H. Han, and C. Lee, "Oxygen deficiency defects in amorphous  $\text{Al}_2\text{O}_3$ ," *J. Appl. Phys.*, vol. 108, no. 1, p. 013501, 2010.
- [32] C. Århammar, A. Pietzsch, N. Bock, E. Holmström, C. M. Araujo, J. Gråsjö, S. Zhao, S. Green, T. Peery, F. Hennies, S. Amerioun, A. Föhlisch, J. Schlappa, T. Schmitt, V. N. Strocov, G. A. Niklasson, D. C. Wallace, J.-E. Rubensson, B. Johansson, and R. Ahuja, "Unveiling the complex electronic structure of amorphous metal oxides," *Proc. Natl. Acad. Sci. U.S.A.*, vol. 108, no. 16, pp. 6355–6360, 2011.
- [33] M. L. Huang, Y. C. Chang, C. H. Chang, T. D. Lin, J. Kwo, T. B. Wu, and M. Hong, "Energy-band parameters of atomic-layer-deposition  $\text{Al}_2\text{O}_3$ /InGaAs heterostructure," *Appl. Phys. Lett.*, vol. 89, no. 1, p. 012903, 2006.

## Bibliography

---

- [34] J. Ahn, I. Geppert, M. Gunji, M. Holland, I. Thayne, M. Eizenberg, and P. C. McIntyre, "Titania/alumina bilayer gate insulators for InGaAs metal-oxide-semiconductor devices," *Appl. Phys. Lett.*, vol. 99, no. 23, p. 232902, 2011.
- [35] I. Krylov, D. Ritter, and M. Eizenberg, "The physical origin of dispersion in accumulation in InGaAs based metal oxide semiconductor gate stacks," *J. Appl. Phys.*, vol. 117, no. 17, p. 174501, 2015.
- [36] M. Choi, A. Janotti, and C. G. Van de Walle, "Native point defects and dangling bonds in  $\alpha$ -Al<sub>2</sub>O<sub>3</sub>," *J. Appl. Phys.*, vol. 113, no. 4, p. 044501, 2013.
- [37] M. Choi, J. L. Lyons, A. Janotti, and C. G. Van de Walle, "Impact of native defects in high-k dielectric oxides on GaN/oxide metal-oxide-semiconductor devices," *Phys. Status Solidi B*, vol. 250, no. 4, pp. 787–791, 2013.
- [38] M. Choi, J. L. Lyons, A. Janotti, and C. G. Van de Walle, "Impact of carbon and nitrogen impurities in high-k dielectrics on metal-oxide-semiconductor devices," *Appl. Phys. Lett.*, vol. 102, no. 14, p. 142902, 2013.
- [39] L. Gordon, H. Abu-Farsakh, A. Janotti, and C. G. Van de Walle, "Hydrogen bonds in Al<sub>2</sub>O<sub>3</sub> as dissipative two-level systems in superconducting qubits," *Sci. Rep.*, vol. 4, p. 07590, 2014.
- [40] J. Weber, A. Janotti, and C. V. de Walle, "Point defects in Al<sub>2</sub>O<sub>3</sub> and their impact on gate stacks," *Microelectron. Eng.*, vol. 86, no. 7-9, pp. 1756–1759, 2009.
- [41] J. R. Weber, A. Janotti, and C. G. Van de Walle, "Native defects in Al<sub>2</sub>O<sub>3</sub> and their impact on III-V/Al<sub>2</sub>O<sub>3</sub> metal-oxide-semiconductor-based devices," *J. Appl. Phys.*, vol. 109, no. 3, p. 033715, 2011.
- [42] H. Li and J. Robertson, "Behaviour of hydrogen in wide band gap oxides," *J. Appl. Phys.*, vol. 115, no. 20, p. 203708, 2014.
- [43] D. Liu, S. J. Clark, and J. Robertson, "Oxygen vacancy levels and electron transport in Al<sub>2</sub>O<sub>3</sub>," *Appl. Phys. Lett.*, vol. 96, no. 3, p. 032905, 2010.
- [44] D. Liu, Y. Guo, L. Lin, and J. Robertson, "First-principles calculations of the electronic structure and defects of Al<sub>2</sub>O<sub>3</sub>," *J. Appl. Phys.*, vol. 114, no. 8, p. 083704, 2013.
- [45] K. Xiong, J. Robertson, and S. J. Clark, "Behavior of hydrogen in wide band gap oxides," *J. Appl. Phys.*, vol. 102, no. 8, p. 083710, 2007.
- [46] J. Carrasco, J. R. B. Gomes, and F. Illas, "Theoretical study of bulk and surface oxygen and aluminum vacancies in  $\alpha$ -Al<sub>2</sub>O<sub>3</sub>," *Phys. Rev. B*, vol. 69, p. 064116, Feb 2004.
- [47] F. Janetzko, R. A. Evarestov, T. Bredow, and K. Jug, "First-principles periodic and semiempirical cyclic cluster calculations for single oxygen vacancies in crystalline Al<sub>2</sub>O<sub>3</sub>," *Phys. Status Solidi B*, vol. 241, no. 5, pp. 1032–1040, 2004.



- [48] K. Matsunaga, T. Tanaka, T. Yamamoto, and Y. Ikuhara, "First-principles calculations of intrinsic defects in  $\text{Al}_2\text{O}_3$ ," *Phys. Rev. B*, vol. 68, p. 085110, Aug 2003.
- [49] H. Momida, S. Nigo, G. Kido, and T. Ohno, "Effect of vacancy-type oxygen deficiency on electronic structure in amorphous alumina," *Appl. Phys. Lett.*, vol. 98, no. 4, p. 042102, 2011.
- [50] B. Shin, J. R. Weber, R. D. Long, P. K. Hurley, C. G. Van de Walle, and P. C. McIntyre, "Origin and passivation of fixed charge in atomic layer deposited aluminum oxide gate insulators on chemically treated InGaAs substrates," *Appl. Phys. Lett.*, vol. 96, no. 15, 2010.
- [51] A. M. Holder, K. D. Osborn, C. J. Lobb, and C. B. Musgrave, "Bulk and Surface Tunneling Hydrogen Defects in Alumina," *Phys. Rev. Lett.*, vol. 111, p. 065901, Aug 2013.
- [52] D. Colleoni, G. Miceli, and A. Pasquarello, "Band alignment and chemical bonding at the GaAs/ $\text{Al}_2\text{O}_3$  interface: A hybrid functional study," *Appl. Phys. Lett.*, vol. 107, no. 21, p. 211601, 2015.
- [53] B. O'Regan and M. Grätzel, "A low-cost, high-efficiency solar cell based on dye-sensitized colloidal  $\text{TiO}_2$  films," *Nature*, vol. 353, no. 6346, p. 737, 1991.
- [54] D. V. Bavykin, A. A. Lapkin, P. K. Plucinski, J. M. Friedrich, and F. C. Walsh, "Reversible Storage of Molecular Hydrogen by Sorption into Multilayered  $\text{TiO}_2$  Nanotubes," *J. Phys. Chem. B*, vol. 109, no. 41, pp. 19422–19427, 2005.
- [55] A. Fujishima and K. Honda, "Electrochemical photolysis of water at a semiconductor electrode," *Nature*, vol. 238, pp. 37–38, 1972.
- [56] C. Garzella, E. Comini, E. Tempesti, C. Frigeri, and G. Sberveglieri, " $\text{TiO}_2$  thin films by a novel sol-gel processing for gas sensor applications," *Sens. Actuators B*, vol. 68, no. 1, pp. 189–196, 2000.
- [57] B. J. Morgan and G. W. Watson, "Polaronic trapping of electrons and holes by native defects in anatase  $\text{TiO}_2$ ," *Phys. Rev. B*, vol. 80, p. 233102, Dec 2009.
- [58] M. Landmann, E. Rauls, and W. G. Schmidt, "The electronic structure and optical response of rutile, anatase and brookite  $\text{TiO}_2$ ," *J. Phys.: Condens. Matter*, vol. 24, no. 19, p. 195503, 2012.
- [59] C. Di Valentin, G. Pacchioni, and A. Selloni, "Origin of the different photoactivity of N-doped anatase and rutile  $\text{TiO}_2$ ," *Phys. Rev. B*, vol. 70, p. 085116, Aug 2004.
- [60] B. J. Morgan and G. W. Watson, "Intrinsic n-type Defect Formation in  $\text{TiO}_2$ : A Comparison of Rutile and Anatase from GGA+U Calculations," *J. Phys. Chem. C*, vol. 114, no. 5, pp. 2321–2328, 2010.

## Bibliography

---

- [61] N. A. Deskins, R. Rousseau, and M. Dupuis, "Localized Electronic States from Surface Hydroxyls and Polarons in TiO<sub>2</sub>(110)," *J. Phys. Chem. C*, vol. 113, no. 33, pp. 14583–14586, 2009.
- [62] F. Ambrosio, N. Martsinovich, and A. Troisi, "What Is the Best Anchoring Group for a Dye in a Dye-Sensitized Solar Cell?," *J. Phys. Chem. Lett.*, vol. 3, no. 11, pp. 1531–1535, 2012.
- [63] C. M. Ip and A. Troisi, "A computational study of the competing reaction mechanisms of the photo-catalytic reduction of CO<sub>2</sub> on anatase(101)," *Phys. Chem. Chem. Phys.*, vol. 18, pp. 25010–25021, 2016.
- [64] J. Cheng and M. Sprik, "Acidity of the Aqueous Rutile TiO<sub>2</sub>(110) Surface from Density Functional Theory Based Molecular Dynamics," *J. Chem. Theory Comput.*, vol. 6, no. 3, pp. 880–889, 2010.
- [65] H. Hussain, G. Tocci, T. Woolcot, X. Torrelles, C. Pang, D. Humphrey, C. Yim, D. Grinter, G. Cabailh, O. Bikondoa, *et al.*, "Structure of a model TiO<sub>2</sub> photocatalytic interface," *Nat. Mater.*, vol. 16, no. 4, p. 461, 2017.
- [66] Z. Guo, F. Ambrosio, W. Chen, P. Gono, and A. Pasquarello, "Alignment of Redox Levels at Semiconductor-Water Interfaces," *Chem. Mater.*, vol. 30, no. 1, pp. 94–111, 2018.
- [67] H. Y. Jeong, J. Y. Lee, and S.-Y. Choi, "Interface-Engineered Amorphous TiO<sub>2</sub>-Based Resistive Memory Devices," *Adv. Funct. Mater.*, vol. 20, no. 22, pp. 3912–3917, 2010.
- [68] D. Muñoz-Rojas, H. Sun, D. C. Iza, J. Weickert, L. Chen, H. Wang, L. Schmidt-Mende, and J. L. MacManus-Driscoll, "High-speed atmospheric atomic layer deposition of ultra thin amorphous TiO<sub>2</sub> blocking layers at 100° C for inverted bulk heterojunction solar cells," *Prog. Photovoltaics*, vol. 21, no. 4, pp. 393–400, 2013.
- [69] K. Ozasa, S. Nemoto, M. Hara, M. Maeda, and K. Mochitate, "The passivation/modification of AlGaAs/GaAs surfaces by amorphous TiO<sub>2</sub> for the bio-sensing use in electrolytes," *Surf. Sci.*, vol. 601, no. 18, pp. 4536–4540, 2007.
- [70] S. Hu, M. R. Shaner, J. A. Beardlee, M. Lichterman, B. S. Brunshwig, and N. S. Lewis, "Amorphous TiO<sub>2</sub> coatings stabilize Si, GaAs, and GaP photoanodes for efficient water oxidation," *Science*, vol. 344, no. 6187, pp. 1005–1009, 2014.
- [71] M. G. Ahmed, I. E. Kretschmer, T. A. Kandiel, A. Y. Ahmed, F. A. Rashwan, and D. W. Bahnemann, "A Facile Surface Passivation of Hematite Photoanodes with TiO<sub>2</sub> Overlayers for Efficient Solar Water Splitting," *ACS Appl. Mater. Interfaces*, vol. 7, no. 43, pp. 24053–24062, 2015.
- [72] W. Niu, X. Li, S. K. Karuturi, D. W. Fam, H. Fan, S. Shrestha, L. H. Wong, and A. I. Y. Tok, "Applications of atomic layer deposition in solar cells," *Nanotechnology*, vol. 26, no. 6, p. 064001, 2015.

- [73] M. T. McDowell, M. F. Lichterman, A. I. Carim, R. Liu, S. Hu, B. S. Brunschwig, and N. S. Lewis, "The Influence of Structure and Processing on the Behavior of TiO<sub>2</sub> Protective Layers for Stabilization of n-Si/TiO<sub>2</sub>/Ni Photoanodes for Water Oxidation," *ACS Appl. Mater. Interfaces*, vol. 7, no. 28, pp. 15189–15199, 2015.
- [74] J. Gu, Y. Yan, J. L. Young, K. X. Steirer, N. R. Neale, and J. A. Turner, "Water reduction by a p-GaInP<sub>2</sub> photoelectrode stabilized by an amorphous TiO<sub>2</sub> coating and a molecular cobalt catalyst," *Nat. Mater.*, vol. 15, no. 4, p. 456, 2016.
- [75] A. C. Bronneberg, C. Höhn, and R. van de Krol, "Probing the Interfacial Chemistry of Ultrathin ALD-Grown TiO<sub>2</sub> Films: An In-Line XPS Study," *J. Phys. Chem. C*, vol. 121, no. 10, pp. 5531–5538, 2017.
- [76] H. H. Pham and L.-W. Wang, "Oxygen vacancy and hole conduction in amorphous TiO<sub>2</sub>," *Phys. Chem. Chem. Phys.*, vol. 17, pp. 541–550, 2015.
- [77] H. H. Pham and L.-W. Wang, "Electronic structures and current conductivities of B, C, N and F defects in amorphous titanium dioxide," *Phys. Chem. Chem. Phys.*, vol. 17, no. 17, pp. 11908–11913, 2015.
- [78] K. K. Ghuman and C. V. Singh, "Self-Trapped Charge Carriers in Defected Amorphous TiO<sub>2</sub>," *J. Phys. Chem. C*, vol. 120, no. 49, pp. 27910–27916, 2016.
- [79] S. U. M. Khan, M. Al-Shahry, and W. B. Ingler, "Efficient Photochemical Water Splitting by a Chemically Modified n-TiO<sub>2</sub>," *Science*, vol. 297, no. 5590, pp. 2243–2245, 2002.
- [80] A. Kudo and Y. Miseki, "Heterogeneous photocatalyst materials for water splitting," *Chem. Soc. Rev.*, vol. 38, pp. 253–278, 2009.
- [81] M. G. Walter, E. L. Warren, J. R. McKone, S. W. Boettcher, Q. Mi, E. A. Santori, and N. S. Lewis, "Solar Water Splitting Cells," *Chem. Rev.*, vol. 110, no. 11, pp. 6446–6473, 2010.
- [82] J. Liu, Y. Liu, N. Liu, Y. Han, X. Zhang, H. Huang, Y. Lifshitz, S.-T. Lee, J. Zhong, and Z. Kang, "Metal-free efficient photocatalyst for stable visible water splitting via a two-electron pathway," *Science*, vol. 347, no. 6225, pp. 970–974, 2015.
- [83] J. Luo, J.-H. Im, M. T. Mayer, M. Schreier, M. K. Nazeeruddin, N.-G. Park, S. D. Tilley, H. J. Fan, and M. Grätzel, "Water photolysis at 12.3% efficiency via perovskite photovoltaics and Earth-abundant catalysts," *Science*, vol. 345, no. 6204, pp. 1593–1596, 2014.
- [84] K. Maeda and K. Domen, "Photocatalytic Water Splitting: Recent Progress and Future Challenges," *J. Phys. Chem. Lett.*, vol. 1, no. 18, pp. 2655–2661, 2010.
- [85] K. Maeda and K. Domen, "New Non-Oxide Photocatalysts Designed for Overall Water Splitting under Visible Light," *J. Phys. Chem. C*, vol. 111, no. 22, pp. 7851–7861, 2007.

## Bibliography

---

- [86] I. E. Castelli, T. Olsen, S. Datta, D. D. Landis, S. Dahl, K. S. Thygesen, and K. W. Jacobsen, "Computational screening of perovskite metal oxides for optimal solar light capture," *Energy Environ. Sci.*, vol. 5, pp. 5814–5819, 2012.
- [87] I. E. Castelli, D. D. Landis, K. S. Thygesen, S. Dahl, I. Chorkendorff, T. F. Jaramillo, and K. W. Jacobsen, "New cubic perovskites for one- and two-photon water splitting using the computational materials repository," *Energy Environ. Sci.*, vol. 5, pp. 9034–9043, 2012.
- [88] H. L. Zhuang and R. G. Hennig, "Single-Layer Group-III Monochalcogenide Photocatalysts for Water Splitting," *Chem. Mater.*, vol. 25, no. 15, pp. 3232–3238, 2013.
- [89] Y. Wu, P. Lazic, G. Hautier, K. Persson, and G. Ceder, "First principles high throughput screening of oxynitrides for water-splitting photocatalysts," *Energy Environ. Sci.*, vol. 6, pp. 157–168, 2013.
- [90] J. E. Katz, T. R. Gingrich, E. A. Santori, and N. S. Lewis, "Combinatorial synthesis and high-throughput photopotential and photocurrent screening of mixed-metal oxides for photoelectrochemical water splitting," *Energy Environ. Sci.*, vol. 2, pp. 103–112, 2009.
- [91] A. J. Cohen, P. Mori-Sánchez, and W. Yang, "Challenges for density functional theory," *Chem. Rev.*, vol. 112, no. 1, pp. 289–320, 2012.
- [92] M. Marsman, J. Paier, A. Stroppa, and G. Kresse, "Hybrid functionals applied to extended systems," *J. Phys.: Condens. Matter*, vol. 20, no. 6, p. 064201, 2008.
- [93] W. Chen and A. Pasquarello, "Band-edge positions in *GW*: Effects of starting point and self-consistency," *Phys. Rev. B*, vol. 90, p. 165133, Oct 2014.
- [94] W. Chen and A. Pasquarello, "Accurate band gaps of extended systems via efficient vertex corrections in *GW*," *Phys. Rev. B*, vol. 92, p. 041115, Jul 2015.
- [95] N. Kharche, M. S. Hybertsen, and J. T. Muckerman, "Computational investigation of structural and electronic properties of aqueous interfaces of GaN, ZnO, and a GaN/ZnO alloy," *Phys. Chem. Chem. Phys.*, vol. 16, pp. 12057–12066, 2014.
- [96] N. Kharche, J. T. Muckerman, and M. S. Hybertsen, "First-Principles Approach to Calculating Energy Level Alignment at Aqueous Semiconductor Interfaces," *Phys. Rev. Lett.*, vol. 113, p. 176802, Oct 2014.
- [97] X. Li, J. Yu, J. Low, Y. Fang, J. Xiao, and X. Chen, "Engineering heterogeneous semiconductors for solar water splitting," *J. Mater. Chem. A*, vol. 3, pp. 2485–2534, 2015.
- [98] V. Stevanović, S. Lany, D. S. Ginley, W. Tumas, and A. Zunger, "Assessing capability of semiconductors to split water using ionization potentials and electron affinities only," *Phys. Chem. Chem. Phys.*, vol. 16, pp. 3706–3714, 2014.

- [99] J. Cheng and M. Sprik, "Aligning electronic energy levels at the TiO<sub>2</sub>/H<sub>2</sub>O interface," *Phys. Rev. B*, vol. 82, p. 081406, Aug 2010.
- [100] Y. Wu, M. K. Y. Chan, and G. Ceder, "Prediction of semiconductor band edge positions in aqueous environments from first principles," *Phys. Rev. B*, vol. 83, p. 235301, Jun 2011.
- [101] J. Cheng and M. Sprik, "Alignment of electronic energy levels at electrochemical interfaces," *Phys. Chem. Chem. Phys.*, vol. 14, pp. 11245–11267, 2012.
- [102] C. G. Van de Walle and J. Neugebauer, "Universal alignment of hydrogen levels in semiconductors, insulators and solutions," *Nature*, vol. 423, no. 6940, pp. 626–628, 2003.
- [103] I. E. Castelli, J. M. García-Lastra, F. Hüser, K. S. Thygesen, and K. W. Jacobsen, "Stability and bandgaps of layered perovskites for one- and two-photon water splitting," *New J. Phys.*, vol. 15, no. 10, p. 105026, 2013.
- [104] Y. Ping, R. Sundararaman, and W. A. Goddard III, "Solvation effects on the band edge positions of photocatalysts from first principles," *Phys. Chem. Chem. Phys.*, vol. 17, pp. 30499–30509, 2015.
- [105] T. A. Pham, D. Lee, E. Schwegler, and G. Galli, "Interfacial Effects on the Band Edges of Functionalized Si Surfaces in Liquid Water," *J. Am. Chem. Soc.*, vol. 136, no. 49, pp. 17071–17077, 2014.
- [106] M. Govoni and G. Galli, "Large Scale GW Calculations," *J. Chem. Theory Comput.*, vol. 11, no. 6, pp. 2680–2696, 2015.
- [107] P. Hohenberg and W. Kohn, "Inhomogeneous electron gas," *Phys. Rev.*, vol. 136, no. 3B, p. B864, 1964.
- [108] W. Kohn and L. J. Sham, "Self-consistent equations including exchange and correlation effects," *Phys. Rev.*, vol. 140, no. 4A, p. A1133, 1965.
- [109] J. P. Perdew, K. Burke, and M. Ernzerhof, "Generalized gradient approximation made simple," *Phys. Rev. Lett.*, vol. 77, no. 18, p. 3865, 1996.
- [110] P. Mori-Sánchez, A. J. Cohen, and W. Yang, "Localization and delocalization errors in density functional theory and implications for band-gap prediction," *Phys. Rev. Lett.*, vol. 100, no. 14, p. 146401, 2008.
- [111] A. D. Becke, "A new mixing of Hartree-Fock and local density-functional theories," *J. Chem. Phys.*, vol. 98, no. 2, pp. 1372–1377, 1993.
- [112] J. P. Perdew, M. Ernzerhof, and K. Burke, "Rationale for mixing exact exchange with density functional approximations," *J. Chem. Phys.*, vol. 105, no. 22, pp. 9982–9985, 1996.
- [113] C. Adamo and V. Barone, "Toward reliable density functional methods without adjustable parameters: The PBE0 model," *J. Chem. Phys.*, vol. 110, no. 13, pp. 6158–6170, 1999.

## Bibliography

---

- [114] M. Guidon, J. Hutter, and J. VandeVondele, "Robust Periodic Hartree-Fock Exchange for Large-Scale Simulations Using Gaussian Basis Sets," *J. Chem. Theory Comput.*, vol. 5, no. 11, pp. 3010–3021, 2009.
- [115] O. A. Dicks and A. L. Shluger, "Theoretical modeling of charge trapping in crystalline and amorphous  $\text{Al}_2\text{O}_3$ ," *J. Phys.: Condens. Matter*, vol. 29, no. 31, p. 314005, 2017.
- [116] J. Heyd, G. E. Scuseria, and M. Ernzerhof, "Hybrid functionals based on a screened Coulomb potential," *J. Chem. Phys.*, vol. 118, no. 18, pp. 8207–8215, 2003.
- [117] A. V. Krukau, O. A. Vydrov, A. F. Izmaylov, and G. E. Scuseria, "Influence of the exchange screening parameter on the performance of screened hybrid functionals," *J. Chem. Phys.*, vol. 125, no. 22, p. 224106, 2006.
- [118] J. Heyd, G. E. Scuseria, and M. Ernzerhof, "Erratum: "Hybrid functionals based on a screened Coulomb potential" [*J. Chem. Phys.* 118, 8207 (2003)]," *J. Chem. Phys.*, vol. 124, no. 21, p. 219906, 2006.
- [119] A. Alkauskas, P. Broqvist, and A. Pasquarello, "Defect levels through hybrid density functionals: Insights and applications," *Phys. Status Solidi B*, vol. 248, no. 4, pp. 775–789, 2011.
- [120] J. VandeVondele, M. Krack, F. Mohamed, M. Parrinello, T. Chassaing, and J. Hutter, "Quickstep: Fast and accurate density functional calculations using a mixed Gaussian and plane waves approach," *Comput. Phys. Commun.*, vol. 167, no. 2, pp. 103–128, 2005.
- [121] M. Guidon, F. Schiffmann, J. Hutter, and J. VandeVondele, "*Ab initio* molecular dynamics using hybrid density functionals," *J. Chem. Phys.*, vol. 128, no. 21, p. 214104, 2008.
- [122] M. Guidon, J. Hutter, and J. VandeVondele, "Auxiliary Density Matrix Methods for Hartree-Fock Exchange Calculations," *J. Chem. Theory Comput.*, vol. 6, no. 8, pp. 2348–2364, 2010.
- [123] C. Freysoldt, J. Neugebauer, and C. G. Van de Walle, "Fully *Ab Initio* Finite-Size Corrections for Charged-Defect Supercell Calculations," *Phys. Rev. Lett.*, vol. 102, p. 016402, Jan 2009.
- [124] M. Leslie and N. Gillan, "The energy and elastic dipole tensor of defects in ionic crystals calculated by the supercell method," *J. Phys. C, Solid State*, vol. 18, no. 5, p. 973, 1985.
- [125] G. Makov and M. Payne, "Periodic boundary conditions in *ab initio* calculations," *Phys. Rev. B*, vol. 51, no. 7, p. 4014, 1995.
- [126] J. G. Kirkwood, "Statistical mechanics of fluid mixtures," *J. Chem. Phys.*, vol. 3, no. 5, pp. 300–313, 1935.
- [127] D. Frenkel and B. Smit, *Understanding Molecular Simulation: From Algorithms to Applications (Academic, San Diego, 2002)*. 2002.

- [128] F. Ambrosio, G. Miceli, and A. Pasquarello, "Redox levels in aqueous solution: Effect of van der Waals interactions and hybrid functionals," *J. Chem. Phys.*, vol. 143, no. 24, p. 244508, 2015.
- [129] M. Todorova and J. Neugebauer, "Extending the Concept of Defect Chemistry from Semiconductor Physics to Electrochemistry," *Phys. Rev. Applied*, vol. 1, p. 014001, Feb 2014.
- [130] D. Chandler, "Introduction to modern statistical mechanics," *Oxford University Press*, Sep 1987. ISBN-10: 0195042778. ISBN-13: 9780195042771, p. 288, 1987.
- [131] X. Gonze, B. Amadon, P.-M. Anglade, J.-M. Beuken, F. Bottin, P. Boulanger, F. Bruneval, D. Caliste, R. Caracas, M. Côté, T. Deutsch, L. Genovese, P. Ghosez, M. Giantomassi, S. Goedecker, D. Hamann, P. Hermet, F. Jollet, G. Jomard, S. Leroux, M. Mancini, S. Mazevet, M. Oliveira, G. Onida, Y. Pouillon, T. Rangel, G.-M. Rignanese, D. Sangalli, R. Shaltaf, M. Torrent, M. Verstraete, G. Zerah, and J. Zwanziger, "ABINIT: First-principles approach to material and nanosystem properties," *Comput. Phys. Commun.*, vol. 180, no. 12, pp. 2582–2615, 2009.
- [132] S. Goedecker, M. Teter, and J. Hutter, "Separable dual-space Gaussian pseudopotentials," *Phys. Rev. B*, vol. 54, pp. 1703–1710, Jul 1996.
- [133] C. Hartwigsen, S. Goedecker, and J. Hutter, "Relativistic separable dual-space Gaussian pseudopotentials from H to Rn," *Phys. Rev. B*, vol. 58, pp. 3641–3662, Aug 1998.
- [134] T. H. Dunning, "Gaussian basis sets for use in correlated molecular calculations. I. The atoms boron through neon and hydrogen," *J. Chem. Phys.*, vol. 90, no. 2, pp. 1007–1023, 1989.
- [135] J. VandeVondele and J. Hutter, "Gaussian basis sets for accurate calculations on molecular systems in gas and condensed phases," *J. Chem. Phys.*, vol. 127, no. 11, p. 114105, 2007.
- [136] G. Miceli, S. de Gironcoli, and A. Pasquarello, "Isobaric first-principles molecular dynamics of liquid water with nonlocal van der Waals interactions," *J. Chem. Phys.*, vol. 142, no. 3, p. 034501, 2015.
- [137] S. Nosé, "A unified formulation of the constant temperature molecular dynamics methods," *J. Chem. Phys.*, vol. 81, no. 1, pp. 511–519, 1984.
- [138] W. G. Hoover, "Canonical dynamics: Equilibrium phase-space distributions," *Phys. Rev. A*, vol. 31, pp. 1695–1697, Mar 1985.
- [139] O. A. Vydrov and T. Van Voorhis, "Nonlocal van der Waals density functional: The simpler the better," *J. Chem. Phys.*, vol. 133, no. 24, p. 244103, 2010.
- [140] R. Sabatini, T. Gorni, and S. de Gironcoli, "Nonlocal van der Waals density functional made simple and efficient," *Phys. Rev. B*, vol. 87, p. 041108, Jan 2013.

## Bibliography

---

- [141] P. Lamparter and R. Kniep, "Structure of amorphous  $\text{Al}_2\text{O}_3$ ," *Phys. B*, vol. 234-236, pp. 405–406, 1997.
- [142] Y. Oka, T. Takahashi, K. Okada, and S. ichi Iwai, "Structural analysis of anodic alumina films," *J. Non-Cryst. Solids*, vol. 30, no. 3, pp. 349 – 357, 1979.
- [143] S.-M. Lee, D. G. Cahill, and T. H. Allen, "Thermal conductivity of sputtered oxide films," *Phys. Rev. B*, vol. 52, pp. 253–257, Jul 1995.
- [144] J. Robertson, "High dielectric constant gate oxides for metal oxide Si transistors," *Rep. Prog. Phys.*, vol. 69, no. 2, p. 327, 2006.
- [145] P. Broqvist and A. Pasquarello, "Oxygen vacancy in monoclinic  $\text{HfO}_2$ : A consistent interpretation of trap assisted conduction, direct electron injection, and optical absorption experiments," *Appl. Phys. Lett.*, vol. 89, no. 26, p. 2904, 2006.
- [146] P. Broqvist and A. Pasquarello, "First principles investigation of defects at interfaces between silicon and amorphous high- $k$  oxides," *Microelectron. Eng.*, vol. 84, no. 9, pp. 2022–2027, 2007.
- [147] A. Alkauskas and A. Pasquarello, "Band-edge problem in the theoretical determination of defect energy levels: The O vacancy in  $\text{ZnO}$  as a benchmark case," *Phys. Rev. B*, vol. 84, p. 125206, Sep 2011.
- [148] H. Li, Y. Guo, and J. Robertson, "Hydrogen and the Light-Induced Bias Instability Mechanism in Amorphous Oxide Semiconductors," *Sci. Rep.*, vol. 7, no. 1, p. 16858, 2017.
- [149] P. Broqvist, A. Alkauskas, J. Godet, and A. Pasquarello, "First principles investigation of defect energy levels at semiconductor-oxide interfaces: Oxygen vacancies and hydrogen interstitials in the  $\text{Si-SiO}_2\text{-HfO}_2$  stack," *J. Appl. Phys.*, vol. 105, no. 6, p. 061603, 2009.
- [150] J. Godet and A. Pasquarello, "Protons at the  $\text{Si-SiO}_2$  interface: a first principle investigation," *Microelectron. Eng.*, vol. 84, no. 9, pp. 2035–2038, 2007.
- [151] J. Godet and A. Pasquarello, "Proton Diffusion in Amorphous  $\text{SiO}_2$  and Hafnium Silicate by Ab Initio Molecular Dynamics," *AIP Conference Proceedings*, vol. 893, no. 1, pp. 195–196, 2007.
- [152] J. Godet, F. Giustino, and A. Pasquarello, "Proton-Induced Fixed Positive Charge at the  $\text{Si}(100)\text{-SiO}_2$  Interface," *Phys. Rev. Lett.*, vol. 99, p. 126102, Sep 2007.
- [153] J. Godet and A. Pasquarello, "Proton Diffusion Mechanism in Amorphous  $\text{SiO}_2$ ," *Phys. Rev. Lett.*, vol. 97, p. 155901, Oct 2006.
- [154] J. Godet and A. Pasquarello, "Ab initio study of charged states of H in amorphous  $\text{SiO}_2$ ," *Microelectron. Eng.*, vol. 80, pp. 288–291, 2005.



- [155] M. Groner, J. Elam, F. Fabreguette, and S. George, "Electrical characterization of thin  $\text{Al}_2\text{O}_3$  films grown by atomic layer deposition on silicon and various metal substrates," *Thin Solid Films*, vol. 413, no. 1, pp. 186–197, 2002.
- [156] W. Cho, K. Sung, K.-S. An, S. Sook Lee, T.-M. Chung, and Y. Kim, "Atomic layer deposition of  $\text{Al}_2\text{O}_3$  thin films using dimethylaluminum isopropoxide and water," *J. Vac. Sci. Technol. A*, vol. 21, no. 4, pp. 1366–1370, 2003.
- [157] H. Li, Y. Guo, and J. Robertson, "Dopant compensation in  $\text{HfO}_2$  and other high K oxides," *Appl. Phys. Lett.*, vol. 104, no. 19, p. 192904, 2014.
- [158] N. Marzari, A. A. Mostofi, J. R. Yates, I. Souza, and D. Vanderbilt, "Maximally localized Wannier functions: Theory and applications," *Rev. Mod. Phys.*, vol. 84, pp. 1419–1475, Oct 2012.
- [159] M. González-Castaño, M. Döbeli, V. Araullo-Peters, L. P. Jeurgens, P. Schmutz, and C. Cancellieri, "Substrate Purity Effect on the Defect Formation and Properties of Amorphous Anodic Barrier  $\text{Al}_2\text{O}_3$ ," *J. Electrochem. Soc.*, vol. 165, no. 7, pp. C422–C431, 2018.
- [160] Y. Hori, C. Mizue, and T. Hashizume, "Process Conditions for Improvement of Electrical Properties of  $\text{Al}_2\text{O}_3/\text{n-GaN}$  Structures Prepared by Atomic Layer Deposition," *Jpn. J. Appl. Phys.*, vol. 49, no. 8R, p. 080201, 2010.
- [161] R. van de Krol, Y. Liang, and J. Schoonman, "Solar hydrogen production with nanostructured metal oxides," *J. Mater. Chem.*, vol. 18, pp. 2311–2320, 2008.
- [162] J. Sarnthein, A. Pasquarello, and R. Car, "Model of vitreous  $\text{SiO}_2$  generated by an ab initio molecular-dynamics quench from the melt," *Phys. Rev. B*, vol. 52, pp. 12690–12695, Nov 1995.
- [163] P. Umari and A. Pasquarello, "Fraction of Boroxol Rings in Vitreous Boron Oxide from a First-Principles Analysis of Raman and NMR Spectra," *Phys. Rev. Lett.*, vol. 95, p. 137401, Sep 2005.
- [164] P. Broqvist, J. E. Binder, and A. Pasquarello, "Band offsets at the  $\text{Ge}/\text{GeO}_2$  interface through hybrid density functionals," *Appl. Phys. Lett.*, vol. 94, no. 14, p. 141911, 2009.
- [165] D. Mergel, D. Buschendorf, S. Eggert, R. Grammes, and B. Samset, "Density and refractive index of  $\text{TiO}_2$  films prepared by reactive evaporation," *Thin Solid Films*, vol. 371, no. 1, pp. 218–224, 2000.
- [166] M. R. Saleem, S. Honkanen, and J. Turunen, "Thermal properties of  $\text{TiO}_2$  films fabricated by atomic layer deposition," *IOP Conf. Ser. Mater. Sci. Eng.*, vol. 60, no. 1, p. 012008, 2014.
- [167] G. Brauer and W. Littke, "Über den schmelzpunkt und die thermische Dissoziation von Titandioxyd," *J. Inorg. Nucl. Chem.*, vol. 16, no. 1, pp. 67–76, 1960.

## Bibliography

---

- [168] V. Petkov, G. Holzhüter, U. Tröge, T. Gerber, and B. Himmel, "Atomic-scale structure of amorphous TiO<sub>2</sub> by electron, X-ray diffraction and reverse Monte Carlo simulations," *J. Non-Cryst. Solids*, vol. 231, no. 1, pp. 17–30, 1998.
- [169] S. Amor, L. Guedri, G. Baud, M. Jacquet, and M. Ghedira, "Influence of the temperature on the properties of sputtered titanium oxide films," *Mater. Chem. Phys.*, vol. 77, no. 3, pp. 903–911, 2003.
- [170] H. Takikawa, T. Matsui, T. Sakakibara, A. Bendavid, and P. J. Martin, "Properties of titanium oxide film prepared by reactive cathodic vacuum arc deposition," *Thin Solid Films*, vol. 348, no. 1, pp. 145–151, 1999.
- [171] Z. Zhao, B. Tay, S. Lau, and G. Yu, "Optical properties of titania films prepared by off-plane filtered cathodic vacuum arc," *J. Cryst. Growth*, vol. 268, no. 3, pp. 543–546, 2004.
- [172] M. Zhang, G. Lin, C. Dong, and L. Wen, "Amorphous TiO<sub>2</sub> films with high refractive index deposited by pulsed bias arc ion plating," *Surf. Coat. Technol.*, vol. 201, no. 16-17, pp. 7252–7258, 2007.
- [173] H. Tang, K. Prasad, R. Sanjines, P. Schmid, and F. Lévy, "Electrical and optical properties of TiO<sub>2</sub> anatase thin films," *J. Appl. Phys.*, vol. 75, no. 4, pp. 2042–2047, 1994.
- [174] H. Tang, H. Berger, P. Schmid, F. Lévy, and G. Burri, "Photoluminescence in TiO<sub>2</sub> anatase single crystals," *Solid State Commun.*, vol. 87, no. 9, pp. 847–850, 1993.
- [175] E. Baldini, L. Chiodo, A. Dominguez, M. Palummo, S. Moser, M. Yazdi-Rizi, G. Auböck, B. Mallett, H. Berger, A. Magrez, C. Bernhard, M. Grioni, A. Rubio, and M. Chergui, "Strongly bound excitons in anatase TiO<sub>2</sub> single crystals and nanoparticles," *Nat. Commun.*, vol. 8, p. 13, 2017.
- [176] P. Perfetti, F. Patella, F. Sette, C. Quaresima, C. Capasso, A. Savoia, and G. Margaritondo, "Experimental study of the GaP-Si interface," *Phys. Rev. B*, vol. 30, pp. 4533–4539, Oct 1984.
- [177] M. Dahmen, U. Rau, M. Kawanaka, J. Sone, and J. Werner, "Band offset variations at Ge/GaAs(100) interfaces," *Appl. Phys. Lett.*, vol. 62, no. 3, pp. 261–263, 1993.
- [178] N. Jain, Y. Zhu, D. Maurya, R. Varghese, S. Priya, and M. K. Hudait, "Interfacial band alignment and structural properties of nanoscale TiO<sub>2</sub> thin films for integration with epitaxial crystallographic oriented germanium," *J. Appl. Phys.*, vol. 115, no. 2, p. 024303, 2014.
- [179] G. Henkelman and H. Jónsson, "Improved tangent estimate in the nudged elastic band method for finding minimum energy paths and saddle points," *J. Chem. Phys.*, vol. 113, no. 22, pp. 9978–9985, 2000.

- [180] Z. Guo, F. Ambrosio, and A. Pasquarello, "Hole diffusion across leaky amorphous TiO<sub>2</sub> coating layers for catalytic water splitting at photoanodes," *J. Mater. Chem. A*, vol. 6, pp. 11804–11810, 2018.
- [181] M. Grätzel, "Photoelectrochemical cells," *Nature*, vol. 414, no. 6861, pp. 338–344, 2001.
- [182] A. J. Nozik and R. Memming, "Physical Chemistry of Semiconductor-Liquid Interfaces," *J. Chem. Phys.*, vol. 100, no. 31, pp. 13061–13078, 1996.
- [183] S. S. Kocha, M. W. Peterson, D. J. Arent, J. M. Redwing, M. A. Tischler, and J. A. Turner, "Electrochemical Investigation of the Gallium Nitride-Aqueous Electrolyte Interface," *J. Electrochem. Soc.*, vol. 150, pp. L238–L240, 1995.
- [184] Y.-H. Li, X. G. Gong, and S.-H. Wei, "Ab initio all-electron calculation of absolute volume deformation potentials of IV-IV, III-V, and II-VI semiconductors: The chemical trends," *Phys. Rev. B*, vol. 73, p. 245206, Jun 2006.
- [185] H. J. Monkhorst and J. D. Pack, "Special points for Brillouin-zone integrations," *Phys. Rev. B*, vol. 13, pp. 5188–5192, Jun 1976.
- [186] M. van Schilfgaarde, T. Kotani, and S. Faleev, "Quasiparticle Self-Consistent GW Theory," *Phys. Rev. Lett.*, vol. 96, p. 226402, Jun 2006.
- [187] S. Lebègue, B. Arnaud, M. Alouani, and P. E. Blochl, "Implementation of an all-electron GW approximation based on the projector augmented wave method without plasmon pole approximation: Application to Si, SiC, AlAs, InAs, NaH, and KH," *Phys. Rev. B*, vol. 67, p. 155208, Apr 2003.
- [188] C. Friedrich, M. C. Müller, and S. Blügel, "Band convergence and linearization error correction of all-electron GW calculations: The extreme case of zinc oxide," *Phys. Rev. B*, vol. 83, p. 081101, Feb 2011.
- [189] B.-C. Shih, Y. Xue, P. Zhang, M. L. Cohen, and S. G. Louie, "Quasiparticle Band Gap of ZnO: High Accuracy from the Conventional  $G^0W^0$  Approach," *Phys. Rev. Lett.*, vol. 105, p. 146401, Sep 2010.
- [190] J. Klimeš, M. Kaltak, and G. Kresse, "Predictive GW calculations using plane waves and pseudopotentials," *Phys. Rev. B*, vol. 90, p. 075125, Aug 2014.
- [191] A. Grüneis, G. Kresse, Y. Hinuma, and F. Oba, "Ionization Potentials of Solids: The Importance of Vertex Corrections," *Phys. Rev. Lett.*, vol. 112, p. 096401, Mar 2014.
- [192] P. Giannozzi, S. Baroni, N. Bonini, M. Calandra, R. Car, C. Cavazzoni, D. Ceresoli, G. L. Chiarotti, M. Cococcioni, I. Dabo, A. Dal Corso, S. de Gironcoli, S. Fabris, G. Fratesi, R. Gebauer, U. Gerstmann, C. Gougoussis, A. Kokalj, M. Lazzeri, L. Martin-Samos, N. Marzari, F. Mauri, R. Mazzarello, S. Paolini, A. Pasquarello, L. Paulatto, C. Sbraccia, S. Scandolo, G. Sclauzero, A. P. Seitsonen, A. Smogunov, P. Umari, and R. M. Wentzcovitch,

## Bibliography

---

- “QUANTUM ESPRESSO: a modular and open-source software project for quantum simulations of materials,” *J. Phys.: Condens. Matter*, vol. 21, no. 39, p. 395502, 2009.
- [193] D. R. Hamann, “Optimized norm-conserving Vanderbilt pseudopotentials,” *Phys. Rev. B*, vol. 88, p. 085117, Aug 2013.
- [194] H.-P. Komsa and A. Pasquarello, “Assessing the accuracy of hybrid functionals in the determination of defect levels: Application to the As antisite in GaAs,” *Phys. Rev. B*, vol. 84, p. 075207, Aug 2011.
- [195] J. Wiktor, I. Reshetnyak, F. Ambrosio, and A. Pasquarello, “Comprehensive modeling of the band gap and absorption spectrum of BiVO<sub>4</sub>,” *Phys. Rev. Materials*, vol. 1, p. 022401, Jul 2017.
- [196] E. Grilli, M. Guzzi, R. Zamboni, and L. Pavesi, “High-precision determination of the temperature dependence of the fundamental energy gap in gallium arsenide,” *Phys. Rev. B*, vol. 45, pp. 1638–1644, Jan 1992.
- [197] M. R. Lorenz, G. D. Pettit, and R. C. Taylor, “Band Gap of Gallium Phosphide from 0 to 900 K and Light Emission from Diodes at High Temperatures,” *Phys. Rev.*, vol. 171, pp. 876–881, Jul 1968.
- [198] I. Vurgaftman and J. R. Meyer, “Band parameters for nitrogen-containing semiconductors,” *J. Appl. Phys.*, vol. 94, no. 6, pp. 3675–3696, 2003.
- [199] R. Pässler, “Parameter Sets Due to Fittings of the Temperature Dependencies of Fundamental Bandgaps in Semiconductors,” *Phys. Status Solidi B*, vol. 216, no. 2, pp. 975–1007, 1999.
- [200] D. G. Seiler, D. Heiman, R. Feigenblatt, R. L. Aggarwal, and B. Lax, “Two-photon magnetospectroscopy of *A*-exciton states in CdS,” *Phys. Rev. B*, vol. 25, pp. 7666–7677, Jun 1982.
- [201] D. Bagnall, Y. Chen, Z. Zhu, T. Yao, M. Shen, and T. Goto, “High temperature excitonic stimulated emission from ZnO epitaxial layers,” *Appl. Phys. Lett.*, vol. 73, no. 8, pp. 1038–1040, 1998.
- [202] A. Mang, K. Reimann, and S. Rübenacke, “Band gaps, crystal-field splitting, spin-orbit coupling, and exciton binding energies in ZnO under hydrostatic pressure,” *Solid State Commun.*, vol. 94, no. 4, pp. 251–254, 1995.
- [203] L. Wang and N. Giles, “Temperature dependence of the free-exciton transition energy in zinc oxide by photoluminescence excitation spectroscopy,” *J. Appl. Phys.*, vol. 94, no. 2, pp. 973–978, 2003.
- [204] Z. Jarzebski and J. Morton, “Physical Properties of SnO<sub>2</sub> Materials III. Optical Properties,” *J. Electrochem. Soc.*, vol. 123, no. 10, pp. 333C–346C, 1976.

- [205] K. Reimann and M. Steube, "Experimental determination of the electronic band structure of  $\text{SnO}_2$ ," *Solid State Commun.*, vol. 105, no. 10, pp. 649–652, 1998.
- [206] D. Reyes-Coronado, G. Rodríguez-Gattorno, M. E. Espinosa-Pesqueira, C. Cab, R. de Coss, and G. Oskam, "Phase-pure  $\text{TiO}_2$  nanoparticles: anatase, brookite and rutile," *Nanotechnology*, vol. 19, no. 14, p. 145605, 2008.
- [207] C. G. Van de Walle and R. M. Martin, "Theoretical study of band offsets at semiconductor interfaces," *Phys. Rev. B*, vol. 35, pp. 8154–8165, May 1987.
- [208] A. Baldereschi, S. Baroni, and R. Resta, "Band offsets in lattice-matched heterojunctions: a model and first-principles calculations for GaAs/AlAs," *Phys. Rev. Lett.*, vol. 61, pp. 734–737, Aug. 1988.
- [209] A. Alkauskas, P. Broqvist, F. Devynck, and A. Pasquarello, "Band Offsets at Semiconductor-Oxide Interfaces from Hybrid Density-Functional Calculations," *Phys. Rev. Lett.*, vol. 101, p. 106802, Sep 2008.
- [210] R. Shaltaf, G.-M. Rignanese, X. Gonze, F. Giustino, and A. Pasquarello, "Band Offsets at the Si/ $\text{SiO}_2$  Interface from Many-Body Perturbation Theory," *Phys. Rev. Lett.*, vol. 100, p. 186401, May 2008.
- [211] K. Steiner, W. Chen, and A. Pasquarello, "Band offsets of lattice-matched semiconductor heterojunctions through hybrid functionals and  $G_0W_0$ ," *Phys. Rev. B*, vol. 89, p. 205309, May 2014.
- [212] C. G. Van de Walle and R. M. Martin, "'Absolute' deformation potentials: Formulation and ab initio calculations for semiconductors," *Phys. Rev. Lett.*, vol. 62, pp. 2028–2031, Apr 1989.
- [213] H.-P. Komsa, P. Broqvist, and A. Pasquarello, "Alignment of defect levels and band edges through hybrid functionals: Effect of screening in the exchange term," *Phys. Rev. B*, vol. 81, p. 205118, 2010.
- [214] W. Chen and A. Pasquarello, "Correspondence of defect energy levels in hybrid density functional theory and many-body perturbation theory," *Phys. Rev. B*, vol. 88, p. 115104, Sep 2013.
- [215] W. Chen and A. Pasquarello, "Accuracy of  $GW$  for calculating defect energy levels in solids," *Phys. Rev. B*, vol. 96, p. 020101, Jul 2017.
- [216] T. A. Pham, C. Zhang, E. Schwegler, and G. Galli, "Probing the electronic structure of liquid water with many-body perturbation theory," *Phys. Rev. B*, vol. 89, p. 060202, Feb 2014.
- [217] K. Leung, "Surface Potential at the Air-Water Interface Computed Using Density Functional Theory," *J. Phys. Chem. Lett.*, vol. 1, no. 2, pp. 496–499, 2010.

## Bibliography

---

- [218] F. Ambrosio, G. Miceli, and A. Pasquarello, "Electronic Levels of Excess Electrons in Liquid Water," *J. Phys. Chem. Lett.*, vol. 8, no. 9, pp. 2055–2059, 2017.
- [219] J. Cheng, X. Liu, J. VandeVondele, M. Sulpizi, and M. Sprik, "Redox Potentials and Acidity Constants from Density Functional Theory Based Molecular Dynamics," *Acc. Chem. Res.*, vol. 47, no. 12, pp. 3522–3529, 2014.
- [220] F. Ambrosio, Z. Guo, and A. Pasquarello, "Absolute Energy Levels of Liquid Water," *J. Phys. Chem. Lett.*, vol. 9, pp. 3212–3216, 2018.
- [221] A. P. Gaiduk, T. A. Pham, M. Govoni, F. Paesani, and G. Galli, "Electron affinity of liquid water," *Nat. Commun.*, vol. 9, no. 1, p. 247, 2018.
- [222] J. Wiktor, F. Bruneval, and A. Pasquarello, "Partial molar volumes of aqua ions from first principles," *J. Chem. Theory Comput.*, vol. 13, no. 8, pp. 3427–3431, 2017.
- [223] H. Flyvbjerg and H. G. Petersen, "Error estimates on averages of correlated data," *J. Chem. Phys.*, vol. 91, no. 1, pp. 461–466, 1989.
- [224] R. Shaltaf, G.-M. Rignanese, X. Gonze, F. Giustino, and A. Pasquarello, "Band offsets at the Si/SiO<sub>2</sub> interface from many-body perturbation theory," *Phys. Rev. Lett.*, vol. 100, no. 18, p. 186401, 2008.
- [225] A. A. Isse and A. Gennaro, "Absolute potential of the standard hydrogen electrode and the problem of interconversion of potentials in different solvents," *J. Phys. Chem. B*, vol. 114, no. 23, pp. 7894–7899, 2010.
- [226] S. Trasatti, "The Absolute Electrode Potential: an Explanatory Note (Recommendations 1986)," *Pure Appl. Chem.*, vol. 58, no. 7, pp. 955–966, 1986.
- [227] M. Shishkin, M. Marsman, and G. Kresse, "Accurate Quasiparticle Spectra from Self-Consistent GW Calculations with Vertex Corrections," *Phys. Rev. Lett.*, vol. 99, p. 246403, Dec 2007.
- [228] W. Chen, F. Ambrosio, G. Miceli, and A. Pasquarello, "*Ab initio* Electronic Structure of Liquid Water," *Phys. Rev. Lett.*, vol. 117, p. 186401, Oct 2016.
- [229] G. W. Gobeli and F. G. Allen, "Photoelectric Properties of Cleaved GaAs, GaSb, InAs, and InSb Surfaces; Comparison with Si and Ge," *Phys. Rev.*, vol. 137, pp. A245–A254, Jan 1965.
- [230] J. Van Laar, A. Huijser, and T. Van Rooy, "Electronic surface properties of Ga and In containing III–V compounds," *J. Vac. Sci. Technol.*, vol. 14, no. 4, pp. 894–898, 1977.
- [231] R. K. Swank, "Surface Properties of II–VI Compounds," *Phys. Rev.*, vol. 153, pp. 844–849, Jan 1967.

- [232] A. Klein, C. Körber, A. Wachau, F. Säuberlich, Y. Gassenbauer, R. Schafranek, S. P. Harvey, and T. O. Mason, "Surface potentials of magnetron sputtered transparent conducting oxides," *Thin Solid Films*, vol. 518, no. 4, pp. 1197–1203, 2009.
- [233] K. Schierbaum, S. Fischer, M. Torquemada, J. De Segovia, E. Roman, and J. Martin-Gago, "The interaction of Pt with TiO<sub>2</sub>(110) surfaces: a comparative XPS, UPS, ISS, and ESD study," *Surf. Sci.*, vol. 345, no. 3, pp. 261–273, 1996.
- [234] G. Cicero, J. C. Grossman, A. Catellani, and G. Galli, "Water at a Hydrophilic Solid Surface Probed by Ab initio Molecular Dynamics: Inhomogeneous Thin Layers of Dense Fluid," *J. Am. Chem. Soc.*, vol. 127, no. 18, pp. 6830–6835, 2005.
- [235] B. C. Wood, E. Schwegler, W. I. Choi, and T. Ogitsu, "Hydrogen-Bond Dynamics of Water at the Interface with InP/GaP(001) and the Implications for Photoelectrochemistry," *J. Am. Chem. Soc.*, vol. 135, no. 42, pp. 15774–15783, 2013.
- [236] S. Kaya, D. Schlesinger, S. Yamamoto, J. T. Newberg, H. Bluhm, H. Ogasawara, T. Kendelewicz, G. E. Brown, L. G. M. Pettersson, and A. Nilsson, "Highly Compressed Two-Dimensional Form of Water at Ambient Conditions," *Sci. Rep.*, vol. 3, p. 1074, 2013.
- [237] X. Shen, P. B. Allen, M. S. Hybertsen, and J. T. Muckerman, "Water Adsorption on the GaN (10 $\bar{1}$ 0) Nonpolar Surface," *J. Phys. Chem. C*, vol. 113, no. 9, pp. 3365–3368, 2009.
- [238] U. Aschauer, Y. He, H. Cheng, S.-C. Li, U. Diebold, and A. Selloni, "Influence of Subsurface Defects on the Surface Reactivity of TiO<sub>2</sub>: Water on Anatase (101)," *J. Phys. Chem. C*, vol. 114, no. 2, pp. 1278–1284, 2010.
- [239] X. Zhang and S. Ptasinska, "Dissociative Adsorption of Water on an H<sub>2</sub>O/GaAs(100) Interface: In Situ Near-Ambient Pressure XPS Studies," *J. Phys. Chem. C*, vol. 118, no. 8, pp. 4259–4266, 2014.
- [240] J. Nozik, "Photoelectrochemistry: Applications to Solar Energy Conversion," *Annu. Rev. Phys. Chem.*, vol. 29, pp. 189–222, 1978.
- [241] J. D. Beach, R. T. Collins, and J. A. Turner, "Band-Edge Potentials of n-Type and p-Type GaN," *J. Electrochem. Soc.*, vol. 150, pp. A899–A904, 2003.
- [242] I. M. Huygens, K. Strubbe, and W. P. Gomes, "Electrochemistry and Photoetching of n-GaN," *J. Electrochem. Soc.*, vol. 147, pp. 1797–1802, 2000.
- [243] R. Schlesinger and P. J. Janietz, "Point of Zero Net Adsorbed Charge of Gallium Arsenide," *J. Electrochem. Soc.*, vol. 139, pp. 1936–1940, 1992.
- [244] D. Benard and P. Handler, "Hole injection and surface state effects at gallium arsenide electrodes," *Surf. Sci.*, vol. 40, no. 1, pp. 141–148, 1973.
- [245] W. Laflere, F. Cardon, and W. Gomes, "On the differential capacitance of the n- and p-type gallium arsenide electrode," *Surf. Sci.*, vol. 44, no. 2, pp. 541–552, 1974.

## Bibliography

---

- [246] W. Laflere, R. V. Meirhaeghe, F. Cardon, and W. Gomes, "On the frequency-dependence of the impedance of n- and p-type gallium arsenide electrodes," *Surf. Sci.*, vol. 59, no. 2, pp. 401–412, 1976.
- [247] J. Bockris and K. Uosaki, "The Rate of the Photoelectrochemical Generation of Hydrogen at p-Type Semiconductors," *J. Electrochem. Soc.*, vol. 124, no. 9, pp. 1348–1355, 1977.
- [248] J. Kelly and R. Memming, "The Influence of Surface Recombination and Trapping on the Cathodic Photocurrent at p-Type III-V Electrodes," *J. Electrochem. Soc.*, vol. 129, no. 4, pp. 730–738, 1982.
- [249] A. B. Ellis, J. M. Bolts, S. W. Kaiser, and M. S. Wrighton, "Study of n-type gallium arsenide- and gallium phosphide-based photoelectrochemical cells. Stabilization by kinetic control and conversion of optical energy to electricity," *J. Am. Chem. Soc.*, vol. 99, no. 9, pp. 2848–2854, 1977.
- [250] M. S. Wrighton, J. M. Bolts, A. B. Bocarsly, M. C. Palazzotto, and E. G. Walton, "Stabilization of n-type semiconductors to photoanodic dissolution: II–VI and III–V compound semiconductors and recent results for n-type silicon," *J. Vac. Sci. Technol.*, vol. 15, no. 4, pp. 1429–1435, 1978.
- [251] M. A. Butler and D. S. Ginley, "Prediction of Flatband Potentials at Semiconductor-Electrolyte Interfaces from Atomic Electronegativities," *J. Electrochem. Soc.*, vol. 125, pp. 228–232, 1978.
- [252] M. Madou, F. Cardon, and W. Gomes, "Impedance Measurements at the N- and P-Type GaP Single Crystal Electrode," *J. Electrochem. Soc.*, vol. 124, no. 10, pp. 1623–1627, 1977.
- [253] W. Gomes and F. Cardon, "Electron energy levels in semiconductor electrochemistry," *Prog. Surf. Sci.*, vol. 12, no. 2, pp. 155–215, 1982.
- [254] R. Memming, "Mechanism of the electrochemical reduction of persulfates and hydrogen peroxide," *J. Electrochem. Soc.*, vol. 116, no. 6, pp. 785–790, 1969.
- [255] H. Yoneyama, H. Sakamoto, and H. Tamura, "A Photo-electrochemical cell with production of hydrogen and oxygen by a cell reaction," *Electrochim. Acta*, vol. 20, no. 5, pp. 341–345, 1975.
- [256] M. Bayer, C. Uhl, and P. Vogl, "Theoretical study of electrolyte gate AlGaN/GaN field effect transistors," *J. Appl. Phys.*, vol. 97, no. 3, p. 033703, 2005.
- [257] G. Steinhoff, M. Hermann, W. Schaff, L. Eastman, M. Stutzmann, and M. Eickhoff, "pH response of GaN surfaces and its application for pH-sensitive field-effect transistors," *Appl. Phys. Lett.*, vol. 83, no. 1, pp. 177–179, 2003.
- [258] S. Park and C. Huang, "The surface acidity of hydrous CdS(s)," *J. Colloid Interface Sci.*, vol. 117, no. 2, pp. 431–441, 1987.



- [259] A. B. Ellis, S. W. Kaiser, J. M. Bolts, and M. S. Wrighton, "Study of n-type semiconducting cadmium chalcogenide-based photoelectrochemical cells employing polychalcogenide electrolytes," *J. Am. Chem. Soc.*, vol. 99, no. 9, pp. 2839–2848, 1977.
- [260] T. Inoue, T. Watanabe, A. Fujishima, and K. Honda, "Investigation of CdS photoanode reaction in the electrolyte solution containing sulfide ion," *Bull. Chem. Soc. Jpn.*, vol. 52, no. 5, pp. 1243–1250, 1979.
- [261] R. Memming, "The Role of Energy Levels in Semiconductor-Electrolyte Solar Cells," *J. Electrochem. Soc.*, vol. 125, no. 1, pp. 117–123, 1978.
- [262] D. Ginley and M. Butler, "Flatband potential of cadmium sulfide (CdS) photoanodes and its dependence on surface ion effects," *J. Electrochem. Soc.*, vol. 125, no. 12, pp. 1968–1974, 1978.
- [263] D. Meissner, R. Memming, and B. Kastening, "Photoelectrochemistry of cadmium sulfide. 1. Reanalysis of photocorrosion and flat-band potential," *J. Phys. Chem.*, vol. 92, no. 12, pp. 3476–3483, 1988.
- [264] T. Watanabe, A. Fujishima, and K. Honda, "Potential variation at the semiconductor-electrolyte interface through a change in pH of the solution," *Chem. Lett.*, vol. 3, no. 8, pp. 897–900, 1974.
- [265] H. Minoura, T. Watanabe, T. Oki, and M. Tsuki, "Effects of Dissolved  $\text{Cd}^{2+}$  and  $\text{S}^{2-}$  Ions on the Flatband Potential of CdS Electrode in Aqueous Solution," *Jpn. J. Appl. Phys.*, vol. 16, no. 5, pp. 865–866, 1977.
- [266] L. Blok and P. Bruyn, "The ionic double layer at the ZnO solution interface," *J. Colloid Interface Sci.*, vol. 32, no. 3, pp. 518–526, 1970.
- [267] J. Dewald, "The charge distribution at the zinc oxide-electrolyte interface," *J. Phys. Chem. Solids*, vol. 14, pp. 155–161, 1960.
- [268] J. F. Dewald, "The Charge and Potential Distributions at the Zinc Oxide Electrode," *Bell Technol. J.*, vol. 39, no. 3, pp. 615–639, 1960.
- [269] F. Lohmann, "The influence of pH on the electrical and chemical properties of zinc oxide electrodes," *Ber. Bunsen-Ges. Phys. Chem.*, vol. 70, no. 4, pp. 428–434, 1966.
- [270] R. V. Berghe, F. Cardon, and W. Gomes, "On the electrochemical reactivity of the redox couple  $\text{Fe}(\text{CN})_6^{3-}/\text{Fe}(\text{CN})_6^{4-}$  at the single crystal zinc oxide electrode," *Surf. Sci.*, vol. 39, no. 2, pp. 368–384, 1973.
- [271] S. A. B. Ab. Aziz, S. H. Amirnordin, H. Z. Abdullah, H. Taib, and H. A. Rahman, "Effect of Zeta Potential of Stannum Oxide ( $\text{SnO}_2$ ) on Electrophoretic Deposition (EPD) on Porous Alumina," *Adv. Mater. Res.*, vol. 795, pp. 334–337, 11 2013.

## Bibliography

---

- [272] J. M. Bolts and M. S. Wrighton, "Correlation of photocurrent-voltage curves with flat-band potential for stable photoelectrodes for the photoelectrolysis of water," *J. Phys. Chem.*, vol. 80, no. 24, pp. 2641–2645, 1976.
- [273] G. Boschloo and D. Fitzmaurice, "Spectroelectrochemistry of Highly Doped Nanostructured Tin Dioxide Electrodes," *J. Phys. Chem. B*, vol. 103, no. 16, pp. 3093–3098, 1999.
- [274] J. Bandara and U. Pradeep, "Tuning of the flat-band potentials of nanocrystalline TiO<sub>2</sub> and SnO<sub>2</sub> particles with an outer-shell MgO layer," *Thin Solid Films*, vol. 517, no. 2, pp. 952–956, 2008.
- [275] Y. G. Bérubé and P. L. de Bruyn, "Adsorption at the rutile-solution interface: I. Thermodynamic and Experimental Study," *J. Colloid Interface Sci.*, vol. 27, no. 2, pp. 305–318, 1968.
- [276] D. O. Scanlon, C. W. Dunnill, J. Buckeridge, S. A. Shevlin, A. J. Logsdail, S. M. Woodley, C. R. A. Catlow, M. J. Powell, R. G. Palgrave, I. P. Parkin, G. W. Watson, T. W. Keal, P. Sherwood, A. Walsh, and A. A. Sokol, "Band alignment of rutile and anatase TiO<sub>2</sub>," *Nat. Mater.*, vol. 12, no. 9, pp. 798–801, 2013.
- [277] M. D. Ward, J. R. White, and A. J. Bard, "Electrochemical investigation of the energetics of particulate titanium dioxide photocatalysts. The methyl viologen-acetate system," *J. Am. Chem. Soc.*, vol. 105, no. 1, pp. 27–31, 1983.
- [278] L. Kavan, M. Grätzel, S. E. Gilbert, C. Klemenz, and H. J. Scheel, "Electrochemical and Photoelectrochemical Investigation of Single-Crystal Anatase," *J. Am. Chem. Soc.*, vol. 118, no. 28, pp. 6716–6723, 1996.
- [279] Y. Matsumoto, T. Yoshikawa, and E. Sato, "Dependence of the band bending of the oxide semiconductors on pH," *J. Electrochem. Soc.*, vol. 136, no. 5, pp. 1389–1391, 1989.
- [280] R. Nakamura, N. Ohashi, A. Imanishi, T. Osawa, Y. Matsumoto, H. Koinuma, and Y. Nakato, "Crystal-Face Dependences of Surface Band Edges and Hole Reactivity, Revealed by Preparation of Essentially Atomically Smooth and Stable (110) and (100) n-TiO<sub>2</sub> (Rutile) Surfaces," *J. Phys. Chem. B*, vol. 109, no. 5, pp. 1648–1651, 2005.
- [281] R. Hengerer, L. Kavan, P. Krtil, and M. Grätzel, "Orientation Dependence of Charge-Transfer Processes on TiO<sub>2</sub> (Anatase) Single Crystals," *J. Electrochem. Soc.*, vol. 147, pp. 1467–1472, 2000.
- [282] B. Enright and D. Fitzmaurice, "Spectroscopic Determination of Electron and Hole Effective Masses in a Nanocrystalline Semiconductor Film," *J. Phys. Chem.*, vol. 100, no. 3, pp. 1027–1035, 1996.
- [283] M. S. Hybertsen and S. G. Louie, "Electron correlation in semiconductors and insulators: Band gaps and quasiparticle energies," *Phys. Rev. B*, vol. 34, pp. 5390–5413, Oct 1986.

- [284] Y. Tachibana, L. Vayssieres, and J. R. Durrant, "Artificial photosynthesis for solar water-splitting," *Nat. Photonics*, vol. 6, no. 8, p. 511, 2012.
- [285] H. Ahmad, S. Kamarudin, L. Minggu, and M. Kassim, "Hydrogen from photo-catalytic water splitting process: A review," *Renewable Sustainable Energy Rev.*, vol. 43, pp. 599–610, 2015.
- [286] X. Zou and Y. Zhang, "Noble metal-free hydrogen evolution catalysts for water splitting," *Chem. Soc. Rev.*, vol. 44, no. 15, pp. 5148–5180, 2015.
- [287] T. Hisatomi, J. Kubota, and K. Domen, "Recent advances in semiconductors for photocatalytic and photoelectrochemical water splitting," *Chem. Soc. Rev.*, vol. 43, no. 22, pp. 7520–7535, 2014.
- [288] F. E. Osterloh and B. A. Parkinson, "Recent developments in solar water-splitting photocatalysis," *MRS Bull.*, vol. 36, no. 1, pp. 17–22, 2011.
- [289] M. Moniruddin, B. Ilyassov, X. Zhao, E. Smith, T. Serikov, N. Ibrayev, R. Asmatulu, and N. Nuraje, "Recent progress on perovskite materials in photovoltaic and water splitting applications," *Mater. Today Energy*, vol. 7, pp. 246–259, 2018.
- [290] S. J. Moniz, S. A. Shevlin, D. J. Martin, Z.-X. Guo, and J. Tang, "Visible-light driven heterojunction photocatalysts for water splitting—a critical review," *Energy Environ. Sci.*, vol. 8, no. 3, pp. 731–759, 2015.
- [291] Z. Zou, J. Ye, K. Sayama, and H. Arakawa, "Direct splitting of water under visible light irradiation with an oxide semiconductor photocatalyst," *Nature*, vol. 414, no. 6864, p. 625, 2001.
- [292] T. W. Kim and K.-S. Choi, "Nanoporous BiVO<sub>4</sub> photoanodes with dual-layer oxygen evolution catalysts for solar water splitting," *Science*, p. 1245026, 2014.
- [293] L. Liao, Q. Zhang, Z. Su, Z. Zhao, Y. Wang, Y. Li, X. Lu, D. Wei, G. Feng, Q. Yu, X. Cai, J. Zhao, Z. Ren, H. Fang, F. Robles-Hernandez, S. Baldelli, and J. Bao, "Efficient solar water-splitting using a nanocrystalline CoO photocatalyst," *Nature Nanotech.*, vol. 9, no. 1, p. 69, 2014.
- [294] F. E. Osterloh, "Inorganic Materials as Catalysts for Photochemical Splitting of Water," *Chem. Mater.*, vol. 20, no. 1, pp. 35–54, 2008.
- [295] P. Gono, J. Wiktor, F. Ambrosio, and A. Pasquarello, "Surface Polarons Reducing Overpotentials in the Oxygen Evolution Reaction," *ACS Catal.*, vol. 8, no. 0, pp. 5847–5851, 2018.
- [296] O. Neufeld, N. Yatom, and M. Caspary Toroker, "A First-Principles Study on the Role of an Al<sub>2</sub>O<sub>3</sub> Overlayer on Fe<sub>2</sub>O<sub>3</sub> for Water Splitting," *ACS Catal.*, vol. 5, no. 12, pp. 7237–7243, 2015.

## Bibliography

---

- [297] T. Hisatomi, F. Le Formal, M. Cornuz, J. Brillet, N. Tétreault, K. Sivula, and M. Grätzel, "Cathodic shift in onset potential of solar oxygen evolution on hematite by 13-group oxide overlayers," *Energy Environ. Sci.*, vol. 4, no. 7, pp. 2512–2515, 2011.
- [298] L. Steier, I. Herraiz-Cardona, S. Gimenez, F. Fabregat-Santiago, J. Bisquert, S. D. Tilley, and M. Grätzel, "Understanding the role of underlayers and overlayers in thin film hematite photoanodes," *Adv. Funct. Mater.*, vol. 24, no. 48, pp. 7681–7688, 2014.
- [299] F. Ambrosio, J. Wiktor, and A. Pasquarello, "pH-Dependent Catalytic Reaction Pathway for Water Splitting at the BiVO<sub>4</sub>-Water Interface from the Band Alignment," *ACS Energy Lett.*, vol. 3, no. 4, pp. 829–834, 2018.
- [300] F. Ambrosio, J. Wiktor, and A. Pasquarello, "pH-Dependent Surface Chemistry from First Principles: Application to the BiVO<sub>4</sub>(010)-Water Interface," *ACS Appl. Mater. Interfaces*, vol. 10, no. 12, pp. 10011–10021, 2018.
- [301] T. A. Pham, Y. Ping, and G. Galli, "Modelling heterogeneous interfaces for solar water splitting," *Nat. Mater.*, vol. 16, no. 4, p. 401, 2017.
- [302] H. Xiao, J. Tahir-Kheli, and W. A. Goddard, "Accurate Band Gaps for Semiconductors from Density Functional Theory," *J. Phys. Chem. Lett.*, vol. 2, no. 3, pp. 212–217, 2011.
- [303] J. Heyd, J. E. Peralta, G. E. Scuseria, and R. L. Martin, "Energy band gaps and lattice parameters evaluated with the Heyd-Scuseria-Ernzerhof screened hybrid functional," *J. Chem. Phys.*, vol. 123, no. 17, p. 174101, 2005.
- [304] F. Tran and P. Blaha, "Accurate Band Gaps of Semiconductors and Insulators with a Semilocal Exchange-Correlation Potential," *Phys. Rev. Lett.*, vol. 102, p. 226401, Jun 2009.
- [305] J. K. Nørskov, J. Rossmeisl, A. Logadottir, L. Lindqvist, J. R. Kitchin, T. Bligaard, and H. Jónsson, "Origin of the Overpotential for Oxygen Reduction at a Fuel-Cell Cathode," *J. Phys. Chem. B*, vol. 108, no. 46, pp. 17886–17892, 2004.
- [306] Á. Valdés, Z.-W. Qu, G.-J. Kroes, J. Rossmeisl, and J. K. Nørskov, "Oxidation and Photo-Oxidation of Water on TiO<sub>2</sub> Surface," *J. Phys. Chem. C*, vol. 112, no. 26, pp. 9872–9879, 2008.
- [307] Y.-F. Li, Z.-P. Liu, L. Liu, and W. Gao, "Mechanism and Activity of Photocatalytic Oxygen Evolution on Titania Anatase in Aqueous Surroundings," *J. Am. Chem. Soc.*, vol. 132, no. 37, pp. 13008–13015, 2010.
- [308] P. Liao, J. A. Keith, and E. A. Carter, "Water Oxidation on Pure and Doped Hematite (0001) Surfaces: Prediction of Co and Ni as Effective Dopants for Electrocatalysis," *J. Am. Chem. Soc.*, vol. 134, no. 32, pp. 13296–13309, 2012.
- [309] J. Cheng, X. Liu, J. A. Kattirtzi, J. VandeVondele, and M. Sprik, "Aligning Electronic and Protonic Energy Levels of Proton-Coupled Electron Transfer in Water Oxidation on Aqueous TiO<sub>2</sub>," *Angew. Chem., Int. Ed.*, vol. 126, no. 45, pp. 12242–12246, 2014.

- [310] J. Cheng, M. Sulpizi, J. VandeVondele, and M. Sprik, "Hole Localization and Thermochemistry of Oxidative Dehydrogenation of Aqueous Rutile  $\text{TiO}_2(110)$ ," *ChemCatChem*, vol. 4, no. 5, pp. 636–640, 2012.
- [311] M. Gerosa, F. Gygi, M. Govoni, and G. Galli, "The role of defects and excess surface charges at finite temperature for optimizing oxide photoabsorbers," *Nat. Mater.*, vol. 17, p. 1122, 2018.
- [312] F. Ambrosio, G. Miceli, and A. Pasquarello, "Structural, Dynamical, and Electronic Properties of Liquid Water: A Hybrid Functional Study," *J. Phys. Chem. B*, vol. 120, no. 30, pp. 7456–7470, 2016.
- [313] H.-P. Komsa and A. Pasquarello, "Finite-Size Supercell Correction for Charged Defects at Surfaces and Interfaces," *Phys. Rev. Lett.*, vol. 110, p. 095505, Feb 2013.
- [314] J. Kim, U. W. Schmitt, J. A. Gruetzmacher, G. A. Voth, and N. E. Scherer, "The vibrational spectrum of the hydrated proton: Comparison of experiment, simulation, and normal mode analysis," *J. Chem. Phys.*, vol. 116, no. 2, pp. 737–746, 2002.
- [315] X. Zhang and S. Ptasinska, "Dissociative adsorption of water on an  $\text{H}_2\text{O}/\text{GaAs}(100)$  interface: in situ near-ambient pressure XPS studies," *J. Phys. Chem. C*, vol. 118, no. 8, pp. 4259–4266, 2014.
- [316] M. T. Koper, "Theory of multiple proton-electron transfer reactions and its implications for electrocatalysis," *Chem. Sci.*, vol. 4, no. 7, pp. 2710–2723, 2013.
- [317] Y. Q. Gao, Y. Georgievskii, and R. Marcus, "On the theory of electron transfer reactions at semiconductor electrode/liquid interfaces," *J. Chem. Phys.*, vol. 112, no. 7, pp. 3358–3369, 2000.
- [318] A. Tilocca and A. Selloni, "Structure and Reactivity of Water Layers on Defect-Free and Defective Anatase  $\text{TiO}_2(101)$  Surfaces," *J. Phys. Chem. B*, vol. 108, no. 15, pp. 4743–4751, 2004.
- [319] R. Schaub, P. Thostrup, N. Lopez, E. Lægsgaard, I. Stensgaard, J. K. Nørskov, and F. Besenbacher, "Oxygen Vacancies as Active Sites for Water Dissociation on Rutile  $\text{TiO}_2(110)$ ," *Phys. Rev. Lett.*, vol. 87, p. 266104, Dec 2001.
- [320] A. C. Meng, J. Cheng, and M. Sprik, "Density Functional Theory Calculation of the Band Alignment of  $(10\bar{1}0)$   $\text{In}_x\text{Ga}_{1-x}\text{N}/\text{Water}$  Interfaces," *J. Phys. Chem. B*, vol. 120, no. 8, pp. 1928–1939, 2016.
- [321] N. Arai, N. Saito, H. Nishiyama, Y. Inoue, K. Domen, and K. Sato, "Overall water splitting by  $\text{RuO}_2$ -dispersed divalent-ion-doped GaN photocatalysts with d10 electronic configuration," *Chem. Lett.*, vol. 35, no. 7, pp. 796–797, 2006.

## Bibliography

---

- [322] X. Yang, A. Wolcott, G. Wang, A. Sobo, R. C. Fitzmorris, F. Qian, J. Z. Zhang, and Y. Li, "Nitrogen-Doped ZnO Nanowire Arrays for Photoelectrochemical Water Splitting," *Nano Lett.*, vol. 9, no. 6, pp. 2331–2336, 2009.
- [323] K. Maeda, T. Takata, M. Hara, N. Saito, Y. Inoue, H. Kobayashi, and K. Domen, "GaN:ZnO Solid Solution as a Photocatalyst for Visible-Light-Driven Overall Water Splitting," *J. Am. Chem. Soc.*, vol. 127, no. 23, pp. 8286–8287, 2005.
- [324] K. Maeda, K. Teramura, D. Lu, T. Takata, N. Saito, Y. Inoue, and K. Domen, "Photocatalyst releasing hydrogen from water," *Nature*, vol. 440, no. 7082, p. 295, 2006.
- [325] K. Maeda and K. Domen, "Solid solution of GaN and ZnO as a stable photocatalyst for overall water splitting under visible light," *Chem. Mater.*, vol. 22, no. 3, pp. 612–623, 2009.
- [326] K. Maeda, A. Xiong, T. Yoshinaga, T. Ikeda, N. Sakamoto, T. Hisatomi, M. Takashima, D. Lu, M. Kanehara, T. Setoyama, T. Teranishi, and K. Domen, "Photocatalytic overall water splitting promoted by two different cocatalysts for hydrogen and oxygen evolution under visible light," *Angew. Chem., Int. Ed.*, vol. 122, no. 24, pp. 4190–4193, 2010.
- [327] T. Ohno, L. Bai, T. Hisatomi, K. Maeda, and K. Domen, "Photocatalytic water splitting using modified GaN:ZnO solid solution under visible light: long-time operation and regeneration of activity," *J. Am. Chem. Soc.*, vol. 134, no. 19, pp. 8254–8259, 2012.
- [328] A. Miyoshi, S. Nishioka, and K. Maeda, "Water Splitting on Rutile TiO<sub>2</sub>-Based Photocatalysts," *Chem. Eur. J.*, vol. 24, pp. 18204–18219, 2018.
- [329] L. Walle, D. Ragazzon, A. Borg, P. Uvdal, and A. Sandell, "Competing water dissociation channels on rutile TiO<sub>2</sub>(110)," *Surf. Sci.*, vol. 621, pp. 77–81, 2014.
- [330] Z. Geng, X. Chen, W. Yang, Q. Guo, C. Xu, D. Dai, and X. Yang, "Highly Efficient Water Dissociation on Anatase TiO<sub>2</sub>(101)," *J. Phys. Chem. C*, vol. 120, no. 47, pp. 26807–26813, 2016.
- [331] R. Asahi, T. Morikawa, T. Ohwaki, K. Aoki, and Y. Taga, "Visible-light photocatalysis in nitrogen-doped titanium oxides," *Science*, vol. 293, no. 5528, pp. 269–271, 2001.
- [332] Z. Zhao, Z. Li, and Z. Zou, "Water Adsorption and Decomposition on N/V-Doped Anatase TiO<sub>2</sub>(101) Surfaces," *J. Phys. Chem. C*, vol. 117, no. 12, pp. 6172–6184, 2013.
- [333] T. Morikawa, R. Asahi, T. Ohwaki, K. Aoki, and Y. Taga, "Band-Gap Narrowing of Titanium Dioxide by Nitrogen Doping," *Jpn. J. Appl. Phys.*, vol. 40, no. 6A, p. L561, 2001.
- [334] C. Wang, Q. Hu, J. Huang, L. Wu, Z. Deng, Z. Liu, Y. Liu, and Y. Cao, "Efficient hydrogen production by photocatalytic water splitting using N-doped TiO<sub>2</sub> film," *Appl. Surf. Sci.*, vol. 283, pp. 188–192, 2013.

- [335] H. G. Yang, C. H. Sun, S. Z. Qiao, J. Zou, G. Liu, S. C. Smith, H. M. Cheng, and G. Q. Lu, "Anatase TiO<sub>2</sub> single crystals with a large percentage of reactive facets," *Nature*, vol. 453, no. 7195, p. 638, 2008.
- [336] B. Wu, C. Guo, N. Zheng, Z. Xie, and G. D. Stucky, "Nonaqueous Production of Nanostructured Anatase with High-Energy Facets," *J. Am. Chem. Soc.*, vol. 130, no. 51, pp. 17563–17567, 2008.
- [337] X. Han, Q. Kuang, M. Jin, Z. Xie, and L. Zheng, "Synthesis of titania nanosheets with a high percentage of exposed (001) facets and related photocatalytic properties," *J. Am. Chem. Soc.*, vol. 131, no. 9, pp. 3152–3153, 2009.
- [338] X. Y. Ma, Z. G. Chen, S. B. Hartono, H. B. Jiang, J. Zou, S. Z. Qiao, and H. G. Yang, "Fabrication of uniform anatase TiO<sub>2</sub> particles exposed by {001} facets," *Chem. Commun.*, vol. 46, pp. 6608–6610, 2010.
- [339] J. Li and D. Xu, "Tetragonal faceted-nanorods of anatase TiO<sub>2</sub> single crystals with a large percentage of active {100} facets," *Chem. Commun.*, vol. 46, pp. 2301–2303, 2010.
- [340] C. Z. Wen, J. Z. Zhou, H. B. Jiang, Q. H. Hu, S. Z. Qiao, and H. G. Yang, "Synthesis of micro-sized titanium dioxide nanosheets wholly exposed with high-energy {001} and {100} facets," *Chem. Commun.*, vol. 47, pp. 4400–4402, 2011.
- [341] X. Zhao, W. Jin, J. Cai, J. Ye, Z. Li, Y. Ma, J. Xie, and L. Qi, "Shape- and size-controlled synthesis of uniform anatase TiO<sub>2</sub> nanocuboids enclosed by active {100} and {001} facets," *Adv. Funct. Mater.*, vol. 21, no. 18, pp. 3554–3563, 2011.
- [342] C. Z. Wen, H. B. Jiang, S. Z. Qiao, H. G. Yang, and G. Q. M. Lu, "Synthesis of high-reactive facets dominated anatase TiO<sub>2</sub>," *J. Mater. Chem.*, vol. 21, pp. 7052–7061, 2011.
- [343] N. Martsinovich and A. Troisi, "How TiO<sub>2</sub> crystallographic surfaces influence charge injection rates from a chemisorbed dye sensitiser," *Phys. Chem. Chem. Phys.*, vol. 14, pp. 13392–13401, 2012.





# Zhendong Guo

École Polytechnique Fédérale de Lausanne (EPFL), Switzerland

Tel: +41-78-694-3316, E-mail: [zhendong.guo@epfl.ch](mailto:zhendong.guo@epfl.ch)

## Personal Information:

**Date of birth:** 14<sup>th</sup>. Jun. 1987

**Place of birth:** Luoyang, Henan Province, China

**Nationality:** Chinese

## Education:

École Polytechnique Fédérale de Lausanne (EPFL), Switzerland	Nov. 2014 – Jan, 2019
Ph. D. in Material Science and Engineering	
Zhejiang University, Hangzhou, China	Sep.2010 – Mar. 2013
Master of Science in Microelectronics and Solid State Electronics	
Northwestern Polytechnical University, Xi'an, China	Sep.2005 – Jul. 2009
Bachelor of Science in Material Physics	

## List of Publications:

- **Z. Guo**, F. Ambrosio, and A. Pasquarello, “Oxygen defects in amorphous Al<sub>2</sub>O<sub>3</sub>: A hybrid functional study”, *Applied Physics Letters*, 109, 062903 (2016).
- **Z. Guo**, F. Ambrosio, and A. Pasquarello, “Alignment of redox levels at semiconductor-water interfaces”, *Chemistry of Materials*, 30, 94-111 (2018).
- **Z. Guo**, F. Ambrosio, and A. Pasquarello, “Hole diffusion across leaky amorphous TiO<sub>2</sub> coating layers for catalytic water splitting at photoanodes”, *Journal of Materials Chemistry A*, 6, 11804-11810, 2018.
- F. Ambrosio, **Z. Guo**, and A. Pasquarello, “Absolute energy levels of liquid water”, *The Journal of Physical Chemistry Letters*, 9, 3212-3216 (2018).
- **Z. Guo**, F. Ambrosio, and A. Pasquarello, “Extrinsic defects in amorphous oxides: hydrogen, carbon, and nitrogen impurities in alumina.” *Physical Review Applied*, 11, 024040 (2019).

